ZINC OXIDE NANOWIRE-BASED MULTIFUNCTIONAL DEVICES

RIDVAN ERGUN

ZINC OXIDE NANOWIRE-BASED MULTIFUNCTIONAL DEVICES

Ridvan Ergun


Trevelyan College

A Thesis Submitted in Fulfilment of requirements for the Degree of Doctor of Philosophy

Advance Materials and Electronic Devices
Department of Engineering
Faculty of Science
Durham University

November 2024

Read in the name of your lord, who created, created humans from a clinging clot. Read!
Your lord is the most honourable, who taught by the pen, tough human, what they knew not.

(Qur'an 96.1-5)

Dedicated to the parents

Filiz and Cetin Ergun…

ZINC OXIDE NANOWIRE-BASED MULTIFUNCTIONAL DEVICES

Ridvan Ergun

Submitted in fulfilment of requirements for the degree of

Doctor of Philosophy

Abstract

This thesis tackles a significant gap in nanotechnology by developing a multifunctional ZnO nanowire-embedded MIS capacitor capable of UV photodetection, non-volatile memory, and pressure sensing within a single device. While ZnO nanowires are recognized for their individual applications, there is limited research on integrating multiple functions into one device. This work demonstrates a straightforward, scalable fabrication approach using randomly dispersed ZnO nanowire networks, offering a low-cost alternative to complex aligned nanowire methods, and making large-area production feasible for industrial applications.

The challenge of understanding charge transport in random nanowire networks—more complex than in aligned configurations—was addressed using percolation theory and Monte Carlo simulations. By establishing a universal scaling function, this approach links computational and experimental analyses, enabling a reliable model of network conductivity. Experimental validation revealed that tunnelling conduction dominates below the percolation threshold, providing crucial insight into charge transport behaviour.

Optimised at 4 wt.% ZnO concentration, this device prototype uniquely combines UV photodetection, pressure sensing, and non-volatile memory within a single MOS configuration, with each functionality capable of operating independently or simultaneously within the same device. For UV sensing, it achieves fast response times and high sensitivity; in pressure sensing, it offers reliable, scalable capacitive response; and as a memory device, it demonstrates stable and large memory window, repeatable performance. By delivering all these capabilities in one assembly, this work advances multifunctional nanowire-based technology, positioning ZnO nanowire networks as a promising solution for versatile, large-area electronic and optoelectronic applications.

Declaration of Authorship

I, Ridvan Ergun, declare that this thesis titled, “Understanding relevance of percolation on multifunctional device performance” and the work presented in it are my own. I confirm that:

- This work was done wholly or mainly while in candidature for a research degree at this University.
- Where any part of this thesis has previously been submitted for a degree or any other qualification at this University or any other institution, this has been clearly stated.
- Where I have consulted the published work of others, this is always clearly at- tributed.
- Where I have quoted from the work of others, the source is always given. With the exception of such quotations, this thesis is entirely my own work.
- I have acknowledged all main sources of help.
- Where the thesis is based on work done by myself jointly with others, I have made clear exactly what was done by others and what I have contributed myself.

Signed: Ridvan Ergun

Statement of Copyright

Acknowledgments

I would like to express my heartfelt gratitude to everyone who has supported me throughout this project. My sincerest thanks go to my academic supervisors, Prof. Dagou Zeze, Prof. Andrew Gallant, and Prof. Del Atkinson. Their continuous guidance, support, and encouragement have been invaluable over the past few years, and this work would not have been possible without their insights and mentorship.

I am also deeply appreciative of Dr. Chris Pearson and Gary Potts for their help with material preparation and for sharing countless lab-based challenges along the way. Special thanks go to Ian Hutchinson, Neil Clarey, and everyone in the electronics lab for their generous assistance. I am grateful to all academic and support staff within the School of Engineering who, whether through cleanroom support or research advice, have contributed to the progress of this project. My sincere thanks also go to Dr Iddo Amit, Dr. Mark Raine and Mr. Leon Bowen for their technical expertise, and Adam Bickerdike, and Heather Sanders for supportive collaboration. I extend special acknowledgement to Dr. Mehmet Artik, Iman Frozanpoor, Amir Ghasemi, Rui Fang, Mana Saeed, and Dr Rajat Sharma for being inspiring colleagues during this PhD journey.

I am grateful to the Initial Training Network (ITN) of the EU Marie Curie Horizon 2020 Innovative Nanowire DEvicE (INDEED) programme (Grant ID: 722176) for the financial support that made this work possible.

I would like to express my sincere gratitude to Harry and Alistair Ward for their invaluable assistance in designing and constructing the pressure loading and load test rig frame. Their technical expertise and dedication were instrumental in ensuring the success of this project, and I deeply appreciate the time and effort they devoted to this work.

Finally, my deepest gratitude goes to my family for their unwavering support and encouragement throughout my studies. I am especially thankful to my parents, Filiz and Cetin Ergun, whose sacrifices and encouragement have allowed me to reach this point. I am forever indebted to them.

Content

List of Figures

List of Tables

List of Abbreviations

UV-PDs	Ultraviolet Photodetectors
MOSFET	Metal-Oxide-Semiconductor-Field-Effect-Transistors
MIS	Metal-Insulator-Semiconductor
CVD	Chemical Vapour Deposition
MBE	Molecular Beam Epitaxy
ZnO	Zinc Oxide
Zn	Zinc
NWs	Nanowires
MOS	Metal-Oxide-Semiconductor
MOM	Metal – Oxide - Metal
MSM	Metal – Semiconductor - Metal
IoT	Internet of Things
I-V	Current - Voltage
MF	Multi - Functional
UI	User – Interface
SMU	Source / Measure Units
LCR	Inductance capacitance and Resistance
DC	Direct Current
C-V	Capacitance – Voltage
DUT	Device Under Test
Al	Aluminium
ADC	Analogue to Digital Converter

PWM	Pulse Width Modulation
LED	Light Emitted Diode
IDE	Integrated Development Environment
CSV	Comma Separated Values
TEM	Transition Electron Microscopy
FEG	Field Emission Gun
SEM	Scanning Electron Microscopy
HRTEM	High Resolution Transmission Electron Microscopy
SEAD	Selected Area electron Diffraction
STEM	Scanning Transmission Electron Microscopy
Z	Atomic Number
EDX	Energy Dispersive X-ray Spectroscopy
XRD	X-ray Diffraction
FWHM	Full Width Half Maximum
RTA	Rapid Thermal Annealing
XPS	X-ray Photoelectron Spectroscopy
DMF	Dimethylformamide
wt.%	Weight ratio
TO	Tunnelling Oxide
BO	Blocking Oxide
PMMA	Poly(methyl methacrylate)
PL	Photoluminescence
UV-Vis	Ultraviolet-visible Spectroscopy
EiM	Evolution-in-Materio

CBM	Conduction Band Maximum
RG	Renormalisation group
SPICE	Simulation Program with Integrated Circuit Emphasis
WTA	Winner Take All
C-t	Time dependent Capacitance
I-t	Time Dependent Current
FG	Floating Gate
CT	Charge Trapping
ITRS	The International Technology Roadmap for Semiconductors

Chapter 1

INTRODUCTION

1.1 General Overview

Nanowires have emerged as a transformative material in modern electronics due to their unique properties that enable them to be utilised in multiple devices. These nanostructures, with their one-dimensional geometry and high aspect ratio, provide exceptional electrical, mechanical, and optical characteristics that make them suitable for various technological applications. Nanowires exhibit semiconducting, piezoelectric, and magnetic properties, which enable their integration into various devices, including tactile sensors, non-volatile memory, ultraviolet photodetectors (UVPDs), solar cells, and biosensing platforms. Despite their considerable promise in experimental settings, nanowire-based devices face significant obstacles to commercial realisation, mainly due to the challenges associated with large-area production and device integration.

The random assembly of nanowires poses a significant challenge in enabling large-scale fabrication by spray deposition or drop-casting. For nanowire-based devices to achieve consistent and reliable performance, precise control over the alignment, density, and connectivity of the nanowires is required. Even though the inherent randomness of nanowire networks often leads to variability in device performance, making it difficult to produce devices with consistent behaviour across their potential applications, it also promises challenging properties such as charge trapping. Moreover, the methods for fabricating aligned nanowires on a commercial scale remain complex and costly, further restricting their adoption in commercial applications. These limitations have hindered the practical deployment of nanowire-based devices despite their substantial potential in enhancing electronic, optical and mechanical systems.

Another critical issue in nanowire research is the challenge of device miniaturisation. As Moore's Law predicted in the 1970s, over the past 40 years, there has been a significant increase in the number of transistors that can be integrated onto a chip at a lower or similar cost. This has resulted in notable advancements in traditional electronic technologies. The latest metal-oxide-semiconductor-field-effect-transistors (MOSFET), the basic components of most electronic circuits, have now reached a gate length of 3 and 5 nm [1-3], enabling chips to contain 5.3 trillion

transistors. Furthermore, recent reports have also confirmed the successful development of 2 nm technology in 2025 [2].

As electronic devices continue to shrink in size, the physical limits of miniaturisation are being reached. Traditional approaches to improving device performance, such as increasing transistor density or reducing the size of individual components, are becoming less effective due to fundamental physical constraints [1, 4]. To overcome these limitations, researchers are exploring the development of devices that can perform multiple tasks within a single device node. Such devices offer a promising solution, enabling integrating multiple functions into a single platform, thereby improving overall device efficiency and reducing the need for additional components.

This thesis presents a novel approach to addressing the limitations of large-scale nanowire-based device fabrication for developing a multifunctional device prototype, which can also be transferred to commercial applications due to low-cost and large-area fabrication availability. The ZnO nanowire-embedded metal-insulator-semiconductor (MIS) capacitor integrates multiple functions within a single configuration, including non-volatile memory, UV photodetection and pressure sensing. At the core of the device is a network of zinc oxide (ZnO) nanowires which possess unique electrical, optical, and mechanical properties that enable the multifunctionality of the device. By embedding ZnO nanowires into the insulator layer of the MIS structure, the device can perform several tasks simultaneously, demonstrating how a single system can be optimised to achieve multifunctionality.

1.2 ZnO Nanowire-Based Electronics

Semiconductor nanowires (NWs) have attracted great interest due to their potential in advancing nanoscale technologies [5]. Zinc Oxide (ZnO) NWs, formed from a II-VI semiconductor, are particularly remarkable for their distinct wide-bandgap semiconducting properties (3.4 eV) and high exciton binding energy [6-8], making them attractive in various applications such as optoelectronic systems [9-11], solar cells [12, 13], photocatalysts, and sensors [14, 15]. Moreover, their low toxicity, biodegradability, affordability and adaptability in various forms have received considerable attention, leading to extensive use in the biomedical and healthcare industries due to their electrochemical and optical features [16].

It is noted that there are several factors affecting the properties of ZnO NWs and the performance of their devices, such as nanowire diameter, length and inter-wire spacing [17] noting the significant surface-to-volume ratio of 1D nanowires. In addition to the physical properties of the nanowires, matrix materials, which are used as transparent reinforcement materials, affect the device performance [18]. ZnO is known to possess a significant exciton binding energy of 60 meV,

making it possible for the excitonic emission of ZnO to persist even at room temperature [8]. This feature is particularly crucial for developing light-emitting devices, including lasers. ZnO tends to exhibit unintentional n-type doping which is attributed to native defects in its crystalline structure [7, 8]. These defects include oxygen vacancies (missing oxygen atoms at regular lattice positions) and zinc interstitials (additional Zn atoms occupying interstitial positions in the lattice) [11, 19].

ZnO NWs also demonstrate piezoelectric and photoelectric characteristics [13, 20]. Recently, owing to their unique electronic-mechanical coupling behaviour, they have been extensively explored for their energy conversion capabilities. Experimental and theoretical research has been undertaken to comprehend their structure, properties, and potential applications, such as piezo-pressure and photo-mechanic applications [21, 22]. The ZnO photoluminescence spectrum consists of several UV emission bands and the visible band in the violet, blue, green, yellow, and orange-red regions. ZnO-based nanocrystal materials feature high electron mobility, robust transparency, a broad bandgap, and optical and electrical properties. Due to the photo-current properties, ZnO-based nanostructures are widely studied in UV-photodetection applications with high sensitivity and response times [10, 23, 24].

The exceptional properties of ZnO nanowires have allowed them to be used in a wide range of applications, but their full potential in multifunctional device prototypes remains unexplored. Current literature provides limited focus on the development of devices that can simultaneously perform more than one function [25], which is a critical requirement for addressing the growing limitations posed by Moore's Law. This thesis aims to bridge that gap by investigating the fabrication and performance of multifunctional devices that utilise ZnO nanowires. Specifically, the thesis details how ZnO nanowire-based devices, particularly those using MIS configurations, can be optimised for UV-PDs (see Chapter 6) while simultaneously performing other functions such as non-volatile memory storage and pressure sensing in Chapter 7 and 8. By demonstrating the feasibility of these multifunctional devices, this work contributes to ongoing efforts to develop scalable, cost-effective solutions that can meet the demands of modern electronics beyond the limitations of Moore's Law.

1.2.1 Challenges in Large-Area Nanowire-Based Device Fabrication

One of the primary barriers to the widespread adoption of nanowire-based devices is the difficulty in producing nanowire-based devices on a large scale. Nanowires are typically synthesised using bottom-up fabrication techniques such as chemical vapour deposition (CVD) [26], molecular beam epitaxy (MBE) [27], and solution-phase synthesis [28]. While these methods can produce high-quality nanowires with excellent control over their properties, they are not well-suited for large-area applications due to the complexity and cost of the processes involved. Moreover, these

fabrication techniques often result in nanowires with random orientations, although it makes it challenging to achieve uniform device performance, the randomness can bring another challenge such as charge trapping for non-volatile memory performance.

In practical applications, nanowire-based devices require precise nanowire alignment and density control to ensure consistent electrical and mechanical behaviour. However, the random assembly of semiconductor nanowires in large-area devices introduces variability in performance, as the connectivity between individual nanowires can vary significantly across different regions of the device. This randomness affects the conduction paths within the network, leading to fluctuations in electrical properties such as network resistance and charge transport.

To address these challenges, various strategies have been proposed to control the assembly of nanowires on a large scale. One approach uses top-down fabrication techniques, such as lithography, to pattern nanowires onto a substrate [29]. While this method offers precise control over nanowire placement, it is limited by the high cost and complexity of the lithography process. Another approach is to use external forces, such as electric or magnetic fields, to align nanowires during deposition. However, these methods are only sometimes scalable and may require specialised equipment that adds to the overall fabrication cost.

This thesis introduces an alternative approach to large-scale nanowire fabrication by employing a drop-casting technique. Drop-casting is a simple and cost-effective method that allows to control for the random distribution of nanowires over large areas explained in Chapter 3. In this process, a solution containing ZnO nanowires is deposited onto a substrate, where it dries to form a random network. While the resulting nanowire network is random, it exhibits functional properties suitable for various applications, including charge storage, UV photodetection, and pressure sensing. Drop-casting makes it possible to fabricate nanowire-based devices on a large scale without complex and expensive fabrication techniques, making them suitable for many potential commercial applications.

1.3 Percolation Theory and Charge Transport in Nanowire Networks

Investigating the dynamic evolution of nanomaterial properties in device assemblies and studying their computational capabilities involves using a low-cost fabrication process for efficient and large-area devices. This process relies on the ability to control the spacing between nanowires in a random network to achieve optimal device efficiencies. Nanowires (NWs) can combine important properties, such as the localisation of charge carriers in one, two, or three dimensions, with complexities of the fabrication process, providing advances over existing planar technologies that currently serve as the foundation of the electronic industry. Recent advances indicate that

NWs with a range of predefined properties (such as size, shape, chemical composition, and crystalline structure) can be grown, offering an excellent paradigm for developing novel functional device prototypes, including biosensors, solar cells, transistors, and lasers. The essential step is to take this critical mass of scientific knowledge and develop routes for effectively transferring NW functionality into device technologies.

The random nature of nanowire networks presents a challenge in controlling their electrical properties [30, 31]. Percolation theory provides a mathematical framework for understanding how connected clusters form in a random medium, such as a network of randomly distributed constituents [32]. To overcome the complication of randomness, percolation theory is applied to model which, in turn, can be used to optimise the behaviour of the random sticks network [33, 34]. Applying the theory makes it possible to determine the percolation threshold which is the critical point at which a sufficient number of nanowires form a continuous conductive path across the device. The percolation threshold plays a crucial role in determining the electrical, mechanical, and sensing properties of the nanowire network.

In the context of this thesis, percolation theory is used to optimise the material composition of the ZnO nanowire network and to model charge transport within the device. Below the percolation threshold, the nanowires are not physically connected, and the primary mode of charge transport is tunnelling between isolated nanowires [35-37]. In this regime, the electrical conductivity of the network is low, and the device may be more sensitive to external impacts but may not perform optimally. However, once the nanowire concentration exceeds the percolation threshold, continuous pathways are formed across the device which allow for percolation-dominated conduction. This transition from tunnelling to percolation conduction is critical for optimising the performance of a device in its various functions.

Despite the utility of percolation theory for modelling random nanowire networks, there remains a significant gap in the literature regarding the experimental validation of these models. Existing studies are often limited in their account of the complexities of charge transport, especially in mixed regimes where both tunnelling and percolation play significant roles. Additionally, the correlation between experimental results and theoretical predictions has been insufficiently explored. This thesis addresses these limitations by employing the shortest-path algorithm for Monte Carlo simulations, which promises faster computing while still accurately predicting percolation thresholds (see Chapter 4). The research question centres on investigating how well percolation theory, supported by the shortest-path algorithm, can be experimentally validated in ZnO nanowire networks and whether adjustments are needed to better account for the dual conduction mechanisms of tunnelling and percolation (see Chapter 5).

1.4 Multifunctional Device Prototype

The MIS capacitor device developed in this thesis is designed to perform multiple functions using the same ZnO nanowire network. The ZnO nanowires are embedded in the insulator layer of the MIS structure, allowing the device to operate as a non-volatile memory storage unit, a UV photodetector, and a pressure sensor. This multifunctionality is achieved by utilising the unique properties of the ZnO nanowires, which can exhibit semiconducting, optical, and piezoelectric characteristics.

The characteristics of the multifunctional (MF) device prototype demonstrate its potential for simultaneous integration of programming and sensing capabilities within a single device node. This makes it highly suitable for advanced applications across various Internet of Things (IoT) technologies, including health monitoring, biomedical systems, robotics, artificial sensing for robotics, and environmental monitoring. This prototype uniquely combines non-volatile memory for programmable functionality with the ability to sense UV light and pressure. The non-volatile memory capability enables reliable on/off programming, while the integrated sensing functionalities provide real-time environmental and mechanical feedback. These attributes establish the device as a robust and versatile platform, offering significant advantages for IoT applications in these critical fields.

1.4.1 Non-Volatile Memory

A non-volatile memory device can retain stored information even when not powered [38], and flash memory and read-only memory are a type of non-volatile memory. Floating-gate flash memory has been developed successfully in recent decades through continuous down-scaling of cell dimensions to achieve high data-storage density [39], fast program/erase speeds, low operating voltage, and low power consumption [40]. The increasing fabrication density of flash memory has been mainly driven by area scaling. As the spacing between adjacent devices decreases, parasitic capacitance plays an increasingly dominant role in the device's performance, as data stored in adjacent cells can interfere with each other through capacitive coupling [41]. Moreover, a limited margin poses a significant challenge to the reliability of floating-gate memory devices, as the number of electrons stored in the floating-gate significantly decreases with continual down-scaling of the cell size [42].

The ability to store data non-volatile is essential for many modern electronic devices [43, 44]. In this device, the ZnO nanowires play a critical role in charge trapping, which is the underlying mechanism for memory storage [45]. The network of ZnO nanowires serves as a charge-trapping layer, where charges are stored in the nanowire junctions. The memory mechanism is based on

the ability of the ZnO nanowires to trap and retain charges, enabling the device to store information even when power is not supplied. This makes the device suitable for applications in data storage, where reliability and data retention are paramount. It should be noted that this thesis focuses on a capacitive non-volatile memory based on a metal-oxide-semiconductor (MOS) or metal-oxide-metal (MOM) device configuration in Chapter 7.

1.4.2 UV Photodetection

The MIS capacitor device also functions as a UV photodetector by utilising the optical properties of ZnO nanowires. ZnO is known for its high sensitivity to UV light, making it an ideal material for UV photodetection [9, 23, 46]. When exposed to UV light, the ZnO nanowires generate electron-hole pairs, leading to changes in the charge density of the network. This change in charge density can be measured by a change in the capacitance, forming the basis of a UV light detector [47]. MIS device formation is based on changes in the charge accumulation because of external impacts on devices, such as UV-light exposure on the gate electrodes. It has been widely studied that ZnO nanowires generate charges under blue and UV light radiation due to the absorption and desorption of oxygen on the ZnO nanostructure's surface [48, 49]. The intensity of the charge generation rate of the device increases proportional to the applied radiation. The optoelectronic effect can be used in two terminal in-plane device formations: Field effect transistor, photodetector [48-50], and solar cells [15]. Therefore, these devices show promising potential for optoelectronic applications.

However, one of the main limitations in the literature lies in the incomplete understanding of the conduction mechanisms affecting UV-PD performance, particularly in metal-semiconductor-metal (MSM) structures. While previous studies have provided theoretical perspectives for the percolation behaviour of nanowire networks, the link between percolation theory and experimental UV-PDs performance has yet to be thoroughly validated in detail. This thesis addresses this limitation by applying percolation theory (in Chapter 4) to model and experimentally validate the conduction mechanisms in ZnO nanowire-based MSM UV-PDs in Chapter 6. Specifically, this research proves that the tunnelling and percolation transition directly impact UV-PD sensitivity and response time, which had been previously theorised but not conclusively demonstrated.

In addition, the study investigates MIS devices, where the ZnO nanowire-embedded architecture shows promising UV photodetection capabilities (in Chapter 6) and exhibits multifunctionality, as explored in Chapter 8. The key research question tackled in this thesis is how well percolation theory and charge transport models can be linked to experimental data to optimize the performance of MSM and MIS UV-PDs by promising low-cost fabrication techniques. By filling this

gap, the thesis contributes to a more complete understanding of charge transport in ZnO nanowire networks, which is critical for developing high-performance, large-area, and cost-effective UV-PDs.

1.4.3 Pressure Sensing

Pressure sensors are critical components in various applications, ranging from medical devices to industrial monitoring systems. They can be broadly classified into several types based on their operating principles. Resistive pressure sensors are one of the most common types and are further divided into strain gauges and piezo resistors, conducting polymer composites, and conductive polymers. These sensors typically rely on the change in resistance when subjected to pressure. Another important category is piezoelectric pressure sensors, which generate an electric charge in response to mechanical stress [51]. Inductance-based pressure sensors operate based on changes in inductance when exposed to pressure, making them suitable for specific environments. Finally, capacitive pressure sensors, which are the focus of this thesis, measure pressure by detecting changes in capacitance between two conductive plates as the distance between them varies under pressure [52]. Capacitive sensors offer high sensitivity, low power consumption, and the potential for integration into flexible and multifunctional devices, making them ideal for modern electronic applications.

Capacitive pressure sensors are versatile across a range of applications. They measure vascular pulse at 10-20 kPa, human fingertip texture and shape sensing at 10-40 kPa, and are suitable for tactile robotics, with a broader pressure range of 10-100 kPa and beyond. Their adaptability makes them ideal for high-sensitivity tasks across these diverse fields [53]. In this thesis, we explore a wide variety of pressure ranges, from 0.5 Pa to 10 kPa, making these devices suitable for applications such as wearable electronics and robotics.

The device not only shows memory and photodetection functionalities but also serves as a pressure sensor by improving the dielectric properties of the embedded ZnO layer [54]. The capacitive pressure sensor operates based on the principles of a parallel plate capacitor, where the dielectric layer in between the plates plays a crucial role. When vertical pressure is applied to the gate electrode, it changes the distance between the plates, causing a measurable change in capacitance. By optimising the permittivity of the dielectric layer without altering ZnO nanowire content, the capacitance is increased, thereby improving the signal-to-noise ratio for pressure detection. The science research question tackled in this thesis is how percolation theory and charge transport models can be adapted to account for these variations in pressure sensitivity, enabling the development of high-performance, multifunctional devices suitable for wide-ranging applications.

1.5 Challenges and Opportunities in Device Miniaturisation

The ever-increasing demand for smaller, faster, and more efficient electronic devices has led to the pursuit of device miniaturisation. As Moore's Law predicted, the number of transistors on integrated circuits has doubled approximately every two years, significantly increasing computational power. However, as devices approach the nanoscale, fundamental physical limits are being encountered, creating a need for novel approaches to overcome the limitations of traditional miniaturisation strategies. The reliance on scaling down single-function components, such as transistors, has reached a saturation point where quantum effects, heat dissipation, and power consumption impose significant challenges [1, 4].

One promising solution to these limitations is the development of multifunctional devices that integrate several functionalities within a single platform. Rather than continuing to scale down individual components, multifunctional devices maximise efficiency by combining tasks requiring multiple individual devices. This approach conserves space, reduces power consumption, minimises heat generation, and enhances overall device performance. Furthermore, multifunctional devices offer the potential to address the growing complexity of modern electronics by integrating sensing, processing, and storage capabilities into a unified system.

The MIS capacitor device prototype developed in this thesis offers this approach by combining non-volatile memory, UV photodetection, and pressure sensing in a single configuration. Using ZnO nanowires as the core functional material enables this multifunctionality, as their semiconducting, optical, and mechanical properties are well-suited to these diverse tasks. Integrating multiple functions into a single device makes it possible to create more compact and efficient systems to perform a wide range of tasks, paving the way for the next generation of miniaturised electronics.

Multifunctional devices are desirable in fields such as wearable technology, the Internet of Things (IoT), and flexible electronics [16], where space is at a premium, and devices must be lightweight, efficient, and capable of operating under diverse conditions. For example, in wearable sensors, a multifunctional device that can monitor UV exposure, store data, and detect pressure changes could provide users with a comprehensive health monitoring system without requiring multiple separate devices. Similarly, in IoT applications, multifunctional nodes that combine sensing, processing, and communication capabilities could reduce power consumption and improve the overall efficiency of interconnected systems.

However, despite the significant potential of multifunctional devices, several challenges must be addressed. One of the key challenges is ensuring that each function operates effectively without

compromising the performance of the others. In the case of the MIS capacitor device, for example, the same ZnO nanowire network is responsible for charge storage in the non-volatile memory function and mechanical sensing in the pressure sensor. Therefore, it is crucial to optimise the material composition and device architecture to ensure that each function performs optimally while maintaining the overall functionality of the device.

As discussed earlier, the application of percolation theory provides a framework for optimising the ZnO nanowire network to ensure that it performs effectively across multiple functions. By tuning the nanowire concentration and understanding the percolation threshold, the device's performance in terms of sensitivity, charge retention, and mechanical stability can be enhanced. Additionally, the drop-casting fabrication technique ensures that the device can be produced on a large scale and low cost, making it feasible for practical applications in industries that require multifunctional devices.

1.6 Research Hypothesis and Thesis Structure

The exceptional properties of ZnO nanowires make them highly suitable for multifunctional device applications; however, the understanding of charge transport mechanisms within random nanowire networks remains incomplete. This thesis hypothesises that by thoroughly modelling and experimentally correlating the charge transport mechanisms in random ZnO nanowire networks, particularly through the percolation theory for evaluate the properties of random nature in optimal device applications, it is possible to develop state-of-the-art multifunctional metal-insulator-semiconductor (MIS) and metal-semiconductor-metal (MSM) devices. This understanding will enable the integration of random ZnO nanowire networks into prototype devices, demonstrating improved performance in UV photodetection, non-volatile memory, and pressure-sensing functionalities. The research question driving this thesis is: How can the percolation theory and charge transport models be experimentally validated and adjusted to optimise the performance of random ZnO nanowire networks in multifunctional devices, particularly in MSM and MIS configurations.

To address this research question, the thesis sets out the following four objectives, each corresponding to a result chapter:

- **Objective 1:** Model the percolation behaviour of random ZnO nanowire networks and validate this using statistical physics approaches, specifically employing the shortest-path algorithm to efficiently simulate percolation thresholds. This objective is addressed in Chapter 4, which focuses on transforming an arbitrary network into a universalised system and understanding its conductive properties.

- **Objective 2**: Correlate the percolation model with experimental charge transport data. Through I-V measurements, evaluate how the percolation threshold influences conductivity in ZnO nanowire networks and how charge transport evolves with nanowire density. This objective is explored in Chapter 5, where the experimental results are compared with Monte Carlo simulations to validate percolation theory in real-time applications.
- **Objective 3**: Investigate the UV photodetection capabilities of ZnO nanowire networks in both MIS and MSM device configurations, focusing on how percolation and tunnelling conduction mechanisms impact UV detection performance. In Chapter 6, the performance of MSM devices is evaluated based on direct current conduction, while MIS devices are examined for their capacitive charge response, highlighting their sensitivity and multifunctionality in UV detection.
- **Objective 4:** Demonstrate the multifunctionality of ZnO nanowire-embedded MIS devices by analysing their non-volatile memory and pressure-sensing capabilities. In **Error! Reference source not found.**, the same ZnO nanowire network that facilitates UV detection is shown to perform reliable memory storage and pressure sensing, offering a robust, multifunctional solution for advanced electronic applications.

This thesis is structured to systematically address the research question and objectives. Each chapter builds upon the previous one to provide a comprehensive understanding of the development, modelling, and testing of the multifunctional ZnO nanowire-embedded MIS capacitor device.

- Chapter 2 introduces the custom-designed multifunctional device testing platform developed for ZnO nanowires-embedded MIS devices. This platform enables the devices to undergo testing for non-volatile memory, UV photodetection, and pressure sensing. An overview of the characterisation equipment is also provided.
- Chapter 3 discusses the materials used for device fabrication, with a focus on the properties of random ZnO nanowire networks and their integration into MIS structures. It details the fabrication process, emphasizing the drop-casting technique used to assemble the nanowire network, and provides background from the literature.
- Chapter 4 explores the application of percolation theory to random ZnO nanowire networks using Monte Carlo simulations. The shortest-path algorithm is used to improve simulation efficiency, providing a critical link between theoretical modelling and real-world device performance. This chapter lays the foundation for understanding the conductive behaviour of ZnO nanowire networks and their role in device functionality.

- Chapter 5 presents experimental results that validate the percolation models developed in Chapter 4. The focus is on correlating the statistical predictions of percolation theory with experimental data from current – voltage (I-V) measurements, analysing the charge transport in ZnO nanowire networks at different densities on microelectrode arrays.
- Chapter 6 investigates the UV photodetection capabilities of ZnO nanowire networks in both MSM and MIS device configurations. In MSM devices, percolation theory and tunnelling conduction mechanisms dominate, resulting in high sensitivity to UV light. In contrast, MIS devices rely on capacitive charge mechanisms, which are influenced by nanowire concentration and electrode separation, enabling multifunctionality. The chapter highlights the differences between the two configurations and explores the factors affecting their UV-PD performance.
- Chapter 7 demonstrates the ZnO nanowire-embedded MIS devices, focusing on non-volatile memory storage capability in addition to UV photodetection. Experimental results are presented, including write/erase cycles with respect to the ZnO intake in network. The chapter presents the versatility of the MIS devices in performing charge storing abilities and the role of ZnO nanowire network simultaneously.
- Chapter 8 explores the capacitive pressure sensing capabilities of ZnO nanowire-embedded MIS devices. The pressure-sensing functionality is tested under semi-automated pressure loading, showing the potential of these devices in pressure-sensitive applications. Following this, the chapter presents the multifunctionality of the device, integrating UV photodetection and non-volatile memory under pressure loading within the same device configuration. The ability of the device to perform multiple functions simultaneously is analysed, highlighting its versatility for the applications presented.
- Chapter 9 provides a final summary of the key findings and discusses the broader implications for nanowire-based multifunctional devices. The contributions to the understanding of percolation theory in nanowire networks and its impact on charge transport are highlighted, along with suggestions for future research directions. The chapter emphasizes potential improvements in fabrication techniques and further optimization of ZnO nanowire networks for future multifunctional applications.

1.7 Summary

This thesis introduces the rationale for a comprehensive study of a MIS capacitor device based on ZnO nanowires network to exhibit multifunctional properties. Integrating non-volatile memory storage, UV photodetection, and pressure sensing into a single device addresses key challenges in large-scale nanowire fabrication and device miniaturisation. The use of percolation theory to model and optimise the ZnO nanowire network provides valuable insights into the electrical and

mechanical properties of random nanowire networks, enabling the development of high-performance multifunctional devices.

The drop-casting fabrication technique employed in this work ensures that the device can be produced on a large scale, making it suitable for practical applications in industries that require multifunctional devices. The experimental results demonstrate that the ZnO nanowire network enhances the performance of the device across its various functions, making it a promising candidate for applications in flexible electronics, wearable sensors, and the Internet of Things.

In conclusion, the multifunctional MIS capacitor device developed in this thesis represents a significant advancement in nanowire-based electronics. By integrating multiple functionalities into a single platform and employing scalable fabrication techniques, this work is proposing a way forward for the next generation of electronics capable of multifunctionality, contributing to the efforts to overcome the limitations of Moore's law.

Chapter 2

EXPERIMENTAL TECHNIQUES

2.1 General Overview

This chapter provides a comprehensive foundation for the experimental work and testing methodologies employed in the subsequent sections of the thesis. It begins by detailing the design and implementation of a multi-functional (MF) device-testing platform, which allows for the simultaneous measurement of capacitance and DC conductivity under varying conditions, such as pressure and UV light exposure. This semi-automated, computer-controlled test rig is integral to the advanced applications discussed later in the thesis, specifically for UV photodetection in Chapter 6 and non-volatile memory and pressure sensing in Chapter 8.

The chapter also presents an overview of the key characterisation techniques used to analyse the properties and crystallography of ZnO nanowire networks and MOS devices. These methods are critical to understanding the material and electrical properties that will be explored in greater detail in the following chapters.

In addition, the fabrication and characterisation of a custom-designed microelectrode array design are presented. This array, featuring 11 in-plane two-terminal electrodes with varying gap sizes between 1 and 50 microns, will be employed in Chapter 5 to correlate the conductivity model introduced in Chapter 4. Furthermore, it will serve as the basis for UV photodetection studies in Chapter 6, using an Al / ZnO-NWs / Al (MSM) device configuration.

The chapter concludes with a detailed discussion of the fabrication processes for MOS and MIS devices, setting the stage for exploring the functional applications of ZnO nanowires in capacitors. These devices will be crucial in demonstrating the multifunctional capabilities of the ZnO nanowire network in Chapters 6, 7 and 8, particularly for photodetection, non-volatile memory, and pressure-sensing applications. Overall, this chapter lays the groundwork for the following experimental investigations and results.

2.2 The Test Station/Rig

This section provides a detailed description of the MF test rig used for conducting electrical and mechanical testing on MF devices. The primary objective of this rig is to measure the accurate

electrical properties of devices reliably under various mechanical loads and UV radiation exposure. The development of this testing rig involved the creation of hardware, software, and user interface (UI) components.

The devices are electrically triggered and monitored using the Keysight Precision Source/Measure Unit (SMU) B2902A [55] and BK Precision Meter 894 Inductance, Capacitance, and Resistance (LCR) meter [56] within the MF test rig, as depicted in Figure 2-1(a). The SMU functions as a highly accurate direct current (DC) power source that applies a specified voltage to the device while concurrently measuring the current. The LCR meter monitors the capacitance (C) and conductance (S) in parallel. The SMU and LCR meter are linked to each other by a DC bias voltage box due to the insufficient maximum DC voltage of the LCR for MF device testing, as illustrated in Figure 2-1(c).

The samples are tested on a test frame (Figure 2-1(d)), on which a DC actuator (Figure 2-1(e)) and a load cell (Figure 2-1(f)) are mounted for pressure testing [57]. These devices are also electrically connected for force and sensing through the devices. The UV source, an SVC 365nm UV LED (Figure 2-1(g)), is carefully connected and powered by the second channel of the SMU for UV radiation [58]. This is crucial for monitoring the effect of UV radiation on the electrical device signal, which is essential in MF device testing. During experiments, the UV source of 365nm is positioned at a constant 5cm distance from the tested sample to ensure uniform UV exposure. Finally, the Arduino Uno controls and monitors the DC motor stepped actuator and load cell (Figure 2-1(h)).

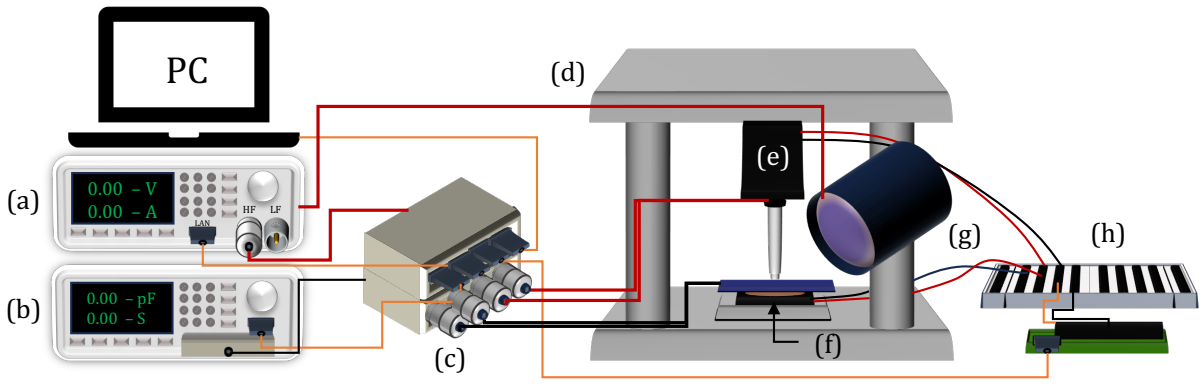

Figure 2-1: Illustration of the multifunctional test-rig consisting of SMU (a), LCR meter (b), interface adapter (c), test-rig frame (d), actuator motor (e), load cell (f), UV torch (g), Arduino Uno (h).

The semi-automated MF device test rig, controlled using Python code, is capable of precisely measuring output current or capacitance while applying either a voltage sweeps or a constant

voltage. Additionally, the attached UV source can provide constant UV radiation during the experiment or be cycled on and off as required. The rig enables devices to undergo MF testing for pressure, UV photodetection, and non-volatile memory performance using various rig test modes, as elaborated in the subsequent section of the thesis.

The development of the testing rig was classified into three distinct categories: hardware, software, and user interface (UI). Each of these categories significantly contributed to shaping the functionality and effectiveness of the final product, as detailed below.

2.2.1 The Hardware of the Rig

2.2.1.1 Sources and Meters

The Keysight B2900A Series bench-top Source/Measure Units (SMUs) are designed to both source and measure voltage and current, making them suitable for a wide range of IV (current versus voltage) measurement tasks that demand exceptional resolution and accuracy [55]. They have a voltage sourcing capability of up to ±40 V and a current sourcing capability of up to ±3 A DC and ±10.5 A pulsed. Moreover, these units provide precision with a minimum 10 fA/100 nV sourcing and measuring resolution.

The 894 LCR meters are precision instruments capable of measuring components and materials' inductance, capacitance, and resistance at DC or within a frequency range from 20 Hz to 500 kHz [56]. They offer flexible AC and DC test signal configuration, allowing for adjustment of AC test signal voltage from 5 mVrms to 2 Vrms, and AC up to 66.7 mArms, depending on the AC impedance selected. Additionally, they permit the addition of a DC bias signal to the measurements.

Both pieces of equipment feature standard USB, RS232, LAN, and GPIB interfaces, enabling remote control through SCPI commands. This facilitates more precise and customised testing using a computer. In this study, a LAN cable was used to connect the SMU, while an RS232 cable was used to connect the LCR meter.

2.2.1.2 DC Bias Box

The four-terminal type test fixture is a is suitable for applications requiring DC biasing from an external voltage source. It is designed to work with the 894 LCR meter. The LCR meter alone has a maximum voltage range of ±2.5 V, meaning that I-V and capacitance-voltage (C-V) could only be perform in the low voltage region of ±2.5 V, which is insufficient to fully characterise the nanocomposites. Therefore, to address this limitation, an additional DC supply box (11CR-8110G201) is used. With a maximum voltage handling capacity of up to ±200 V, it is a robust and

reliable solution for device testing that requires high DC bias [59]. Its input resistance of 100 kΩ with 2% tolerance is also valuable for achieving precise and accurate results. Additionally, it can work within a frequency range of 50 Hz to 2 MHz, making it an ideal choice for MF device characterisation seeking a reliable and versatile solution.

2.2.1.3 The Frame

The frame illustrated in Figure 2-1(d) was created in SolidWorks [60] to transfer stress from the actuator to frame flex rather than minimise the device under test (DUT). To test multiple devices in a grid format without moving the sample, the frame needed to move in the x and y direction for semi-automatic testing integration. This was achieved using two aluminium (Al) IGUS slides. The compressing direction is the z-axis. The top section of the frame accommodates the dimensions of the linear actuator (with space for heat dissipation) so that the force exerted downwards during displacement is resisted by the actuator frame alignment with the top slide. The precision of the SolidWorks design was crucial since the actuator had a total stroke of just 19.05 mm, and tests were required both with and without the 7 mm height load cell.

2.2.1.4 Arduino Uno

The Arduino Uno microcontroller is equipped with an 8-bit RISC microprocessor purchased from Arduino (n.d.) [61]. It has the capability to compile programs externally and load them via a USB, which also functions as a serial communication tool. This allows for an easy input-output interface to a PC, enabling precise and autonomous pressure tests.

The Arduino Uno has 32KB of flash memory for program storage, with 0.5KB reserved for the bootloader. Due to memory limitations, it's important to carefully compartmentalise the test-rig functions. It uses a 2048 SRAM to store all dynamic memory. It is crucial to avoid the storage of excessively long analogue input data arrays. The analogue input voltage is converted using an on-board 10-bit analogue to digital converter (ADC) and indexed with an 8-bit address. To store around 600 separate data points, 25% of the on-chip dynamic memory is reserved for other local variables. Storing the analogue data on-chip is a key strategy, instead of immediately outputting the values to the serial connection, as two analogue readings need to be taken simultaneously for some functions (i.e. voltage from the load cell and voltage from the sample). Iteratively outputting the pair of values would make retrieving the data more manageable. With its 14 independent pulse width modulation (PWM) output pins, the Arduino Uno can deliver a 0V logic low voltage and a 5V logic high voltage.

2.2.1.5 Actuator

The 21H4U-2.5-907 Captive Hybrid Linear Actuator (seen in Figure 2-2a) was carefully chosen based on precise stepping control requirements. The actuator driver, controlled by an Allegro A3967 micro stepping driver chip [62], which is the key component controlling the movement of the actuator for controlled pressure load onto the MF devices. Among the crucial factors was the need for a maximum force of over 50 N at a low driving rate of less than 100 Steps/second, which was necessary for compressing larger Young's modulus materials.

All inputs to the driver except the 6V DC motor power supply, provided by an AC to DC mains adaptor, are triggered with 5V PWM and are therefore compatible with the Arduino's outputs. The A3967 can step the actuator at a selectable full-step, half-step, quarter-step, or eighth-step mode. The driver is fitted with a current limiting potentiometer delivering per-phase current ranging from 150 mA/phase to 700 mA/phase since the actuator requires a different per-phase current for each step mode. A rising edge on the STEP pin triggers a single step at the selected step mode. High voltage on the DIRECTION pin actuates outwards and low voltage inwards. A high voltage is applied to the ENABLE pin to allow the driver to start operating. The driver is grounded to one of the two ground pins of the Arduino Uno. A step mode of an 1/8 was selected by prioritising shaft displacement precision over actuator speed. This results in the minimum shaft displacement of 4.125µm. The step mode is selected with a 2-bit PWM signal from the microcontroller.

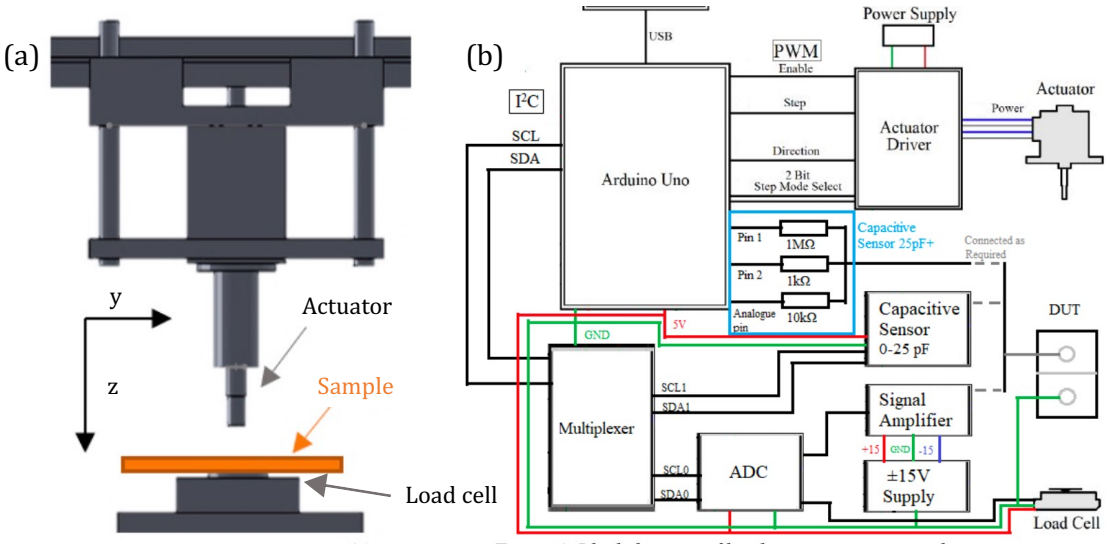

Figure 2-2: (a) Demonstration of linear actuator sample compression, (b) block diagram of hardware components and interconnections taken from Master dissertation by Alistair Ward [63].

The movement of the actuator was controlled by a stepper motor driver board that had a variable current per phase, ranging from 150 to 700 mA. This provided a significant margin for the required 490 mA. The board was capable of micro-stepping, which means splitting motor steps into less than 1.8° increments. Two drivers were tested, and the Allegro A3967 chip was selected because it can cause significant accuracy problems regarding actual versus triggered step displacement movement. The maximum output force for this step was found to be below 10N. As no duty cycle frequency testing was required, shaft speed was unimportant, so 1/8th was selected. The micro-stepping scale was selected using a 2-bit PWM signal, and the DIRECTION and ENABLE inputs polarity required for the movement was controlled by the Arduino digital pins. Every step was triggered by a rising edge on the STEP input. Figure 2-2(b) shows that the driver was used.

2.2.1.6 Load Cell

Alistair Ward designed the rig, which is responsible for applying pressure and measuring the resultant force during the tests as a part of master dissertation [63]. The low-force load cell labelled FS2050 [64] was chosen for its maximum capacity of 14.7 Newton (N), which covers most of the actuator's 18 N micro stepped force range. This load cell uses four piezoresistive strain gauges arranged in a Wheatstone bridge configuration, connected to an amplifier/comparator. This setup provides a voltage output range of 1.08 V to 5 V for a force range of 0 to 14 N, respectively. The Arduino supplies the required 5V and ground, while the external ADC measures the output differential [57, 63].

The FS2050 low-force load cell was selected to enable self-sufficient pressure analysis of multifunctional ZnO nanowire-embedded devices. It not only allows controlled precise loading on the sample but also provides electrical contact with the sample. To achieve a high level of autonomy, the load cell is designed to work with a stand-alone governing program hosted on an embedded system. This program is hosted on an Arduino Uno that interfaces with each element of the linear actuator and the load cell. Figure 2-2(b) depicts how the Arduino Uno communicates with an actuator driver and a linear actuator. Additionally, Figure 2-1(a-h) describes the interconnections between each element of the test rig.

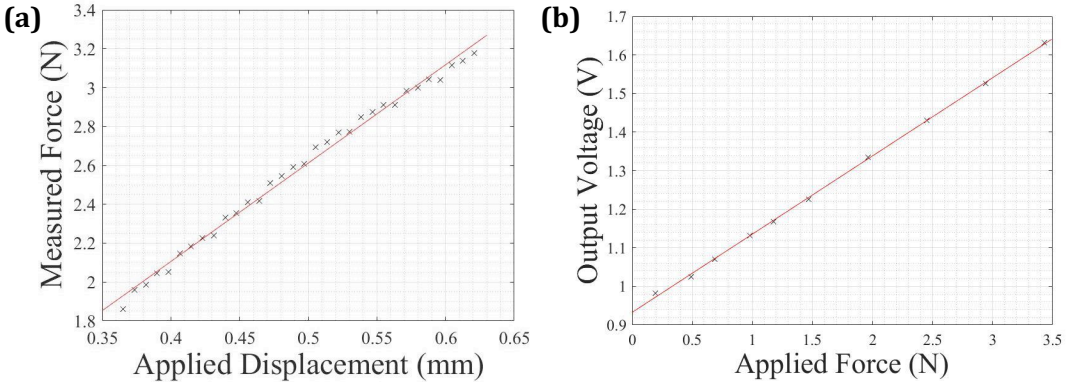

Figure 2-3: (a) Calibration of the voltage output from the load cell, and (b) the load cell output characteristic, for a given displacement taken from dissertation report by Harry Whittaker [57].

The load cell output voltage was calibrated against compressive force using a combination of set weights and containers with water, which were measured on a milligram weighing scale as depicted in Figure 2-3: (a) Calibration of the voltage output from the load cell, and (b) the load cell output characteristic, for a given displacement taken from dissertation report by Harry Whittaker [57].(a). The results demonstrated a strong linear relationship with an R2 value of 0.9933. The gradient of 4.723 N/V was employed to convert the voltage output to an applied force in the Arduino code. A uniform test start point of an applied 0.8 N was selected, representing the displacement "0" point. The determination of the displacement zero point would be based on the sample thickness and step size of the motor for consistent samples.

To calculate the stress applied to a sample on top of the load cell, it is important to eliminate the stress loss via the load cell. A stepper motor is used to apply the required pressure to move a triggered step, and the displacement remains consistent despite sample compression, while the applied force varies, as depicted in Figure 2-3:(a) Calibration of the voltage output from the load cell, and (b) the load cell output characteristic, for a given displacement taken from dissertation report by Harry Whittaker [57].(b). The loading and unloading phases must be interpreted separately due to significant hysteresis. The applied force per step varied for this sample, and it appears that a 5^{th}-order polynomial would likely be necessary for gradient calculations in later sections, as it yielded larger R2 values of 0.9933 and 0.9765 for loading and unloading, respectively.

2.2.1.7 UV LED Torch

In order to facilitate UV sensing of MF devices, a 365nm UV light emitted diode (LED) from SVC was utilised to emit the required UV light. This LED was connected and powered by the SMU, as illustrated in Figure 2-1(g). Throughout the experimentation, the LED was consistently maintained at a precise distance of 5 cm from the tested sample, resulting in a maximum luminous power of 2400 mW, at 3.4 V which can also be modulated as a function of the bias applied. The illuminance, calculated as 7.63 mW/cm^2 using the inverse square law, played a pivotal role in comprehending the variation in light intensity at different distances. By employing the inverse square law to the luminous power of the LED, the illuminance was derived as 7.63 mW/cm^2. To ensure the validity of the results, a probe stage, or actuator, was positioned to avoid interference when making contact with the gate electrodes. Integrating the UV lamp and controlling it with the software/user interface (sections 2.2.2/2.2.3) meant that experiments could be conducted very reliably and reproducibly. This addressed the uncertainty that is inherent to the manual operation of the UV lamp.

2.2.2 The Software of the Test-rig

The integration of the test rig and its corresponding software was essential for ensuring accurate pressure application and UV exposure with data acquisition. Alistair Ward designed the rig, which is responsible for applying pressure and measuring the resultant force during the tests as a part of master dissertation [63]. To complement in the thesis, a computer interface that bridges the test rig with the measurement sections, ensuring that users can control the system effectively and collect relevant data seamlessly by communicating the LCR, the SMU and UV torch in Python.

The user-friendly software interface plays a crucial role in enabling efficient control between the test parameters and the data acquisition systems organised by Harry Whittaker as a part of Master dissertation [58]. His contribution is elaborated in the subsequent sections of this report, where the interface's design and functionality are discussed in further detail (refer to Section 2.2.3 for Harry's work on the user interface).

2.2.2.1 Python

The Python code was developed using SPYDER, an open-source integrated development environment (IDE) offering an advanced coding environment for developers. The code employed standard SCPI (Standard Commands for Programmable Instruments) commands to communicate with the programmable instruments, specifically the SMU and LCR meter, for conducting tests. These instruments are commonly used in the field of electronics to measure and analyse electrical properties such as voltage, current, resistance, and capacitance. The test data obtained from the

instruments was automatically saved onto the computer in CSV (Comma Separated Values) format, providing a flexible and user-friendly method for data analysis and processing.

2.2.2.2 Arduino IDE

At the outset of each operation, a menu of operational choices is presented via serial communication. The initial step involves relocating the actuator to the DUT. This is achieved by controlling the actuator's movement and measuring the force exerted on the load cell. The actuator's movement halts when the force reaches a threshold of one newton. This force threshold is carefully selected to ensure that the DUT is firmly positioned between the actuator and load cell, maintaining alignment during the testing process [63].

Subsequently, the actuator is programmed to advance at its default step mode of one-eighth, recording values from the specified analogue input pins during the testing phase. The voltage input is converted to a digital format using a 10-bit ADC, which produces an integer value between 0 and 1023, linearly corresponding to a voltage range from 0V to 5V. Consequently, the voltage precision is restricted by a 5mV tolerance. Given the single ADC setup, it is not feasible to measure analogue signals concurrently. Additionally, a one-millisecond delay is introduced between successive voltage measurements to allow the ADC to stabilise back to zero.

2.2.3 User Interface

In order to maintain the independence of the timing for measurements of the SMU or LCR from the timing of the UV LED under pressure or compression, it was necessary to allow the user to independently select timings for both tasks. This was achieved using threading, a technique that allowed the simultaneous execution of both tasks [65]. A robust and user-friendly system was implemented to manage the input data to further streamline the testing process. This system enabled the automation of multiple cycles of the same test and setting controlled by computer, as shown in Figure 2-1(a), where the "Number of Cycles" can be edited, and numerous tests to be run on the same sample with varying parameters, such as the "AC Frequency", DC sweep range, and UV on/off. All the listed parameters could be set for testing MF device prototype [58]. Each cycle was saved individually, and the file name was automatically adjusted to specify the cycle number or the value of AC Frequency. All the equipment parameters and limitations have been defined to protect the system overload. For instance, a frequency less than 500 kHz for the AC Frequency is the maximum value of the LCR meter.

2.3 Aluminium Micro-Electrode Array

The design of the aluminium electrode arrays varies depending on their purpose: electrical characterisation or device testing under a probe station or device test rig, respectively. Electrical characterisation under the probe station involves a two-terminal in-plane I-V measurement design. Meanwhile, an array of electrodes for out-plane testing uses a parallel plate electrode design for MIS capacitor device tests.

2.3.1 The Design

2.3.1.1 In-plane Electrode Array

The first design, depicted in Figure 2-4(a), outlines a top-down nanofabrication technique for the growth of microelectrode arrays made of aluminium on 2" circular glass substrates. Five individual samples are fabricated on a substrate. These arrays feature 11 electrode separations, ranging from 1 to 50 µm as seen in optical image of electrode array in Figure 2-4(b). Specifically, the separations are 1, 2.5, 5, 7.5, 10, 10, 15, 20, 30, 40, and 50 µm, with each electrode having a width of 50 µm. The separation between all parallel array pitches is 100 µm. Additionally, a 1000 µm wide square is located on the edge of each contact, linking the array to facilitate contact with the probe station for testing, as detailed in the next section.

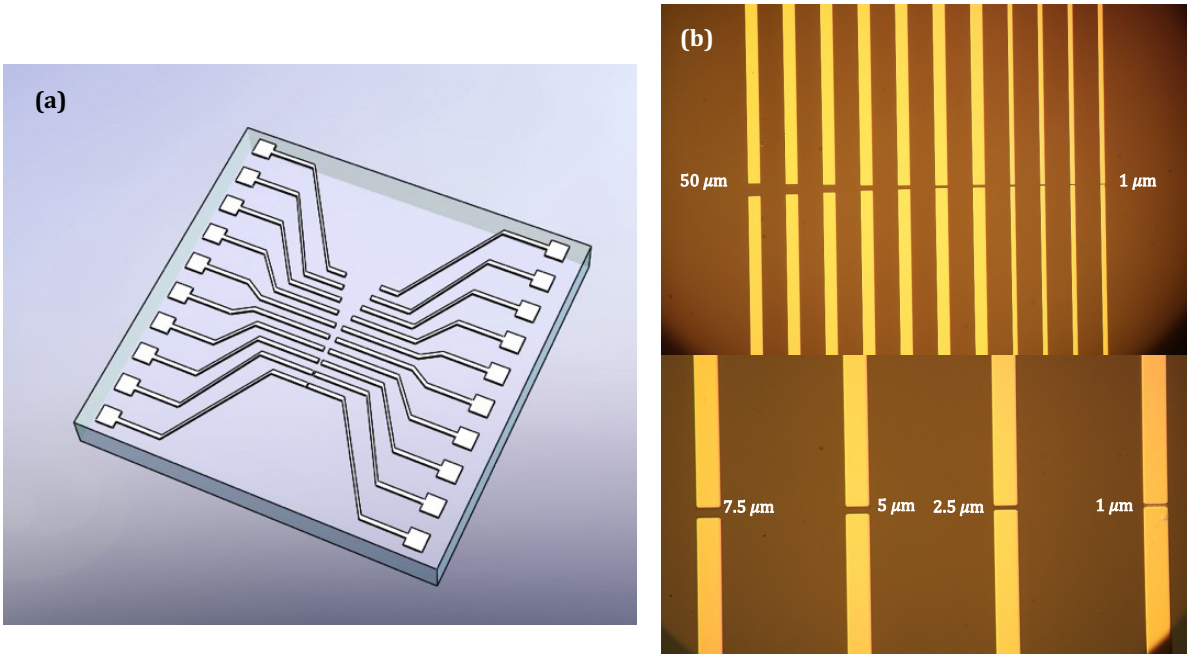

Figure 2-4: (a) illustration of an aluminium electrode array with electrode separations ranging from 1 to 50 µm, and (b) optical microscopy image of varied gap electrode arrays with dimensions.

In Chapter 5, these arrays, with their varying electrode separations, are utilised to study the conductivity of ZnO nanowire networks to correlate the percolation model with experimental results. The ratio between the array's dimensions and the nanowire length will be referenced in the conductivity analysis of the random nanowire network. Furthermore, the effect of the array's electrode separations on the MSM UV-PD performance of the photodetectors will be discussed in Chapter 5.

2.3.2 Fabrication

A standard washing procedure and substrate cleaning procedure were followed to ensure the 2" glass wafers were free from any impurities. The process involved cleaning the wafers in batches, where each wafer was rinsed with water, followed by a 15-minute ultrasonic bath with water and a second rinse. The slides were then dried with nitrogen. This procedure was repeated for propan-2-ol, acetone, Decon 90, and DI water. By using this washing process, any contaminants or debris that may have been present on the slides were effectively removed, ensuring the wafers were clean and ready for use. Building an electrode array with varying electrode spacing using 100 nm aluminium (Al) metal contact involved UV-positive lithography. The first step involves depositing a 100 nm thick layer of aluminium onto a 2" glass substrate through thermal evaporation of a metal wire source. The material was deposited in a high vacuum environment ($<10^{-6}$ bar) using an Edwards 306 thermal evaporator. An Edwards RV12 rotary pump backing an Pfeiffer Balzers Turbo Pump (PMP 01 320 B/R8132L) was used to achieve the high vacuum.

The deposited film's thickness and deposition rate were closely monitored using an Edwards film thickness monitor (FTM7) connected to a quartz crystal microbalance. Next, a lithography process was performed on the aluminium-coated glass wafers. It involved spin-coating the photoresist S1813 onto the substrate at 3700 rpm for 60 seconds, then baking it to 95 ℃ for 90 seconds. The spin-coater used for the thin-film deposition was a Laurell Technologies WS-400A-6NPP-LITE. The photoresist was then exposed to UV light at 75 mj/cm^2 for 7 seconds using EVG620 Mask Aligner and baked at 95 ℃ for 60 seconds. Afterwards, the baked photoresist was developed by immersing it into 351 developer for 20 to 25 seconds to remove the areas of the photoresist that were exposed to UV light during the positive lithography process. The developed photoresist was immersed in a deionised water beaker to stop the development of fine arrays on the surface.

Finally, the 100 nm thick aluminium layers were wet etched using an acid solution composed of phosphoric acid (H_3PO_4), nitric acid (HNO_3), acetic acid (CH_3COOH), and deionised water (H_2O) in the following ratio: 80% H_3PO_4, 5% HNO_3, 5% CH_3COOH, and 10% H_2O. This etching process was employed to selectively remove aluminium from specific regions of the thin film, enabling precise patterning and device fabrication. The developed surface was immersed in acid etching

mixture for 6 minutes to remove the aluminium layer where the photoresist had been removed during the developing process. As soon as the final aluminium array's etching was completed, it was immersed in deionised water to stop the etching of the layer. After all, the processed substrates were immersed in acetone and isopropanol solution for 10 minutes to remove all the photoresist and other residuals from the surface. Air drying with a nitrogen purge on the surface followed.

2.4 Preparation of ZnO Nanowires Dispersion

ZnO nanowires (CAS number: 1317-13-2) were bought from Sigma Aldrich in powder form, shown in Figure 2-5. The nanowires vary in length from 4 to 5 µm, as noted on the package. They were mixed in dimethylformamide (DMF) to spread even on the substrates on in-plane electrode arrays or devices. The process involves dispersion and drying, which will be detailed in later sections.

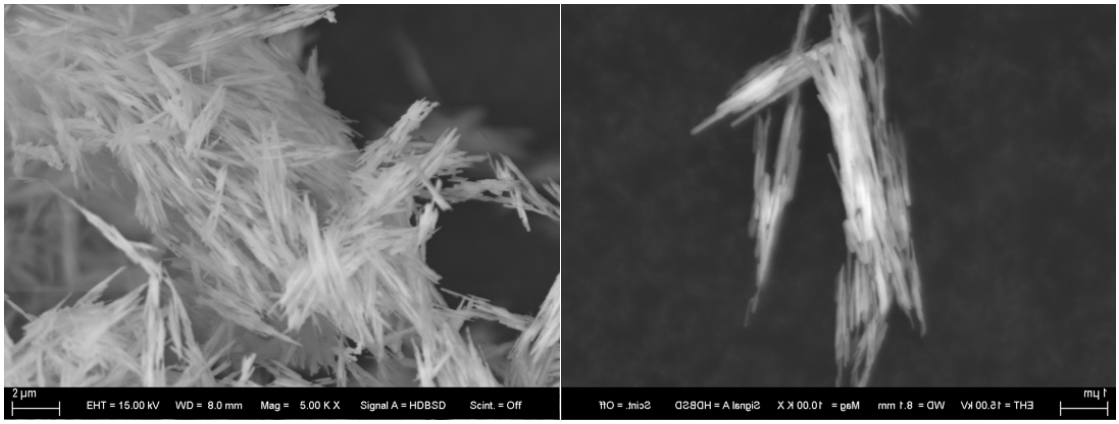

Figure 2-5: SEM image of the powder form of ZnO nanowires purchased from Sigma Aldrich (CAS number: 1317-13-2).

2.4.1 ZnO Nanowires Dispersion

After an intended amount of ZnO nanowires were dispersed in the DMF solvent by continuous magnetic stirring, the resulting solution exhibited excellent stability and homogeneity for drop-casting deposition. The high dielectric constant of DMF [66] made it an ideal solvent for the dispersion of polar or polarisable molecules [67], allowing the ZnO nanowires to be easily dispersed and preventing them from clumping together. In addition, DMF's adhesive properties on glass substrate helped to ensure that the ZnO particles were well dispersed and well distributed [68]. This method of dispersing ZnO nanowires in DMF solvent could have using homogenous distribution through the varied electrode array design for detailed electrical characterisation of random ZnO nanowire network.

To create the initial dispersion, the weight ratio of ZnO nanowires to DMF solvent must be determined. The process begins with accurately weighing the ZnO nanowires. Based on the desired weight ratio, the appropriate amount of DMF solvent is then calculated. For instance, to prepare a 0.1 wt.% ZnO nanowire solution, the weight of the nanowires is first measured, and the required amount of DMF is then calculated. Given the density of DMF (0.944 g/ml), the necessary volume of DMF is determined and added to the vial containing the ZnO nanowires. The final weight ratio of the ZnO nanowires in the mixture is calculated using the following eq. (2-1).

$$ZnO\ NW\ wt.\% = \frac{w_{ZnONW}}{w_{ZnONW} + w_{DMF}} \times 100 \quad (2\text{-}1)$$

Once the mixture has been prepared, the mixture was kept mixing with magnetic stirrer over 72 hours at room temperature to be sure homogenous dispersion of nanowires in the DMF.

2.4.2 ZnO Nanowire Deposition

The ZnO nanowire-DMF solution was subjected to thorough mixing by being left to blend overnight on a stirrer to ensure the uniform dispersion of the nanowires throughout the mixture. Additionally, the composite underwent ultrasonic treatment at an elevated temperature of 40 – 45 ℃ for 30 minutes prior to the deposition stage to further homogenize the mixture. Subsequently, 50 µl of the final mixture was deposited onto the surface. The deposited drops were left to dry slowly overnight under vacuum conditions at a controlled temperature of 45 ℃ to ensure complete desiccation.

In the final stage, the prepared samples underwent annealing using a customised RTA method. The samples were exposed to a temperature of approximately 500 ℃ for a duration of 10 minutes. This critical annealing step significantly enhanced the nanowires' junction interface and crystallinity, laying a solid foundation for subsequent conduction analysis. The homogenous mixing, controlled deposition, and annealing collectively ensure the integrity and homogeneity of the drop-casted nanowire network.

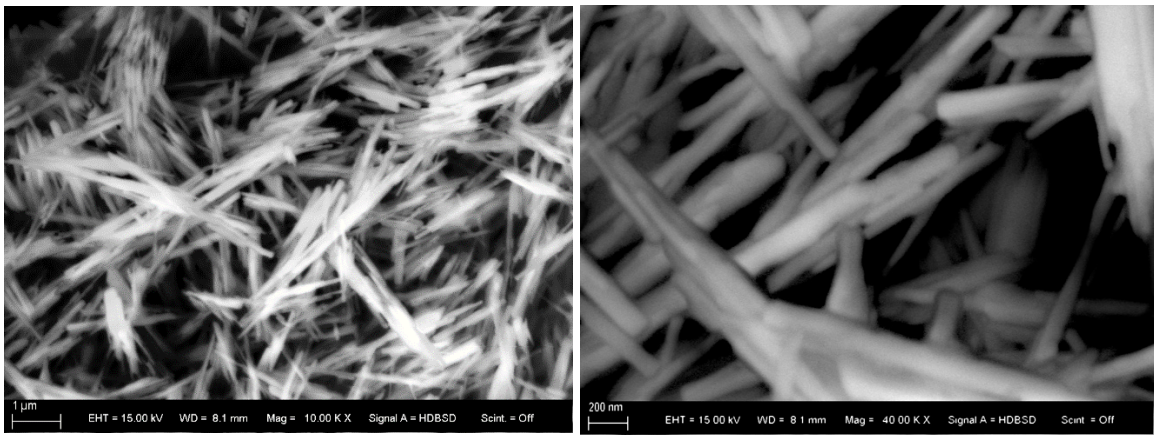

Figure 2-6: SEM images of random ZnO nanowire network on microelectrode array.

Figure 2-6 presents the SEM image of a random ZnO nanowire network deposited on the microelectrode array, as depicted in Figure 2-4(b), and subsequently annealed as detailed. The image conclusively demonstrates that the network achieves a fully random dispersion across a large area exceeding 100 μm^2. Furthermore, the figure provides clear evidence that the deposition technique successfully mitigates ZnO nanowire agglomeration, effectively overcoming the Van der Waals force associated with their high surface energy.

2.5 MOS and MIS Device Fabrication

MOS and MIS devices were fabricated to reveal the functionalities of a random ZnO nanowire network embedded between tunnelling-oxide (TO) and blocking-oxide (BO) layers [47, 69]. The designation MOS will refer to the n-Si/SiO_2/Al and n-Si/SiO2-PMMA/Al device configurations, while MIS will be employed when the ZnO nanowire network is drop-casted between SiO_2 TO and Poly(methyl methacrylate) (PMMA) BO layers. This section will mainly detail the fabrication process of the MOS and MIS devices for later use in the thesis.

The n-type silicon wafers used in the thesis were purchased from Testbourne Ltd., with the product code S4-9000-079. These wafers have a diameter of 2 inches and a thickness of 300 microns, with a <100> crystallographic orientation. The wafers are doped with phosphorus to achieve n-type conductivity, with a range of 10-30 ohm-cm resistivity. The corresponding dopant density is approximately $(1 - 3) \times 10^{15}\ cm^{-3}$, varying slightly depending on the exact resistivity of the wafer. One side of each wafer is polished, providing a smooth surface ideal for subsequent device fabrication and characterisation. These specific properties make the wafers well-suited for the MOS and MIS device structures and various functional applications in this thesis.

2.5.1.1 Tunnelling-Oxide deposition

The MOS device structure utilised in this study consists of a 300 μm thick n-type silicon wafer coated with a 30 nm SiO_2 layer. The SiO_2 tunnelling oxide layers was deposited via sputtering, a widely used method for thin film growth due to its uniform deposition capabilities and precise control over thickness [70].

The deposition process was conducted under the following conditions: a power of 300 W was applied, and Argon gas was introduced at a flow rate of 5 sccm to create the plasma necessary for sputtering. The process pressure during deposition was maintained at 5 mTorr, while the base pressure before deposition was reduced to below 2 μTorr, ensuring a clean vacuum environment. These conditions allowed for the controlled and uniform deposition of the 30 nm SiO_2 layer onto the silicon wafer, providing an ideal dielectric layer for the subsequent fabrication of the MOS device.

2.5.1.2 Blocking-Oxide Deposition

In this research, PMMA is used as the blocking-oxide layer in MOS and MIS devices. The primary purpose of the PMMA BO layer is to encapsulate the ZnO nanowire network to protect the device's leakage current under testing thanks to high resistivity ($10^{13}\ \Omega.cm$ at $10^{6}\ \mathrm{V.cm^{-1}}$ applied field) [71, 72]. The PMMA layers were spin-coated on SiO_2 layers.

The process begins by preparing a solution containing PMMA in chloroform, with a weight ratio of 1:99. This solution is left to mix overnight at room temperature and then subjected to ultrasonic stirring at 50°C for 30 minutes to ensure complete dissolution.

Following this, the TO-deposited n-Si wafer is perfectly cleaned using acetone and isopropanol (IPA) and exposed to UV ozone for 15 minutes. Subsequently, the PMMA solution is uniformly deposited onto the TO layer using a Laurell spin coater at 5000 rpm. To conclude, the final PMMA thin film is carefully baked on a hotplate at 125°C for 30 minutes, ensuring the formation of the solvent-free thin film.

2.5.1.3 Rapid Thermal Annealing

RTA is a high-temperature heat treatment process conducted in a controlled atmosphere, enabling rapid and precise annealing at elevated temperatures in either a vacuum or specific gas environment. Prior to depositing the blocking-oxide PMMA layer, RTA was employed on both the MOS reference samples and MIS devices In this case, a post-treatment is observed to enhance breakdown strength of the deposited oxide layers [73]. The purpose was to enhance the integrity

of the devices at the interface between the crystalline Si and amorphous SiO_2 layer and to improve the crystallinity of the ZnO nanowire as well as the overall integrity of the nanowire network. These enhancements will be discussed in the Chapter 7 of the thesis. Additionally, the RTA process was performed on the SiO_2 TO layer and, when applicable, on the drop-casted zinc oxide (ZnO) nanowire network on the TO film.

This annealing step was conducted at a temperature of 450°C for 10 minutes in a vacuum environment. After turning off the system to cool down to room temperature, the samples were allowed to cool down to room temperature under vacuum to prevent the passivation of dangling bonds [74]. The use of RTA under these controlled conditions aims to enhance the silicon wafer and oxide interface. The material properties, such as crystallinity and surface morphology, are critical for improving the overall efficiency and the stability of the devices.

2.5.1.4 Gate Electrode Deposition

An aluminium gate electrode pattern, 200 nm thick and shaped like a 2 mm radius circle, was deposited onto the BO surface using thermal evaporation. The evaporation process took place in a high vacuum environment (<10^{-5} mbar) using an Edwards 306 thermal evaporator. The high vacuum was achieved using an Edwards RV12 rotary pump to back an Edwards E04K diffusion pump. In addition, a quartz crystal microbalance was connected to an Edwards film thickness monitor (FTM7) to measure the deposition rate and film thickness. As a result, several parallel plate capacitor devices have been formed on a single device of each array, with each capacitor having an area of around 0.125 cm^2.

2.6 Summary

In conclusion, this chapter outlines the basic methods required for the development of a versatile multi-functional device testing platform capable of sensing capacitance and DC conductivity under various conditions such as pressure, UV light exposure, or a combination of both. The computer-controlled, semi-automated test rig is designed for advanced device applications. It will be used for UV photodetection of MIS diodes in Chapter 6, as well as non-volatile memory and pressure sensing in Chapter 7. Additionally, this chapter introduces the characterisation techniques employed to understand the properties and crystallographic structure of ZnO nanowire networks and MOS devices, with the corresponding results presented in the following chapter.

The second part of the chapter discusses the design and fabrication of a microelectrode array comprising 11 in-plane two-terminal electrodes, with electrode gaps ranging from 1 to 50

microns. This array will be utilised in Chapter 5 to validate the conductivity model introduced in Chapter 4 . It will also serve in UV photodetection experiments for the Al/ZnO nanowire/Al MSM device configuration in Chapter 6.

Finally, the chapter describes the fabrication processes of MOS and MIS devices, which are critical to demonstrating the functionality of ZnO nanowires in capacitors. These devices will be further explored in Chapter 6 and Chapter 7, where their applications in UV detection, memory devices, and pressure sensing will be fully characterised. The foundation laid in this chapter ensures a comprehensive understanding of the devices and characterisation methods used throughout the thesis.

Chapter 3

MATERIALS AND CHARACTERISATIONS

3.1 General Overview

This chapter provides a comprehensive overview of the ZnO nanowire and characterisation techniques used in the research, focusing on the literature background and experimental results. The first section focuses on the properties and applications of ZnO nanowires, with an emphasis on their unique electrical and crystallographic characteristics. Relevant studies from the literature are integrated with the characterisation results obtained during this research, highlighting how the ZnO nanowires behave in the specific device configurations explored here. The second section of the chapter focuses on the characterisation of the base MOS capacitors, which will serve as the foundational devices for further experimentation later in the thesis. Detailed analyses of these MOS devices' electrical performance and structural integrity, including the impact of treatments such as RTA, are provided. This chapter, therefore, lays the groundwork for understanding the material behaviour and device characteristics that will be pivotal in the subsequent chapters of the thesis.

3.2 Zinc Oxide Nanowires

Zinc oxide (ZnO), a semiconducting material from the II-VI group, is drawing increasing research interest due to its attractive and fascinating properties, including a direct wide bandgap of approximately 3.37 eV at 300 K and an exciton binding energy of approximately 60 meV [7], rendering it an attractive option for various applications in optoelectronic [48, 50, 75, 76] and biomedical devices [16]. Specifically, ZnO micro- and nanostructures have demonstrated promising results in a range of sensing devices such as UV sensors [10, 23, 77], biosensors for detecting proteins [78], DNA, and cancer cells [79], as well as gas sensors [28].

ZnO NW piezo-electronic-based device assemblies are based on the resistivity change at the Schottky contact with the metal. Owing to the piezoelectrical potential throughout the NWs, the resistivity state at the metal-semiconductor NW interface reversibly changes a threshold voltage [21, 22]. The resistivity shift is recorded and read out, which has the potential for application in

non-volatile memory devices, stress and tactile sensors, touchpad technology, artificial skin, etc. [51, 52, 80, 81]. The other device architecture, p-n junctions of ZnO NWs piezo-photonic devices, is based on the change in the depletion zone at the pn junction interface due to the mechanical stress of the NWs. The intensity of the recombination rate of the device increases proportionally to the applied force. The piezo-photonic effect can be used in light-remitted diodes [18, 82], photocells, photodetectors (PDs) [10, 23], and solar cells [15]. Therefore, various Schottky and p-n junction-based piezo-electronic and piezo-photonic devices can be assembled [18, 83, 84].

It is noted that there are several factors affecting the properties of ZnO NWs and the performance of their resulting devices, such as nanowire diameter, length, and inter-wire spacing [18, 85]. In addition to the physical properties of the nanowires, matrix materials, which are used as transparent reinforcement materials, affect the device's performance. Due to increasing oxygen vacancy by decreasing the size of NWs, electrical and optical properties change drastically [11]. Increasing the number of charge carriers caused by missing oxygen atoms in the structure enhances the transmittance [86] and Young's modulus of ZnO NWs [85], whereas the size of NWs decreases. Photoluminescence spectroscopy (PL) and ultraviolet-visible spectroscopy (UV-VIS) are two of the key methods to analyse the change in the electronic structure of the NWs depending on their size [11], and Evolution-in-Materio (EiM) can evolve the results to determine the optimal condition for the best device efficiency [87].

On the other hand, size-dependent Young's modulus of NWs and their impact on piezoelectric yield and device performance can be computed by the software while their electronic properties are being implemented. The density of ZnO NWs through the surface is the other factor affecting device performance because the stress on the single ZnO nanowire increases by decreasing the density of the NWs, which enhances the piezoelectric effect of the NWs [18]. By using EiM software, each of these selected parameters will evolve while the others are kept constant to analyse the effects of all these parameters [87].

In addition to the electrical, optical, and mechanical properties of NWs, the characterisation of device performance is the other key factor. Because of piezo potential along the NWs, the change in depletion zone at the interface of Schottky contact or p-n junction is caused by applied extra forward-bias [14, 21]. I-V measurement is a commonly used technique to analyse device performance of ZnO piezoelectric devices. Moreover, to analyse the piezo-electronic and piezo-photonic performance of the devices, dielectric field change under applied stress can be analysed by C-V test. The effect of the chosen physical parameters of ZnO NWs, depending on device performance, can be observed by I-V and C-V measurements.

Although best device performance is one of the main aims of the project, the processing cost is another crucial consideration because of the need for commercial viability. Even though the

smaller diameter of NWs shows better piezoelectric efficiency according to numerical calculations and studies, the fabrication of nanoscale ZnO NWs can be quite expensive. Therefore, optimum conditions are needed to produce the optimal device at the lowest possible cost to achieve industrial or commercial viability.

3.2.1 Crystal Structure of ZnO Nanowire Network

ZnO can form three different crystal forms: hexagonal wurtzite (B4), zinc blende (B3), and cubic rocksalt (B1) [6-8] as seen in Figure 3-1(a), (b) and (c), respectively [7]. Zinc oxide nanowires are hexagonal wurtzite structures that grow preferentially on c-axis (200) planes [88]. Four cations enclose each anion in a tetrahedral arrangement and vice versa. The surface favours planes (002), (100), and (101) due to high deposition rate and energy, leading to parallel growth in a polycrystalline structure with three lattice parameters: a=b=3.3 Å and c=5.2 Å. It is a non-centric symmetry (no inversion symmetry), which is the source of ZnO's piezoelectric and pyroelectric properties [89, 90].

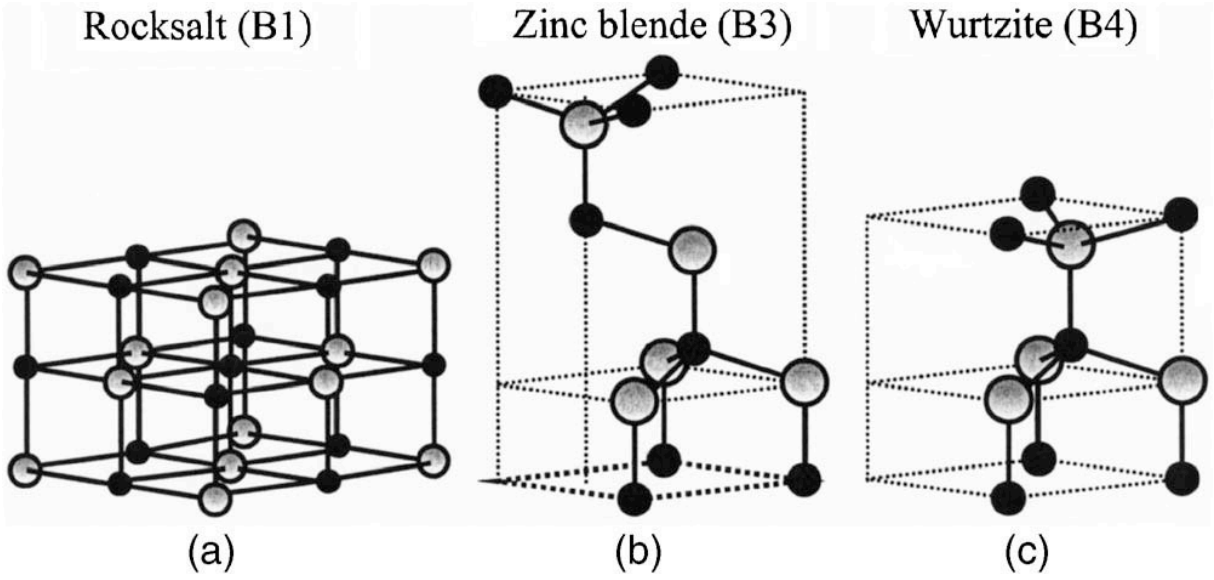

Figure 3-1: Representation of various ZnO crystal structures (taken by [7]): (a) cubic rock salt (B1), (b) cubic zinc blende (B3), and (c) hexagonal wurtzite (B4). The shaded grey and black spheres denote Zn and O atoms, respectively.

X-ray diffraction (XRD) is used to characterise the crystallography of ZnO nanowires. It is a technique that involves directing X-ray radiation onto a specimen. When X-rays interact with the specimen's electrons, they cause constructive and destructive interference due to the atomic arrangement [91]. This interference occurs as a result of wave scattering, which can be either constructive or destructive depending on the phase difference of the scattered waves. Constructive interference, leading to X-ray diffraction, occurs when the scattered waves are in

phase and their path length differences are integer multiples of the wavelength (λ). This phenomenon is described by Bragg's law represented in Figure 3-2:

$$2d_{h,k,l}\, sin\, \theta = n\lambda \tag{3-1}$$

Where $\boldsymbol{d_{h,k,l}}$ is the interplanar spacing, and θ is the Bragg angle. The interplanar spacing is calculated as:

$$d_{h,k,l} = \frac{a_0}{\sqrt{h^2 + k^2 + l^2}} \tag{3-2}$$

where $\boldsymbol{a_0}$ is the lattice parameter for the crystalline direction (h k l).

An X-ray diffractometer measures the intensity of these constructive interferences as a function of the scattering angle, producing Bragg peaks at angles satisfying Bragg's conditions. These peaks correspond to the diffraction of various crystal planes, allowing determination of the crystal structure and lattice parameters of the material by analysing the XRD spectrum.

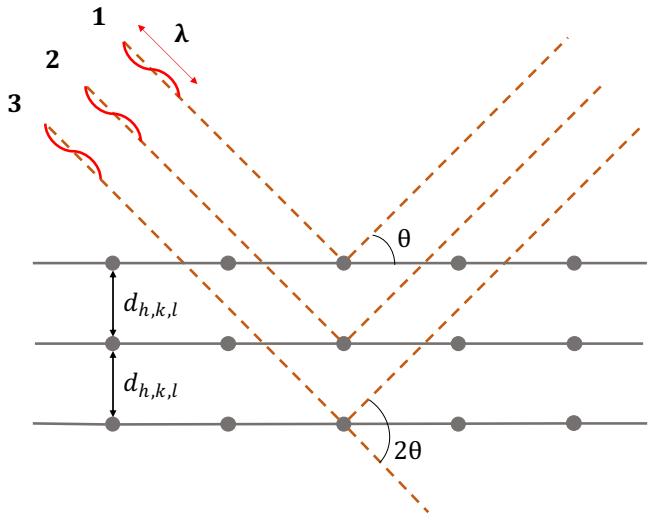

Figure 3-2: Schematic representation of Bragg's law along with the mathematical expression shown in eq. (3-2).

Additionally, XRD can estimate the nanometric crystallite size of crystalline materials. This is done by analysing the broadening of peaks in the diffraction pattern using the Debye Scherrer equation:

$$\tau = \frac{K\lambda}{\beta\, cos\, \theta} \tag{3-3}$$

where τ is the mean size of the crystallite, K is a shape factor (approximately 0.9), λ is the wavelength of the X-ray, β is the line broadening at half the maximum intensity (FWHM), and θ is the Bragg angle.

In this study, XRD was applied to both the drop-cast random ZnO nanowire network and MOS devices before and after rapid thermal annealing (RTA) to investigate their crystalline orientation and structure. The ideal ZnO nanowire growth was associated with a (002) crystalline orientation in any seed layer. Therefore, XRD was used to analyse the crystalline orientation of various seed layers and their impact on nanowire growth. The crystalline orientation of the nanowires was also determined by XRD and correlated with results from SAED analyses. Crystallite sizes for the seed layers were estimated using the Debye Scherrer equation.

XRD experiments were conducted using a Bruker D8 Venture diffractometer with high-intensity Mo/Cu dual IμS 2 sources. For optimal alignment and signal acquisition, 2 cm x 2 cm samples were prepared and laid flat on the X-ray sample holder. Typical XRD analyses were performed between 10° and 50° at a rate of 0.05° per second, focusing on significant ZnO peaks situated below 50° with Cu X-rays. This detailed XRD characterisation provides insights into the crystal structure, crystalline orientation, and crystallite sizes of the random ZnO nanowire networks, enhancing the understanding of their morphological properties and their influence on nanowire growth.

Figure 3-3 displays the XRD patterns for the randomly dispersed ZnO nanowire network before and after RTA treatment under vacuum conditions. All peaks observed after heating the precursor at 500°C correspond to the standard hexagonal wurtzite ZnO crystal structure (JCPDS 36-1451) [92]. Perfectly aligned nanowires perpendicular to the surface are typically in the (002) orientation due to surface thermodynamic energy [7, 8]. The high deposition rate and associated energy result in the preference of adatoms for the (002), (100), and (101) planes, leading to parallel growth and a polycrystalline structure.

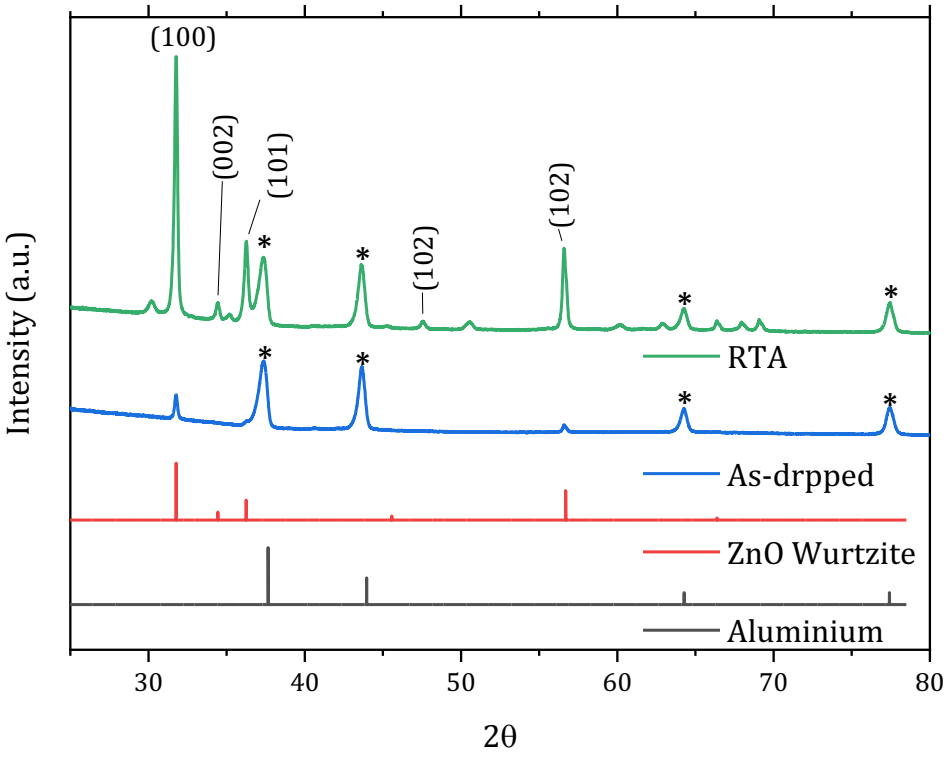

Figure 3-3: XRD analysis of random ZnO nanowire network before and after RTA treatment.

XRD can identify the alignment of nanowires, which exhibit the (100) and (101) planes along with the (002) plane, as seen in Figure 3-4. Additionally, peaks less intense than the (002) peak in the XRD diffractograms of ZnO nanowires may indicate a polycrystalline structure or poor alignment [88]. A strong (100) peak on the as-drop-cast ZnO nanowire network (red line in Figure 3-3) suggests the as-drop-cast ZnO nanowire networks are oriented along the c-axis [27, 88, 89, 93, 94]. The peak identification from the series of samples aligns with the ICDD database sheet (36-1451) [92], confirming a single-phase hexagonal wurtzite structure. A strong preferential direction along the c-axis is highlighted, with the (002) peak at a diffraction angle of $2\theta = 34°$. The intensities of the (100), (103), and (202) planes increase, likely due to the horizontal orientation of the ZnO nanowires on the surface [88]. As seen in Figure 3-4, other low-intensity orientations of the planar layer may result in weak (100), (103), and (202) peaks due to the randomness of the ZnO nanowire network on the surface. The crystalline size (D) of the nanowires have calculated as 61.23 and 70.42 nm before and after RTA, respectively.

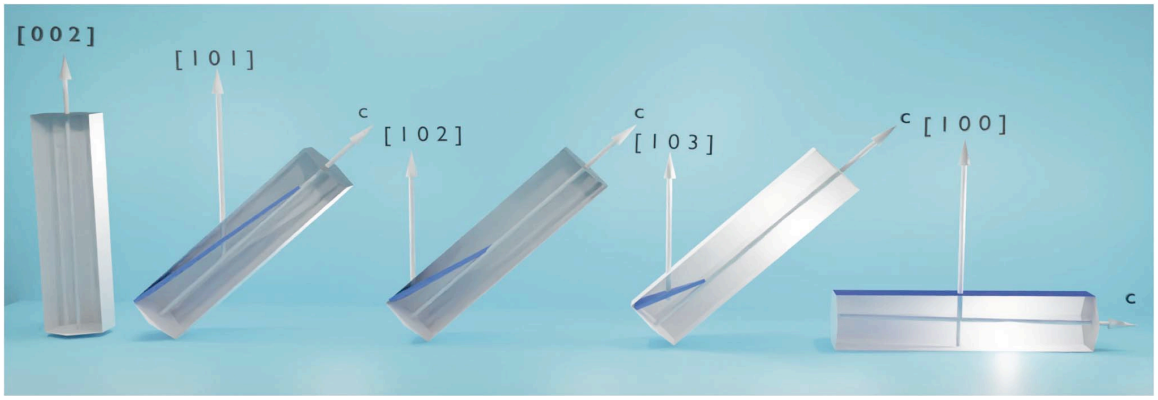

Figure 3-4: The orientation of the nanowires in the (h k l) planes with respect to the substrate plane [88].

The black line in Figure 3-3 shows the XRD patterns of the rapid thermal annealed ZnO nanowire network (annealed at 500°C for 10 min). All samples display a hexagonal wurtzite crystal structure with enhanced (100), (110), and (101) peak intensity. The strongest peaks seen at 2-theta values of 31.7, 34.4, 36.2, 47.5, 56.5, 62.8, 66.3, 67.9, and 69.1 correspond to specific lattice planes: (100), (002), (101), (102), (110), (103), (200), (112), and (201) respectively. The diffraction peaks correspond to a ZnO hexagonal wurtzite structure and align with published ZnO data (a = 3.249 Å, c = 5.205 Å JCPDS File, 5-664)[93, 94].

The (002) peak intensity decreases at 500°C. Higher annealing temperatures provide atoms with sufficient activation energy to occupy energetically favourable sites within the ZnO crystal lattice, promoting the growth of larger grains with lower surface energy. This results in more intense (100) and (110) peaks, as the (100) plane has the lowest surface energy in ZnO and is also linked to horizontal alignment of the ZnO nanowires, increased oxygen vacancy defects at 500°C [88]. Additionally, higher temperatures increase molecular motion, disrupting crystal lattice perfection, as observed at 500°C. All (002) peak positions are similar before and after annealing, indicating residual tensile stress in the nanowires. No additional peaks corresponding to impurity phases are observed, confirming the high purity of the ZnO nanowires [88].

3.2.2 Electronic structure of ZnO

X-ray Photoelectron Spectroscopy (XPS) has been used to determine the binding energy of ZnO nanowires in case of understanding the electronic structure of them. it was developed by Kai Siegbahn [95]. This technique involves irradiating the material with X-rays of known and fixed energy. These X-rays are absorbed, leading to the ionisation of the atoms in the material. Electrons are emitted via the photoelectric effect from core levels (or from electronic levels in the valence band). The photoelectrons originating from the material's surface are detected, and their kinetic

energies are measured. It is possible to determine the binding energy of each photoelectron using the following relation in eq. (3-4) [95]:

$$E_L = hv - E_c - W \tag{3-4}$$

where hv is the energy of the incident X-ray photons E_L is the binding energy of the photoelectron in its core level, E_c is the kinetic energy of the emitted photoelectron, and W is the work function of the analyser.

The binding energy of these collected photoelectrons is characteristic of the emitting atoms. The binding energies of photoelectrons emitted by each element are summarised in a database [96] maintained by NIST (National Institute of Standards and Technology) and in the scientific literature.

The binding energy of an electron depends not only on the level at which the photoemission mechanism occurs but also on the valence state of the atom and its environment. The core electron is subject to a Coulomb force exerted by the charges of neighbouring atoms [97]. Suppose another element replace this neighbouring atom. In that case, this force varies, leading to a spatial redistribution of the valence charges and generating a new potential experienced by the electron in question. As a result, its binding energy is altered. A change in the chemical environment of the core electrons induces shifts in the characteristic peak of an element. This chemical shift depends on the nature and number of atoms bonded to the emitting atom, as well as the electronegativity of neighbouring atoms [97].

The variation in the analysis depth of the substrate depends on the angle θ, which represents the angle between the axis of the analyzer and the normal to the surface. The corresponding analysis depth for each angle θ is equal to $3\,\lambda\cos\theta$. This expression indicates that the analysis depth decreases as the angle θ increases. Using the AR-XPS technique [98], we can schematically represent the electronic structure of ZnO nanowires before and after RTA [99, 100].

The tetrahedral coordination of the hexagonal wurtzite ZnO lattice structure is common in sp3 covalent bonding. These materials exhibit both sp3 covalent and ionic characteristics. ZnO, an II-VI compound semiconductor, demonstrates adjacent ionicity between covalent and ionic semiconductors [6, 7, 101]. Zinc oxide (ZnO) usually contains unintentional n-type doping caused by defects in its crystal structure [102], such as oxygen vacancies and zinc interstitials. These defects also serve as centres for adsorption at the atomic or molecular level, making ZnO useful for UV photodetection [11]. However, the challenge of achieving p-type doping in ZnO, primarily due to native defects, has been a longstanding issue in ZnO nanoengineering [103, 104]. This limitation has restricted the range of applications for ZnO in semiconductors. Despite this, n-type

ZnO demonstrates high electron mobility and intense luminescence. Its abundance and ease of production have positioned ZnO as a highly researched semiconductor material in the electronics industry [6-8]. For a comprehensive analysis of semiconductor properties of ZnO and applications, consult Janotti's work [8].

The oxygen vacancy (V_O) significantly influences the properties of metal oxides, impacting doping, processing, device degradation and more. Determining if n-type conductivity stems from V_O has long been challenging in ZnO[105, 106]. Although V_O has the lowest formation enthalpy, it creates a deep electronic state in ZnO, which may limit its conductivity at room temperature[107, 108]. Theoretical studies show conflicting results due to methodological limitations. Experimental data suggests V_O concentrations far exceed theoretical predictions[100, 109]. Models for V_O in ZnO often rely on indirect evidence, and its charge state remains contentious[110].

In conclusion of the literature, the n-type conductivity of ZnO results from group-III impurities, hydrogen substitution, and possibly group-IV impurities. Shallow donors show distinct peaks in the PL spectrum. Oxygen vacancies act as deep double donors with specific energy levels relative to the conduction band minimum (CBM). Zinc vacancies are deep acceptors associated with red, blue, and green emissions [111, 112]. Oxygen vacancies dominate diffusion with identified activation enthalpy. Migration enthalpy is determined, showing changes in V_O formation enthalpy. Liu et al. [110] reported a study exploring oxygen-isotope ZnO heterostructures with precise control of chemical potential and Fermi level. They found the challenge of the neutral state assumption of V_O in ZnO, establishing them as primary donor-like defects, explaining n-type conductivity.

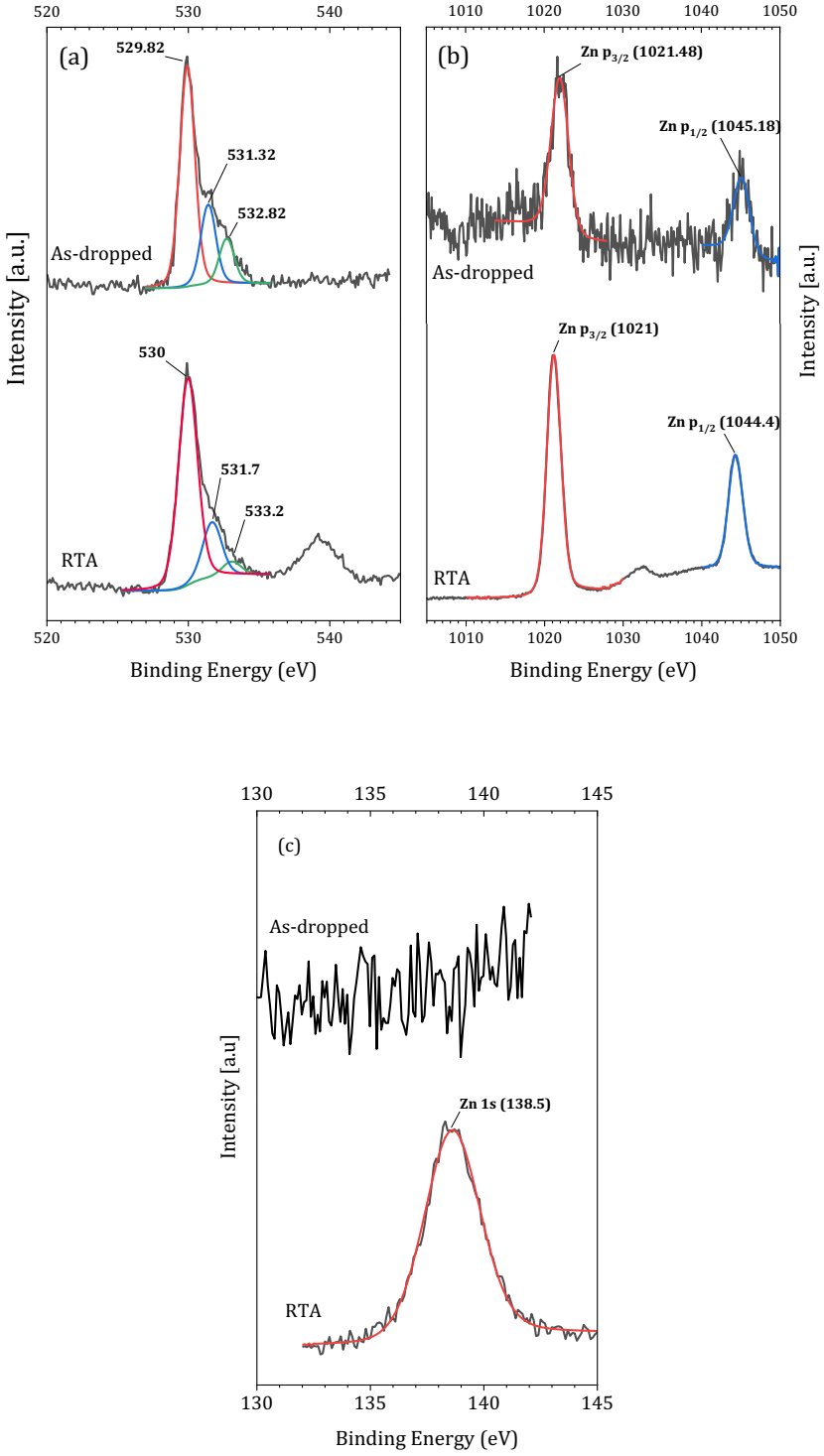

Figure 3-5: XPS characterisation of as-deposited (top) and RTA-treated (bottom) ZnO nanowire networks presented in this thesis; (a) O 1s, (b) Zn $2p_{3/2}$, (c) Zn 1s.

The O 1s peak spectrum can be deconvoluted into three contributions, with their peak located at 530 eV, 531.7 eV, and 532.8 eV, as seen in Figure 3-5(a). The 530 eV peak represents O^{2-} from the wurtzite structure of the ZnO lattice 20, while the 531 eV peak is associated with O^{2-} in the oxygen-deficient

region within the ZnO matrix [113]. The 532.4 eV peak originated from surface oxidation when the ZnO films were exposed to air [99, 114].

The observed intensity decreases after RTA treatment at 450 ℃ under vacuum, as depicted in Figure 3-5, indicating a reduction in the intensity of the as-deposited and RTA-annealed ZnO network. The peak located at 530 eV exhibits a relatively larger intensity and integrated area than that at 531.7 eV in the as-deposited and RTA-treatment ZnO network, suggesting that this oxygen signal primarily originates from the Zn–O bond [110, 115]. The addition of RTA annealing promotes the formation of the Zn–O bond and effectively decreases oxygen deficiency. The Zn and O atomic concentration in the Zn–O state can be determined from the peak area of the Zn 2p3/2 in Figure 3-5(b) and O 1s at 530 eV in Figure 3-5(a). The Zn content relative to the O 1s peak increases due to RTA treatment, indicating that the deviation from stoichiometry induces electrons in the film, resulting in an n-type ZnO film. The drop-casted nanowire network exhibits more oxygen deficiency, but the annealing process under vacuum conduction decreases oxygen deficiency by Zn-O bonds.

This improvement in stoichiometry, confirmed by the increased Zn-to-O ratio in the XPS analysis, is expected to enhance charge transport characteristics. Specifically, the reduction of oxygen vacancies, which act as electron donors, is crucial in tuning the carrier concentration and overall conductivity of the ZnO network. These findings set the stage for the electrical characterization in section 3.3, where the I-V measurements will be discussed. By linking the chemical modifications revealed by XPS to the electronic behaviour analysed through I-V measurements, we can better understand how annealing and compositional adjustments affect charge transport mechanisms in the ZnO nanowire network. The I-V analysis in section 3.3 will thus provide further evidence of how the improvements in material stoichiometry translate into changes in conductivity, supporting the overall thesis goal of optimising the ZnO network for enhanced performance in device applications.

3.3 Electrical Characteristics of the Network

The study aims to investigate the I-V characteristics of the ZnO nanowire network on the in-plane electrode array to understand the conduction hierarchy of the ZnO-NW network. In Chapter 4, an analysis will be conducted step-by-step on how the material ratio of the ZnO-NW network influences conductivity by characterizing the aluminium micro-electrode array. Before a detailed investigation of the I-V characteristics of the ZnO nanowire network, the conductivity of the ZnO nanowire network on the microelectrode array will be presented in this section. The I-V measurements will be calibrated using the control electrode. Subsequently, the electrical

conductivity of ZnO nanowires prior to the RTA annealing process will be assessed to determine the effects of RTA on the ZnO-NW network's electrical properties.

As depicted in Figure 3-6, a control electrode exhibits low electrical conductivity when used alone. The electrode responses to 0.25 V voltage sweep, ranging from 0 to 10 V and then back to 0 V, are almost identical with small hysteresis. The negative current levels in the graph result from an offset in the source meter. As seen in Figure 3-6, there is no charge transport on the undeposited electrode array. Therefore, the charge transport of random ZnO nanowire networks with varied nanowire densities can be investigated on the microelectrode array.

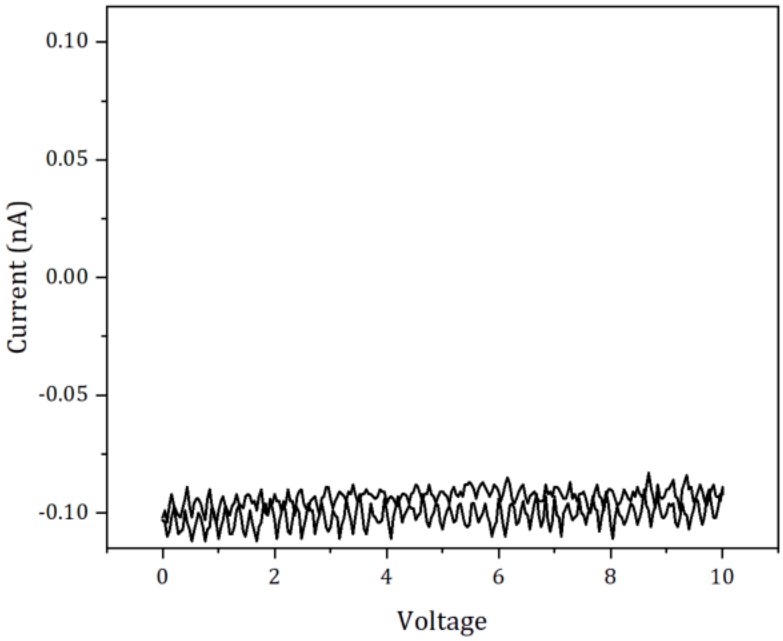

Figure 3-6: I-V characteristics of a 10μm gap microelectrode array.

An investigation was conducted on the properties of randomly dispersed ZnO nanowires in DMF solvent with varying concentrations. ZnO nanowires in ratios between 0.01 and 4.5 wt.% were drop-casted on a 10μm gap of aluminium microelectrode arrays, as shown in Figure 2-4. The conductivities of the randomly dispersed ZnO nanowires were tested on two-terminal in-plane devices, resulting in different current levels ranging from nanoamp to milliamp levels, as presented in Figure 3-5. The I-V tests of ZnO nanowire networks displayed a non-linear sweep range of ±20V due to the semiconducting nature of the ZnO nanowires. The increase in the electrical conducting of the random-ZnO nanowire networks could be verified by the number of nanowires in the channel with increasing nanowire weight ratio in drop-casted DMF solution.

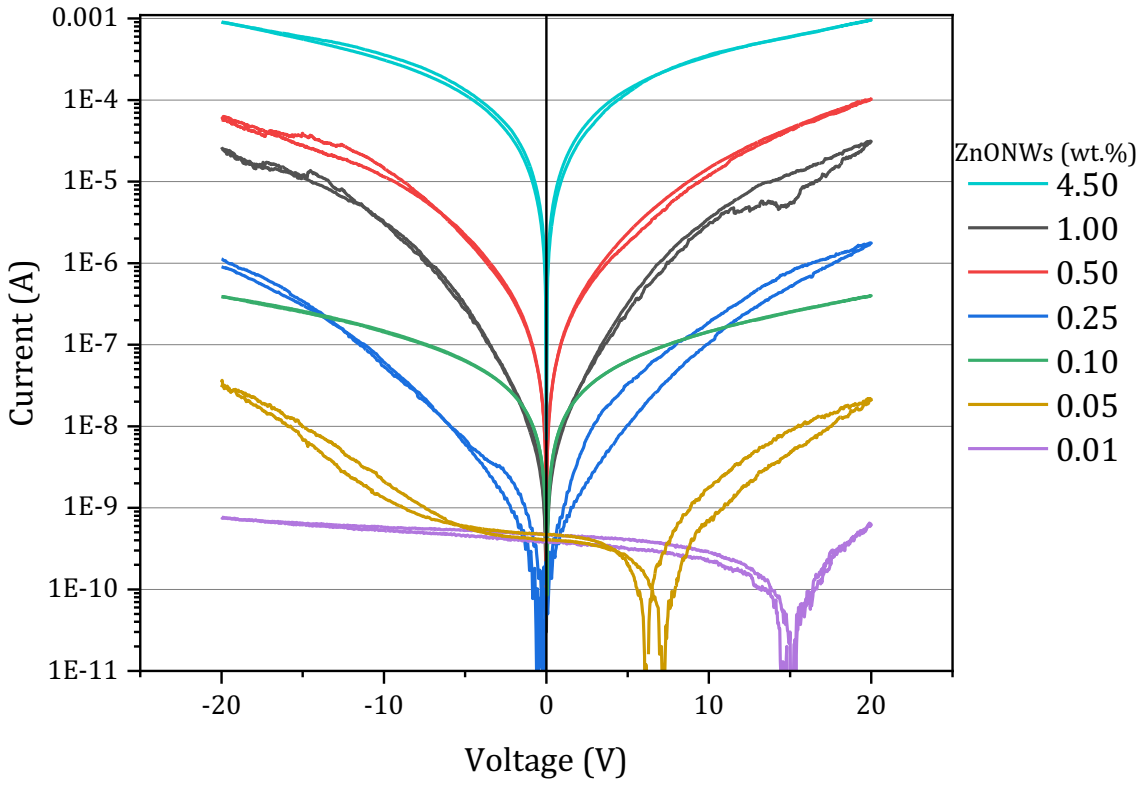

Figure 3-7: I-V characteristics of drop-cast and RTA-treated ZnO nanowire network with a variation of the material ratio between 0.01 and 4.50 wt.% on 10 µm gap microelectrode arrays.

In addition to the non-linear characteristic I-V, the system shows a rectifying behaviour I-V characteristics when a low nanowire concentration at 0.01 and 0.05 wt.% is drop-casted on the 10 µm gap microelectrode array, as seen in Figure 3-7. The appearance of the rectifying behaviour in such an asymmetrical I-V characteristics for low-nanowire concentrations (0.01–0.51 wt.%) can be attributed to the existence of interface dipoles at metal-nanowire contacts, resulting in the depinning of the Fermi level at the metal-nanowire contact [116]. In the context of nanowires, the Fermi level is consistently located, or "pinned," within them. The choice of low and high work-function metals does not impact the creation of uneven barrier heights for charge injections in the densely drop-casted networks of nanowires. This phenomenon is observable in most metal-semiconductor junctions with bulk-contact structures [117-119]. Furthermore, the dielectric constant of the nanowires plays a critical role in the number of nanowires and has implications for charge injections at nanotube-metal contacts [120]. Consequently, when densely packed networks are involved, tunnelling current supersedes thermionic emission current in nanowire-nanowire junctions, resulting in I-V characteristics that adhere to Ohm's law [121].

As presented in Figure 3-8, the current-voltage characteristics of random ZnO nanowire networks are shown when the electrode separation was 1 and 10 μm, illustrated as black and red lines respectively. It is evident that the system displays a non-linear I-V relationship for both electrode separations. This can be attributed to the semiconductor properties of ZnO nanowires and the complex conduction mechanism through the nanowire network.

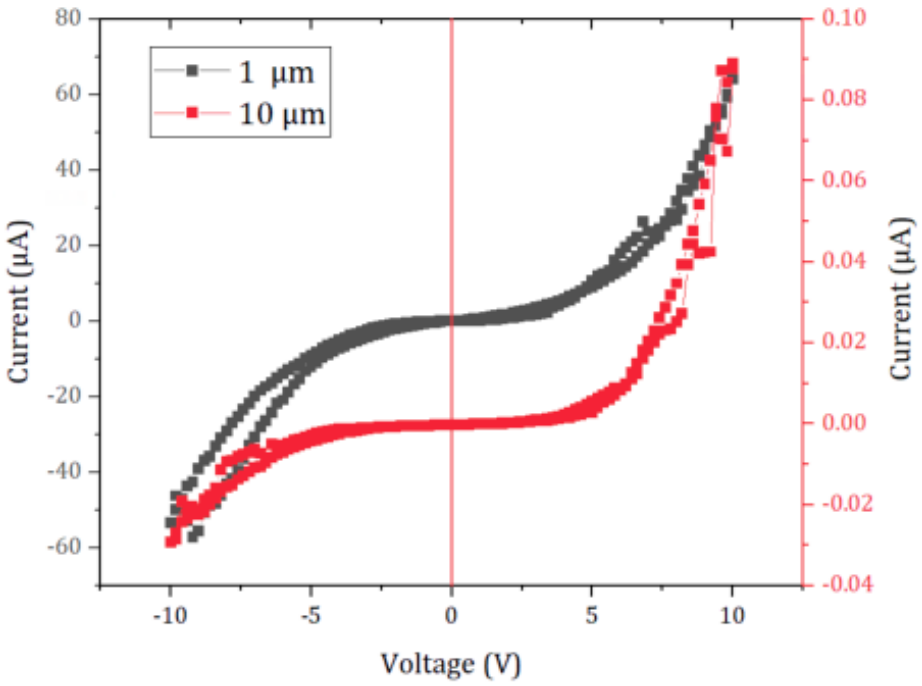

Figure 3-8: I-V characteristics of 0.1 wt.% ZnO nanowire network on 1 and 10 μm gap microelectrode array.

Figure 3-8 illustrates two different electrode separations to demonstrate how the nanowire itself and a network can affect the I-V characteristic of the system. The length of the nanowire is 5 μm, which is significantly larger than the 1 μm electrode separation, causing the majority of the current to flow through individual nanowire which span the electrodes. However, when the electrode separation is increased to 10 μm, the current flows through nanowire-nanowire junctions. The I-V characteristic of the two different electrode separations displays a non-linear I-V relation as discussed, but the symmetry of the I-V characteristic varies [116]. Typically, the expected outcome when aluminium metal forms an ohmic contact with ZnO on both ends of the nanowire network is a linear and symmetrical I-V characteristic [122]. Above the threshold voltage, the results of this study indicate a non-linear and asymmetric I-V nature where thermionic emission becomes dominant [121]. Therefore, the asymmetric I-V characteristics are

attributed to the formation of dissimilar contact resistance and various barriers on nanowire junctions and nanowire metal ends [116].

According to the results obtained from the voltage sweep, which ranged from -10 to 10 V and back to -10 V, each system has narrow hysteresis due to asymmetric aluminium contact. However, the electrode responses showed a noticeable contrast in the symmetry of positive bias in comparison to negative bias for electrode separations of 1 and 10 μm. Figure 3-8 shows that the current flow through the 1 μm electrode separation was nearly symmetrical in both positive and negative bias, with the highest current at 10 V reaching approximately 60 and -60 μA for the positive and negative 10 V bias, respectively. On the other hand, the current flow was asymmetrical for the 10 μm electrode separation. The highest current observed was 0.09 and -0.03 μA for positive and negative 10 V, respectively. The result shows that the larger electrode separations may rectify the I-V characteristic. It was expected that the current level would differ for both electrode separations due to the effect of junction resistivity between two nanowires [116, 120, 121], but the ratio of the differences between negative and positive bias was also varied due to the forward rectifying I-V characteristic with pinched hysteresis loop as shown in Figure 3-8. The other possibility is the contact between the ZnO nanowire and the Al electrode. Any differences between the one side of the Al electrode may result in asymmetrical I-V characteristics [117].

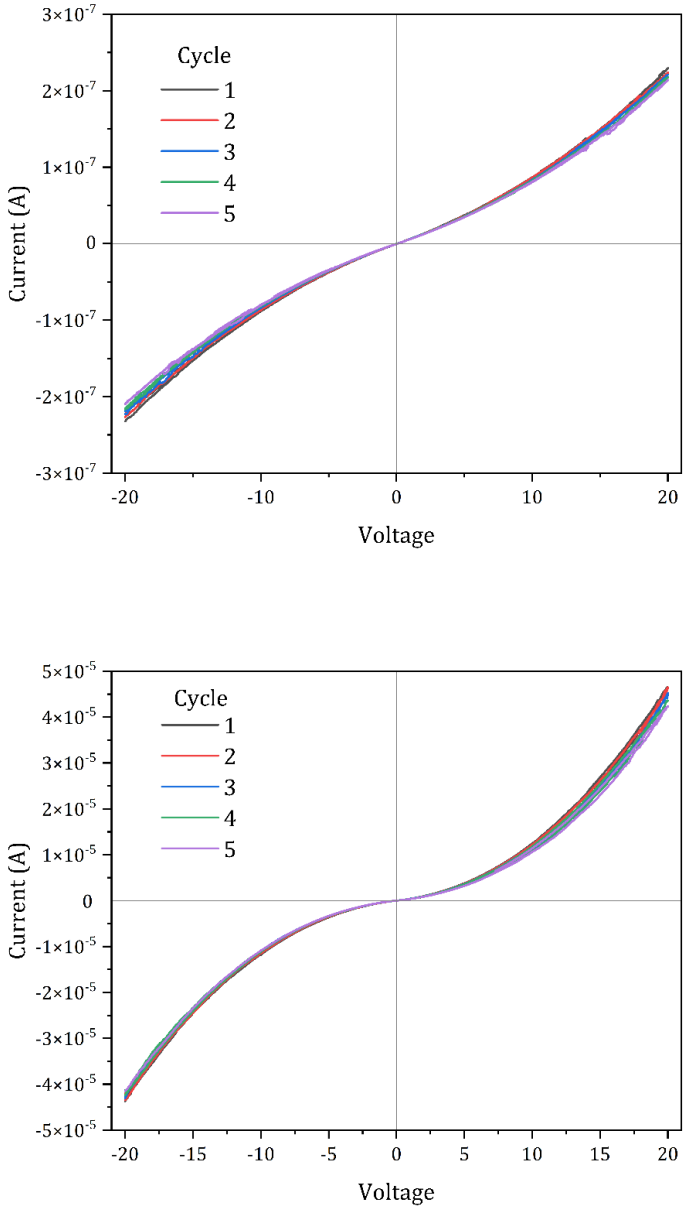

Figure 3-9: I-V sweep of (a) 0.1 and (b) 1.0 wt.% ZnO nanowires on 10μm gap microelectrode array.

Five cycles of the symmetrical I-V characteristics of 0.1 and 1.0 wt.% ZnO nanowire networks on a 10 μm electrode gap, shown in Figure 3-9, present different levels of nonlinearity in their I-V characteristics. Increasing the channel length leads to the flow of current through nanowire-nanowire junctions, in line with the literature [123]. Therefore, it is important to understand the properties of these junctions to gain insight into the charge transport in a random ZnO nanowire network. The purpose of conducting multiple cycles of the I-V sweep test is to ensure the reproducibility and stability of the conductivity. When an electric field is applied to the conductive

path, it can alter the filling trap states of the nanowire-nanowire junctions in the network, resulting in a slight change in conductivity [31]. The 5 cycles of I-V characteristics for 0.1 and 1.0 wt.% in Figure 3-9 (a) and (b) demonstrate that the network exhibits reproducible and stable conductivity.

The resistivity of junctions is a critical factor influencing the conductivity of random networks. At low potential, the I-V characteristics exhibit linear ohmic conductivity, indicating that junction resistivity governs charge transport [124]. As the voltage increases, a sharp rise is observed, as shown in Figure 3(a-b). However, the nonlinearity at 0.1 and 1.0 wt.% is not identical due to distinct percolation characteristics of each network. The varying percolation characteristics result from changes in inter-particle distances as the ZnO nanowire content fluctuates. This fluctuation in inter-particle distances is the physical mechanism causing the voltage dependence on the conductivity of random nanowire networks [125, 126]. Consequently, the level of nonlinearity varies depending on the percolation characteristics of the ZnO nanowire content.

In conclusion, this section investigates the general electrical characteristics of random ZnO nanowires on microelectrode arrays. The I-V characteristic may exhibit a rectifying effect at the lowest nanowire intake values due to high junction resistivity. However, the investigation demonstrates that ZnO nanowire networks exhibit repeatable and stable nonlinear I-V characteristics. This same principle will be utilised in the following chapters, where the conductivity of ZnO nanowires will be modelled in Monte Carlo simulation and experimentally correlated. A detailed investigation of charge transport in a random ZnO nanowire network will be conducted in Chapter 5 by integrating the scaling factor of a percolative nanowire network described in Chapter 4.

3.4 MOS and MIS Devices

The utilisation of MIS or MOS devices has become prevalent in contemporary device technology, particularly in the fabrication of capacitors and transistors. However, the ongoing miniaturisation of devices, often associated with Moore's Law, is now reaching its technological limitations [1, 2]. To address this challenge, a promising approach is to introduce multifunctional ZnO nanowires into MIS devices, thereby enabling the generation of digital signals through the simultaneous impact of multiple external factors [7, 8, 15]. The integration of ZnO nanowire-based device assemblies can lead to significant changes in resistivity or charge density [9, 15, 22, 127], resulting in the production of electrical signals at the gate contact in response to external stimuli such as exposure to light, pressure, or charge accumulation. The potential applications of ZnO nanowire network-embedded MIS devices will be expounded in Chapters 6 and 7, with a preliminary focus

on providing a general characterisation of the MIS device configuration before exploring their specific applications.

The other functionalities of the embedded dielectric layer of MIS device formation are based on changes in the charge accumulation because of external impact on devices, such as UV-light exposure and pressure on the gate electrodes. It has been widely studied that ZnO nanowires generate charges under blue and UV light radiation due to the absorption and desorption of oxygen on the ZnO nanostructure's surface [48, 49]. The intensity of the charge generation rate of the device increases proportional to the applied radiation. The optoelectronic effect can be applied in two terminal in-plane device formations: Field effect transistor, photodetector [48-50], and solar cells[18]. Therefore, a variety of anisotropic electrode configurations and transistor-based optoelectronic sensors and photodetector devices can be assembled.

It is noted that there are several factors affecting the properties of ZnO NWs and the performance of their devices, such as nanowire diameter, length and inter-wire spacing [17] because of the high improvement of surface-to-volume ratio of high aspect ratio of 1D nanowire formation. In addition to the physical properties of the nanowires, matrix materials, which are used as transparent reinforcement materials, affect the device's performance [18]. Zinc Oxide (ZnO) is known to possess a significant exciton binding energy of 60 meV, making it possible for the excitonic emission of ZnO to persist even at room temperature. This feature is particularly crucial for the development of light-emitting devices including lasers. ZnO tends to exhibit unintentional n-type doping, which is attributed to the presence of native defects in its crystalline structure. These defects include oxygen vacancies (which are missing oxygen atoms at regular lattice positions) and zinc interstitials (which are additional Zn atoms occupying interstitial positions in the lattice) [11, 19].

3.4.1 MOS Capacitor Device Assembly

Owing to extensive usage of the Si, silicon oxide (SiO_2) metal-oxide/insulator-semiconductor (MOS/MIS) capacitors, the functionalities of ZnO nanowires will be performed by embedding them into the highly studied MIS device configuration illustrated in Figure 3-10(a). This thesis will present three types of MOS device assemblies: (i) a reference MOS device assembly (D_r) formed as n-Si/SiO2/Al, (ii) a MOS assembly with a PMMA blocking oxide (D_p) formed as n-Si/SiO2/PMMA/Al, and (iii) a ZnO nanowire embedded MIS device assembly ($D_{nw,i}$), where 'i' indicates the weight percentage (wt.%) of ZnO nanowires.

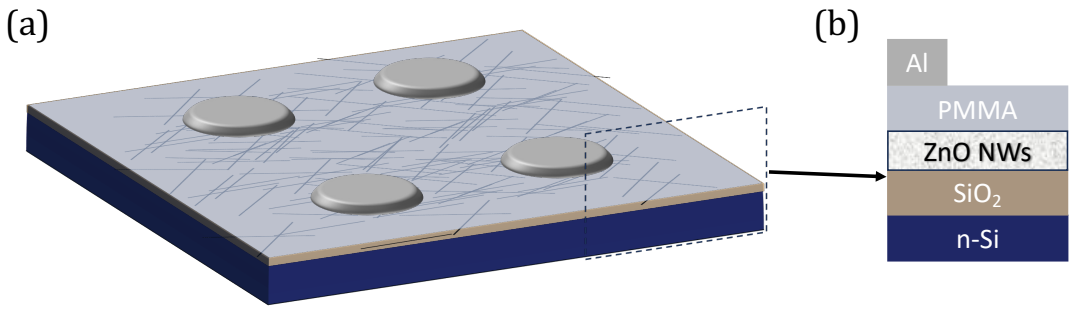

Figure 3-10: (a) MIS device formation of highly doped n-Si/SiO_2/ZnO-NWs/PMMA/Al, (b) Illustration of the cross-section of MF device formation.

In Figure 3-8 (b), a cross-sectional illustration of the MIS capacitors configuration is presented, demonstrating the deposition of TO and BO on the n-Si wafer. The MIS devices are manufactured on a doped n-type Si (n-Si) wafer (100) that is phosphorus-doped and has a resistivity of 10-30 Ω-cm. This wafer was purchased from Testbourne Ltd (S4-9000 D79). A 30 nm thick layer of sputtered SiO_2 is used for the TO. ZnO nanowires (ZnO-NWs) are drop-casted onto the tunnelling layer in Section 2.4.2, forming a nanowire network intended to act as the charge-trapping (interface trapping) layer for memory function and as a photo-active material under UV radiation.

Furthermore, a thin PMMA BO layer encapsulates the ZnO nanowires, preventing against charge leakage. The 200-nm Al thermally deposited contacts are patterned using a shadow mask. It is noted that bridging between the top electrode and ZnO may introduce leakage current, potentially resulting in unreliable memory behaviour in the devices. Previous reports have highlighted the impact of poor encapsulation of the conductive charge storage element in hybrid insulators, leading to unreliable memory behaviour due to high charge leakage [128].

3.4.2 Characterisation of MOS and MIS Devices

The interaction between an amorphous and a crystalline material at the SiO_2/Si interface is complex due to differences in atomic positioning. This results in some silicon atoms within the crystal structure being unpaired with either oxygen or another silicon atom, forming dangling bonds [129]. The main effect of Rapid Thermal Annealing (RTA) is to cause hydrogen desorption from existing silicon dangling bond defects. Compared to conventional furnace annealing, the RTA process does not create additional interface defects [74]. Therefore, applying RTA annealing treatment to the samples on the SiO_2 growth n-Si wafers under a hydrogen-free vacuum

environment is crucial to passivate dangling bonds and improve the n-Si and oxide surface [129-131].

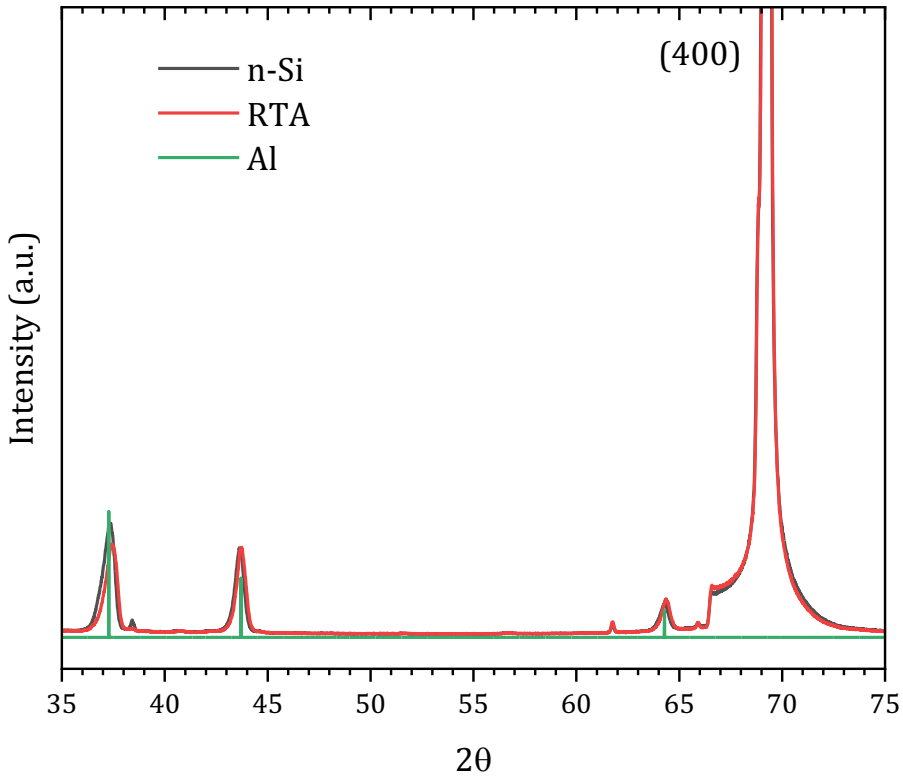

Figure 3-11: XRD of reference MOS (D_r) devices before and after RTA treatment.

Figure 3-11 shows the XRD result of SiO_2 grown n-Si wafer before and after RTA treatment under vacuum conditions. The X-ray diffraction (XRD) analysis of n-doped (100) oriented silicon wafers was performed to assess the crystallographic changes before and after rapid thermal annealing (RTA). The diffraction patterns revealed characteristic peaks for silicon at 2θ values of approximately 69°, corresponding to the (400) crystallographic plane. These reflections confirm the crystalline structure of silicon and align with standard diffraction patterns for cubic silicon. After RTA treatment, the intensity of these peaks remained consistent, indicating that the thermal processing did not induce significant structural degradation. In addition to the silicon peaks, reflections corresponding to aluminium were also observed, suggesting the presence of the aluminium electrode pattern on the reference MOS devices. The XRD spectrum revealed prominent Al peaks associated with characteristic diffraction angles for aluminium, as indicated by stars in Figure 3-11. Overall, the XRD results suggest that the RTA process maintained the structural integrity of the silicon wafers while potentially enhancing the Si and SiO_2 interface.

Therefore, the devices will be annealed to enhance not only the charge transport through the ZnO nanowire network, but also enhance dielectric properties and charge states at the interface between the Si and oxide layer.

3.4.3 Characterisation of Two Terminal MOS Capacitors

Since the primary device configuration of the MF is to integrate the ZnO-NWs network into the insulator layer of MIS, it is essential to prepare the D_r device formation of n-Si/SiO_2/Al and D_p n-Si/SiO2/PMMA/Al to distinguish the effect of ZnO nanowire intake into the insulator, before the investigation the potential for the device produced from the random ZnO-NW network to exhibit multifunctional capability. Here, the D_r MOS formation of n-Si/SiO_2/Al (in Figure 3-12(a)) will be called a reference MOS capacitor. In contrast, n-Si/SiO_2/ZnO-NWs/PMMA/Al formation (as illustrated in Figure 3-10(a) will be addressed as $D_{nw,i}$ MIS capacitors to distinguish between configurations.

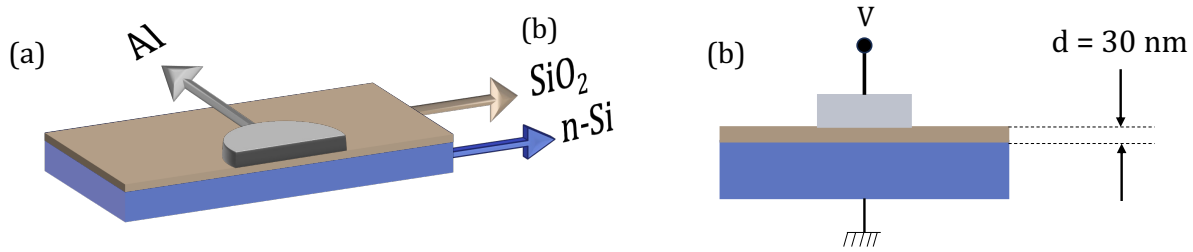

Figure 3-12:Structure of a Dr (n-Si/SiO_2/Al) MOS capacitor: (a) perspective view, (b) cross-section.

3.4.3.1 C-V Measurement of MOS

The performance of MOS/MIS capacitors is influenced by variations in the oxide and traps at the SiO_2-Si interface. A study was conducted to observe the charge-trapping effect of the sputtered SiO_2 layer. This involved performing a reference C-V cycle without ZnO nanowires, illustrated in Figure 3-12(a), with results presented in Figure 3-13(a). The electrical characterisation of the devices was carried out using a multifunctional test station detailed in Chapter 2, which enables measurements of the C-V and I-V sweep gate characteristics.

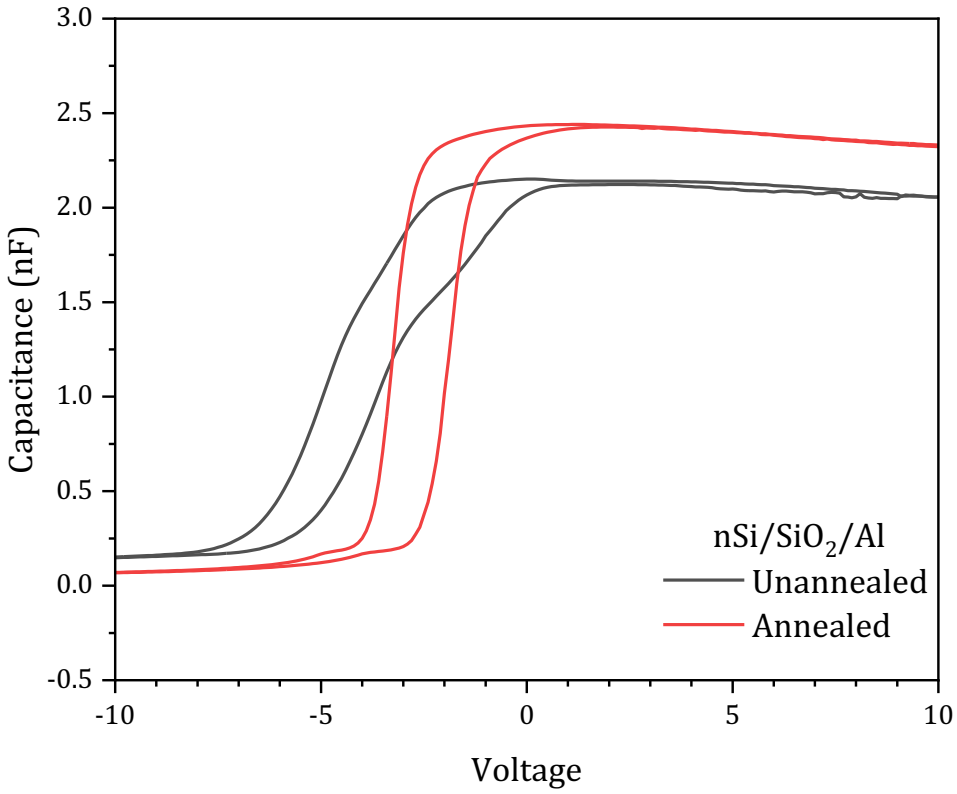

Figure 3-13: C-V characteristics of reference MOS devices before and after RTA treatment described in Section 2.5.1.3.

The band structure of the n-doped silicon semiconductor with a 1.1 eV band gap bends when a negative or positive potential is applied to the Al gate terminal, while the n-Si remains at ground potential (as shown in Figure 3-12(b). Applying potential to the gate terminal causes the band of the n-Si to bend and induces charge into the n-Si at the oxide interface. Figure 3-13(a) shows the typical C-V characteristics of n-type Si semiconductors named accumulation, depletion, and inversion from positive to negative bias, respectively. The band bending of the n-Si under accumulation, depletion, and inversion are presented from Figure 3-14(a) to Figure 3-14(c) [129-131].

When a positive voltage is applied to the gate of the MOS, the band of n-Si bends downward due to the potential difference between the gate and n-Si. This results in the accumulation of electrons at the n-Si interface, causing the conduction band to move closer to the Fermi level. Consequently, the silicon becomes more n-type at the interface, leading to the accumulation of charge (Q_{acc}) in

the n-Si due to the positive gate voltage, resulting in a larger capacitance, as shown in Figure 3-14(a).

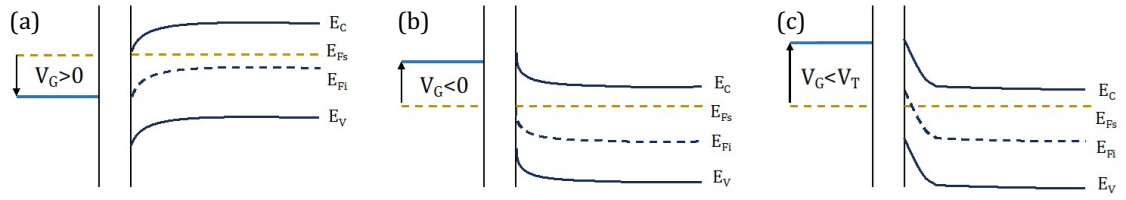

Figure 3-14: Energy band diagram of reference MOS at (a) accumulation, (b) Depletion, and (c) inversion region.

Conversely, when a negative voltage is applied to the gate, it induces a positive charge in the n-Si, causing upward band bending as depicted in Figure 3-14(b) [131]. This creates a negative charge on the metal gate and a positive charge in the MOS due to the depletion in the n-Si, resulting in a gradual decrease in capacitance, illustrated in Figure 3-13(a). As a result of applying a larger negative gate voltage, there is an increase in negative and positive charge accumulation at the gate and n-type silicon (n-Si) regions, respectively. As depicted in Figure 3-14(c), this increased charge accumulation causes further upward bending of the energy bands, ultimately resulting in the Fermi level (E_{Fs}) crossing the intrinsic Fermi level (E_{Fi}) [129, 131]. Consequently, the Fermi level (E_{Fs}) becomes closer to the valence band than to the conduction band. By applying a sufficiently negative voltage to the gate, exceeding the threshold voltage (V_t), the majority of the carriers accumulate at the interface between the semiconductor and the oxide, creating a depletion region characterised by a depletion distance (x_d). This scenario implies that the hole density in the inversion layer near the silicon surface becomes equivalent to the electron density in the neutral n-Si region. Further increases in the negative gate voltage cause the Fermi level to approach the valence band more closely, resulting in a more significant inversion layer charge density (Q_n) [74, 130-132].

3.4.3.2 I-V Measurements on MOS and MIS

The I-V characteristics of the base MOS capacitor were analysed before and after the RTA process, as shown in Figure 3-15. The multifunctional test rig has been exploited for the I-V test of MIS devices. The I-V curve of the base MOS capacitor exhibits a typical behaviour, with negligible leakage current within the ±10 V range. After RTA treatment, a slight improvement in the current conduction was observed, likely due to the enhanced quality of the SiO_2 layer and reduced interface trap density.

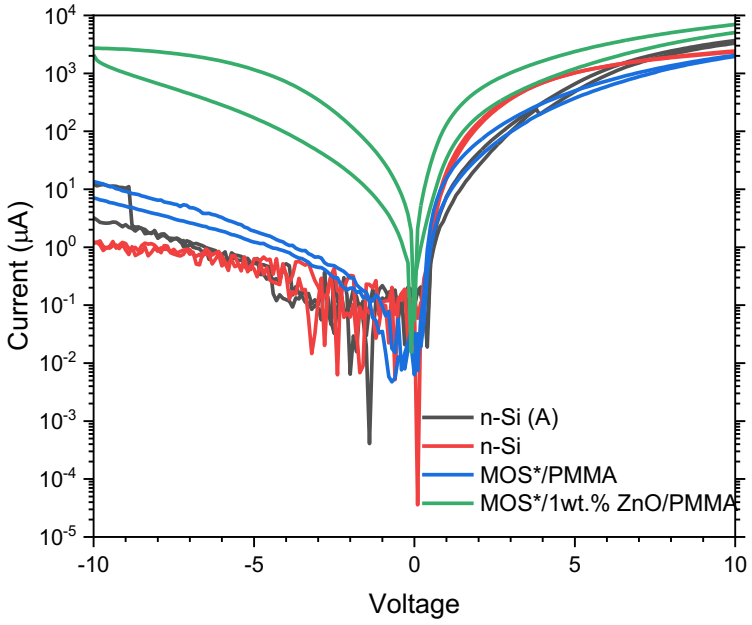

Figure 3-15:I-V characteristics of base MOS devices before and after TRA treatment, MIS devices with PMMA, and MIS devices with 1 wt.% ZnO nanowire network.

Additionally, the I-V characteristics of the MIS structure with a thin PMMA layer deposited on the MOS capacitor show a slight increase in leakage current compared to the D_r MOS capacitor. This increase could be attributed to the influence of the PMMA layer on the overall dielectric properties of the MIS. Furthermore, the $D_{NW,1.0}$ MIS capacitor with 1 wt.% ZnO nanowires embedded between the SiO_2 and PMMA layers demonstrated a noticeable rise in leakage current. This increased leakage is attributed to the ZnO nanowires, which introduce additional conduction pathways and defects, potentially enhancing charge carrier transport through the structure. The I-V measurements confirm that the presence of ZnO nanowires significantly affects the leakage current, while the PMMA layer alone has a more moderate influence.

3.5 Summary

In conclusion, the ZnO-NW networks were characterised both before and after the RTA process to assess the impact of heat treatment on the network's structural and electrical properties. The analysis revealed that the RTA process significantly enhanced the crystallinity of the nanowires, which, in turn, positively influenced the conductivity of the random ZnO-NW networks. This improvement in crystallinity and conductivity lays the groundwork for further exploration in subsequent chapters. In Chapter 5, a detailed evaluation of the conductivity across variable-gap

microelectrode arrays will be performed to provide a comprehensive understanding of the network's electrical behaviour. Additionally, the photodetection capabilities of the ZnO-NW network, particularly under UV light, will be examined in Chapter 6, highlighting the multifunctional potential of these networks in device applications.

The final MIS devices will undergo comprehensive testing to evaluate their performance subject to various stimuli in Chapter 6, 7 and 8. The RTA process enhanced the interface between the SiO_2 layer and n-Si substrate, improving device characteristics. Additionally, the RTA treatment significantly improved charge transport in the random ZnO nanowire network, suggesting its positive effect on conductivity and device performance. Based on these results, the MIS devices will be subjected to RTA treatment after the random ZnO nanowire network is drop-cast on the tunnelling-oxide layer, prior to the spin-coating of the PMMA blocking-oxide. This approach is expected to optimise the device properties and overall performance further.

Chapter 4

THE UNIVERSALIZATION OF RANDOM NANOWIRE SYSTEMS

4.1 General Overview

Understanding the behaviour of random ZnO nanowire networks is critical for fabricating low-cost, large-area MF devices, especially given the inherent complexity of randomness. Computer simulations, supported by experimental validation, provide a vital pathway to link the complexity of random networks with real-world applications. However, a significant limitation arises from the geometrical arbitrariness of conductivity simulations, as results can vary depending on system-specific parameters. Universalizing the geometry of random networks resolves this limitation by ensuring consistency and applicability of ZnO nanowire networks across diverse system sizes, orientations, and configurations, including in-plane electrodes and embedded structures. This universalization not only enhances the understanding of how conductivity behaviour influences specific applications but also establishes a unique contribution by bridging theoretical models with experimental observations.

This chapter applies a robust Monte Carlo analysis to simulate a complex random stick system within an asymmetric cell. By incorporating a time-efficient shortest-path and cluster-finding algorithms into percolation theory, the study aims to detect the universalised cluster parameters by calculating the universal scaling function, thereby achieving universality in random nanowire networks and enabling more realistic modelling. The resulting universally scaled system serves as a foundation for conducting comprehensive conductivity analyses in Chapter 5 and impact on device performances in Chapter 6 and 7. Percolation, a phenomenon extensively studied in statistical physics, addresses the universal scaling properties of randomness. While the random stick system has theoretically been a model for percolation studies, prior research predominantly relied on union-find algorithms for Monte Carlo simulations, which are computationally demanding. This study adopts a more efficient shortest-path algorithm, enabling rapid detection of spanning characteristics and validating its results against established literature, thereby advancing the field of percolation-based network analysis.

4.2 Percolation Theory for Universalization

Understanding the connection between computer-generated models and real-world experimental conditions is essential for scientific research. Renormalisation group (RG) theory [32, 133] highlights the universal principles that govern the behaviour of systems across different scales and conditions. It points out that the scaling functions for the probability of spanning are universal for systems with the same dimensionality, spanning rule, aspect ratio and boundary conditions. This means that similar systems share universal scaling functions for the spanning probability. This universality results from the fixed point in the renormalisation group flow, which dictates the system's behaviour at large scales. This theory is valuable as it allows researchers to predict and draw conclusions based on a few fundamental principles, leading to a better understanding of complex systems. The renormalisation group theory has been applied successfully in site percolation by Reynold *et al.* [134]. The theory is also combined with square and rectangular systems [133, 135-137]. Its broad applicability and deep insights into complex systems make it an essential concept in conduction in random networks [138-146].

In materials science, it is widely recognised that a common feature of random nanowire networks is a sharp increase in conductivity at a critical volume fraction of the conductive phase. This phenomenon is a subject of intense research. It is typically explained by percolation theory which concludes the formation of an electrically connected cluster of filler particles that spans the entire sample. The conductivity further increases as the cluster grows with the addition of more filler particles. A power-law behaviour of conductivity near the critical volume fraction is commonly observed, as seen in eq. (4-1) These findings have significant implications for the design and optimisation of materials and a range of practical applications in the charge transport behaviour of the composites.

$$\sigma \propto \sigma_c \left(\frac{p - p_c}{p_c}\right)^t \tag{4-1}$$

In research, a statistical approach called universal finite-size scaling analysis, combined with Monte Carlo simulations, can help predict and understand real-world phenomena in a precise conduction model. This approach simplifies complex systems by identifying fundamental scaling parameters that control their behaviour, allowing us to focus on essential elements without getting lost in the details of individual systems. This helps develop generalised charge transport models that can be applied to a wide range of systems, saving time and resources by reducing the need for extensive experimentation.

A percolation model must be built using a statistical Monte Carlo analysis of a random stick network to create a universalized cluster in order to start analysing conductivity. Monte Carlo

methods are a class of computational algorithms used to model the probability of different outcomes in systems with inherent uncertainty. By relying on repeated random sampling, these techniques are especially useful for complex systems that are difficult to model deterministically. In this thesis, Monte Carlo simulations are employed to study the percolation behaviour and charge transport in random ZnO nanowire networks, allowing for more accurate modelling of conductivity and device performance under varied conditions. This involves creating a universalised random nanowire network that can serve as the basis for conduction analysis. A statistical percolation function and a cluster-finding algorithm are used to identify and isolate clusters within the network. Then, we conduct a Monte Carlo study to determine the stick density in the unit cell, which helps establish a probability function for conduction analysis in the next stage.

Both percolation theory and clustering are fundamental approaches that play a crucial role in the universalisation of detected clusters for further charge transport analysis, as discussed in the next chapter. Percolation theory has already proven its ability to universalise any geometrical system, including dots, circles, squares, and sticks, for both isotropic and even high aspect ratio anisotropic unit cells [32, 144, 147, 148]. Percolation theory offers a promising approach to standardising random stick systems in anisotropic unit cells. Meanwhile, clustering is a valuable technique in exploratory data analysis that involves grouping objects based on their similarity or connection while ensuring that they differ from objects in other groups or clusters. With its widespread use in statistical data analysis, clustering has many applications in various fields, such as pattern recognition, image analysis, information retrieval, bioinformatics, data compression, computer graphics, and machine learning.

This chapter aims to run MATLAB by practically applying the two algorithms. The focus is on hands-on learning and experimentation. By tackling the examples presented, one can gain a solid understanding of the inner workings of MATLAB. The chapter starts by demonstrating how MATLAB handles simple numerical expressions and mathematical formulas, and then the universalisation of the network is explained.

To ensure precise conductivity analysis, we bring two primary algorithms to work together to create universalised clusters. The first algorithm, the shortest path algorithm, carefully examines the network to determine whether it is spanned between two opposite borders in the specified direction. In addition to the shortest path algorithm, the code also runs the cluster-find algorithm. This algorithm is designed to identify individual-spanned clusters and track essential parameters within the network, such as the number of sticks and nodes and the distance between each node in the cluster. By monitoring these data from the Monte Carlo simulations, we can gain a comprehensive understanding of the specific parameters of each cluster, which is essential for

accurate network analysis for reconstructing the regular lattice. By combining these two algorithms, the code can assess the probability of network connectivity and gain a thorough understanding of the specific parameters of each cluster. This enables accurate and reliable probability data that can be used for conduction analysis in the next chapter.

The primary objective of the shortest path algorithm is to determine whether the network is percolated during all the individual iterations of the loop. This is done by checking if the system spans from one selected edge to the opposite side of the asymmetric cell. The code records how many times the network is spanned for the total number of iterations. The MATLAB shortest path algorithm is integrated into the code to achieve this task. In addition to detecting the probability of spanning the network, the shortest path function identifies the most efficient route from the starting point on one edge to the destination on the opposite edge. This algorithm for statistical analysis of the system plays a crucial role in network analysis and has numerous applications in various fields, including transportation [149, 150], telecommunications [151, 152], and computer science [153, 154].

The process of identifying clusters within a given system involves a thorough examination of each stick to detect any instances of contact with its neighbouring counterparts. Once such contact is established, the sticks in question are then grouped together as a cluster. If this particular cluster spans from one end of the system to the opposite edge, it is recorded, and the relevant parameters are saved for future reference. This algorithmic approach ensures a comprehensive and accurate identification of all clusters within a given system.

4.2.1.1 Important notation and definition

Table 4-1 presents significant parameters, variables, indices, and results with their respective symbols and definitions. Refer to the subsequent text for a more comprehensive grasp of these concepts.

Table 4-1 Index definitions and essential notations.

Notation	Definition	Parameter	Variable
N	Number of stick or site		√
l	Stick length		√
θ	The angle of the sticks to the -x axis	√	
n	Stick density		√
n_c	Critical stick density at percolation threshold	√	

p_c	Critical percolation probability at percolation threshold	√	
p_c^x	Critical percolation probability in the horizontal direction	√	
p_c^y	Critical percolation probability in the vertical direction	√	
L	System size		√
L_x	Oriented inside the rectangular system of width (vertical)		√
L_y	Oriented inside the rectangular system of width (horizontal)		√
R(n,L)	Renormalization factor for given stick density and system size	√	
r	Aspect ratio of the system	√	
$\boldsymbol{n_c^{eff.x}}$	Effective stick density in the horizontal direction	√	
$\boldsymbol{n_c^{effy}}$	Effective stick density in the vertical direction	√	
$\boldsymbol{P_{(n,L,r)}}$	The probability distribution function for a given stick density and system size	√	
$\boldsymbol{m^{(x)}}$	Prefactors in the horizontal direction	√	
$\boldsymbol{m^{(y)}}$	Prefactors in the vertical direction	√	
ϑ	correlation exponent	√	
$\mathbf{F(x)}$	Boundary condition	√	
$\mathbf{b_0}$	Constant	√	
σ	Conductivity	√	
$\boldsymbol{\sigma_c}$	Conductivity at the percolation threshold	√	
t	Conductivity exponent	√	

4.3 Percolation of Random Stick System in Anisotropic Unit Cell

The percolation behaviour of a stick system within a 2-dimensional asymmetric finite-scale system has been extensively investigated using Monte Carlo simulation. Previous studies have indicated that the random stick system exhibits the same universality, even in structures with high aspect ratios and pronounced cell asymmetry [133, 135, 139, 144, 147, 155, 156]. The critical percolation threshold has already been calculated as 5.63726 by Li et al. [141]. An algorithm known as "Weighted union-find, with path compression" is employed to determine whether a cluster spans the opposite boundary [136]. This algorithm involves the repeated addition of a random bond to the lattice, followed by the identification of the clusters to which the sites at either end of the bond belong through the traversal of their respective trees until the root nodes are reached. If necessary, the two trees are merged using a process known as amalgamation. However, the algorithm requires individual checks to determine whether it belongs to the tree, which can be time-consuming, particularly for small system sizes where the nanowire length is much smaller than the size of the system.

In contrast to the Union-Find algorithm, the shortest-path algorithm, when used in conjunction with MATLAB, seeks to determine a path between the identified two opposite boundaries of the system. Instead of working with each stick to determine whether it is part of the tree, the shortest-path algorithm focuses on the sticks connected to the selected boundaries and checks for a possible path between them. This approach eliminates the need to build a cluster, thereby saving time that would otherwise be spent on probabilistic percolation analysis. Moreover, the shortest-path algorithm is efficient because it enables the user to identify the least number of sticks in a spanned system and the number of individual spanning paths that exist [157]. In the context of the winner-takes-all conduction approach, it is imperative to have accurate information about the number of paths and their respective characteristics to undertake a practical conduction analysis. This information can be invaluable for analysing the universalised system, allowing users to release these spanned clusters if needed.

A percolated system is determined by implementing an unweighted shortest-path algorithm in MATLAB. This algorithm is designed to identify the route with the lowest number of sticks connecting the two opposite boundaries of the cell instead of minimising the overall distance. It is more efficient for its high-speed response, enabling efficient analysis of percolation phenomena within the examined stick system. This section aims to determine the correlation between simulated results and established literature on stick percolation, specifically concerning high asymmetrical finite cells.

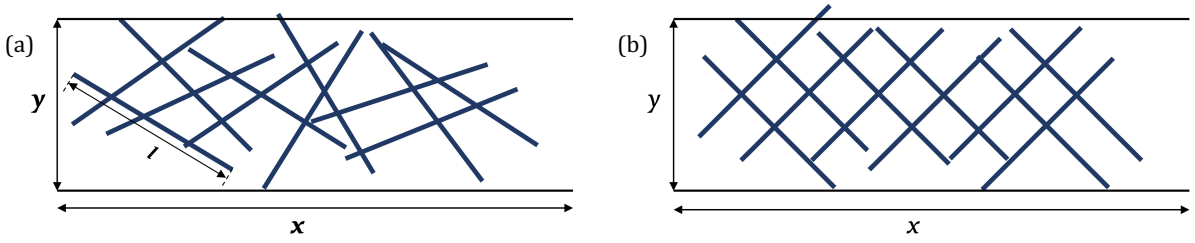

Figure 4-1: Typical configuration of randomly dispersed stick system through perpendicular direction where the system aspect ratio, $r = x/y$, (b) illustrates a renormalised and rebuilt system depending on universalised scaling parameters.

The percolation of randomly distributed sticks in an asymmetric system size was studied using the MATLAB shortest path package in the simulation. N seeds of the generated sticks were randomly dispersed in an asymmetric system (r), where the ratio between the percolation direction and the opposite direction defines the aspect ratio of the short and long sides of the system. Thus, the percolation at the y-axis, as shown in Figure 4-1(a), represents the system asymmetry in the horizontal direction where r=y/x and perpendicular direction where r=x/y. The N widthless (i.e. 1D) sticks with the length (l) are dispersed in a 2-dimensional system where the system asymmetry r=y/x, and a random angle (θ) between ±90° to the x-axis, as shown in Figure 4-1(a). The system size of the asymmetric cells is determined depending on the ratio between sides (short (L_y) and long (L_x) sides) of the system and sticks unit length. The normalised size of the asymmetric rectangular system, L, is calculated as in previous studies[143, 155];

$$\boldsymbol{L = \sqrt{L_x L_y}} \tag{4-2}$$

Where the oriented system width in the horizontal (L_x) and perpendicular directions (L_y) are,

$$\boldsymbol{L_x = \frac{x}{l}} \qquad \boldsymbol{L_y = \frac{y}{l}} \tag{4-3}$$

Once the system size is normalised with respect to stick length (l), the stick density, n, as in previous finite-size analysis as in refs [34, 136, 142, 143, 155];

$$\boldsymbol{n = \frac{N}{L^2}} \tag{4-4}$$

A statistical percolation function represents 10^6 iterations at each step of stick density n for a selected system aspect ratio, r, and system size L. The shortest path-finding algorithm is run at each iteration to check whether the system is percolated through the opposite side of the axis of the unit cells. Thus, the percolation probability function, $R_{(N, L,r)}$ for a given stick density is created concerning stick density. However, an arbitrary probability function of stick density cannot be obtained due to the relation $n = N/L^2$. Because binominal distribution is not suitable for the continuum percolation [136, 155], Poisson distribution is performed instead.

$$\boldsymbol{R_{(n,L,r)} = \sum_{n=0}^{\infty} \frac{(nL^2)^N e^{-nL^2}}{N!} R_{N,L,r}} \tag{4-5}$$

The critical probability in the vertical direction (p_c^x) and the horizontal direction (p_c^y) is the probability of forming a path cross-section through horizontal and vertical directions, respectively. It is obvious that more particles must be connected for percolation in the horizontal direction than in the vertical direction. Thus, the effective percolation threshold for the horizontal and vertical directions is calculated as the ratio of the change in stick density and critical probability ($P_{(n,L,r)} = \partial R_{(n,L,r)}/\partial n.$). The Gaussian distribution is then approximated to the critical percolation density of the system. The other way to calculate the effective stick percolation density n_c^{eff} for each system size that the system percolates, most likely in horizontal or vertical directions, is;

$$\boldsymbol{n_c^{eff} = \frac{1}{L} \int_{n=0}^{\infty} n P_{(n,L,r)} dn} \tag{4-6}$$

Since the scaling factor is the dominant behaviour of the system percolation, it can be calculated for both directions as given in eq. (4-7);

$$\boldsymbol{n_c^{eff.x} = n_c + m^{(x)} L^{\frac{-1}{\vartheta}}}$$
$$\boldsymbol{n_c^{eff.y} = n_c + m^{(y)} L^{\frac{-1}{\vartheta}}} \qquad \textbf{(4-7)}$$

where ϑ is a universal scaling factor that equals $4/3$ for the 2D system. Here, n_c $(= 5.63726)$ is the numerically calculated critical stick density of the randomly distributed stick at the percolation threshold [34]. $m^{(x)}$ and $m^{(y)}$ are the factors of scaling exponent if the average percolation threshold may vary in the horizontal and perpendicular direction, respectively.

To solve the universality problem of the formed asymmetric system, R(n, L,r) should read with universal function;

$$\mathbf{R(n, L) \sim F(x) + b_0/L} \qquad \textbf{(4-8)}$$

where b_0 is system constant and F(x) polynomial form of x $(= (\boldsymbol{n - n_c})\boldsymbol{L^{\frac{-1}{\vartheta}}})$ in percolation transition. Thus, the function turns into universality [34, 133].

Balberg et al. noted that the percolation threshold is isotropic even for an anisotropic system such as an isotropic stick distribution [138, 139]. They also showed numerically that the critical percolation threshold is isotropic [34]. Zezelj et al. [143, 155] also showed that high asymmetric geometries have an isotropic percolation threshold, which is calculated by [34]. The conductivity of the system must be isotropic at the critical percolation probability for the anisotropic percolation threshold. Thus, the conductivity exponent of the percolated cluster is calculated as in eq. (4-1). Even though the universal conductivity exponent is calculated as ~1.3 [32], experimental conductivity exponent results fluctuated sharply due to junction density and hierarchy of the conduction that will be investigated in Chapter 5.

4.4 Implementation of Monte Carlo Analysis

This section aims to introduce the strategy of how the algorithm performed to detect a percolated network through the system, whilst illustrating the formation of the clusters for different

variables, demonstrating the application of percolation theory by integrating the shortest path, and comparing the universalised renormalisation function for percolation of a random stick system.

4.4.1 The shortest-path algorithm

The percolation behaviour of a stick system within a 2-dimensional asymmetric finite-scale system has been extensively investigated using Monte Carlo simulation. Previous studies have indicated that the random stick system exhibits the same universality, even in structures with high aspect ratios and pronounced cell asymmetry. The critical percolation threshold has already been calculated as 5.63726 by Li et al. [34]. To determine whether a cluster spans the opposite boundary, an algorithm known as "Weighted union-find with path compression" is employed [158]. This algorithm involves repetitively adding a random bond to the lattice and then identifying the clusters to which the sites at either end of the bond belong through the traversal of their respective trees until the root nodes are reached. If necessary, the two trees are merged using a process known as amalgamation. However, the algorithm requires individual checks to determine whether it belongs to the tree, which can be time-consuming, particularly for small system sizes where the nanowire length is much smaller than the size of the system.

In contrast to the Union-Find algorithm, the shortest-path algorithm, when used in conjunction with MATLAB, seeks to determine a path between the opposite boundaries of the system. Instead of working with each stick to determine whether it is part of the tree, the shortest-path algorithm focuses on the sticks connected to the selected boundaries and checks for a possible path between them. This approach eliminates the need to build a cluster, thereby saving time that would otherwise be spent on probabilistic percolation analysis. Moreover, the shortest-path algorithm is helpful because it enables the user to identify the least number of sticks in a spanned system and the number of individual spanning paths that exist. In the context of the winner-takes-all conduction approach, it is imperative to have accurate information on the number of paths and their respective characteristics to undertake an effective conduction analysis. This information can be invaluable for analysing the universalised system, allowing users to release these spanned clusters if needed.

A percolated system is determined by implementing an unweighted shortest-path algorithm in MATLAB. This algorithm is designed to identify the route with the lowest number of sticks connecting the two opposite boundaries of the cell instead of minimising the overall distance. It is more efficient for its high-speed response, enabling efficient analysis of percolation phenomena within the examined stick system. This study aims to determine the correlation between

simulated results and established literature on stick percolation, specifically in relation to high asymmetrical finite cells.

4.4.2 Efficient Analysis of Random Stick System Using Shortest Path Algorithm

The percolation of randomly distributed sticks in an asymmetric system size was studied using the MATLAB shortest path package, the simulation. N seeds were randomly dispersed in an asymmetric system (r) where the ratio between the percolation direction and the opposite direction defines the aspect ratio of the short and long sides of the system. Thus, the percolation at the y-axis, as shown in Figure 4-2 represents the system asymmetry in the horizontal direction where $r = \frac{y}{x}$ and perpendicular direction where $r = \frac{x}{y}$. The N widthless (1D) sticks with length (l) are dispersed in a 2-dimensional system where the system asymmetry r=y/x, and a random angle (θ) between ±90° with respect to the x-axis, as shown in Figure 4-2 produced by MATLAB figures. In this study, an asymmetric system is formed where $r = 5$ and $r = 0.2$ in vertical and horizontal directions.

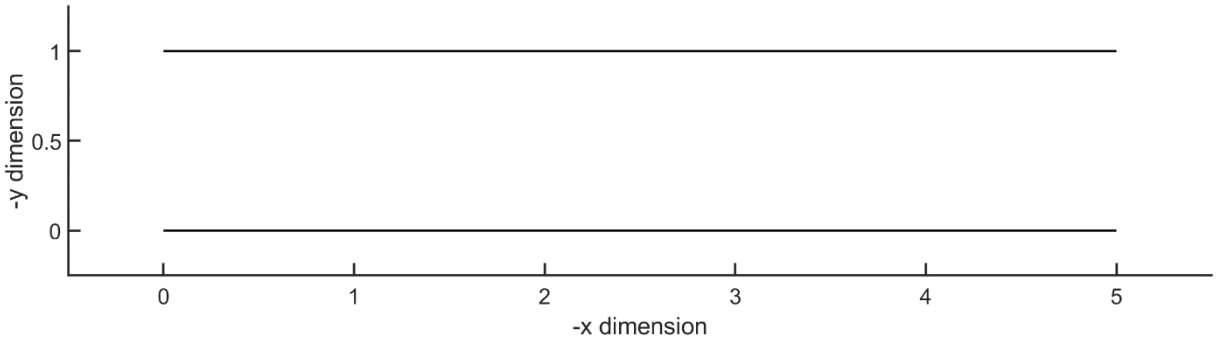

Figure 4-2: The asymmetric system, which has dimensions of 5 in the -x direction and 0.2 in the -y (horizontal) direction.

Figure 4-2 illustrates the process of identifying the boundary conditions of the system before generating N randomly distributed sticks within the cell. To form the sticks, the code randomly assigns seed coordinates (x_i, y_i) and creates sticks with these coordinates as the centre points, with a length of l. As shown in Figure 4-3, to ensure that the sticks are randomly distributed with a 360° angle, they were assigned a random angle of ± 90° degrees with the -x axis. This approach ensures that there are no limitations on the distribution of the sticks, as they can be oriented in any direction within the cell. The utilisation of these methods provides uniform conditions and assumes that there is no effect on randomness due to external conditions.

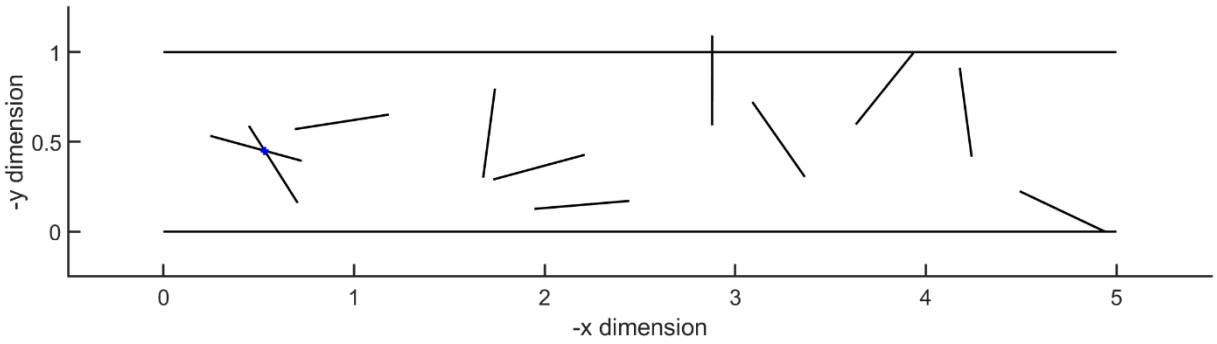

Figure 4-3: Illustration of randomly dispersed N stick in the asymmetric cell. (N = 11, l = 0.5)

Once all the sticks are formed, the algorithm first checks for pairs of touching sticks using a function into the shortest-path algorithm which geometrically calculates whether an individual stick in the network intersects with any other neighbouring sticks. If sticks intersect, a node is formed at the point of intersection. Once the algorithm checks all the possible intersections between the pairs, a nodes list is created for cluster analysis. Figure 4-4 illustrates the application of this method in a system of 29 randomly dispersed sticks with a length of 0.5 in an asymmetric cell. The resulting clusters, denoted by dashed circles, consist of at least two sticks, while the blue coloured plus signs display the nodes where two sticks intersect.

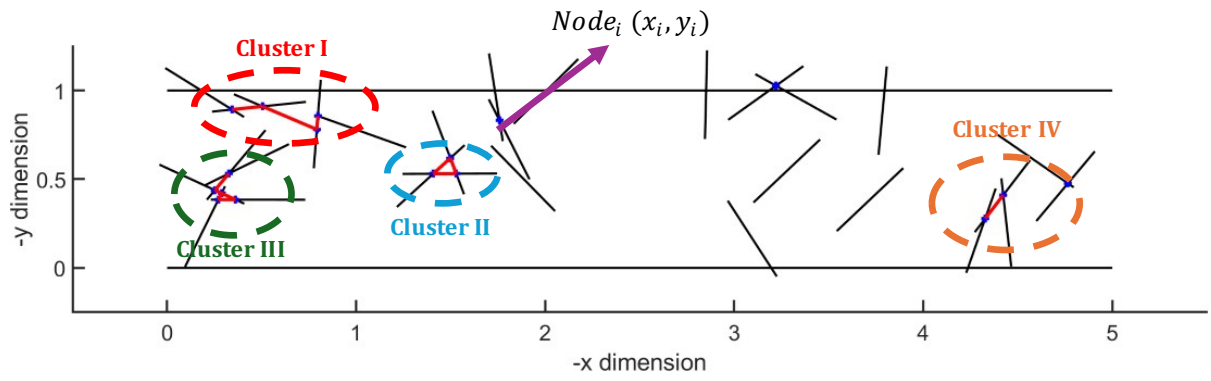

Figure 4-4: Illustration of finding pairs intersecting between 29 widths less sticks with 0.5 length. Blue-coloured plusses and dashed circles represent the nodes and clusters, respectively.

In the final stages of the algorithm, the shortest path-finding package in MATLAB runs between the two boundaries on opposite sides of the cell, seeking a possible path through the list of created nodes, as illustrated in Figure 4-4. If the system spans between the two opposite boundaries, as shown in Figure 4-5, the loop is recorded as having percolated over 106 iterations. This calculation determines how many times the system percolates over a million iterations.

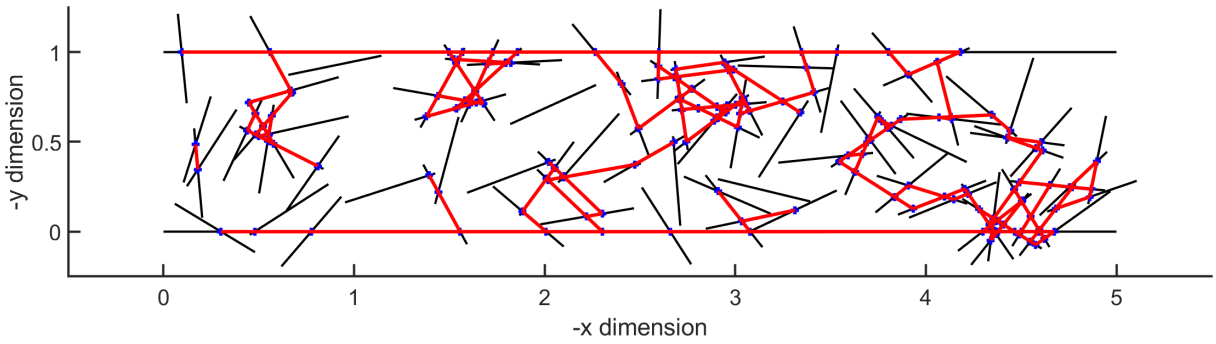

Figure 4-5: An example of a spanned 100 random sticks (l=0.5) system between two opposite boundaries in the horizontal direction.

4.4.3 Variables of system formation

This study is focused on an asymmetric system where the degree of cell asymmetry (variable r) is maintained at a stable level by 5x1 dimensions. The system size and stick densities are the variables for the renormalisation function R(n, L, r) of the asymmetric system. This function provides universalisation for percolating between the two opposite boundaries of the system. Section 4.2 emphasises the importance of scaling the computer-generated system for universalization. Section 4.3 demonstrates how the renormalization function of the percolated random stick system is applied to the asymmetric cell using the shortest path algorithm.

Our method involves gradually increasing N (and consequently n for the given L) to link the effect of ZnO-NW density with the change in the conductivity of an individual electrode separation. As shown in eq. (4-1), the material properties near the critical percolation probability are dominated by a specific parameter. Since this parameter is n-dependent, we run the code step by step, increasing on N to demonstrate how n affects the spanning behaviour of the system L. Figure 4-6 shows the random stick dispersion in the asymmetric cells for various N between 25 and 225 while keeping L constant. Scaling the stick density, Figure 4-6 illustrates how the sticks' dispersion affects the cluster formation for the given system size L=4.47.

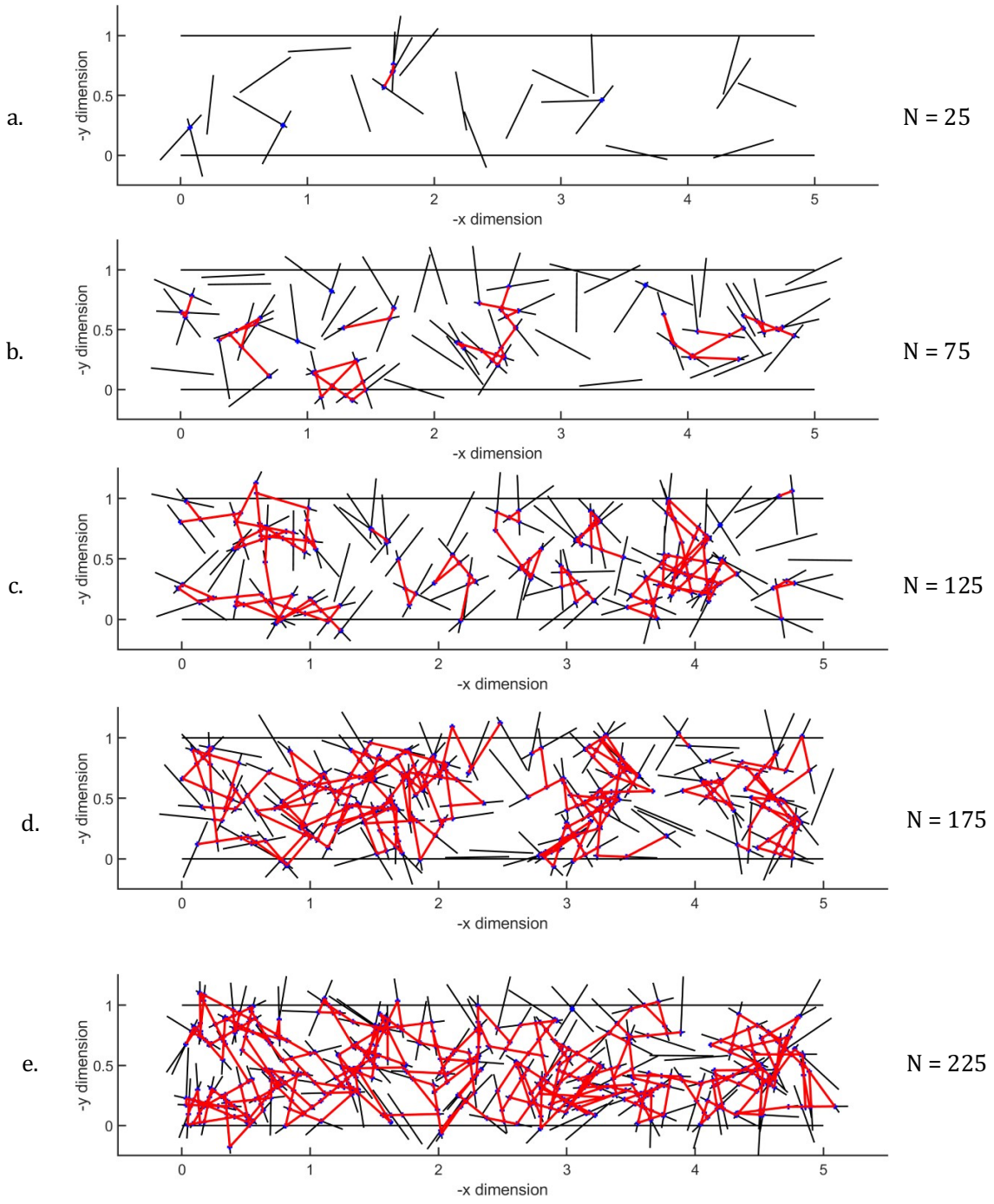

Figure 4-6: Visualisation of random stick density through the system of 5x1 and L=4.47 for the N= 25 (a), N=75 (b), N=125 (c), N=175 (d), and N=225 (e).

Based on our simulation, The simulation has determined that the system reaches the critical percolation threshold, $n_c^{eff.y}$ when n=3.05. This occurs when there are 61 sticks in the system, as calculated by eq. (4-7) When the stick density is below the critical point, with N=25, the system can only create a few small clusters consisting of two sticks, as illustrated in Figure 4-6 (a). It is

improbable that the system will create a continuum path between the borders. Just above the critical stick density, with N=75, the system will link the opposite side by the preliminary spanning clusters, as shown in Figure 4-6 (b). If the stick density is further increased to N=125, two prominent individual spanning clusters will form, as shown in Figure 4-6 (c). Eventually, the main spanned clusters will merge, although there may still be small clusters not part of the big one, as seen in Figure 3-6 (d). However, with a further increment in stick density to N=225, all the sticks will span into one big cluster, as shown in Figure 4-6 (e).

The other variable, L, represents the length ratios between the ZnO-NWs and electrode separation. Just as the spacing of nanowires and electrodes affects the formation of a path formation of nanowires between two electrodes, the ratio of stick length to system dimensions will similarly affect the formation of a spanning continuum network. For this reason, as seen in Figure 4-7 (a-d), while N in the system is kept constant at 500, the ratios between the sticks and the dimensions of the system through -x and -y are varied. This figure shows the effect of varying L between 5.59 and 22.36. To simulate the variation of the electrode distance in a real experimental system, the stick length is set at an equivalent ratio of L in the simulation to replicate

accurately the experimental conditions between the electrode width and gap and ZnO nanowires length discussed in the next chapter.

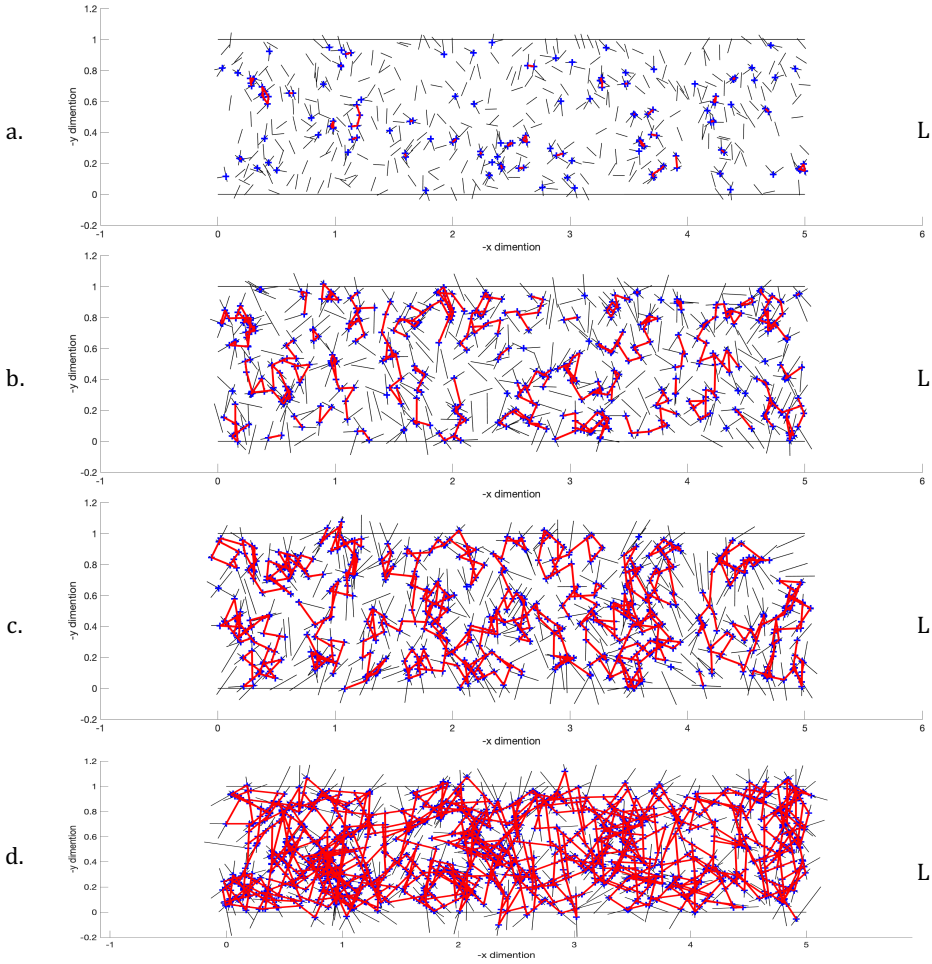

Figure 4-7: Distribution of 500 random sticks in the asymmetric system (r=1/5) for various L = 22.36 (a), 11.18 (b), 8.94 (c), and 5.59 (d).

As illustrated in Figure 4-7(a), the phenomenon of the sticks forming clusters in a large system (L=22.36) is apparent, and they can only produce small clusters with a limited number of sites. Even when the system size is reduced by half, as shown in Figure 4-7(b), the likelihood of forming a continuous network remains significantly low, even with increased sticks within the clusters. However, when the system size is further decreased to L=8.94, the probability of forming a spanning network rise, as seen in Figure 4-7(c), although some sites remain isolated from the spanned clusters. Ultimately, upon a further decrease in the system size, all the sites become members of the main cluster, as illustrated in Figure 4-7(d).

A significant factor impacting the specific behaviour is the system size, which is crucial in scaling the sticks in a rectangle cell. As depicted in Eq. (4-4), the density of sticks per unit area is directly proportional to the system size of the asymmetric rectangle cell. Accordingly, stick density is

frequently regarded as a variable in system scaling. To comprehensively consider the influence of the system's size, the number of sticks must be transformed into a distribution based on stick density, which is subsequently amenable to scaling using the Gaussian distribution, as evidenced in Eq. (4-5). By incorporating the system size into the differential renormalisation function, as expounded in Eq. (4-8), it becomes an intrinsic part of the universal percolation equation. These computations lead to a better understanding of the correlations between system size, stick density, and overall behaviour.

4.4.4 Hamilton Supercomputing

Even though the shortest-path algorithm promises more efficient computing than the union-find algorithm, the Monte Carlo simulation still requires intensive GPU usage for 10^6 iterations. Hamilton is an exceptional High-Performance Computing (HPC) service, centrally operated and readily accessible to trained researchers at Durham University. In this study, the HPC was crucial for executing large-scale Monte Carlo simulations, specifically running the MATLAB script 10^6 times for stick percolation across various system sizes. The extensive computational power of the HPC enabled parallel processing of these iterations, which would otherwise be computationally prohibitive on standard systems. MATLAB scripts were modified to run in parallel using the 'parfor' function, distributing the workload across 48 CPU cores, each with 128 GB RAM. As a result, the 'parfor' function efficiently divided multiple iterations among the cores, significantly reducing the program's execution time in 72 hours, which is the limit of allowed supercomputing time by Hamilton.

4.5 Universal Finite-size Scaling Function for Random Stick Percolation in Asymmetric Cells

This section aims to show how an arbitrary system turns into a universal system by scaling the function of percolation theory. For this purpose, it summarises how the Monte Carlo method is applied to the percolation of the random stick system in asymmetric cells ($r = 1/5\,, 5$) by integrating the shortest-path package of MATLAB.

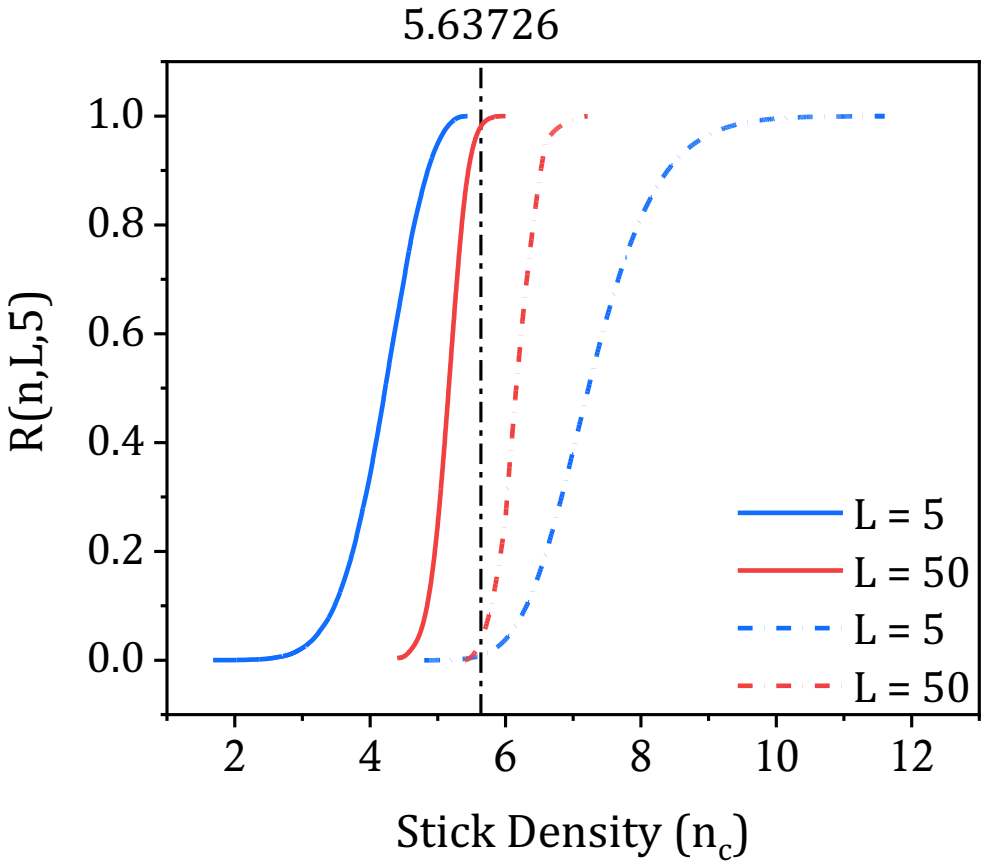

Figure 4-8: Demonstration of the probability distribution for two different system size of L=5 (black line) and L=50 (red line), and both horizontal (dashed Line) and vertical (strait line) directions.

Figure 4-8 shows the probability distribution of the sticks at perpendicular (solid line) and horizontal (dashed line) directions when the system size L equals 5 (black line) and 50 (red line). As detailed in Section 4.4, Figure 4-8 is generated by simulating the distribution of random sticks in an asymmetric cell and then using a shortest-path algorithm to determine whether the system is spanned. The simulation was repeated 10^6 times for each stick density data point (n) and for each system size (L) to produce statistical spanning possibilities of the system for the stick densities and system sizes. Thus, the figure shows the probability of the continuum path between 0 and 1 for the given stick density of a system size.

Furthermore, Figure 4-8 indicates that the increment in scaling of the system (which means the increment in system size) converges the efficient system percolation to the universal percolation threshold for horizontal and vertical directions. On the other hand, the system converges the universal percolation threshold where the percolation probability is close to 1 in the vertical direction while it is close to 0 in the horizontal direction. This means the system exhibits isotropic

physical properties in the horizontal direction when the p_c is close to 1. However, the system is expected to present universal physical properties at a very low degree of p_c.

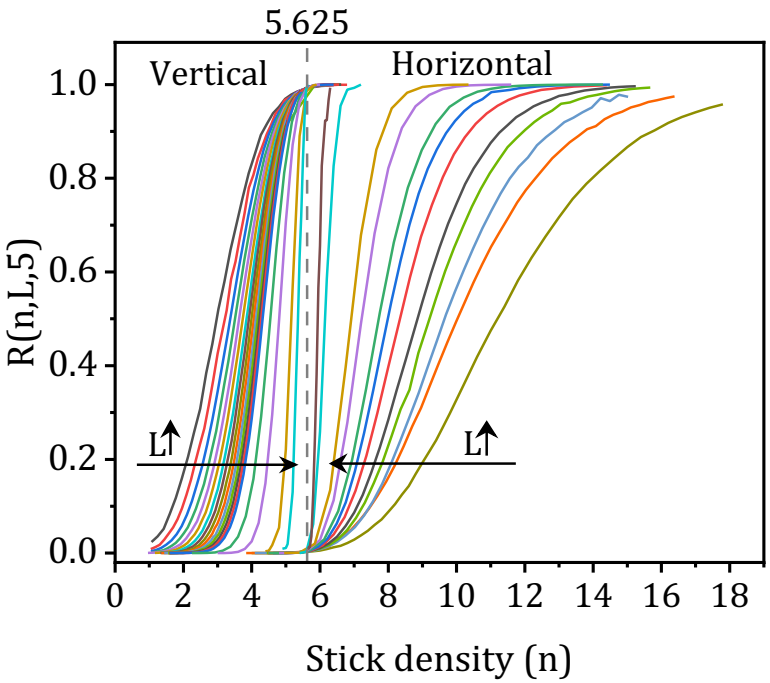

Figure 4-9: Monte Carlo simulation for the probability distribution of various system sizes between L=2.24 and L=100, horizontal (right side of the dot-dashed line) and vertical (left side of the dot-dashed line) directions. The dot-dashed line point at the universal percolation threshold calculated by ref [34]. The arrows in both directions of the dot-dashed line indicate the direction where the system sizes are increasing.

The current algorithm allows for the analysis of large-scale stick systems using Monte Carlo analysis with a significant number of iterations. The extended results of the stick percolation simulation for asymmetric systems up to large sizes between L = 2.25 and 100 are listed in Figure 4-9. The figure provides a comprehensive overview of the probability of spanning at various system sizes in vertical (L=0.2) and horizontal (r=5) directions, detected using the shortest path algorithm outlined in the previous section. The dashed line on the graph represents universal stick percolation based on Ref. [34]. The arrows indicate the direction in which the system size L increases for both axial directions of the system. The dashed line in the figure is the theoretical universal percolation threshold of 5.63726.

The representation of large-scale data offers valuable data on system size-dependent percolation behaviour for scaling the system. As depicted in Figure 4-8 and Figure 4-9, a discernible trend emerges: the percolation probability distribution experiences an increase in slope along both dimensions with an expanding system size. This phenomenon indicates system convergence,

indicated by the steeper curves observed in the percolation probability function as the system dimensions expand. Notably, even in considerable system asymmetry, an observation is made regarding the intersection of percolation probability function curves at a specific value denoted as n_c, described by ref. [155]. The consistent convergence at n_c, irrespective of the system's asymmetry, underscores the significance of this particular point in the behaviour of percolation probability with systematic system scales.

Furthermore, a pivotal finding emerges concerning the standard deviation of the probability distribution function, which diminishes to zero as the system size tends to infinity. This signifies an increased concentration and predictability in the probability distribution, attributable to the reduced independence of the system factor for larger values of L, as articulated in eq. (4-7). Consequently, with the approach towards an infinite system size, the probability of percolation tends towards either 1 or 0, symbolic of highly predictable behaviour in an infinitely large system.

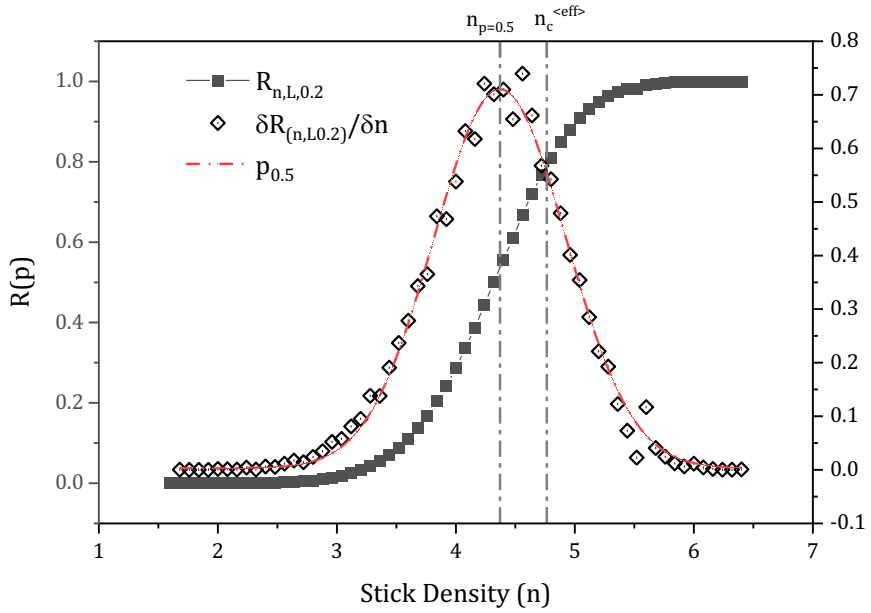

Figure 4-10:The black solid squares indicate the probability distribution of the system with L=11.18. The diamond symbols represent the probability distribution, while the red dashed line shows the Gaussian distribution function data fitting.

Before advancing the investigation to the subsequent stage, it is imperative to provide a clear explanation of the numerical calculation of the related parameters. Figure 4-10 shows the probability distribution of the system along the vertical direction when the system size (L) is fixed at 11.18. The black squared symbol line in Figure 4-10 corresponds to the probability distribution concerning stick density, as previously illustrated in the group of the probability distribution of

the various system sizes in Figure 4-9. This representation is intended to elucidate the methodology employed in calculating the effective percolation threshold for the given system size (L=11.18).

The distribution of the black diamond symbols in Figure 4-10 shows the list of the changes in the probability distribution (P) where $P_{n,L} = \left(R_{L,n} - R_{L,n-1}\right)/\delta n$, meaning the canonical average position of the percolation threshold [159]. For each step of the increment in the stick density. The effective critical stick density, n_c, represents the point at which, for the initial instance, a percolating cluster establishes connectivity between the system's boundaries. The Gaussian distribution fitting of the P will give the effective percolation threshold for each system size. The compilation of effective stick density values corresponding to various system sizes and percolation directions is presented in Figure 4-11.

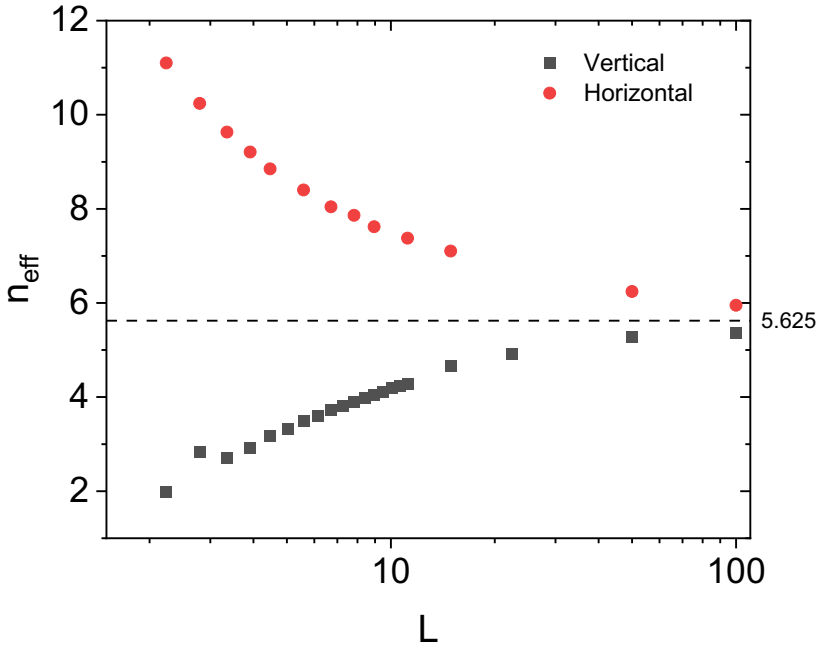

Figure 4-11: Dependence of average stick percolation density, n_c^{eff}, on system size, L, and aspect ratio, r=0.2 and r=5. Values were calculated using Eq. 7 and obtained from Monte Carlo simulations for various system sizes between 2.24 and 100. The horizontal dashed line represents the percolation threshold, n_c.

Moreover, the maximum of the probability distribution function, also known as the effective stick percolation density $\langle n \rangle_{L,r,5}$ and $\langle n \rangle_{L,r,0.2,}$ approaches the percolation threshold n_c with increasing system size as seen in Figure 4-11. For systems with an aspect ratio of more than one (r > 1), the average stick percolation density $\langle n \rangle_{L,r}$ converges to n_c with the increment on the system size L. This is because large finite systems are more likely to be spanned in the longitudinal direction at

larger stick densities than n_c. In comparison, larger systems are more likely to percolate in the transverse direction at lower densities than the critical value. On the other hand, for systems with an aspect ratio greater than one (r > 1), the average stick percolation density $\langle n \rangle_{L,r}$ converges from above.

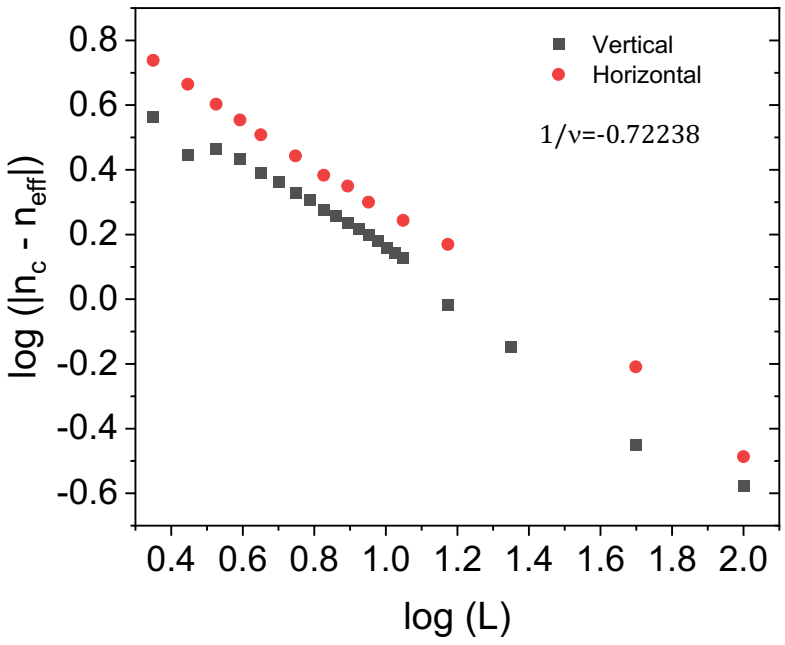

Figure 4-12: Calculation of scaling factor for both percolation dimension (r=0.2 and r=5), represented in eq. (4-7).

Owing to the strong dependence of the system size on the n_c^{eff}, the correlation exponent (ϑ) is the dominant behaviour of the system percolation. The exponent can be calculated for both directions using eq. (7a) and (7b), where $\frac{-1}{\vartheta} = -0.75$ for 2-dimensions finite-system [133]. Here, n_c (= 5.625) is the numerically calculated critical stick density of the randomly distributed sticks at the universal percolation threshold. $m^{(x)}$ and $m^{(y)}$ are the factors of the scaling exponent for an average percolation threshold, which may vary differentially in the horizontal and perpendicular direction, respectively. In Figure 4-12, the horizontal scaling exponent also converges to a 2D scaling exponent of -0.75 for system asymmetry as simulated [34], and the exponent is equal for the vertical and horizontal directions [155]. Our calculation also agrees with the comment that the scaling exponent is -0.72238 for both planar directions.

To address the universality challenge even in small system sizes (where L<5), an important step involves the determination of the critical stick density through simulation of the $R_{(n,L,r)}$ function. This determination is reliant on a universal function as in eq. (4-7).

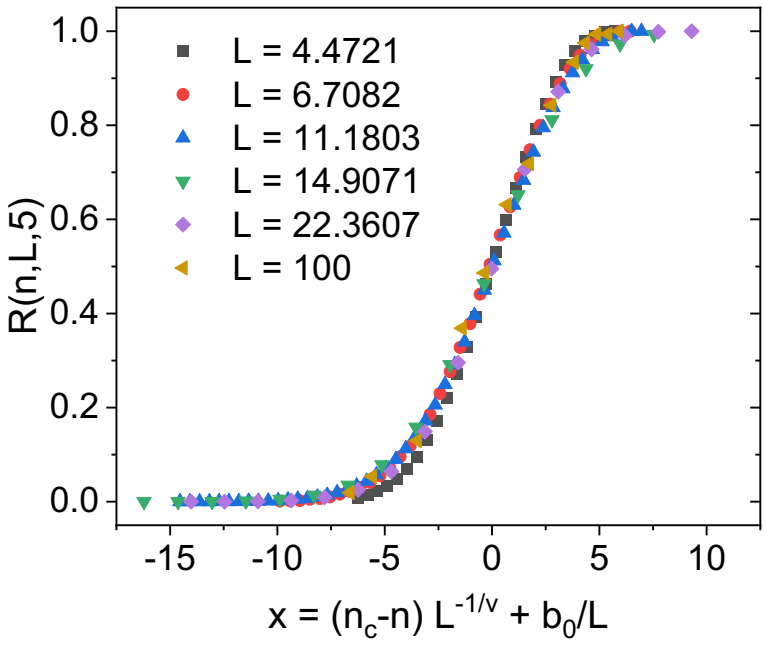

Figure 4-13:R plot demonstrating finite-size scaling and the universal scaling function for finite-size corrections in a system with n_c=5.63726.

Figure 4-13 presented above illustrates the universalised scaling function of the system denoted as F(x), wherein b_0 represents a constant, and $(n_c - n)L^{-\frac{1}{\nu}}$ serves as the scaling variable, with v representing the correlation-length exponent as calculated and depicted in Figure 4-12. Incorporating this scaling function into the probability distribution for variable system sizes, ranging from small to large systems, leads to strong convergence. This convergence implies a wide range of system sizes adheres to the same scaling function, exhibiting consistent universality across diverse scales.

Figure 4-13 visually presents the universalised probability $R_{(n,L,0.2)}$ function for the asymmetric system, as outlined in eq. (4-7). By incorporating a metric factor, $\hat{A}$ (a_1=0.1062) in eq. (4-8), we have defined a universal polynomial function $\hat{F}(\hat{x})= 1/2+\hat{x}+A_3\hat{x}^3+A_5\hat{x}^5+\cdots$, where A_3=-1.061 and A_5=0.752, aligning closely with the results reported in [34, 135, 136]. These outcomes indicate the feasibility of transforming our asymmetric system to exhibit universality akin to isotropic systems and lattice percolation.

4.6 Summary

This chapter presents the application of percolation theory to analyse random stick systems using a finite-scale analysis method. The shortest-path algorithm was run rather than the weighted

Union-Find algorithm due to its faster detection of spanning networks and effectiveness in gathering data for conductivity analysis of ZnO nanowire networks. The results demonstrate a percolation threshold consistent with the values reported in the literature, validating using the shortest path algorithm. This serves as a foundation for further analysis in subsequent sections.

The next chapter will focus on a detailed conductivity analysis of random ZnO nanowire networks and explore the relationship between conductivity mechanisms and percolation behaviour. This correlation has yet to be extensively studied and is addressed in detail. Chapter 6 will then examine UV photodetection performance in the same ZnO nanowire networks, linking the efficiency of UV photodetection to the conduction mechanisms influenced by percolative behaviour.

The final chapter will extend the percolation theory to investigate the charge storage capacity of these networks when embedded in the dielectric layer of MIS capacitors. The findings from this chapter provide not only a faster solution for stick percolation in finite-scale analysis but also a critical link between percolation behaviour and optimal device performance. These insights are essential in developing effective device prototypes in later sections.

Chapter 5

EXPLORING CHARGE TRANSPORT THROUGH RANDOM NETWORKS: A COMPARATIVE STUDY OF THEORETICAL MODELS AND EXPERIMENTAL INVESTIGATIONS

5.1 General Overview

The chapter presents a significant contribution to the field by proposing a model that addresses the correlation of composite conductivity between experiments and simulations. As discussed in Chapter 4, using a universalised random stick system is crucial for a more realistic simulation, moving away from arbitrary system parameters. This approach holds promise for a realistic simulation of the experimental results of a random ZnO-NWs network between two Al electrodes.

Recognising the time inefficiency of generating a random stick system by Monte Carlo simulation for each parameter of conduction analysis, we implemented a more efficient approach. By running a cluster-finding algorithm in parallel to the shortest path approach, we were able to identify critical parameters that reflect the structure of the random system, detailed in section 4.3. This helps to establish the validity of our approach and the thoroughness of our analysis.

Once the clusters are reconstituted for each system size, we proceed to simulate the conduction of the system using LTspice. This simulation allows us to discuss and reflect on critical parameters, which, in turn, helps us correlate the experimental findings of random ZnO-NWs networks on various electrode-separated Al electrode arrays. The details of this process are explained in Section 5.4.

5.2 Approach to Charge Transport through a Random Network

The accuracy of conduction in composites consisting of random constitutes in their structures is based on the lattice geometry of a network and the hierarchy of conductance between constituents. Anticipating charge transport through a composite is important when device modelling for an application where charge transport is essential for an efficient device. Modelling the conduction of a random nanowire network requires both scaling of the network and consideration of the hierarchical conduction mechanism for the realistic scenario, even though

one of them is systematically underestimated in the literature [30, 124, 160]. As mentioned in Chapter 3, the universal scaling of constituents in a random network with respect to the system size is critical for replicating the fact that the cluster realised in a simulation can be related to experimental data. However, hierarchy in the conduction process is equally important when modelling charge transport across percolated networks of constituents. The proposed approach suggests a state-of-the-art solution for anticipating conduction in random nanowire networks. The proposed model uses a combination of theory and algorithms to predict how random ZnO nanowire networks transport charges accurately. Combining the percolation model with real-world I-V data of random ZnO nanowire networks on the microelectrode array presented in Chapter 2 aims to gain an essential link between the model and experimental data.

A systematic series of steps was undertaken to demonstrate our model for the realistic prediction of charge transport through a random ZnO-NW network. As explained in Chapter 3, the initial phase involved the construction of a universal random nanowire network by applying the Monte Carlo method to the percolation of a random stick system in an asymmetric unit cell. Following the establishment of this universalised nanowire cluster, the model facilitates a comprehensive analysis of its conductivity, allowing for predictions and comparisons pertinent to experimental evidence. This methodological approach ensures a robust foundation for evaluating and extrapolating charge transport behaviour within the specified ZnO nanowire network.

The process of conductivity modelling is a crucial aspect of predicting conduction. It often involves the utilisation of advanced software tools. One such tool that has gained considerable popularity in recent years is the LTspice program [161]. This program enables researchers to model and simulate various systems' electrical behaviour accurately. By determining the critical variables involved in the system in Chapter 3, we can use LTspice to create detailed models that accurately reflect the system's behaviour under different conditions, as discussed in Section 4.3.

LTspice, a sophisticated computer software precisely designed to simulate analogue electronic circuits grounded in the SPICE (Simulation Program with Integrated Circuit Emphasis) platform, stands as an important tool in the exploration and analysis of conduction phenomena. This software offers plenty of components that enable simulation of the conductivity of any system. It makes the simulations adaptable with various software. Originally developed by Linear Technology and currently maintained by Analog Devices, LTspice stands out as the most widely utilised SPICE software within the research and industry [162]. Notably, despite being freeware, LTspice lacks artificial restrictions on its capabilities, boasting no limitations on features, nodes, components, or subcircuits. The software includes an extensive library of SPICE models derived from Analog Devices, Linear Technology, Maxim Integrated, and various third-party contributors.

In this thesis, LTspice software is being used to analyse conduction in the constituent universalised random ZnO-NWs network, as explained in Section 5.3.1. This computational framework offers a unique feature wherein node lists, delineating sticks and their junctions with each other can be seamlessly integrated. As a result, it is adaptable to a range of configurations, as summarised in Section 5.3.2, and allows users to adjust conduction parameters by individually changing the attributes associated with each node. This approach allows for fine-tuned parameter adjustments, enabling a more detailed examination of conduction characteristics in the universal ZnO-NWs system, as discussed in Section 5.3.3.

As mentioned in Chapter 4, junction and contact resistance emerges as a predominant factor influencing the ultimate conduction within the random system of constituents [31, 124, 143, 146, 160, 163-165]. Furthermore, the ZnO nanowires, identified as n-type semiconductors [6, 7] with a nonlinear conduction behaviour (as presented in Chapter 2), influence the electronic structure of the ZnO nanowire network. Given the complicated nature of these physical phenomena, a rigorous integration of junction and nanowire properties becomes important for the analysis of conduction within the network. Consequently, as explained in Section 4.4, the properties of each resistance node are assigned accordingly, taking into consideration the specificities of the constituent physical phenomena, thus contributing to a comprehensive understanding of the intricate conduction dynamics at play.

In this chapter, LTspice is used to simulate the conductivity of ZnO nanowire networks, focusing on the I-V response across various gap Al microelectrode arrays (as introduced in Chapter 2) and different nanowire ratios, detailed in Section 4.4.1. The variation of electrode separation aims to generate I-V data for various system sizes, L, while the nanowire ratio dictates the stick density (n) in the simulations. Eq. (4-3) describes the system size as the ratio between the nanowire length and the dimensions of the electrode width and gaps. Since the nanowire length remains constant throughout, each electrode separation corresponds to a distinct system size, allowing a systematic exploration of how electrode separation and nanowire ratio influence the conductivity of the ZnO nanowire networks. The objective is to ensure that the scaling behaviour observed in Chapter 4's simulations applies meaningfully to the experimental results discussed in this chapter.

The experimental investigation involves I-V testing of ZnO nanowire networks on Al microelectrode arrays with varying concentrations of ZnO nanowires, measured in wt.%. Testing begins when the system first exhibits measurable conductivity and continues until charge transport saturates. Current density values at 10 V will be recorded for each electrode array and ZnO nanowire concentration. In parallel, the ZnO nanowire networks will be simulated using the universal scaling principles established in the previous chapter through percolation theory. LTspice will simulate the I-V characteristics, with diodes and resistors representing the electrical

behaviour of the nanowires and their junctions. This approach ensures that the simulations are grounded in a universal model rather than relying on arbitrary methods frequently seen in the literature [31, 160].

The final step involves comparing the experimental and simulated conductivity data at 10 V to evaluate the model's accuracy in predicting network behaviour based on nanowire density and electrode separation. This comparison will confirm the robustness of the universal model and its broader applicability, distinguishing it from the more limited, arbitrary models often cited in previous research [31, 160, 163, 164]. By demonstrating the correlation between simulation and experimental results, this study validates the predictive power of the model for understanding and optimising the conductivity of ZnO nanowire networks.

5.3 Exploring Conductivity through Simulation: A Computational Study

This section demonstrates how the clusters can be reformed using the universalised parameters obtained in Chapter 4. The section is divided into three subsections that explain in detail the complexities of building pathways and modelling conduction through these pathways in LTspice. Each subsection provides practical information about the processes of path formation and modelling conduction phenomena within the LTspice simulation environment.

5.3.1 Formation of the Universal Clusters

The study begins by using statistical calculations and percolation theory to establish the universality of a random ZnO nanowire network. It then explores the use of universalised cluster parameters to develop a model for simulating the conductivity of any randomly distributed percolated network. This model involves reconstructing the universalised clusters in the simulation to determine the conductivity of nanowire composites within the percolated network. By monitoring and adjusting specific variables, it becomes possible to simulate the percolated clusters needed to determine the conductivity of each sub-system. This methodology enables the assessment of the conductivity of any randomly distributed percolated network of nanomaterial composites.

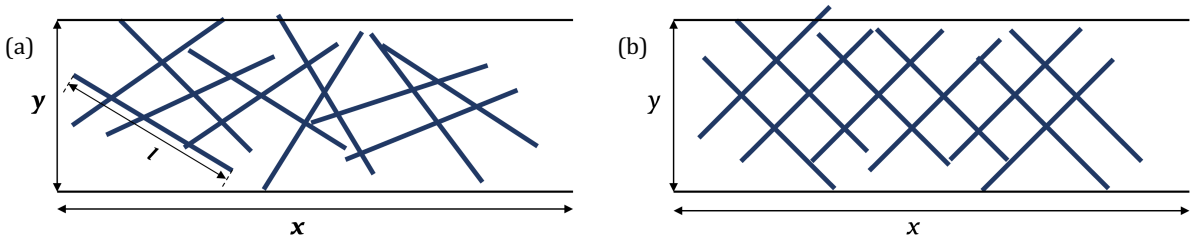

Figure 5-1: (a) illustration of random ZnO-NWs network in an asymmetric cell representing the electrodes at both opposite sides of the y-axis. (b) illustration of reconstituted ZnO-NWs system by considering data from the Union-find algorithm.

The algorithm utilised enables continuous tracking of the mean percolated cluster size for a defined anisotropy and system size. This facilitates the generation of universally interconnected clusters for conductivity analysis, providing valuable insights into the behaviour of percolated systems. Once the Cluster Find algorithm is integrated into the MATLAB script and gathers parameters on percolated clusters, the goal is to reconstruct these clusters, as shown in Figure 5-1(b). This assumes that (i) the sticks can only form $\pm 45°$ to the x-axis for the isotropic case and (ii) the nodes are evenly spaced with an average length along the sticks. An example of the universalised cluster is depicted in Figure 4-1b. Inserting geometrical parameters into these assumptions allows us to calculate the number of sticks required to form a percolative path through the selected direction, eq. (5-1).

$$N_{SP} = \frac{d}{n_l * B_c} * \frac{2}{\sqrt{2}} \tag{5-1}$$

where N_{SP} is the least number of sticks required to create the shortest path between two opposite sides of the cell, d is the distance between the two opposite boundaries of the direction selected, and n_l is the average distance between two neighbouring nodes on a stick. Once the required number of rods has been calculated for the shortest path, and each stick contacts amount of B_c of other rods, and the total required number of sticks of the cluster to produce the shortest path is:

$$N_{path} = B_c \times N_{SP} \tag{5-2}$$

Where N_{path} is the total number of sticks used to build a spanning cluster in the direction where the shortest path connects the two opposite boundaries in the direction of percolation. Then, how many of the percolated paths (P_N) that the system can produce is calculated by:

$$P_N = {N_c}/{N_{path}} \tag{5-3}$$

where N_c is the total number of sticks that are any spanned cluster member. Therefore, the system's ability to generate clusters can be evaluated by determining the number of clusters it can produce. Ultimately, the universalised probability function governing cluster formation yields the constant (α) given in eq. (5-4). This coefficient (α) is a characteristic of the composite. It considers the number of paths a system can create and their likelihood of occurrence, as illustrated by the probability function depicted in Figure 5-2(a). Thus, the coefficient will be introduced into the final conductivity modelled by the simulation if percolation is valid for the given condition.

$$\alpha = R_{(n,L.r)} \times P_N \tag{5-4}$$

The clusters are reconstructed by exploiting the critical parameters acquired through the Union-Find algorithm, such as n_l, B_c, stick density, and asymmetry, which play a crucial role in determining the formation of universalised clusters in simulation, as evidenced in Figure 5-2(a). The reconstruction process of universalised clusters involves leveraging these parameters to develop an accurate representation of the cluster's morphology and structure for a given stick density and system size. By utilising the Union-Find algorithm, the study aims to provide a comprehensive understanding of the factors that govern the clustering behaviour of the sticks and their relationship with percolation theory. Overall, the findings of these clusters have significant implications for the design and understanding of the system conductivities by fine-tuning between system parameters such as stick and junction conductivities.

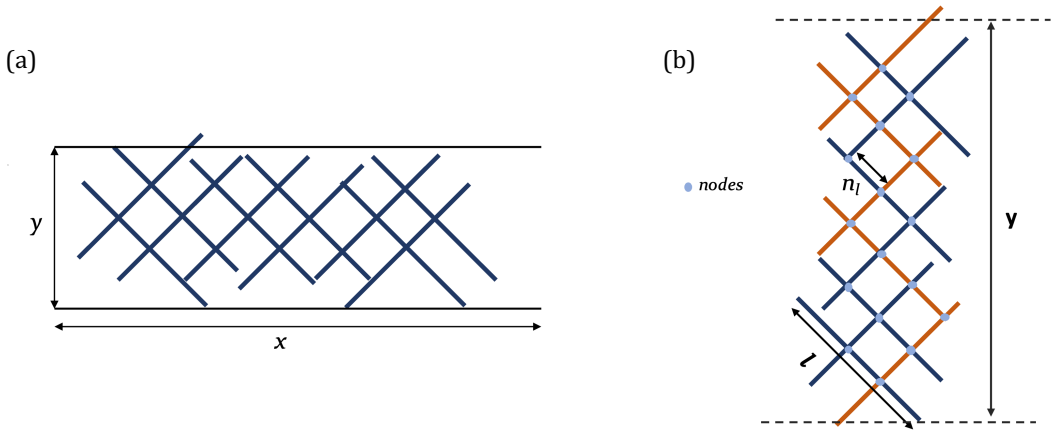

Figure 5-2: (a) Illustration of the nodes where nanowire junctions are and the shortest path (red sticks), and (b) the tunnelling distance between nanowire-nanowire junctions.

5.3.2 Charge Transport through Random Network

Percolation theory is widely used to study the conductivity mechanism of complex networks in electronic applications [141, 142, 147, 164, 166, 167]. The theory associates system conductivity with filler size, orientation and isotropy, even for high asymmetric system parameters [142, 143]. It has been observed that even for highly asymmetric systems, the system conductivity remains uniform at the critical percolation threshold probability [139]. This highlights the relevance of the system conductivity with theory in the context of isotropic percolation threshold.

Percolation studies on the conductivity of randomly dispersed 1D sticks in 2-dimensions and 3-dimensions have revealed a universal conductivity exponent, which is a measure of how the conductivity changes as the density of sticks increases relative to critical stick density. The universal exponent for 2D systems is t = 1.3, and for 3D systems, t = 2 (eq. (4-1)).

However, experimental and numerical studies on the conductivity of carbon nanotubes (CNT) [168, 169] and nanowires [31, 37, 164, 170] have shown a significant discrepancy between the observed conductivity exponent and the calculated universal value. The discrepancy is attributed to the relationship between the conductivity exponent and the stick-to-stick junction ratio [143, 164], stick resistivity, and junction density [141, 143, 169], playing a vital role in the conduction models based on the percolation theory. Therefore, a more comprehensive model is needed to explain the non-universal critical exponent of the network. This is because the existing model does not consider the conduction mechanism when determining network conductivity using the percolation theory-based conductivity of random networks.

Various approaches can be employed to simulate the junction resistivity and its impact on the conduction behaviour of a system. One such strategy involves setting the junction resistivity (R_J) by providing a ratio with respect to the nanowire resistivity (R_S) as studied in [143] for various ranges of asymmetric system sizes. This is because it has been previously discussed in the literature that junction resistivity is assumed to have a critical role in the random network conductivity [31, 146]. As a result, the R_J becomes the dominant characteristic of the network, and the system's conductivity depends on the physical interaction between the constituents through the network.

Tunnelling conduction is a widely explored method to simulate conduction in random networks where constituents have interparticle distance allowing hopping between them. It enables conduction even when there is some distance between the constituents [171, 172]. In this approach, the constituents are assumed to physically touch each other in the simulations. However, tunnelling conduction can occur because they may only electrically interact with each other rather than direct charge transport. Figure 5-2(b) illustrates that even if the components overlap each other in 2D, tunnelling conduction can still occur. Studies have demonstrated that the distances between the components in a percolated network can vary depending on the filler density, resulting in the variation of R_J as a function of component density [171]. Therefore, unlike the constant junction resistivity, this approach suggests a variable junction resistivity associated with the nanowire density in the system. With its ability to model conduction in networks with distance between components, it can provide a better way to comprehend the behaviour of these complex systems, which can help determine the correlation between the experimental conduction of ZnO-NWs and the simulation.

Simulations of complex structured filler materials have shown that they behave in specific ways in certain systems. The electronic charge can be transferred over the path with the least resistance or energy barrier, particularly under low potentials when the junction resistance is dominant. This phenomenon is known as the "Winner-takes-all" approach [124]. To estimate the non-universal critical conductivity exponent, simulations have been carried out on the conductivity calculated over the complex structures formed in these systems. Therefore, focusing on the shortest path or the least resistive path is crucial for detecting and simulating charge transport analysis [160, 173]. The simulation is carried out on the shortest path and the number of such paths formed through the system.

To establish a clear connection between the critical conductivity exponent and experimental results, it is essential to develop a precise model. Currently, our research is focused on studying the conductivity mechanism of a complex ZnO-NWs network in charge transport behaviour. The conductivity mechanism through the network plays a significant role in the conduction exponents.

Therefore, it is crucial to conduct experimental reflection of random ZnO-NWs network in various electrode separations to determine the conduction mechanism accurately. Our goal is to achieve a comprehensive understanding of the conduction mechanism and establish a clear link between the critical conductivity exponent and the experimental results.

5.3.3 Conductivity Analysis with LTspice

Subsequently, LTspice software facilitates conduction measurement by exploiting the defined shortest path as in Figure 5-2(a) and utilising resistivity values assigned to stick-to-stick junctions (R_J), stick-to-boundaries (or electrodes) (R_C) and sticks (or ZnO-NWs) (R_S) as seen in Figure 5-3. These resistivity values are crucial as they determine the current flow through the system, thereby influencing the overall conduction behaviour. With clusters now exhibiting a standardised behaviour and a connected node list, a seamless integration of a conduction model can be extracted. This involves incorporating universalised spanned paths into LTspice for comprehensive analysis.

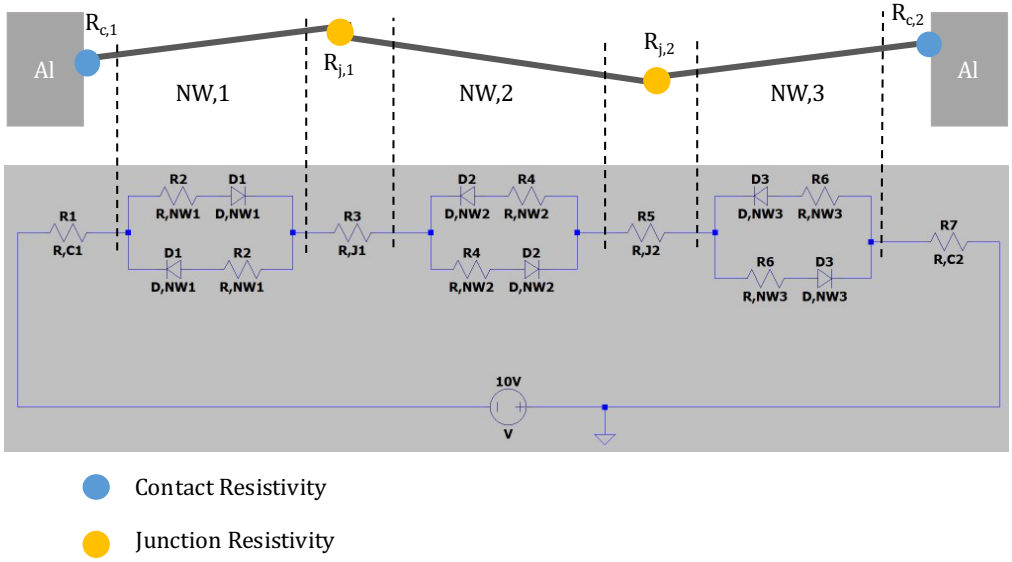

Figure 5-3: The upper side illustrates the three conjugated ZnO-NWs contacted by two aluminium electrodes, blue and yellow dots point out where ZnO-NWs/Al-electrodes and ZnO-NWs/ZnO-NWs junction positions. The bottom side shows the circuit formation of three ZnO-NWs contacts in LTspice software.

Figure 5-3 illustrates the detailed conduction simulation through a path, visually depicting three connected ZnO nanowires positioned between two aluminium electrodes at the upper section. Simultaneously, the lower section of the figure provides a schematic replication of the corresponding circuit in LTspice. The simulation of the system's conduction involves the

consideration of three key parameters. The first parameter consists of the contact resistivity (R_C) between the ZnO-NWs and the aluminium electrode, denoted by the blue dot point in Figure 5-3. The yellow dot in the figure represents the second parameter, which refers to the resistivity between two connected nanowires, commonly referred to as junction resistivity (R_J). All these resistivities are adjustable parameters aiding to vary them for precise simulation.

The third parameter that needs to be considered in the analysis of ZnO nanowires is the resistivity inherent to the nanowire structure. A diode tool [174] is introduced to facilitate conductivity simulation for ZnO nanowire networks, coupled with a serial resistance to model the nonlinear ohmic behaviour of ZnO conduction[6]. This tool enables the user to change parameters such as carrier density, band gap, and breakdown current, which significantly impact the electronic structure of the ZnO material. This feature provides greater control and flexibility when analysing the system.

A 'serially' connected resistivity is introduced to allow adjustments in the nanowire resistivity. Since diodes permit current flow in only one direction, two diodes are connected in parallel but in opposite directions relative to their counterparts. This configuration captures the conduction behaviour in ZnO nanowires for both negative and positive directions by allowing current to pass for both bias polarities. As a result, the simulation provides a more comprehensive understanding of the system's behaviour, which is essential for developing efficient and effective applications.

5.4 Correlation the Conduction of Random ZnO-NWs Network

This section aims to make use of the conductivity models to establish a correlation between experiments and simulations for the reconstituted universal clusters. These clusters have been accomplished by reconstituting the clusters with data obtained from the union-find algorithm for different system sizes and densities of ZnO-NWs, elaborated in Section 4.4. To establish an experimental correlation with the model, we have randomly dispersed ZnO-NWs with various weight ratios onto Al microelectrode arrays for I-V characterisation, as mentioned in Chapter 3 and presented in Section 5.4.2. Finally, we have identified the critical parameters to establish a correlation between the collected conduction data from the simulation and the experimental data in section 5.4.3.

5.4.1 Simulation of the Clusters and Conductivity

As mentioned in the previous section, the current-voltage characteristic of the shortest path of various stick densities, has been presented in Figure 5-4. The conductivity values detected by LTspice for the given system parameters were multiplied by a factor α, as explained in eq. (4-4),

to obtain the final conduction of the systems if the system percolated. This unique approach allows fine-tuning the overall conduction behaviour in random ZnO-NWs networks for various electrode separations of Al electrode arrays, a significant finding in our research.

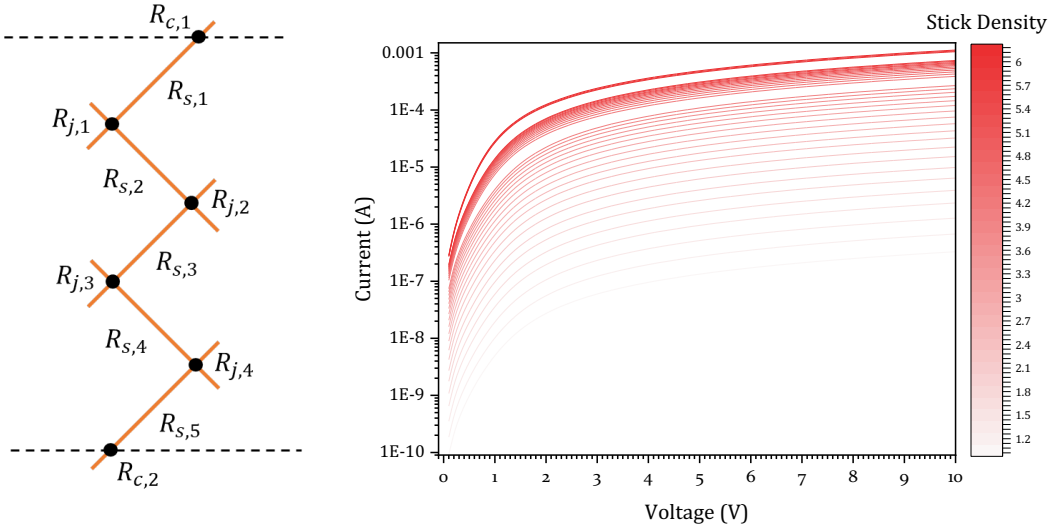

Figure 5-4: (a) Illustration of an LTspice simulation for the shortest path of a system that consists of five nanowires; dashed lines represent the system borders at the two opposite sides. (b) I-V sweep of the system (L=8.94) through the shortest path of the system for various stick densities between n=1.2 and n=6.

The formation of a Winner-Take-All (WTA) pathway in networks is a crucial aspect of network connectivity. The conductivity of the networks is dominated by the junctions when junction resistivities are much larger than the nanowires itself. This WTA pathway exhibits distinct conductance plateaus that remain stable across a range of current compliances. It represents the pathway with the lowest possible energy connectivity within the network, as illustrated in Figure 5-4(a). The conduction of the shortest path is measured by LTspice, with a node listed in Figure 5-4(a).

Thanks to the least energy path approach of WTA, the charge has the potential to be efficiently carried between the furthest nodes on the same ZnO-NW. In other words, due to a lower energy barrier than any junction, the charge prefers to flow through a nanowire until it must pass the other neighbour nanowire through a junction between them. Therefore, the charge will be expected to flow through the lowest number of nanowires, demonstrating the efficiency of the WTA pathway as illustrated in Figure 5-4(b).

Using this approach, LTspice allows the simulation of the charge transport over the estimated shortest path. Once the current flow is simulated over the path, the total flow is calculated by multiplying with the constant value a, that the universal probability of the system can produce a number of clusters with the probability p. Figure 5-4(b) shows the simulated Log(I)-V sweep between 0 – 10 V range for various stick density when the system size L =8.94 in red colour scale from light to dark in a case depicting the stick density scale from lower to higher. The non-ohmic behaviour of the ZnO-NWs system is reflected in the simulated conductivity thanks to the integration of the model diode reflecting the ZnO-NWs electronic behaviour.

As detailed previously, the cluster analysis algorithm, which produces data for the cluster structure as a function of stick density, is illustrated in Figure 5-2(a). The universal statistical cluster parameters for four different system sizes are presented in Figure 5-5. As previously explained in sections 3-6, the number of clusters gradually increases with the addition of more sticks to the system until all the sticks are members of the same cluster, so the total cluster number decreases to one. An effective percolation, n_{eff}, threshold for the horizontal direction of spanning probability of random stick system is reached around a stick density lower than the universal stick density due to the nature of asymmetric system dimensions, as presented in Figure 4-9. As clearly shown in Figure 5-5, the system size critically impacts the behaviour of the cluster formation. While the system still produces new clusters above the n_{eff} for the systems smaller than L=6.7, the larger systems subsequently cannot form a new cluster as the stick density increases because clusters have already begun to merge beyond this threshold point above the point.

The system generates spanning clusters with low probability in lower stick densities and then systematically creates new clusters with slightly higher stick densities. It is important to note that the number of clusters produced eventually plateaus and then decreases. This increase in stick density, an important factor in the conduction behaviour, results in the merging of individual clusters. The formation of a new homogeneous system results from creating new conduction paths beyond system saturation, which leads to increased stick-to-stick junctions due to the coalescence of clusters (refer to Figure 5-5). The conductivity behaviour of the system is affected by the n_{eff} characteristic of the system size variation above these critical points when the t values listed in eq. (4-1) are varied as a function of system size. It is important to note that this behaviour

is a direct consequence of the system's inherent properties, which will be discussed in Section 5.3.3.

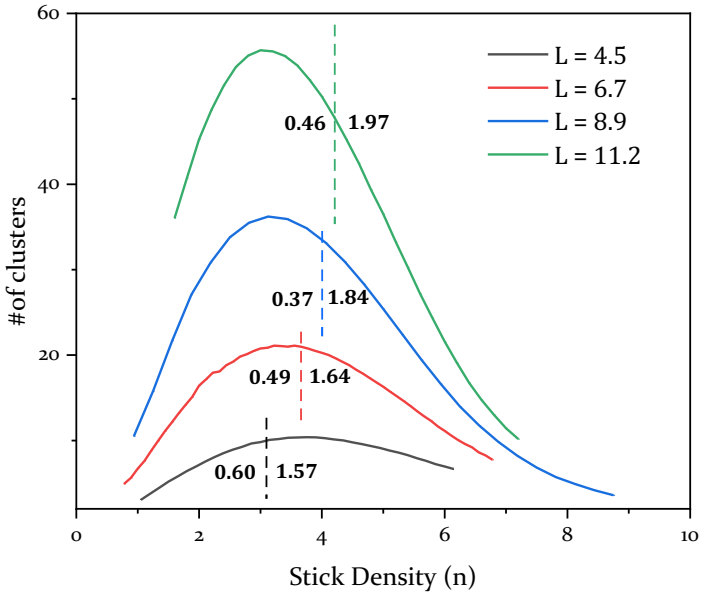

Figure 5-5: Formation of the clusters as a function of the stick density for 4 different systems size L=4.5, 6.7, 8.9 and 11.2. The perpendicular dashed lines are the positions of the n_{eff} for the system.

In summary, the section has demonstrated an important part of understanding the reconstitution of the universal clusters. Using the Union-Find algorithm function in MATLAB script, we created the node list of interconnected groups of components within the system. Through the integration of percolation theory demonstrated in Chapter 4, we have ensured the universal applicability of these clusters, which is a fundamental concept in our methodology. With the help of an advanced tool library, LTspice can simulate the current flow of the clusters on the nodes list of ZnO-NWs and their junction with each other and Al electrodes. By reforming the shortest paths and integrating their universal probability of formation, we can better understand the current flow of these clusters and the potential effects of conduction mechanisms on the system conduction.

5.4.2 Conductivity of Random ZnO-NWs Networks

A range of nanowire densities in DMF solutions were applied to electrode arrays with various electrode separations to demonstrate the relationship between the conductivity model and the universalised cluster approach in the experimental correlation of randomly dispersed ZnO nanowires. The ZnO nanowire ratios indicate stick densities in the simulation, while the variations

in electrode array dimensions represent the system sizes of the simulations. The size of the system is calculated using eq. (4-2), which is modified with respect to the length of the nanowires (5 µm) and the dimensions of the electrode separation and width. The conductivity of the random network is then tested through two-terminal in-plane I-V measurements, as detailed in Section 3.3. Figure 5-6 shows the I-V characteristics of various ratios of ZnO-NWs on a ten-micron electrode-separated Al microelectrode array and an LTspice simulation with the same system size as the electrode separation and nanowire length. The experimental and simulated results are listed in the legends of the figure as the weight ratio of ZnO-NWs in DMF solution and stick density, respectively.

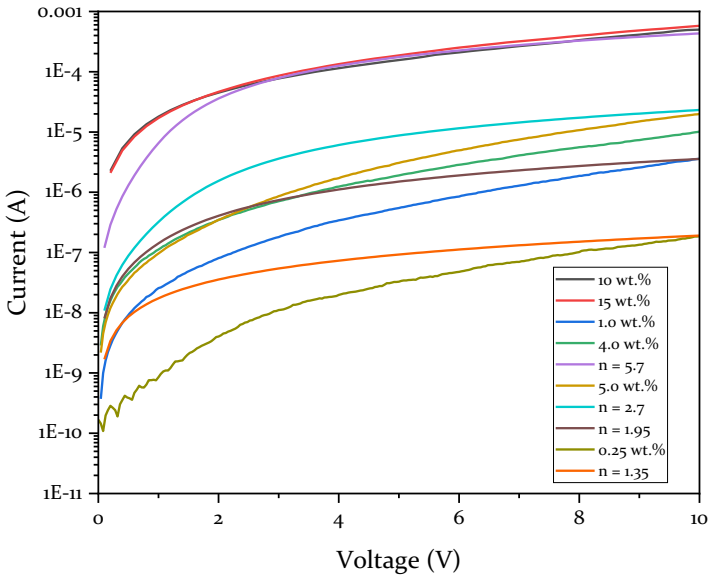

Figure 5-6: I-V sweep of ZnO nanowires on 10 µm gap Al microelectrode array, labelled as wt.% and simulated random stick system on the horizontal direction (L=4.50) labelled with n.

The conduction behaviour of ZnO nanowire networks at various concentrations has been analysed using a comprehensive I-V simulation. In Figure 5-6, while an I-V sweep is presented for ZnO nanowire concentrations of 0.25, 1, 4, 5, 10, and 15 wt.% in a DMF solution, all situated within a 10 µm electrode separation, the simulated I-V is shown for n=1.35, 1.95, 2.7 and 5.7. The electrodes were subjected to a voltage sweep from 0 V to 10 V in 0.1 V steps, and the resulting current was tested using the SMU and simulated using LTspice. The measured and simulated data were compared, and the results are illustrated in Figure 5-6. The distinctive nonlinear

characteristics inherent in semiconductor nanowires are evident for both tested ZnO-NWs and simulated clusters [6, 174].

As discussed in Chapter 4, we calculated the critical stick density to be 5.625, consistent with the literature [34]. The shortest path integrated Monte Carlo simulation also provided similar results. The value of n=5.7 is just above the critical stick density, at which point the conductivity of the system becomes universal regardless of its size and dimensions. Figure 5-6 also indicates that the I-V results of 10 and 15 wt.% random ZnO-NWs networks align with the simulation of universal stick density. Additionally, the conductance remains relatively constant beyond this point despite a one-third increase in the nanowire density. This stable conductivity beyond the critical density indicates that the universal parameter is approaching the saturation point of the ZnO-NW network's conductivity for the given system size and dimensions. The available data support this observation and serves as a clear indication of the system's robustness and reliability [33, 143]. Another observation is that the change in ZnO-NWs density between 1 and 5 wt.% corresponds with the conductivity change between n=1.9 and n=2.7 in the simulation.

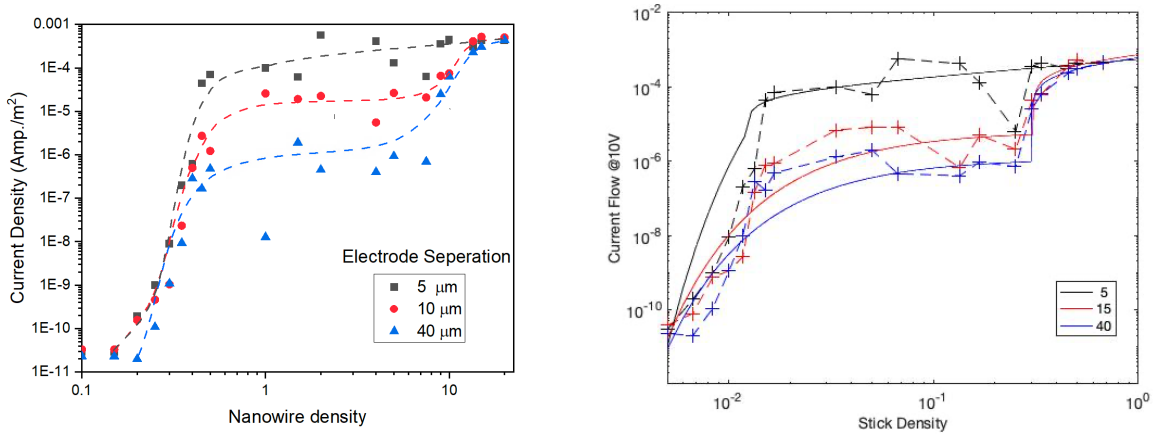

Figure 5-7: Current flow of ZnO-NWs network at 10 V for 5, 10 and 40 µm electrode separations of Al electrodes marked as cross-points. The fitted data are marked with a straight line.

The relationship between current flow and nanowire density was examined in a ZnO nanowire network at 10V for three different electrode separations (5, 15, and 40 µm) as shown in Figure 5-7. The system sizes were calculated using eq. (4-2) and (4-3)as demonstrated in Chapter 4, with corresponding system sizes of 2.00, 5.48, and 8.94 for the electrode separations of 5, 15, and 40 µm, respectively.

A notable difference in the conductivity characteristics was observed when comparing the electrode separations of 5 µm and larger. An increase in nanowire density led to a sharp increase

in conduction up to the saturation point of 0.015. However, increasing the nanowire density beyond a certain point resulted in fluctuations in conduction, occurring two or three times. The system exhibited two conductivity steps along two distinct percolation behaviours, in addition to the percolation staircase with two transitions demonstrating a hierarchical pattern of tunnelling conductance [36, 157]. These observations indicate that there is a high level of control over the conductivity properties of the nanowire network.

The observation of stair-like behaviour can be attributed to a conduction mechanism between particles or random clusters, which are subject to two different transport regimes: sub-percolative or tunnelling and percolative conduction [37, 166, 171]. It is important to note that despite the overlapping positioning of the sticks, direct physical contact is not always guaranteed. The transportation of charges is closely linked to traversing the optimal energy barrier between two adjacent elements. Through extensive research, the conductivity properties of fillers have been thoroughly examined regarding varying shapes and electron flow processes. This has included a detailed analysis of both extreme cases of hopping and percolation conduction and the intermediate regimes between these two characteristics. By utilising real data presented in the literature, the approach has been effectively applied with great success [37].

To summarise, we used LTspice software to systematically adjust component conductance for an accurate simulation of conductivity properties. By employing various conduction models and identifying junction conductivity through experimental findings, we obtained reliable and consistent results between experimental conductivity and simulations. It is important to note that due to the stair-like conduction behaviour of the experimental data, hopping conduction between the nanowire-nanowire junction will be the focus for accurately simulating the system. In the upcoming section, we will investigate the tunnelling conduction mechanism through the ZnO-NWs network and analyse the experimental data to evaluate the network parameters such as R_J, R_C, and R_{NW} for a more precise simulation. Our analysis will also involve examining the role of universal percolation probability in integrating the conduction model.

5.4.3 Analysis of the Conductivity

This section investigates conduction models in a random nanowire network to identify the correlation with experimental results. The findings presented in this section demonstrate a clear understanding of the subject universal percolation probability on network conductivity. The tunnelling conduction approach is used to determine junction resistance and explore the impact of the universal percolation probability on network conductivity.

4.4.3.1Random Resistive Network

Percolation theory is a well-established methodology used to analyse the electrical properties of complex universalised systems. The method is based on a homogenous assessment of the electrical properties of the continuous network present throughout the system [143, 146, 160, 165]. The approach involves defining a list of connected junctions on the universal network continuum as active nodes and simulating the total current flowing through the system by applying Kirchhoff's current law. This method has been proven effective in numerous studies. In this approach, the resistivity of the network points is considered constant throughout the system, and the resistances outside are assumed to be negligible. Percolation theory is widely employed to simulate the conduction of percolated networks and to establish a connection between the universal conductivity exponent, t, and the capacity to evaluate universal complex systems. Overall, percolation theory is a powerful tool that facilitates the evaluation of the electrical properties of complex systems systematically and reliably, making it an asset for understanding the charge transport behaviour of the continuum network.

The first method employed in this study, while rooted in the same principles, introduced the approach in percolation theory. It was evaluated using the shortest path method. This unique twist marked active connections as resistance points along the shortest path while considering resistance points outside the shortest path inactive. The total current along this path was then simulated, leading to the determination of the final conductivity of the universal system. This was achieved by taking the product of the total conductivity with the system coefficient, as detailed in Section 5.3.1.

Comparing the effect of the variation of the system sizes on n_{eff}, presented in Figure 4-11, suggests that the larger system sizes require more clusters to create a spanning one through the vertical direction of the system. The effective stick density is lower than the universal percolation stick density due to the nature of the asymmetry of the system. The analysis of the conduction at the range of 10 V (Figure 5-7) shows that the currents increase with the stick density before percolation, which may be linked to the numbers cluster. However, after percolation, the current still increases with the stick density but at a significantly lower rate, i.e. the larger the system size, the slower the increase in the current. This is consistent with the increase of the conductivity exponent extracted from eq. 3-1 and listed in Figure 4-5 for four different system sizes.

The findings presented in the figure highlight the effect of system size on determining the conductivity exponent of a given asymmetric system. In summary, for systems with L=4.45, the conductivity exponent t=0.60 and 1.67 below and above the threshold, respectively. Similarly, for systems with L=6.70, the conductivity exponent t=0.49 and 1.64 below and above the threshold, respectively. For larger systems, with L=8.90 and L=11.20, the conductivity exponent shows a

similar trend, with t=0.37 and 1.84, and t=0.46 and 1.94 below and above the threshold, respectively. These results provide valuable insights into the effect of junction densities on the system conductivity behaviour, as they demonstrate the importance of considering system size in understanding the electrical conductivity of system size.

The results, as shown in Figure 5-5, indicate that the conductivity exponent increases with increasing system size above the effective percolation threshold. However, it is the opposite for below the threshold. This means that the system conductivity exponent converges to the universal conductivity exponent (t=1.3 for 2 dimensions) with a decrease in system size. This phenomenon may be due to the fact that the number of junctions in the shortest path increases with an increment in system size. This is because the shortest path consists of more sticks when the system size becomes larger. It is also widely studied that the ratio between the junction resistivity versus stick resistivity and the number of junctions causes the nonuniversal conductivity exponent[143, 164]. Thus, the results confirm that the density of R_J causes the deviation of the universal conductivity exponent.

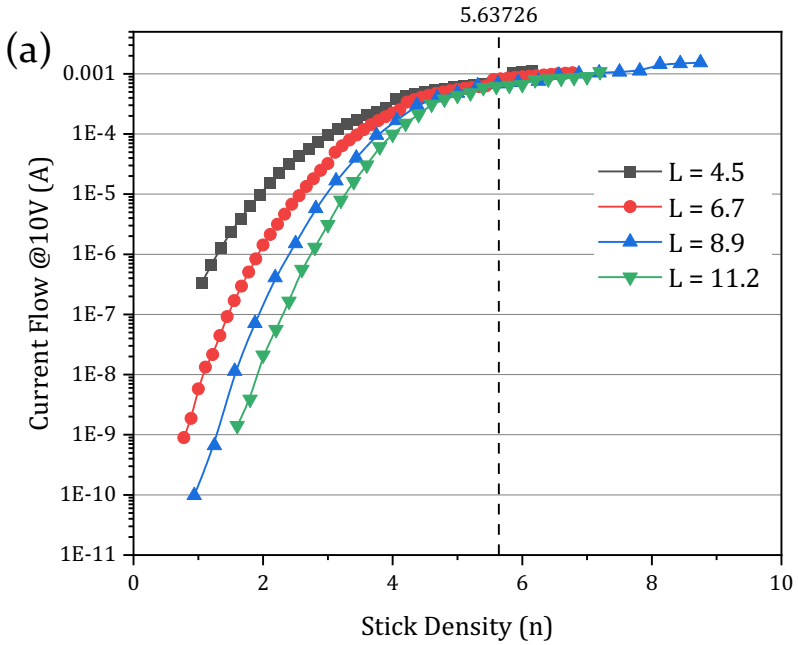

Figure 5-8: Simulated current flow at 10 V for the systems where L=4.50 (black square), 6.7 (red circle), 8.9 (blue upside triangles), and 11.2 (green downside triangles).

In our analysis of the critical conductivity exponent of the asymmetric cells for a percolated random stick system, we have uncovered findings that have practical implications. Figure 5-5 reveals the cluster number's relationship with stick density for various system sizes. In contrast, Figure 5-8 illustrates the current flow of the system for different stick densities at 10 V. As the

number of clusters increases, there is a more pronounced rise in current flow for the lower stick densities. However, for larger stick densities, the conductivity increment becomes less dependent on stick density, particularly after merging small clusters. Moreover, Figure 5-8 depicts that the conduction exponents of the systems are different below and above the effective percolation threshold. The formation of a new path and merging of these paths exhibit unique characteristics of network formation within a system that can significantly impact the absolute conduction of the system, highlighting the relevance of the findings to conduction in a random ZnO-NWs network.

The analysis of current flow in the vertical direction reveals a strong dependence on the size of the system, as depicted in Figure 5-8. Larger sticks in the lower system size exhibit more significant charge transport in the vertical direction for lower stick densities. However, the charge transport across various system sizes tends to converge around the critical stick density (n_c =5.625), consistent with the expectations of percolation theory. These results confirm that our model adheres to the percolation rule, which mandates that the system properties must be isotropic at the critical stick density. However, Figure 5-8 illustrates that the conduction behaviours of the random nanowire network do not align with experimental results (seen in Figure 5-7) for the lower nanowire density of the system. This suggests that the classical conduction model does not apply to lower stick density.

As our analysis demonstrates, the increment of the conduction with respect to system size aligns with the increment to be more dominant for larger system sizes, as indicated by the conductivity exponent increment. However, despite the good match of the steady R_J approach above the n_{eff}, the conduction behaviour of the system does not correspond to the experimentally reflected staircase conductivity behaviour of ZnO-NWs below this critical point. This discrepancy suggests that the conductivity approach of the percolation theory (eq. (4-1)) is valid for systems larger than the correlation length ξ, where $\xi \propto |n - n_c|^{-\vartheta}$ [173].Therefore, it is necessary to explore alternative conduction mechanisms for points under the effective percolation threshold, which will be discussed in the next section.

5.4.3.1 Tunnelling conduction

The conductivity properties of fillers have been thoroughly examined about varying shapes and electron flow processes. This has included a detailed analysis of both extreme cases of hopping and percolation conduction and the intermediate regimes between these two characteristics. By utilising real data presented in the literature, the approach has been effectively applied with great success[36, 37, 171]. Percolation theory allows calculation of the distance between two constituents with the relation of $nL^2r_S=1$[175], where r_S is the shortest distance between the two

adjacent particles as seen in Figure 5-2(b). When an electron flows through the distance, D, of the shortest path by tunnelling, it accumulates a number of stick-to-stick junction times.

Assigned were two types of individual conductivity behaviour to model electrical conductance: tunnelling and percolation conduction. For this purpose, various microscale conductances have been assigned to the junctions. For example, it is assumed that the interparticle conductance remains constant and independent of stick density above the percolation threshold (Figure 5-8). On the contrary, below the percolation threshold (Figure 5-2(b)), it has been observed that tunnelling conductance between the constituents, specifically for pairs of sticks over distance x, may decrease exponentially as the distance between them increases, as seen in Figure 5-7. In summary, any conductivity between two sticks is assumed to follow these principles [36].

$$g_j = \begin{cases} g_c & for\ \ n \geq n_c \\ g_t e^{-2^{(r_s - d)}/\xi} & for\ n < n_c \end{cases} \tag{5-5}$$

Where r_s is the shortest distance between two adjacent sticks, d is the diameter of the sticks in 3-dimension, and ξ is the tunnelling decay length. The perfectors, g_c and g_t in eq. (4-5a) and (4-5b) for above and below the critical stick density. The g_t is expected to be larger than g_c since the electrons have to overcome the energy barrier caused by the inter-constituent distance. In our model, below the system's threshold point, we will utilise the dynamic conductance of g_t based on the distance between particles and the tunnelling decay length instead of relying on a constant junction conductance of g_c above the critical stick length.

The intermediate conductance between extreme hoping and percolation conduction of the random network for the stick has also been obtained, where the tunnelling part of the conduction is [36]:

$$g \cong g_t exp\left[\frac{2D}{\xi}\frac{\gamma(d/l)^2}{\phi}\right] \tag{5-6}$$

Where D is the cluster size, γ is the constant with respect to filler shape, and d and l are the diameter and length of the sticks. At this point, we were tasked with developing a basic, observational model that outlines the relationship between the conductivity of the sticks network and the variance of φ with respect to the critical threshold. Thus, the relevance of the percolative conduction seen in Eq. (4-1) is dominant above the threshold of the system, while eq. (4-6) leads

the conduction below the critical point. Therefore, we can extract the microstructure parameters from the experimental results presented in Figure 5-7.

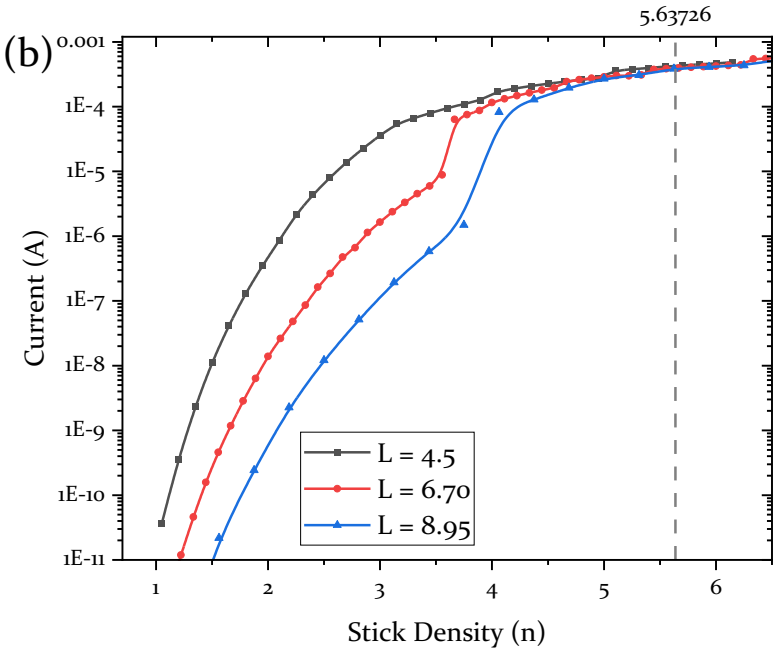

Figure 5-9: Simulated current flow at 10 V for the systems where L=4.50 (black squares), 6.7 (red circles), and 8.9 (blue triangles).

As discussed in the previous section, it is important to note that the phenomenon of dynamic junction conduction plays a vital role in determining the path conductivity of a system below its critical stick density. This is because the interparticle distance between adjacent constituents, which causes hopping conduction, is formed through the shortest path. Figure 5-9 clearly illustrates the conductivity for the range of stick densities when tunnelling conduction as in eq. (4-5a) and (4-5b) for below and above the effective stick densities, respectively, are linked to the constituent network. This relationship is well-supported by research [36, 160] and should be considered when analysing similar systems. The parameters for the conduction of two adjacent constituents were confidently determined by fitting percolation conduction (eq. (4-1)) and hopping conduction (eq. (4-6)) to the experimental data of randomly dispersed ZnO nanowires. These parameters are presented in Figure 5-7 as a straight line on the experimental data points. The results demonstrate the approach to presenting the conduction through the shortest path integrated into the universal scaling function. The universalised shortest-path conduct revolutionary approach, acknowledging the potential for differing perspectives and adjustment on the conduction.

Moreover, the final calculation of the shortest path for both sides of the stick density introduce a constant, α, which is determined by eq. (4-4). This is because the analysed shortest path data is formed using the same principle as the union-find algorithm. However, Figure 5-9 still needs to align better with the experimental data points for lower stick densities below the n_{eff}. Figure 5-9 shows a linear dependence in the system's conductivity results below the critical stick density, which is not align with Figure 5-7 for low nanowire densities because it shows that there is a large plateau of similar conduction behaviour before the percolative conduction behaviour becomes the dominant conduction mechanism after the tunnelling regime. When α is excluded from the analysis of conduction in the system with a stick density below the n_{eff}, the conductivity results align more closely with the simulated conductivity, as shown in Figure 5-10. This suggests that only a critical path significantly contributes to the charge flow when hopping conductivity is dominant [124, 173]. This result has significant implications and sheds light on the underlying behaviour of the random ZnO-NWs system, which will aid in developing the charge transport.

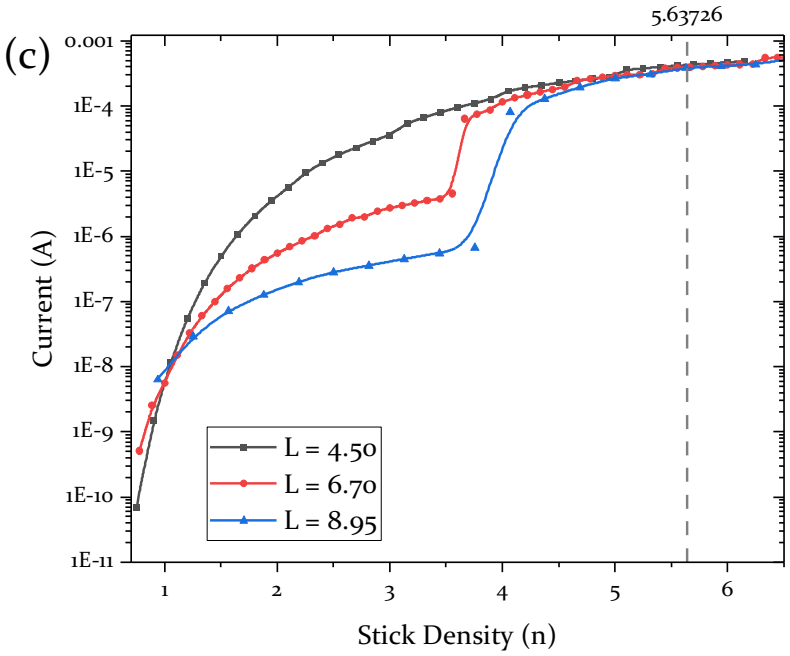

Figure 5-10: Simulated current flow at 10 V for the systems where L=4.50 (black squares), 6.7 (red circles), and 8.9 (blue triangles).

To summarise the analysis of a random ZnO-NWs network, the universal scaling approach is a convenient tool to simulate the random nanowire network for experimental correlations. Even though the percolation transport mechanism is insufficient to explain the conduction of the network when lower nanowire densities than the effective percolation threshold, the universality of reconstitute nanowire network is a fascinating approach to simulate the conductivity. The processes on the universalised network below the threshold point have remained universal even

though the percolation transport is not applicable in that region of nanowire density, providing a reassuring consistency to the conduction studies on the low density of ZnO nanowires even below the n_{eff} of the system.

The experimental conductivity findings of ZnO-NWs across various electrode separations on the microelectrode array and nanowire densities exhibit a staircase-like conduction pattern, as depicted in Figure 5-7. This behaviour is explained by the tunnelling regime of each composite component in [37]. Hence, the assumption that the junction resistivity remains constant regardless of nanowire density, as shown in Figure 5-8, is invalid below the effective percolation threshold, as the conductivity behaviour does not align with experiments below n_{eff}.

Consequently, the hopping conduction behaviour through nanowire-to-nanowire junctions is employed below the critical threshold, as indicated by Figure 5-7, which considers the literature [36, 37, 171]. As a result, the derivative R_J is fitted by eq. (4-6) to the experimental data below the threshold points, which are then applied to the simulation to conclude. Figure 5-9 illustrates the simulated tunnelling conductivity for the nanowire densities below the n_{eff} of the systems, where the universalised probability function is introduced to the shortest path of the systems. However, as observed in Figure 5-9, the conductivity exhibits a linear dependence on nanowire density through the tunnelling regime of the system, which is not align to Figure 5-7. Nevertheless, Figure 5-10 aligns with the experimental behaviour when the universal conductivity constant in eq. (5-4) is removed from the final conductivity measurement. This leads to the conclusion that the charge can only flow through one specific path, which must have the lowest energy barrier, as discussed in the literature [124, 160].

Therefore, the model presented in this chapter effectively describes the system behaviour and provides a novel visualisation of the universal conduction path. This approach, with its time-saving capabilities, offers a practical tool for device modelling and applications, using accessible and essential software for realistic simulations.

5.5 Summary

The correlation between the conductivity of the random ZnO nanowire network in simulations and experimental results shows that using a shortest-path approach, based on percolation theory, is valid for understanding charge transport in a random ZnO nanowire network. This approach, discussed in Chapter 4 and supported by existing literature, was used to analyse the conductivity of the random ZnO nanowire network in simulations by finding the shortest paths through the network. By incorporating parameters from the universalised network, the LTspice simulation

provided a more comprehensive understanding of the conductivity behaviour of the random ZnO nanowire network.

The results suggest that the model can accurately predict conductivity by simulating the parameters, such as junction and nanowire resistivities based on stick density and electrode separation. Experimental findings revealed a two-step, stair-like conductivity pattern at 10 V. While the system remains conductive below the effective percolation threshold, percolation theory alone cannot fully explain this behaviour. Instead, the observed conductivity, especially below the effective percolation threshold, is better explained by the tunnelling conduction approach, where conductivity is maintained through a single critical path, as described in Section 5.4.3.

These findings show that realistic modelling of random ZnO nanowire networks is feasible for practical applications. The insights gained will be further explored in Chapter 6, focusing on the application of these networks to UV-PD devices. The practical applications that could benefit from the realistic conductivity model of random ZnO nanowire networks include non-volatile memory, UV photodetection, and pressure sensing. The knowledge gained from the conductivity analysis could potentially lead to advancements in these areas, offering more efficient and reliable devices for non-volatile memory storage, UV photodetection, and pressure sensing applications, which are discussed in subsequent chapters.

Chapter 6

UV-Photodetection of Random ZnO Nanowires

6.1 General Overview

In the previous chapter, we fitted the theoretical percolation model from Chapter 4 with experimental in-plane I-V characterisation to study the impact of the random ZnO network ratio on the conduction mechanism. In this chapter, we will investigate two prototypes of ZnO nanowire-embedded devices: MSM and capacitive MIS. The MSM in-plane device prototype aims to explore the connection between the network's percolation-related conduction mechanism and UV-PD. On the other hand, the formation of the MIS device aims to study capacitive UV-PDs when the ZnO nanowire network is embedded between TO and BO.

Recent studies have employed various methods to enhance the performance of ZnO UV PDs [9, 10, 23, 77, 176-179]. These include using diverse ZnO nanostructures, such as zero-dimensional nanoparticles [180], nanowires [23, 176], tetrapods [10, 24], and other forms. Some studies have focused on optimising the dimensions of these nanostructures, such as the diameter of nanowires, to improve oxygen absorption and conductivity. Extensive research has also been conducted on doping ZnO NWs with elements like Ga, Sb, Mg, Ag, and Nd to enhance optoelectrical properties [177, 178, 181-192]. Additionally, efforts to increase ZnO conductivity through material composites and nanoparticle decoration, such as nanodiamonds, single-walled carbon nanotubes, and graphene-quantum-dots, have been explored [186, 192, 193]. Post-fabrication processes like pulsed light treatment and rapid thermal annealing have also been investigated to reduce surface defect trap centres [194].

However, the impact of inter-nanowire junctions on the performance of ZnO-NW PDs, as well as the influence of inter-electrode gap and nanowire concentration, has not been sufficiently quantified in existing research. While theoretical predictions exist in the literature, there remains a significant need for a detailed, empirical study to provide a clearer understanding of these factors. Therefore, this chapter will focus on applying percolation theory to examine how variations in the nanowire concentration and the resulting changes in conduction mechanisms affect the sensitivity and response of MSM devices used for UV photodetection.

Additionally, while the capacitive response of ZnO nanowire-embedded MIS devices has been briefly touched upon in the literature, comprehensive studies are still lacking. In the second part

of this chapter, we will investigate the capacitive behaviour of ZnO-NW embedded devices in detail, aiming to fill this gap in the current body of knowledge. This section seeks to provide a deeper understanding of how these factors influence the performance of ZnO nanowire-based photodetectors, ultimately contributing to the optimisation of device sensitivity and response.

This chapter investigates the effects of inter-electrode gap and low-cost drop-casting solution concentration on the photo response of MSM and MIS structured ZnO UV PDs. Three solution concentrations (1, 4, and 20 wt.%) and three inter-electrode gaps (2.5 μm, 10 μm, and 50 μm) were tested for MSM devices to investigate the impact of the charge transport on UV-PDs capability of in-plane MSM devices. On the other hand, capacitive UV-PD for MIS capacitors has also investigated with three different ZnO NWs intake (0.25, 0.50 and 1.00 wt.%) for three different capacitors $D_{NW,0.25}$, $D_{NW,0.5}$, $D_{NW,1.0}$, respectively.

Quantitative characterisation was performed to calculate the rise and decay times and the dark-to-light current ratio of the PDs, optimising the developed UV PD. This study aims to contribute to the growing research in this field by exploring the significance of the inter-electrode gap and conduction mechanism for MSM devices while MIS capacitors will be investigated as a part of MF device application of ZnO NWs in creating electronically practical and commercially viable UV sensors.

6.2 Method

The design, fabrication, and characterisation of MSM and MIS-structured ZnO-embedded devices and their detailed fabrication processes are explained in Chapter 3. The process begins with preparing the substrate and depositing aluminium electrodes using UV-positive lithography for MSM structures. ZnO nanowires are then drop-cast onto these electrodes for MSM and silicon dioxide (SiO_2) configurations at varying concentrations to form a ZnO nanowire network. Three different inter-electrode gaps (2.5 μm, 10 μm, and 50 μm) are tested to observe their impact on the performance of MSM UV-PDs. The electrical performance of the fabricated UV PDs is characterised under a 365 nm UV light source using the test rig presented in Chapter 2. The experimental setup maintains the LED at a constant distance from the sample, and a probe stage is used to make electrical contact with the electrodes. Performance metrics such as responsivity, sensitivity, photo response rate, and stability are evaluated through current-voltage (I-V) sweeps and UV radiation cycles. The study also aims to understand the impact of percolation and conduction mechanisms on UV-PDs by varying electrode separations.

Electrical characterisation involves performing I-V sweeps in dark and UV-illuminated conditions to measure photocurrent and dark current. Responsivity (R) and sensitivity (S) are calculated

using the photocurrent generated and the incident light power. The UV enhancement factor, which compares the UV-illuminated current to the dark current, is also determined. Once the UV-PD response of the ZnO nanowire network is validated, the aim shifts to analysing the UV photo response of MIS diodes where ZnO nanowires are embedded into the MIS device configuration, as detailed in Chapter 2. The semi-automated testing rig facilitates precise and repeatable I-V and C-V measurements under periodically applied UV light. The rig is validated against known benchmarks to ensure accuracy and reliability.

The electrical performance of the UV PDs was measured using the Keysight B2902A Precision Source/Measure Unit (SMU), which served as the power source and simultaneously measured the current, and LCR meter to read capacitance spontaneously as described in Section 3.4.3. The UV source was an SVC 365nm UV LED, connected and powered by the SMU, and kept at a constant 5 cm distance from the tested sample. The LED's luminous power was 2400 mW, and its illuminance was calculated to be 7.63 mW/cm^2 using the inverse square law. A probe stage was used to contact the electrodes on the glass substrate, ensuring the probes did not obstruct the UV LED.

Modern high-performance PDs are evaluated based on their responsivity, sensitivity (S), photo response rate (R), and stability. These parameters guided the sample characterisation in this study. Initially, a typical I-V test was performed, sweeping the voltage from -15V to 15V and back to -15V in both dark and constant UV illumination conditions. Each sample underwent ten successive tests to ensure stability, with the sweep selected for quantitative analysis determined by identifying when the response stabilised after UV exposure.

Two crucial parameters, responsivity and stability were calculated from these tests. The responsivity, the ratio of generated output current to incident light power, was calculated using the equation:

$$R_{MSM} = \frac{I_{ph}}{P_{in}} \tag{6-1}$$

$$R_{MIS} = \frac{C_{ph}}{P_{in}} \tag{6-2}$$

where I_{ph} is the photocurrent (calculated as $\Delta I_{ph} = I_{UV} - I_d$, with I_{UV} being the UV-illuminated current and I_d the dark current), and P_{in} the incident light power. The same way, C_{ph} is the change in capacitance (calculated as $\Delta C_{ph} = C_{UV} - C_d$) with C_{UV} being exposed UV and C_d the dark capacitance. Sensitivity, a measure of the PD's ability to detect weak UV signals, was calculated using:

$$S_{MSM} = \frac{\Delta I_{ph}}{I_d} \times 100 \tag{6-3}$$

$$S_{MIS} = \frac{\Delta C_{ph}}{I_d} \times 100 \tag{6-4}$$

The UV enhancement factor, the ratio between ΔI_{ph} and ΔC_{ph}, was calculated to analyze the increase in conductivity under different voltage biases. To further characterize the device, samples were exposed to cycles of UV radiation at a constant bias voltage above the threshold voltage. The UV radiation was applied until the measured current stabilized and then turned off. This process was performed using the testing rig developed to allow for the calculation of the response and recovery times. These are defined as the time required to reach 90% of the maximum UV-illuminated current from the dark current and vice versa as seen in Figure 6-1(a) and (b). The device's stability was assessed by periodically turning it on and off and comparing each cycle to ensure a consistent response.

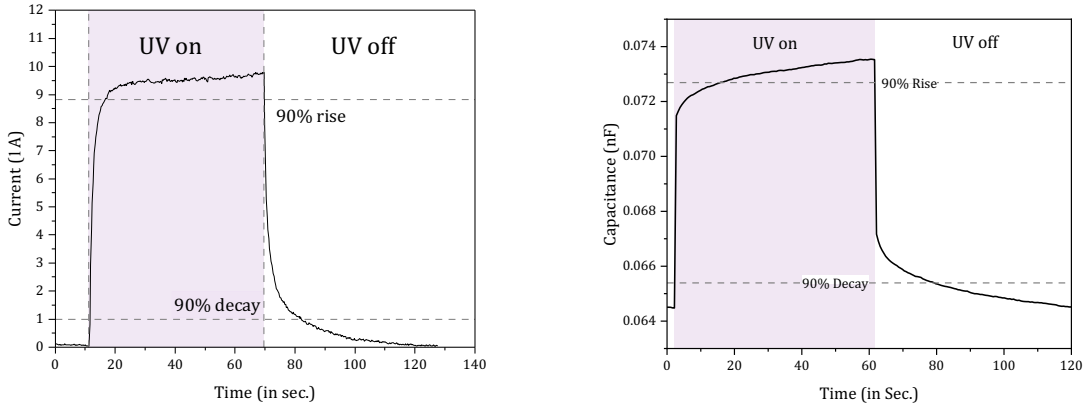

Figure 6-1 *One UV cycle with 10 V device bias - 60s on/60s off. (a) MSM sample – 4 wt.% solution concentration 50μm electrode gap, (b) MIS sample 1 wt.% embedded into the insulator layer.*

Lastly, the performance limitations of the material and device were investigated by reducing the ON-and-OFF cycle periods until the MSM sample could no longer reliably distinguish between the states. This involved incrementally decreasing the UV LED ON-time below the calculated rise time of the PD (from 1s to 0.5s then 0.25s) while maintaining a sufficient off-time (15 seconds) to allow the device to recover/reset to I_d. The peak I_{UV} and I_d ratios were calculated to ensure reliable

distinction, and the off-time period was also reduced from the calculated decay time to determine the device's response speed limitations.

6.3 UV Photodetection of ZnO nanowire Network

Under UV exposure, ZnO exhibits several key reactions. When ZnO is exposed to UV light, electron-hole pairs are created as the UV photons have enough energy to excite electrons from the valence band to the conduction band, leaving behind positively charged holes [6, 7, 127, 183]. These photogenerated holes migrate towards the surface of the material, driven by the electric field created by the band bending at the surface. Upon reaching the surface, the holes discharge the chemisorbed oxygen ions present on the surface of ZnO. These negatively charged oxygen ions capture free electrons from the n-type ZnO, creating a depletion layer near the surface and causing further band bending [9, 24, 195].

The discharge of chemisorbed oxygen ions by the photogenerated holes leads to their desorption from the surface of ZnO, which in turn destroys the depletion layer and increases the electrical conductance of the material [9, 196-198]. The photogenerated electrons, separated from the surface by the band bending, enhance the conductivity of the ZnO film, contributing to the photocurrent generated by the material. The amount of chemisorbed molecules on the ZnO nanowire's surface can be derived as a conclusion from increasing conductance since absorbed oxygen molecules may locally change the surface states, work function and band alignment, resulting in an increment in charge carrier and their mobility [196, 197].

Comparing the dark current (I_d) of the PDs to the UV-illuminated current (IUV) reveals that the UV-illuminated current is significantly higher by more than 10^3 orders of magnitude, indicating a strong UV photoelectric conversion capability in the PDs. This observation is consistent with established research, which identifies the photocarrier generation mechanism in ZnO UV photodetectors primarily influenced by the absorption and desorption of oxygen on the surface of ZnO nanowires [199]. In the absence of UV light, oxygen molecules adsorb onto the ZnO surface, capturing free electrons through the reaction [199, 200].

$$O_2 + e^- \rightarrow O_2^- \tag{6-5}$$

This process creates an electron-depleted layer with low conductivity, with the thickness of this depletion layer being equal to the Debye length of the material, which is 19 nm for ZnO at room

temperature [179, 201]. Upon exposure to UV light, photons with energy greater than the ZnO bandgap generate electron-hole pairs in the NW layer according to the reaction [202];

$$hv \rightarrow e^- + h^+ \tag{6-6}$$

The electron-hole pairs are then separated by a local electric field within the depletion region, resulting in photo-generated electrons populating the conduction band and significantly enhancing conductivity. Meanwhile, the photo-generated holes are driven towards the ZnO surface by the electric field, where they neutralise the absorbed oxygen ions through surface electron-hole recombination [203], described by the reaction:

$$h^+ + O_2^- \rightarrow O_2 \tag{6-7}$$

This recombination reduces the depletion layer's thickness, thereby further increasing photoconductivity. Additionally, the photocurrent transient in ZnO under UV exposure typically shows a slow decay process, attributed to the slow charge-transfer processes involved in oxygen chemisorption and photodesorption. Carrier capture over the potential barrier and the thermal activation of physiosorbed oxygen molecules also contribute to this slow decay[197, 199, 204].

ZnO-based nanostructures, particularly nanowires, are highly regarded for UV photodetection due to their high surface-to-volume ratio, which enhances their interaction with UV light [6, 7]. The literature on ZnO-based PDs primarily focuses on two critical areas of improvement [9]. The first is improving the sensitivity of PDs, which involves achieving a higher current contrast between the ON and OFF states of the UV source. This improvement allows for more accurate differentiation between the presence and absence of UV light, resulting in more reliable and precise measurements [9, 77, 179]. The second focus is on improving the response and decay times of ZnO-based PDs. A faster response time allows the photodetector to react more quickly to UV light, while a shorter decay time ensures the device returns to its initial state promptly after the UV light is turned off [9, 10, 23]. Addressing these areas aims to develop ZnO-based photodetectors that are more sensitive to UV light and faster and more efficient, making them suitable for a wide range of applications, from environmental monitoring to communications.

One effective method to enhance the sensitivity of devices to UV exposure is the incorporation of a thin dielectric layer between the metal-semiconductor-metal (MSM) formation, transforming them into metal-insulator-semiconductor (MIS) structures [77, 205, 206]. The presence of a thin insulator layer acts as a dielectric barrier, resulting in a significant increase in conductivity under

UV light exposure and leading to more sensitive UV photodetectors (PDs). Young et al. [77] compared the UV photo response sensitivity of ZnO-based MSM and MIS structures. Their findings highlight that the inclusion of a 5 nm thick SiO_2 insulator layer significantly enhances the photodetection performance of ZnO-based devices through several key mechanisms [77]. Firstly, the SiO_2 layer acts as an insulating barrier between the metal contact and the ZnO layer, effectively suppressing leakage current and leading to a substantial reduction in dark current. Experimental results have demonstrated that the dark current in ZnO MIS photodetectors is significantly lower than in ZnO MSM photodetectors [77].

Young et al. [206] observed in a separate study that MIS PDs have a photo-to-dark current ratio that is about 200 times higher than that of MSM-structured PD. Notably, with a silicon dioxide layer thickness of 98 nm, the rejection ratio is significantly improved. The silicon dioxide layer effectively reduces noise and enhances the detectivity of the device.

Furthermore, the SiO_2 layer not only reduces dark current but also increases photocurrent, thereby improving the photocurrent to dark current contrast ratio. This increased contrast ratio indicates a higher sensitivity of the ZnO MIS photodetector to incident light, as it can achieve a more pronounced distinction between photocurrent and dark current compared to ZnO MSM photodetectors. In a parallel study, aluminium-doped zinc oxide (AZO) based metal-insulator-semiconductor-insulator-metal (MISIM) PDs with a thin SiO_2 insulating layer showed a lower dark current compared to the MSM formation of the same device, resulting in two times better UV on/off contrast [205].

They also used three different in-plane electrode separations (10, 20, and 50 μm), finding that the largest electrode separation showed the highest photo response, three times larger than the lowest electrode separation [205]. In summary, the SiO_2 insulator layer improves photodetection performance by reducing dark current, increasing the photocurrent to dark current contrast ratio, and enhancing the UV-to-visible rejection ratio, making ZnO MIS photodetectors more sensitive and selective in UV detection. Electrode separation has also been noted to contribute to the sensitivity of the ZnO PDs [205].

The presence of numerous deep-level states at the surfaces of the ZnO nanostructures, along with gas desorption and reabsorption processes, can lead to high photosensitivity. The size of nanomaterials and various surface treatments, such as heat treatments and gold nanoparticle (Au-NP), silver nanoparticles (Ag-NPs) and other inorganic nanostructure decorations, influence surface band bending, which in turn affects photon-electron conversion behaviours. By adjusting the thin depletion region near the surface, the optoelectronic properties of PDs based on ZnO nanostructures can be tuned. However, due to slow photocarrier relaxation from surface

adsorption and desorption processes, PDs based on single ZnO often exhibit long recovery times [9].

Strategies such as introducing heterojunctions and constructing core-shell and network geometries to modulate interface carrier transport have been proposed to enhance photosensitivity and recovery time [178, 183, 184, 200]. For instance, Chen et al. [197] developed ZnO nanobelt (NB) networks on prefabricated Ti/Au electrodes using a vapour-liquid-solid method, resulting in ZnO NB-network PDs. These PDs displayed a fast recovery time of 0.53 seconds, significantly shorter than the 32.95 seconds observed in single ZnO NB-based PDs, due to enhanced electron transport facilitated by numerous NW-NW junction barriers in the network [197].

Gedamu *et. al.* [9] highlights the remarkable UV photodetection performance of ZnO nano-tetrapod networks, similar to a random nanowire network with a similar nanostructure [9]. The device displays reversible current switching when UV light is toggled on and off while maintaining a constant bias voltage of 3.6 V. The on/off current ratio is roughly 254.5 at 3.6 V, significantly increasing to about 3277 at 3.0 V and approximately 4500 at 2.4 V. These findings demonstrate a highly sensitive response to UV light. Additionally, the device exhibits a quick response time and rapid recovery time. A detailed analysis reveals rise time constants of about 68 milliseconds and a primary decay time of approximately 32 milliseconds, with a secondary decay constant of around 200 milliseconds [9]. They demonstrate the superior efficiency of the ZnO nano tetrapod network-based device for rapid and effective UV photodetection. Due to the structural resemblance of randomness in nano-tetrapods to a random nanowire network, this notable performance underscores the potential of comparing with a random nanowire network for UV-PDs.

The results from various studies demonstrate the remarkable UV photodetection capabilities of ZnO-based nanostructures. Under UV exposure, ZnO generates electron-hole pairs as UV photons excite electrons from the valence to the conduction band, creating positively charged holes [127]. These holes migrate to the surface, neutralising chemisorbed oxygen ions and increasing the material's electrical conductance. This process enhances photocurrent due to the high surface-to-volume ratio of ZnO nanostructures, making them highly sensitive to UV light [127]. The transient photocurrent typically shows a slow decay due to the prolonged charge-transfer processes involved in oxygen chemisorption and desorption.

Various studies have focused on enhancing both the photosensitivity and recovery time of ZnO-based photodetectors. Incorporating a thin dielectric layer, such as SiO_2, in MIS structures, has been shown to improve performance as summarised above dramatically. MIS photodetectors exhibit a photo-to-dark current ratio 200 times higher than metal-semiconductor-metal (MSM)

structures [77]. Strategies like introducing heterojunctions and constructing core-shell and network geometries have further improved device performance. For instance, ZnO nanobelt networks could achieve a rapid recovery time of 0.53 seconds compared to 32.95 seconds for single ZnO nanobelts, thanks to enhanced electron transport through numerous nanobelt-to-nanobelt junction barriers [197]. Similarly, Gedamu et al. highlighted the efficiency of ZnO nano-tetrapod networks, which showed an on/off current ratio of up to 4500 and fast response and recovery times. These findings underscore the potential of random ZnO nanostructures in developing highly sensitive and efficient UV photodetectors [9].

This chapter lies in the development of highly manufacturable ZnO nanowire UV-PDs, which are well-suited for large-area fabrication, offering both scalability and practical application potential. This work provides a detailed experimental examination of UV-PD performance, bridging the gap between theoretical predictions and experimental results. By systematically investigating the influence of electrode separation—comparing charge transport through single nanowires at small gaps (2.5 μm) to larger gaps (10, and 50 μm) within random ZnO nanowire networks—this research uncovers the critical role of inter-nanowire junctions and conductivity mechanism in defining device performance.

The study further explores two device architectures: MSM and MIS, highlighting how differing charge transport mechanisms influence UV-PD functionality. MSM devices, which rely on DC current transport, are analysed across the entire percolation regime of ZnO nanowire networks, while MIS devices, governed by capacitive charge, are examined specifically in the sub-percolative regime due to protecting them charge leakage in highly percolative network. This dual-architecture approach provides better understanding how device structure impacts charge transport and overall photodetector performance. By integrating experimental results with percolation theory, this work presents a novel contribution to the understanding of random ZnO nanowire networks in UV photodetection, with important implications for optimizing device design and functionality.

6.4 Analysis and Insights into ZnO UV Photodetector Performance

6.4.1 The UV photodetection in MSM Devices

The optimal sensitive contact lies somewhere between a distant, touching and full interpenetration. This suggests that the types of nano-junctions formed between nano-microstructures in the network bridge play a crucial role in the photodetection mechanism of these photodetectors [9, 127, 199, 207]. Three nanowire concentrations have been selected for

investigation to explore the conduction mechanism of UV photodetector response. Three different samples were fabricated using the methods outlined to assess the influence of electrode gap and solution concentration on the photo response of ZnO PDs. The solution concentrations utilised were 1%, 4%, and 20%, and the inter-electrode gaps selected from the micro-electrode array were 2.5, 10, and 50 μm.

The initial step in characterising the MSM PDs involved conducting a current-voltage (I-V) sweep from -15 V to 15 V and back to -15 V with 0.25 V voltage sweep. This range was chosen to capture the relationship between voltage and current accurately. Figure 6-2(a-f) displays the I-V results for the 1 to 20 wt.% concentration samples under dark and UV illumination conditions for three different electrode separations (2.5, 10, and 50 μm). These results represent the patterns observed across all three concentrations and electrode separations, with additional data for various voltage biases provided in Table 6-1.

The I-V curves exhibited a non-linear shape, characteristic of semiconductors like ZnO, as previously discussed in Chapter 2. This non-linearity, also observed by Kumar et al. [177] indicates the formation of an energy barrier between individual ZnO nanowires and microstructures within the random network patterns.[208]. While this supports the notion of metal-semiconductor junctions exhibiting Schottky rather than ohmic behaviour, the instability of free electrons, which may recombine with non-O_2-paired holes, and the slow adsorption and desorption of O_2, pose significant challenges for ZnO-based PDs [177], limiting their market utilisation.

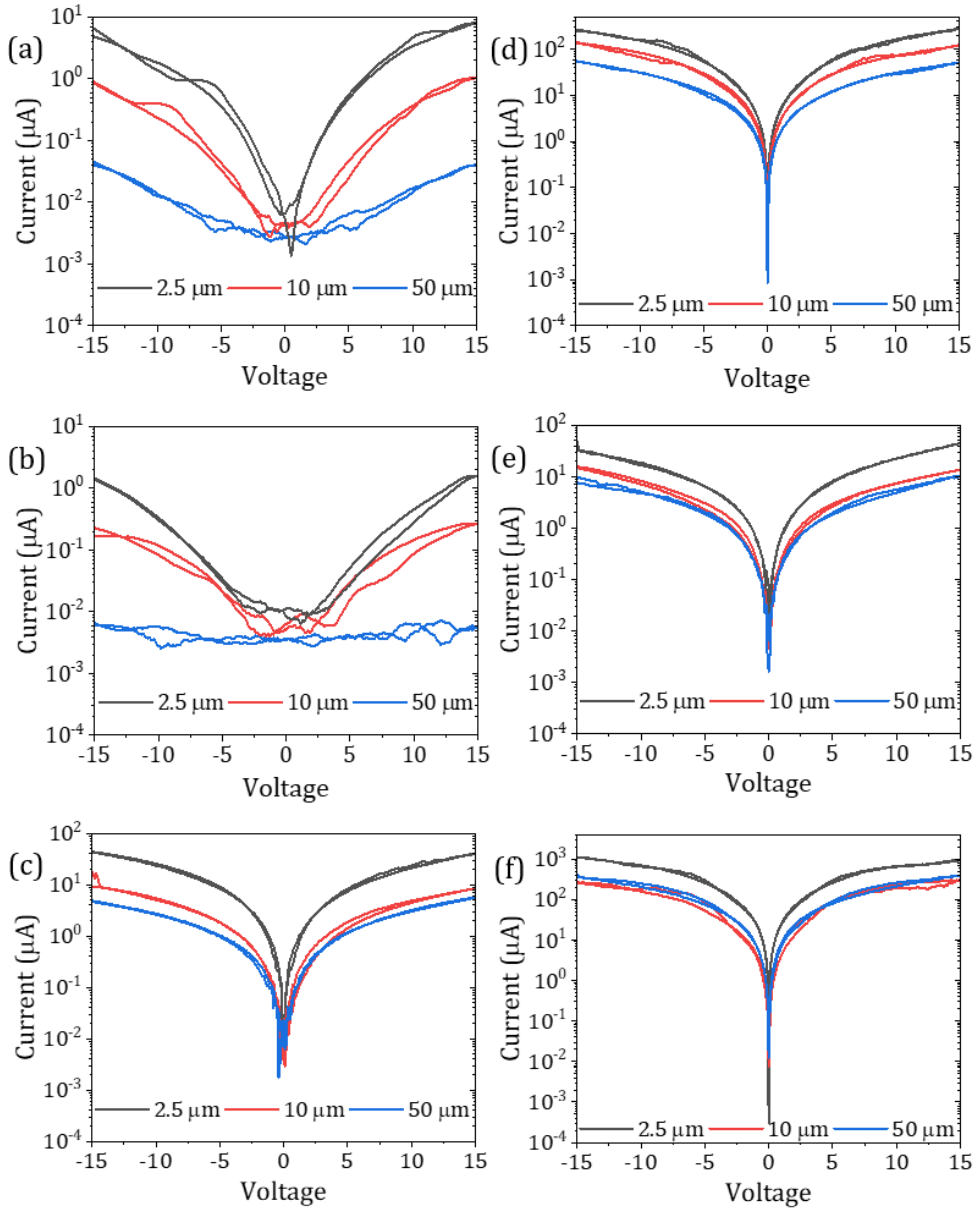

Figure 6-2: *Current-Voltage (I-V) Characteristics of ZnO Nanowire Networks under Dark and UV Exposure. The figure illustrates the I-V response of ZnO nanowire networks for different ZnO nanowire concentrations under dark (a-c) and UV exposure (d-f). The measurements were taken for three different electrode separations: 2.5 μm (black lines), 10 μm (red lines), and 50 μm (blue lines). The concentrations of ZnO nanowire intake were 1 wt.% (a, d), 4 wt.% (b, e), and 20 wt.% (c, f).*

The conduction mechanism of a random ZnO nanowire network depends on the nanowire ratio, as discussed in Chapter 5. Figure 6-2(a-c) illustrates the full double I-V sweep for samples with 1, 4, and 20 wt.% ZnO nanowire ratios. It has been noted that the interfaces are crucial for the sensitivity and efficiency of UV-PDs [9, 127]. The impact of the conduction mechanism related to percolation on MSM UV-PDs performances will be investigated in this section.

In the 1 wt.% sample, the tunnelling conduction mechanism is dominant, while a fully percolative network is achieved in the 20 wt.% sample. The 4 wt.% sample represents the transition region where tunnelling conduction is nearing saturation and approaching the percolative regime. These results aim to observe the impact of the conduction mechanism on the UV-PD performance of in-plane MSM formation of a random ZnO nanowire network.

Table 6-1: *List of the dark current (I_d), UV exposure current (I_{UV}) at 15V presented in Figure 6-2, sensitivity (S) (as calculated using eq. (*6-3*), and responsivity (as calculated in eq.* (6-4) *for ZnO UV MSM photodetectors as a function of electrode separations and ZnO-NW ratio (wt%).*

MSM Sample	Electrode Separation (μm)	Dark Current (μA)	UV Exposure (μA)	Sensitivity (eq.5-2) (% × 10^3)	Responsivity (A/W)
1 wt.%	2.5	8.00	200	2.4	50300
	10	1.00	100	9.9	26000
	50	0.04	50	124	260
4 wt.%	2.5	2.000	60	2.9	15203
	10	0.250	30	11.9	780
	50	0.006	25	417	131
20 wt.%	2.5	40.0	980	2.3	246395
	10	21.5	750	33.88	19109
	50	13.8	1000	71.76	5170

The samples were subjected to a UV sensitivity test lasting a total of 600 seconds. During this test, each sample experienced alternating periods of UV light on/off cycles, with each cycle consisting of 30 seconds of exposure followed by 30 seconds of dark. This pattern was repeated continuously for the entire 600-second test duration. The most significant characteristic of Figure 6-2 is the relation between the current level under dark and UV. The percolation behaviour of the random ZnO nanowire network is dominant in dark current conditions, as seen in Figure 6-2(a-c), a detailed study presented in Chapter 4. However, the conductivity behaviour of these random networks does not obey the percolation-dependent-conductivity model, as evidenced in Figure 6-2 (e-f) and the listed results in Table 6-1. To further assess the significance of the data reported in Table 6.1, we will later compare these findings against existing literature to evaluate their consistency and identify any deviations or novel trends.

In low nanowire concentration (1 wt.%), the dominant conduction mechanism is tunnelling, where junction resistivities dominate the nanowire network conductivity due to a non-physical contact between nanowires. Thus, the conductivity is strongly dependent on the electrode separation; with larger electrode separations, the conductivity is far lower than smaller electrode separations, as seen in Figure 6-2(a). The depletion of electrons by surface oxygen interacting with nanowires creates a high potential barrier [9, 209]. The conductivity at 2.5 μm, where there is no junction barrier, is 8 and 2000 times higher than at 10 μm and 50 μm electrode separation, respectively, as seen in Table 6-1. Similarly, in 4 wt.% ZnO nanowire networks, where tunnelling conduction behaviour remains dominant despite nearing the percolative regime, the conductivity at 2.5 μm is 8 and 400 times higher than at 10 μm and 50 μm electrode separation, respectively, as seen in Figure 6-2(b). However, the conductivity is less dependent on electrode separation in the higher concentration samples (20 wt.%), where the universal percolation conductivity rules charge transport, resulting in nearly identical conductivity levels regardless of the electrode separation, as seen in Figure 6-2(c).

Under UV exposure, the potential barriers between the junctions significantly decrease, particularly penetrating junctions [9, 127, 199, 209], and the sample conductivity levels increase to the hundred-microamp level, regardless of the ZnO nanowire concentration and electrode separations., as seen in Figure 6-2(d-f). There is not an apparent relation to the initial rise observed. However, the final conductivity of the random network may vary slightly due to the random nature of the ZnO nanowire network. Consequently, less conductive samples under dark conditions become more sensitive under UV exposure.

The results of UV exposure summarised in Table 6-1 show that UV-PD sensitivities varied between approximately 2×10^3 and 4×10^5, depending on electrode separation and nanowire concentration. The sensitivity was calculated using eq. (6-3) shows a marked dependence on electrode separation and ZnO concentration. Higher sensitivities are observed for configurations with greater electrode separations due to the impact on the potential barrier between the junctions [9, 127]. As the electrode separation increases from 2.5 μm to 50 μm, sensitivity rises substantially across all ZnO concentrations. For the 1 wt.% sample, sensitivity surges from 2.4×10^3 to 1.24×10^5, demonstrating significant enhancement in sensitivity. The 4 wt.% sample shows an even more pronounced sensitivity enhancement, rising from 2.9×10^3 to 4.17×10^5, more than a 10^2 times increment. The 20 wt.% sample also follows this trend, with sensitivity escalating from 2.3×10^3 to 7.18×10^4. However, the 4 wt.% sample at 50 μm separation notably achieves the highest sensitivity of 4.17×10^5, highlighting its superior performance in UV PDs, which is significantly higher than 1 and 20 wt.% samples.

This significant sensitivity improvement with larger electrode separations can be attributed to the increased distance, which reduces recombination losses and enhances the effective photo-generated charge collection. ZnO tetrapod (ZnO-T) is like a 1D ZnO nanowire structure consisting of four 1D nanowires linked to a central core. ZnO-T legs have the like nanowire properties [9, 179]. Detailed studies on ZnO-T for UV-PS have noted a high sensitivity ranging between 2.8-4.5×10^3 depending on deposition technique and electrode separations. Our random ZnO nanowire networks have shown 4.17×10^5 sensitivity, almost 2 orders of magnitude larger than the published data [9, 179].

A recent study on UV photodetection of ZnO-T for different deposition methods (drop casting, micro-drop casting, spray coating and slot-die coating) on various electrode separations (5, 10 and 15 μm) [179]. In the study, it was observed that there was no discernible correlation between the distance separating the electrodes and their light sensitivity. Each deposition method exhibited optimal performance at different electrode distances. Moreover, various deposition techniques performed a comparable range of photo response (~10^2 - 10^3) at their peak point despite spray deposition yielding the highest responsivity (=2.8×10^3) [179]. The intended final film thickness was the same for all methods, but the percolation behaviour varied. Therefore, the differences in UV-PD performance related to electrode separation may be due to the varying percolation behaviours of ZnO-T resulting from different coating techniques.

Our results indicate that understanding the percolation behaviour of the network is crucial to gain insight into the photo-response mechanism of UV-PDs. Our study suggests that the UV photo response is most efficient at the critical material ratio, where tunnelling conductivity transitions to percolation behaviour. The efficiency decreases above and below this critical point. A similar content has also been theoretically discussed in [9], which postulates that the ideal sensitive contact would be between a slight touching and a complete interpenetration because UV exposure overcomes the potential barrier when nanowires have just penetrated each other. Additionally, the number of junctions with energy barriers is vital for higher sensitivity in the performance of ZnO nanowire UV-PDs when correlated with the application of percolation theory. The application of percolation theory and its correlation with experimental results in Chapter 4 and Chapter 5 are promising to comprehensively understand UV photodetection experimentally, and the theory and experimental UV-PD has not been practically achieved before. Thus, experimentally correlated percolation of ZnO nanowire network is promising contribution for the gap in the literature.

6.4.2 Response of Random ZnO Nanowire Networks on MSM

In the previous section, it was observed that the sensitivity of the 1 wt.% and 4 wt.% random ZnO nanowire networks in MSM device configurations was highest when the electrode separations

were set at 50 µm. Additionally, it is important to evaluate the response and decay times of UV photodetectors, which indicate the device's reaction to UV exposure and its efficiency in returning to its initial off state after exposure. This section aims to assess these two devices under periodic UV exposure with various on/off cycles to thoroughly examine their response and decay characteristics. This analysis will offer a deeper understanding of the dynamic behaviour of these UV photodetectors and their practical utility in scenarios where rapid switching and recovery are crucial.

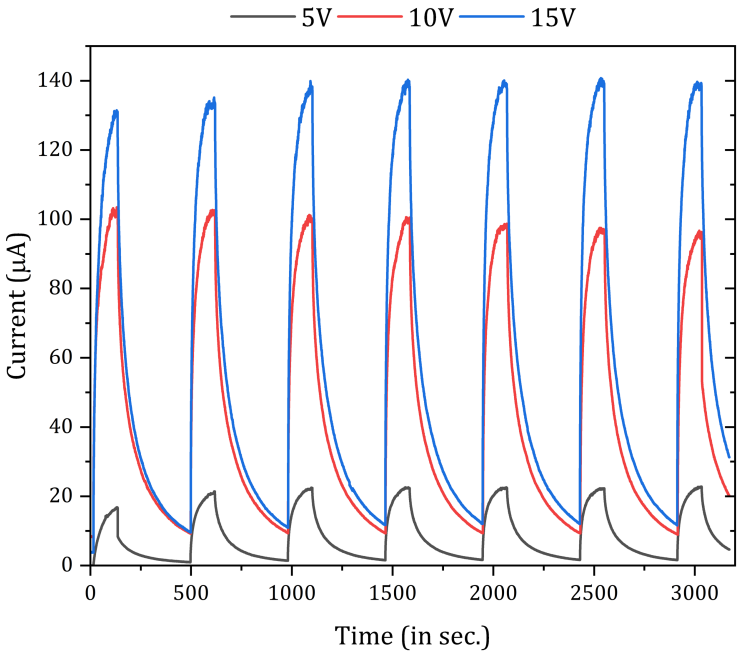

Figure 6-3: Time-dependent photo response of the 1 wt.% ZnO nanowire network photodetector with a 50 µm electrode separation under periodic UV exposure and dark cycles. The device was subjected to 120 seconds of UV illumination followed by 360 seconds of dark conditions under DC biases of 5V, 10V, and 15V.

Figure 6-3 illustrates the photo response of a 1 wt.% ZnO NW network photodetector with a 50 µm electrode separation under periodic UV exposure and dark cycles, with different applied biases of 5V, 10V, and 15V. The photodetector's current increases rapidly upon UV illumination and gradually decreases when the light is turned off, demonstrating its responsiveness and recovery capabilities. Furthermore, the cycles are consistent and repeatable over multiple on/off periods, highlighting the device's stability and reliability under prolonged UV exposure.

The response and decay times are calculated as the time between 90% change in condition before the on/off states, as described in Figure 6-1(a). At a 5V bias, the device exhibits a response time of 62.12 seconds and a decay time of 272.49 seconds. The initial rapid rise in current indicates

efficient photocarrier generation upon UV exposure. At the same time, the slower decay suggests a gradual recombination of photogenerated carriers and desorption of oxygen molecules from the ZnO nanowire surface [7, 9, 199, 209].

As the bias voltage increases to 10V, the response time decreases to 52.6 seconds, while the decay time increases to 343.85 seconds. The reduction in response time indicates faster carrier generation and collection due to the higher electric field [209]. On the other hand, the extended decay time could be attributed to more photogenerated carriers requiring additional time to recombine or desorb [9]. At the highest bias of 15V, the response time decreases to 42.72 seconds, indicating the most rapid photo response among the tested biases. The decay time is 321.39 seconds, slightly shorter than at 10V, but it still suggests a substantial carrier recombination and desorption process.

In summary, the results demonstrate that increasing the bias voltage improves the photodetector's response time, making it react faster to UV illumination. However, the decay time does not exhibit a simple trend, suggesting complex interactions between photogenerated carriers and the surface states of the ZnO nanowires. These findings, combined with the large electrode separation of 50 µm, offer the opportunity to optimise and fine-tune the operating conditions of ZnO-NW-based UV photodetectors for various applications.

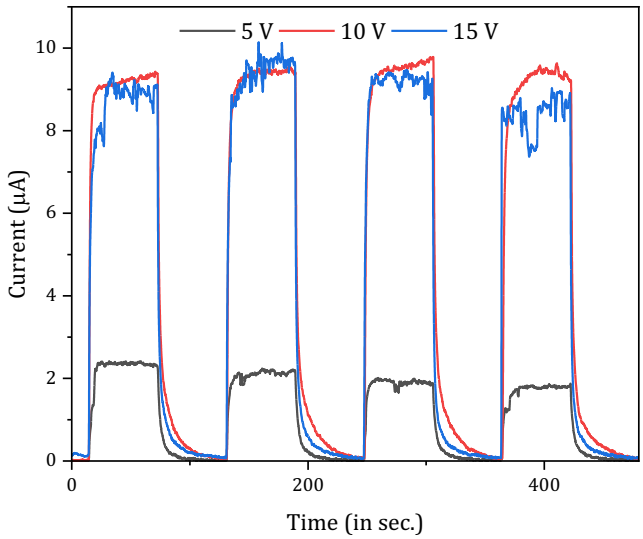

Figure 6-4: *Time-dependent photo response of the 4 wt.% ZnO nanowire network photodetectors with a 50 µm electrode separation under UV duty cycles of 60s ON/OFF at 5V (black), 10V (red) and 15V (blue).*

Figure 6-4 presents the photo response of a 4 wt.% ZnO nanowire network photodetector with a 50 μm electrode separation under periodic 60s UV exposure and 60s dark cycles, with incremental applied biases of 5V, 10V, and 15V. The photodetector's current sharply increases upon UV illumination and decreases rapidly when the light is turned off, demonstrating its quick response and recovery capabilities. At a 5V bias, the device exhibits a response time of 5.52 seconds and a decay time of 9.73 seconds. The swift rise in current indicates efficient photocarrier generation upon UV exposure, and the rapid decay suggests effective recombination of photogenerated carriers and desorption of oxygen molecules from the ZnO nanowire surface [9, 210]..

When the bias voltage is increased to 10V, the response time decreases to 4.2 seconds, and the decay time increases to 13.13 seconds. The reduced response time indicates faster carrier generation and collection due to the higher electric field, which is consistent with the best performance in the literature [9, 10, 23]. In contrast, the slightly prolonged decay time could be attributed to increased photogenerated carriers requiring more time to recombine or desorb. At the highest bias of 15V, the response time decreases to 3.46 seconds, showing the most rapid photo response among the tested biases. The decay time is 18.78 seconds, indicating a slower recovery compared to the lower biases, which may be due to the higher electric field causing more significant carrier generation and slower desorption processes.

When comparing the response of a 1 wt.% ZnO nanowire network photodetector under similar conditions, the 4 wt.% sample shows faster response and decay times at all bias voltages. Specifically, the response times for the 4 wt.% sample are significantly shorter, indicating a more efficient photocarrier generation process due to the critical material ratio around the percolation threshold where tunnelling conduction turns into percolative conductivity [9]. Additionally, the decay times, while longer at higher voltages, remain generally shorter than the 1 wt.% sample, reflecting a more rapid recombination and desorption process.

The shortest response time, 3.52 s, is almost half of the most sensitive device of the ZnO-T network deposited spin-coating [179]. The same material fabricated by vacuum-based burner flame transport synthesis showed a slightly lower response time of 2.4 s [9]. On the other hand, a study reported fast response and decay time in a few hundred microseconds for random ZnO nanowires fabricated by a low-cost method on 3 μm electrode separations but extremely low sensitivity ratio [23]. Our findings indicate that we have achieved both high sensitivity and rapid response in UV photodetectors using a low-cost drop-casting method that permits easy scalability for large-area production. Subsequently, we will conduct an in-depth analysis of the device's responsiveness to ascertain its capacity to generate electronically detectable signals for real-time applications.

6.4.3 Analysis of 4 wt.% ZnO-NW Network Photo-response

In the previous section, a comparative analysis between 1 wt.% and 4 wt.% ZnO nanowire network photodetectors was conducted, highlighting the superior sensitivity and faster response times of the 4 wt.% samples, especially with larger electrode separations of 50 µm. This comparison sets the stage for a focused investigation into how well the 4 wt.% ZnO nanowire networks perform in quickly detecting signals. After observing promising results, the next section looks at how the 4 wt.% samples react to different ON/OFF duty cycles of UV light. By studying these changes, we aim to understand the fast response and high sensitivity of the 4 wt.% ZnO nanowire network photodetectors and therefore, their potential for advanced UV detection applications.

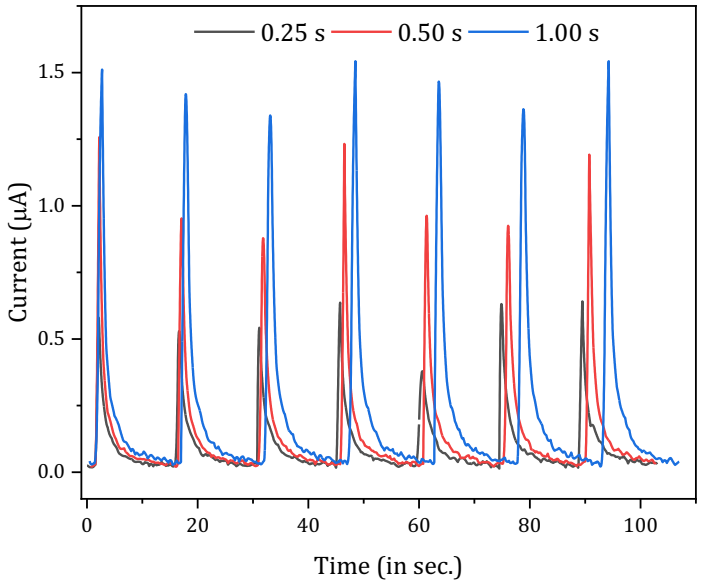

Figure 6-5: *Time-dependent photo response of the 4 wt.% ZnO nanowire network photodetector with a 50 µm electrode separation under a UV duty cycle of 0.25 (Black), 0.50 (Red) and 1.00 (Blue) second ON 15 seconds OFF.*

Figure 6-5 shows the photo response of the 4 wt.% ZnO nanowire network photodetectors under incremental UV duty cycles of 0.25, 0.5, and 1 second ON, followed by 15 seconds OFF under 10V constant bias. The device exhibits a sharp and quick increase in current upon UV exposure, followed by a gradual decay when the UV light is turned off. The response is faster for shorter UV ON cycles, indicating the device's capability to react quickly to changes in UV illumination.

Table 6-2: *Performance metrics of the 4 wt.% ZnO nanowire network photodetector with a 50 μm electrode separation under various UV on/off duty cycles presented in* Figure 6-5.

On cycle (s)	Dark Current (μA)	UV Current (μA)	Decay Time (s)	Sensitivity (%)
0.25	0.02399	0.63679	4.25	2554±3.39
0.50	0.02158	1.23226	3.00	5610±4.92
1.00	0.02133	1.58725	3.25	7341±4.11

Table 6-2 presents detailed performance metrics for the photodetector under different UV duty cycles. The results are as follows: For a 0.25-second UV on cycle, the dark current is 0.02399 mA, the UV current is 0.63679 μA, the decay time is 4.25 seconds, and the sensitivity is 2554%. When the UV on cycle increases to 0.5 seconds, the dark current slightly decreases to 0.02158 mA, the UV current increases to 1.23226 μA, the decay time shortens to 3 seconds, and the sensitivity rises to 5610%. Finally, for a 1-second UV on cycle, the dark current measures 0.02133 mA, the UV current reaches 1.58725 μA, the decay time is 3.25 seconds, and the sensitivity peaks at 7341%.

The results suggest that the sensitivity and UV current of the photodetector increase with longer UV exposure cycles. However, the decay time does not follow a simple linear trend. It shows a minimum of 0.5 seconds and slightly increases for the 1-second cycle. The varied duty cycles of UV exposure demonstrate that the device has high sensitivity, even for a 0.25-second duty cycle. Compared to previously published research on the ultra-fast UV response of random ZnO nanowires [23]/rods [176], the devices exhibit extremely high sensitivity within a 250-millisecond UV exposure, enabling the device to generate digital signals within 250 milliseconds.

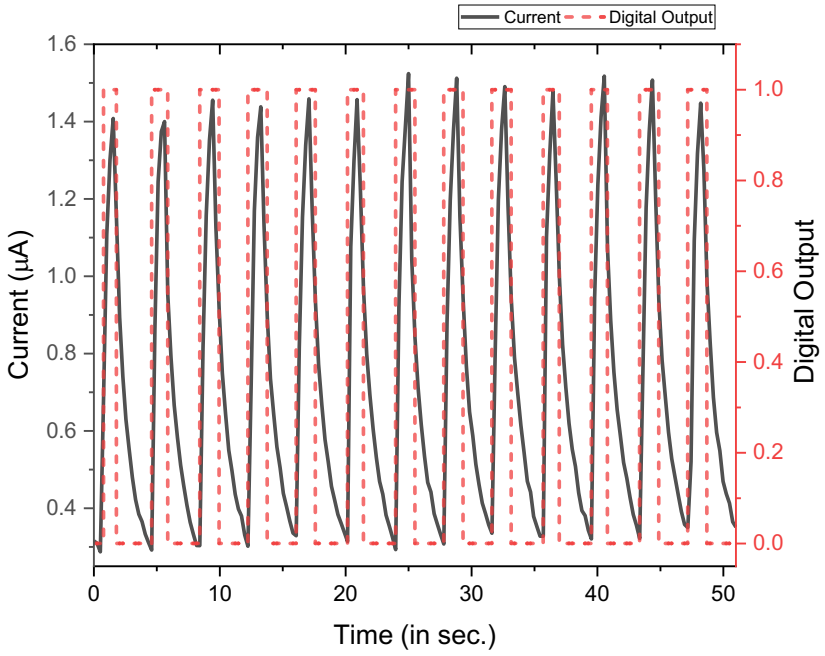

Figure 6-6: *Time-dependent photo response of the 4 wt.% ZnO nanowire network photodetectors with a 50 μm electrode separation under a UV duty cycle of 1 second ON and 3 second OFF.*

Figure 6-6 presents the photo response of the 4 wt.% ZnO nanowire network photodetectors with a 50 μm electrode separation under a UV duty cycle of 1 second ON and 2 seconds OFF. An automated real-time digital converter was integrated into the testing apparatus to further support the idea that waiting for the full on-off period is unnecessary. This code simplifies the process by automatically selecting I_d and I_{UV} values from the collected data up to that point, eliminating the need to preprograming current values. It then determines the midpoint between these values. If UV light is detected, the output is 1; if not, it is 0. Figure 6-6 presents the digital output alongside the corresponding analogue data. This illustrates that full rise and decay times are not essential for creating an accurate UV PD. The consistency across numerous cycles demonstrates the device's stability during continuous use and its lack of requirement for extended recovery periods between subsequent UV exposures.

The 4 wt.% ZnO nanowire network photodetectors, featuring a 50 μm electrode separation, demonstrate outstanding photo response characteristics. They exhibit fast response times and high sensitivity. Two key challenging points have been addressed in this section. Firstly, the importance of percolation theory, presented in Chapter 4, is focused on determining optimal device performance. The application of percolation theory is essential for the most optimal device sensitivity and response. The critical percolation threshold, where the tunnelling conduction

mechanism turns to percolative conductivity, showed the most efficient performance. This finding is also in agreement with published papers [9, 127]. The second challenging point is that the fabrication of the device is quite a low-cost deposition of a random ZnO nanowire network. Besides, it does not require a high-cost lithography technique for the most optimal UV-PD applications. These results emphasise the significance of optimising UV on/off cycles to achieve optimal performance in UV photodetectors.

6.5 UV Photodetection of the MIS Capacitors

In the previous section, the UV photocurrent detection capabilities have been presented. Another UV-PD approach is capacitive detection in MIS capacitor device formation. Capacitive UV-PD is a promising device concept in health monitoring [211, 212] and tactile sensing [51, 213], even though most research on capacitive sensors focuses on strain and pressure sensing [52, 80]. As proved in the previous section, ZnO-NWs are known to generate carriers under UV exposure, leading to changes in capacitance that can be monitored to assess the response of ZnO-based MIS photodetectors. This characteristic provides valuable information about the device's reliability for various applications. In this section, UV light will be periodically applied to MIS devices to monitor their response in terms of capacitance changes. Three samples will be tested with ZnO nanowire concentrations of 0.25 wt.%, 0.50 wt.%, and 1 wt.% in order to investigate their sensitivity with respect to the ZnO nanowire intake encapsulated between SiO_2 and PMMA. By analysing the capacitance response of these samples under UV exposure, we aim to gain insights into their performance, sensitivity, and stability. This analysis will help determine the most effective ZnO concentration for reliable and efficient UV photodetection in MIS capacitors [47].

6.5.1 UV Photodetection of MIS Device Prototype

The UV photodetection tests of ZnO-embedded ZnO nanowires integrated into the dielectric layer on a highly doped n-type silicon wafer were conducted using a UV torch, as described in Section 2.2. The experimental setup employed our precisely designed multifunctional test probes, with a load probe applying a consistent base force of 0.5N to the top gate electrode, and conductive tape establishing contact with the n-Si wafer from the bottom. The aim of this section is to calculate the capacitive UV sensitivity of the samples using a 30-second on/off cycle. The C-V Constant Voltage interface in Python was utilized to capture measurements during the repeated UV torch on/off cycles, ensuring consistent detection intervals.

Three different nanowire concentrations, as well as a bare n-Si wafer with a 30 nm sputtered oxide layer, were tested to assess the photodetection capabilities of the multifunctional device

prototype. The signal was found to be strong and detectable within the 30-second on/off duty cycle, providing clear evidence of the system's UV sensitivity. A lower concentration of ZnO nanowires was systematically used to minimize device leakage, as a dense, continuous nanowire network within the blocking and tunnelling oxide layers is challenging to encapsulate and can form a current bridge with the gate electrode [71]. The results, which highlight the relationship between nanowire concentration and UV sensitivity, are summarized in Figure 6-7.

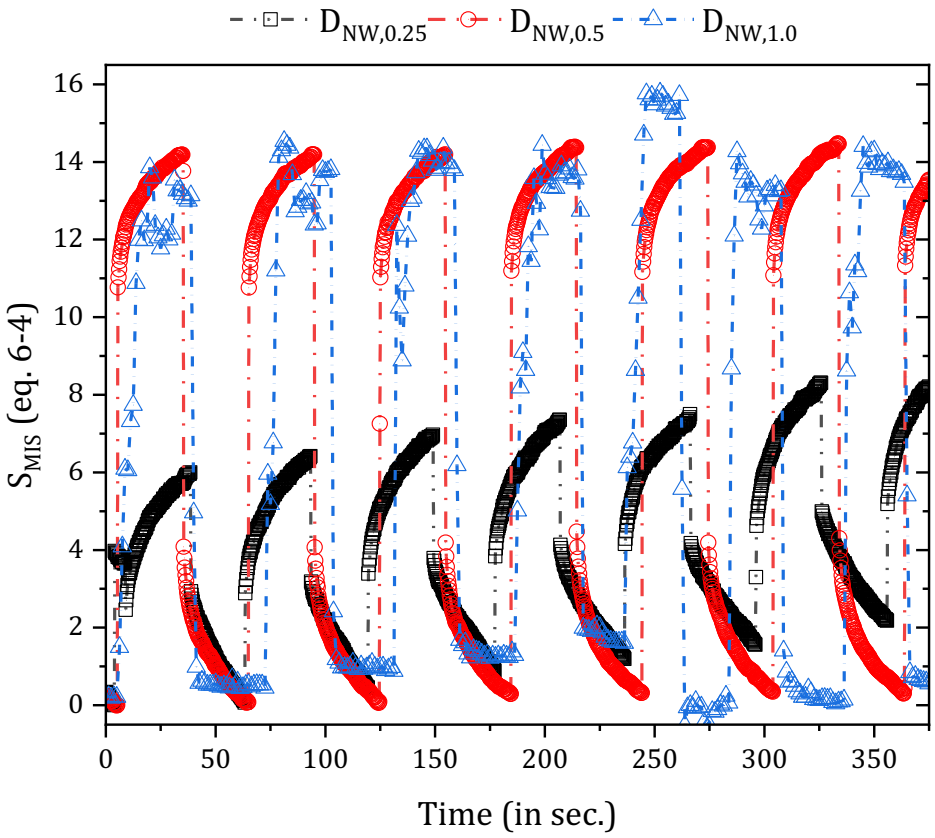

Figure 6-7: *Sensitivity (S_{MIS}) of ZnO nanowire-embedded MIS samples with concentrations of $D_{NW,0.25}$, $D_{NW,0.5}$ and $D_{NW,1.0}$ under UV duty cycles of 30 seconds ON and 30 seconds OFF.*

Figure 6-7 illustrates the sensitivity (S_{MIS}) of ZnO nanowire-embedded MIS (Metal-Insulator-Semiconductor) samples with three different ZnO concentrations ($D_{NW,0.25}$, $D_{NW,0.5}$ *and* $D_{NW,1.0}$) under periodic UV exposure cycles of 30 seconds on and 30 seconds off. The sensitivity is plotted over time to show the response of each sample to the UV illumination duty cycles. The sensitivities are calculated using the eq. (6-4). The results of these three different samples are summarised in Table 6-3.

Table 6-3: *Performance metrics of ZnO nanowire embedded MIS samples with different ZnO concentrations ($D_{NW,0.25}$, $D_{NW,0.5}$ and $D_{NW,1.0}$) under UV ON/ OFF duty cycles of 30 seconds.*

Sample	Response (s)	Decay Time (s)	Sensitivity (%)
0.25 wt.%	20.075	36.025	5.88
0.50 wt.%	6.325	31.900	14.46
1.00 wt.%	1.250	0.500	15.47

As noted in Chapter 5, the 0.25 wt.% ZnO drops on the MSM structures were barely conductive due to the inter-nanowire distance, resulting in tunnelling conduction. However, isolated ZnO nanostructured islands previously showed charge chemisorption and desorption under UV exposure, which result in change in the charge in the capacitors [44, 69]. UV-PDs The UV photodetectors (PDs) performance of $D_{NW,0.25}$ MIS devices (represented by black squares in Figure 6-7 the lowest sensitivity and the most extended response and decay times among the tested samples. This sample reaches its maximum sensitivity more slowly and takes longer to return to its baseline state once the UV light is turned off. Specifically, the response time is 20.075 seconds, the decay time is 36.025 seconds, and the sensitivity is 5.88%. This extended response and recovery period indicates that the low concentration of ZnO nanowires limits the efficiency of charge carrier generation and collection, thereby affecting the overall performance of the device.

In contrast, $D_{NW,0.5}$ sample (represented by red circles in Figure 6-7) shows a significant improvement in performance. It achieves higher sensitivity and faster response and decay times compared to the $D_{NW,0.25}$. The response time for this sample is 6.325 seconds, the decay time is 31.900 seconds, and the sensitivity is 14.46%. The enhancement in performance can be attributed to the increased conductivity resulting from the saturation of the tunnelling distance between nanowires, leading to improved charge carrier generation and collection efficiency. This suggests that an optimal concentration of ZnO nanowires is critical for enhancing the performance of MIS photodetectors, balancing the need for sufficient conductive pathways while maintaining effective photodetection capabilities.

The 1.00 wt.% sample (represented by blue triangles) demonstrates the highest sensitivity and the quickest response and decay times among the three samples. It responds almost immediately to the UV light, with a response time of just 1.250 seconds, and returns to its baseline state rapidly with a decay time of half a second. The sensitivity for this sample is the highest at 15.47.

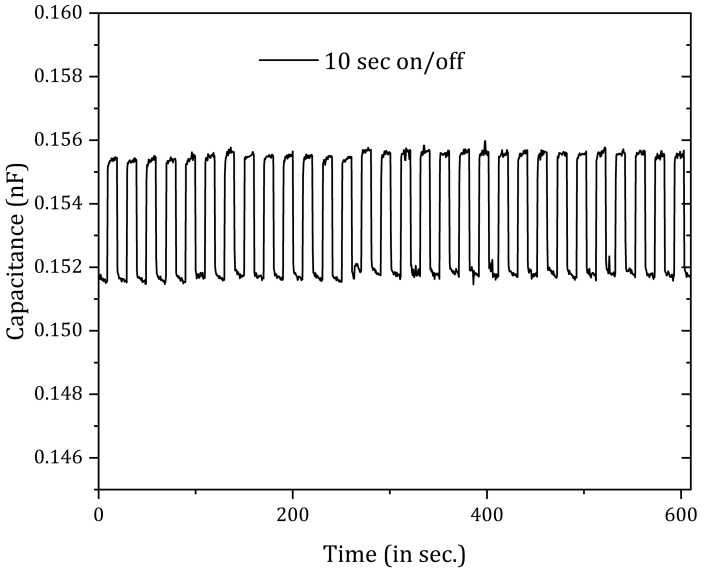

Figure 6-8: *Capacitance response of the $D_{NW,1.0}$ MIS capacitor with a 50 µm electrode separation under UV duty cycles for 10 seconds on/off.*

Figure 6-8 illustrates the capacitance response of a $D_{NW,1.0}$ MIS capacitor under UV duty cycles of 10 seconds on/off. The device exhibits a consistent and repeatable change in capacitance with each cycle, highlighting its reliability and fast response to the UV duty cycle with a 1.25 response and 0.5s decay time. The baseline capacitance of the device is approximately 0.152 nF in the absence of UV light. Upon UV exposure, the capacitance increases to about 0.156 nF, reflecting the additional charge injection facilitated by the ZnO nanowires. The device responds swiftly to the UV illumination, as evidenced by the sharp rise in capacitance at the beginning of each on cycle. Similarly, the capacitance drops quickly when the UV light is turned off, indicating efficient recovery to the baseline state. The repeated cycles over a 600-second period show minimal variation in capacitance response, demonstrating the device's stable performance under prolonged UV exposure.

These results indicate that the $D_{NW,1.0}$ ZnO nanowire MIS capacitor responds quickly to UV light and maintains consistent performance over multiple cycles. This reliability and rapid response make it suitable for applications requiring stable and efficient UV detection. Figure 6-8 reinforces the earlier findings that the MIS capacitor devices, with their enhanced charge injection properties, are highly effective in UV detection. The stable capacitance changes observed in this test further validate the device's potential for use in reliable and fast-responding UV photodetector applications.

The data indicates that increasing the ZnO nanowire concentration in the MIS samples enhances their sensitivity and reduces both response and decay times. The $D_{NW,1.0}$ shows a fast response of 1.25 s and a high sensitivity of 15.47. Analysis of ZnO nanowires using capacitive methods is a new approach, and there are limited studies on capacitive UV photodetectors (PDs) using ZnO nanomaterials. Initial studies have indicated that 700 $\mu W/cm^2$ UV light irradiation resulted in approximately 1.5 sensitivity [212]. Our results show sensitivity of 14.46 and 15.47 for 0.50 and 1.00 wt.% ZnO nanowire-embedded MIS capacitors with a fast-speed response of 6.325 and 1.250 seconds, respectively. This trend suggests that lower concentrations of ZnO nanowires regime improve the photodetector's ability to respond to UV light quickly and efficiently, making them suitable for applications requiring rapid detection and high sensitivity.

6.6 Summary

This study investigated the performance of ZnO NWs based UV-PDs with a focus on two key device configurations: MIS and MSM. The overarching goal was to develop UV-PDs that are highly sensitive, fast-responding, and scalable for large-area applications, while also investigating how device structure and nanowire concentration affect UV detection performance.

For MSM devices, the percolation behaviour of the random ZnO nanowire network played a critical role in determining device performance, particularly in the context of UV photodetection. Unlike MIS devices, MSM devices rely on DC conductivity mechanisms, and this study was the first to coherently integrate both simulation and experimental data to prove the impact of percolation in these devices. The results showed that the MSM devices were most efficient just below the percolative conductivity threshold, where tunnelling conductivity through the random ZnO nanowire network reached saturation before percolative conductivity.

Among the various concentrations tested, the 4.00 wt.% ZnO nanowire samples exhibited the highest sensitivity and response time, with a maximum sensitivity of 4.17×10^5. This sample, when combined with a 50 μm electrode separation, showed superior performance, as the ZnO nanowire junctions acted as barriers when UV light was off, significantly reducing conductivity and enhancing the on/off contrast. Moreover, the MSM devices were able to detect signals with UV exposure as short as 0.25 seconds, highlighting their ultrafast and sensitive response capabilities.

The integration of simulation and experiment in the study of MSM devices provided new presents the percolation behaviour of random ZnO nanowire networks. This demonstrates the critical role that percolation plays in enhancing device performance and further validates the use of ZnO nanowires in high-sensitivity UV-PDs.

In the MIS devices, the UV photodetection capabilities were significantly influenced by the concentration of ZnO nanowires embedded in the dielectric layer. The study examined ZnO nanowire concentrations of $D_{NW,0.25}$, $D_{NW,0.5}$ and $D_{NW,1.0}$ under periodic UV exposure. The $D_{NW,1.0}$ sample showed the fastest response and decay times (1.25 sec and 0.5 sec, respectively), demonstrating superior UV sensitivity. This result underscores the importance of optimizing ZnO nanowire concentration for enhanced device performance. However, beyond 1.00 wt.%, stable UV signals could not be detected, likely due to charge leakage caused by inadequate encapsulation of the high nanowire density in the PMMA layer. This limitation suggests that while higher concentrations may increase sensitivity, they also increase the risk of signal instability.

The findings from the MIS devices emphasize the potential for large-area applications, particularly in low-cost, easily producible UV-PDs. These devices offer promising applications in areas such as wearable electronics and robotics, where fast response and low-cost fabrication are critical. The study demonstrated that a well-optimized ZnO nanowire concentration enables high sensitivity and rapid UV detection, but careful control of nanowire density is essential to prevent device.

This chapter successfully demonstrated that ZnO nanowire-based UV-PDs can be easily fabricated for large-area applications, offering scalable, low-cost solutions for sensitive and rapid UV detection. The integration of simulations with experimental data provided new perspectives on the understanding the relationship between nanowire concentration, percolation, nanowire scaling and charge transport mechanisms in both MIS and MSM devices. The findings confidently prove the importance of optimizing ZnO nanowire concentration and electrode separation to balance sensitivity, response time, and device stability.

Further investigation from the capacitive MIS devices will be discussed in the next chapter, focusing on developing non-volatile memory and pressure sensing for the same device configuration. This ongoing research aims to understand the unique properties of ZnO nanowires to create advanced photodetectors with improved performance and wider applications. The findings from this study provide a strong foundation for future work in optimising ZnO nanowire-based photodetectors and exploring their potential in multifunctional devices.

Chapter 7

MIS CAPACITOR FOR NON -VOLATILE MEMORY

7.1 General Overview

This chapter is concerned with the thorough study of the performance of a randomly distributed ZnO nanowire-embedded layer in a metal-insulator-semiconductor (MIS) device structure. Chapter 2 discusses the use of nanowires embedded in a PMMA layer in the device, while Chapter 3 covers the universalised percolation probability of a random nanowire system. Chapter 4 discussed the theoretical principles of charge transport in a random ZnO nanowire network. This chapter concerns the measurement of two distinct functions from the same ZnO nanowire-embedded device: non-volatile memory and pressure sensing, along with the UV-photodetection capability of the ZnO nanowire-embedded MIS capacitor presented in Section 6.5.

C-V, time-dependent capacitance (C-t), I-V, and time-dependent current (I-t) measurements were performed both under UV illumination and dark conditions, as described in Chapter 2. To ensure that the measurements accurately reflected stable, functional behaviour, the samples were tested by running a set of cyclic potential sweeps ten times to eliminate any transitional effects. These techniques provide information on the versatile functionalities generated by the MIS devices, their capability of non-volatile charge-storing behaviour, and the efficiency with which they produce digital signals because of external pressure on gate electrodes.

Different weight varieties of ZnO nanowires embedded in the insulator layer were studied to understand how the percolative behaviour of random ZnO networks related to the conduction mechanism affects the performance of these functionalities individually. In this case, the results presented in Chapter 5 have been considered in the relations between the network charge transport and ZnO nanowire intake. The overall goal was to find the optimal configuration that would maximise these versatile functionalities of MIS devices with respect to the nanowire ratio.

7.2 MIS Capacitor Non-volatile Memory

The function of memory involves three distinct processes: programming memory to store data, storing data, and retrieving data by reading the memory's state. The storage of data in the memory involves an extra layer incorporated into the gate oxide. This additional layer enables the

realisation of two types of memory cells: Floating gate (FG) based memory, initially demonstrated by Guterman et al., and charge trapping (CT) memory [214].

In 1967, the first memory cell using Si_3N_4 as a charge-trapping material was developed. This type of charge-trapping memory, known as SONOS, consists of a structure involving poly-Si/oxide/Si_3N_4/oxide/Si substrate. Both floating gate and charge trapping layers are embedded between two dielectric layers. The TO is conventionally made of silicon dioxide, while the upper oxide can vary depending on the device type. For floating gate memory, the upper oxide is typically composed of a stack of $SiO_2/Si_3N_4/SiO_2$ (ONO), known as the inter-gate dielectric or interplay dielectric. In CT memory devices, the upper oxide is a SiO_2 layer called the BO. Initially, SiO_2 was used as the material for TO and BO due to its good interface quality with Si, but Al_2O_3 is now used to prevent charge leakage as flash memory scales [44, 69]. Additionally, research is being conducted on other higher-k oxides to scale the memory further [215].

According to The International Technology Roadmap for Semiconductors (ITRS) projections for memory devices, the charge-trapping memory is viewed as the most promising and feasible device, particularly for NAND structures [216]. In CT memory devices, electric charges are stored in states of CT within a dielectric material rather than in a conductive or semiconductor, as seen in floating gate memory. The necessity for a lithographic definition of a floating gate is eliminated in the process flow. The gate oxide comprises three layers of dielectrics integrated between the channel and the gate. This gate oxide stack offers greater scalability than floating gate memory, consequently allowing for more scalable program/erase voltages.

7.2.1 Basic Non-volatile Memory Cell Operation

In non-volatile memory devices, data storage is achieved by modulating the threshold voltage (V_t) by injecting and removing charges in the charge-trapping layers. During the programming phase, electrons are introduced into the charge storage layer via mechanisms such as Fowler-Nordheim tunnelling, leading to a positive shift in V_t. Conversely, the erasure process involves extracting these charges, resulting in a negative V_t shift. The memory state is read by applying a gate voltage between the programmed and erased states, allowing for the detection of either a "0" (programmed) or "1" (erased) state [217].

Charge leakage challenges the retention of these states over time, primarily due to defects in the TO and BO layers. These defects can be intrinsic, originating from the device structure, or extrinsic, resulting from the operational stress of programming and erasing cycles. While beneficial for lower power consumption, a thinner TO layer may have more significant leakage due to increased electron back-tunnelling.

The degree of Vt shift, known as the threshold voltage shift (ΔV_t), is a critical parameter, as it directly correlates with the density of charge trap states within the CT layer. This relationship is quantified by eq. (7-1), which allows for the estimation of the memory cell's charge trap state. The elementary charge (q). The ability to precisely control and maintain ΔV_t is crucial for the reliable operation of memory devices, ensuring data retention and future memory technologies' scalability.

$$N = \frac{C_t \Delta V_t}{q} \tag{7-1}$$

The equation expressing the V_t can be monitored by the flat-band voltage change (V_{FB}) shown in eq.(7-2) [218].

$$V_t = V_{FB} - 2\phi_p + \frac{t_{ox}}{\epsilon_{ox}} \sqrt{2\epsilon_{Si} q N_D (2\phi_p)} \tag{7-2}$$

Where ϕ_p is the potential in the Si substrate, ϵ_{ox}, ϵ_{Si} Si are the gate stack and Si permittivity, t_{ox} is the gate stack thickness, N_D is the substrate doping (donor).

7.2.1.1 Characterisation

The memory devices are evaluated by analysing the frequency-dependence of their capacitance-voltage (C-V_{gate}) characteristics (100 kHz - 500 kHz) with 0.250V voltage steps to determine their programmed/erased states. The erased state is achieved by sweeping the gate voltage from negative to positive potentials. In contrast, the programmed state is achieved by sweeping the gate voltage from positive to negative potentials. The observed negative shift is due to the storage of electrons in the insulator layers in MIS. The ΔV_{FB} shift, and the ΔC_t values are obtained, with the threshold voltage extracted at a capacitance of 500 pF around the onset of the depletion region. The memory hysteresis measured at different operating voltages illustrates that the memory cell exhibits a broad shift at low P/E voltages.

7.2.2 Charge Trapping Layer and Materials

CT layers play a crucial role in performing non-volatile memory devices by offering high charge trapping density, which is essential for achieving a larger memory window at consistent operating voltages. Utilising materials with a high dielectric constant (high-k) enhances the electric field across the TO, thereby enabling either a larger memory window or reduced operating voltages. A thinner CT layer can further increase the electric field across the TO, contributing to lower power consumption [43, 219]. Additionally, amorphous CT layers are preferred over crystalline ones to

minimise charge leakage, as grain boundaries in crystalline materials can serve as leakage paths. Finally, a CT layer with a large band offset relative to the TO and BO effectively confines the charges stored, improving memory retention characteristics.

7.2.3 Defects in The Tunnelling Oxide

In TO materials, several high-k oxides are being explored to enable further scaling of memory devices while maintaining charge retention [220]. High-k oxides allow the use of physically thicker TO layers with equivalent or smaller oxide thickness compared to SiO_2. Key requirements for TO materials include a large bandgap and a significant band offset with the Si channel to prevent charge leakage. Amorphous TO materials are preferred to minimise leakage through grain boundaries [219]. A high breakdown electric field is also crucial as device scaling increases the electric field across the TO. Good interface quality with the Si channel is also essential, with Al_2O_3 being a commonly used material due to its high interface quality and low defect density [221]. Therefore, this section aims to characterise the oxide layer without ZnO nanowires to distinguish the contribution of the oxide layer on MIS device memories.

During the growth of the oxide layer, positive fixed charges usually exist in the oxide layer called Q_{ss} due to defects in the oxide layer. The oxide defects can be attributed to two main reasons. One common cause is the presence of dangling covalent oxygen bonds in the oxide layer and the bonding of oxygen with silicon at the silicon surface. As a result, a thermal annealing process may lead to an excess of silicon in the oxide near the interface, while an excess of oxide may form at the silicon interface due to dangling oxygen atoms. A rapid thermal post-annealing process has been conducted after the oxide growth on the n-Si layer to mitigate the effects of oxygen diffusion and oxide layer formation at the interface [222]. One cause of interface state formation is the mismatch between the lattices of silicon and SiO_2 at the oxide-semiconductor interface. This results in traps at the interface within silicon's forbidden energy bandgap around the Fermi Level (E_F) of n-doped silicon due to the mismatch between the 100 or 111-oriented silicon crystal lattices and the SiO_2 layer [223].

The net fixed charge in SiO2 is concentrated near the interface of the MOS structure, assuming that no other oxide charge is present. This net charge is measured as electronic charge per unit area (C/cm^2). The flat band voltage is the potential where no band bending occurs, leading to a zero-space charge region. Interface charge traps in MOS devices significantly affect electrical characteristics, shifting the flat band voltage either positively or negatively depending on the type and density of the traps. This shift influences the device's turn-on behaviour and alters the subthreshold slope, which impacts the turn-on speed as the gate voltage increases. Additionally, these traps can cause leakage current, which is detrimental to low-power applications.

Moreover, interface charge traps affect the flat-band voltage, consequently altering charge accumulation or depletion and modifying the C-V characteristics. These changes reshape the C-V curve's form and gradient. The impact of interface charge traps is determined by their density, energy levels, and distribution, as well as the presence of oxide charges and work function differences. Therefore, analysing the TO on the base MOS device is essential for improving the e-beamed TO on the n^{++} doped Si wafer. This topic will be further discussed in the next section.

7.2.3.1 Characterisation of Tunnelling Oxide

To enhance our understanding of the characteristics of TO, Figure 7-1 illustrates the C-V cycle of MIS formation without ZnO nanowires. This is intended to determine the effect of nanowires on the functionalities of the final MIS devices. Figure 7-1(a) shows the C-V characteristics of the MOS devices both before and after RTA treatment. The term MOS indicates that only TO SiO_2 is present on the base devices, while MIS includes an additional layer on the TO, such as ZnO nanowires and BO PMMA layers. Lastly, Figure 7-1(b) presents the C-V characteristics of MIS devices where a BO PMMA layer is spin-coated on the RTA-treated TO layer.

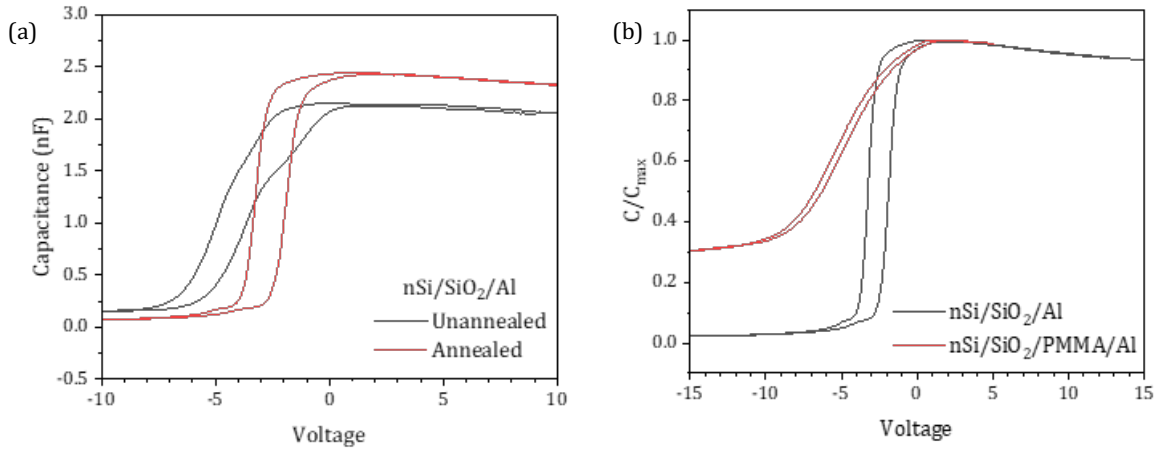

Figure 7-1: C-V characteristics for annealed and unannealed devices. (a) C-V curves of D_R comparing annealed and unannealed samples, showing the effect of annealing on capacitance. (b) Normalised C-V curves (C/C_{max}) comparing D_R and D_B structures, illustrating the impact of the PMMA layer on the device's characteristics.

Figure 7-1(a) presents the CV characteristics of MOS capacitors at 100 kHz, both before and after annealing. As detailed in Chapter 2, the devices are positioned on the test rig for C-V_{gate} measurements. The gate voltages are swept from −20 V to +20 V in the forward direction and from +20 V to −20 V in the reverse direction, with a step size of 0.1 V. A reference device (D_R) made of

n-Si/SiO_2/Al, without ZnO nanowires and PMMA layers, was fabricated to examine the effect of thermal treatment on the device characteristics. Two versions of this control device were tested: one exposed to rapid thermal annealing and one not exposed. The depletion region in the unannealed MOS is much larger than in the annealed one, which may indicate a higher number of interface traps. This is because more charges are needed to fill the more traps at the interface states, requiring a broader voltage sweep to achieve the same surface potential. The additional PMMA BO layer on the TO layer (D_B) results in a larger depletion, linking additional interface states between them. However, the flat band voltage remains similar to the annealed MOS structure, indicating the apparent role of the PMMA layer in the D_B device formation.

The MOS structure includes an insulator capacitance (C_{Ins}) and a semiconductor capacitance (C_S) in series. C-V characteristics of the control devices help determine fabrication parameters. In the accumulation region, most carriers gather at the interface, and the maximum accumulation capacitance (C_{ox}) is used to estimate the insulator stack's dielectric constant: 2.1 and 2.4 nF for unannealed and annealed samples, respectively, and 0.52 nF for the MIS test sample. The dielectric constant indicates a material's ability to store electrical energy in an electric field and is calculated using eq. (7-3).

$$\varepsilon_r = \frac{C_{Ox} d_{Ox}}{\varepsilon_0 A} \qquad 7\text{-}3$$

where C_{Ox} is the maximum capacitance in the accumulation region, d_{Ox} is the oxide layer thickness, ε_0 is the permittivity of free space ($8.854 \times 10^{-12}\ {}^{F}/_{m}$), and A is the capacitor area ($=6.625 \times 10^{-3} cm^2$). In a MOS capacitor, C_{Ox} is obtained from C-V measurements. This formula links the oxide layer's physical properties and the MOS structure's dimensions to the material's electrical charge storage capability, which is essential for semiconductor device design. The results are presented in *Table 7-1*.

Table 7-1: The dielectric constant of control MIS devices without ZnO nanowires.

Sample	$d_{Ox}(nm)$	$C_{Ox}\ (nF)$	$\varepsilon_r\ ({}^{F}/_{m})$ @100 kHz
D_R	30	2.31	4.44
D_R (RTA)	30	2.44	4.69
D_B	90	0.52	3.04

d_{Ox} represents the combined insulator thickness of SiO_2 and PMMA insulator layers of MIS (n-Si/SiO_2/PMMA/Al). With the insulator stack thickness is monitored during sputtering and determined by ellipsometry to be ~30 nm, we calculated that ε_r in F/m corresponds to an effective relative permittivity of 4.44, 4,69 and 3.04 for as-sputtered, and RT-annealed SiO_2 and combined with PMMA, respectively. It can be concluded that applying the RTA annealing process to oxide layer enhances dielectric properties. Thus, the RTA-treated oxide sample results in a better interface quality with Si.

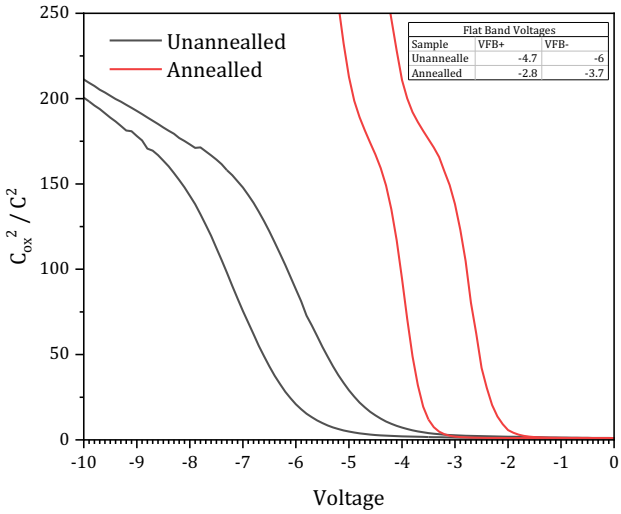

Figure 7-2: Illustration of the $1/C^2$ method to find VFB for annealed and unannealed D_R devices presented in Figure 7-1.

Figure 7-1(a) clearly shows that the control device displayed typical characteristics of MOS structures based on n-type semiconductors, with a narrow flat-band (V_{FB}) shift in an anticlockwise direction. This indicates the presence of a fixed oxide charge in the silicon oxide, which will be discussed later. Moreover, the flat band voltage and complete semiconductor depletion (threshold voltage, V_t) differ before and after thermal annealing. As shown in Figure 7-2, the V_{FB} is calculated by $1/C^2$ method is detailed in Section 3.4.2. The crossing point of the tangent of the straight region $V - C_{ox}^2/C^2$ on the voltage axis gives V_{FB+} and V_{FB-} under forward and reverse bias, respectively, as listed in the table inset in Figure 7-2. After RTA at 450°C for 10 minutes (Section 2.5.1.3), V_{FB+} and V_{FB-} shift from -4.7 V and -6.0 V to -2.8 V and -3.7 V, respectively. The full semiconductor depletion (or Vt) also changes from -8.5 V to -6.2 V post-annealing.

Figure 7-1(a) reveals a significant finding: the flat band voltage of the MOS base devices exhibits a negative flat band characteristic, potentially linked to positive interface charge (Q_{it}), fixed oxide charges (Q_f) and work function differences between the gate metal and oxide. This has important

implications, as Q_f is independent of the applied voltage, unlike Q_{it}. A positive oxide charge can cause a parallel shift in the gate bias direction. The effect on the voltage shift is weighted according to the charge's location; the closer to the oxide-semiconductor interface, the more significant the shift. Positive charge is equivalent to an added positive gate bias for the semiconductor, necessitating a more negative gate bias to achieve the same original semiconductor band bending. Notably, the oxide field is no longer 0 V in the new flat band condition.

As mentioned above, the V_{FB} shift the MOS in the C-V characteristic is associated with the interface charge (Q_{it}), fixed oxide charge in SiO_2 layer (Q_f) and metal-semiconductor work function differences (Φ_{ms}) [130, 131, 222] formulated in eq. (7-4).

$$V_{FB} = \Phi_{ms} - \frac{(Q_{it} Q_f Q_m)}{C_{ox}} \qquad 7\text{-}4$$

The shift in the C-V sweep before and after RTA in Figure 7-1(a) and calculated in Figure 7-2 is the evidence of the existence of the positive charge in the interface and oxide due to a negative shift in the V_{FB} [130]. Although RTA shifts V_{FB} towards zero potential, the final VFB still shifts negatively, indicating residual positive charging in the system. This change might be due to the presence of Q_{it} from the majority carrier trapping in the forbidden bandgap. Band bending under potential causes the Fermi level to overlap the interface trap states (D_{it}), resulting in a positive or negative charge depending on the traps' location relative to the Fermi level.

During the inversion of the n-type MOS under negative voltage, fermi level crosses the intrinsic fermi level of the Si because the band is bending upward due to negative potential. Because of the electron donation of the interface trapping states below the intrinsic fermi level, the states are positively charged. When the fermi level of n-doped Si crosses the intrinsic fermi level of n-Si, the fermi level overlaps the trapping states resulting positive interface charging (Q_{it}). The number of interface states (D_{it}) are proportional to the interface charge (Q_{it}) and the distance of the states to the fermi level as formulised in eq. (7-5) [131].

$$D_{it} = \frac{1}{q}\frac{dQ_{it}}{dE} \qquad (7\text{-}5)$$

Where q is the unit charge which equals to $1.6 \times 10^{-19} C$ and dE is the energy level differences between intrinsic and doped fermi levels.

Therefore, positive interface charge result VFB shift on negative side as also seen in Figure 7-1(a). The parallel shifted of V_{FB} through the less negative side and narrowed depletion in C-V can be associated with lower positive Q_{it} charge due to the depth of the state's relative to the fermi level or electrically passivation of the interface by the annealing process. [130] [224]. Since the

interface trap at the interface may partly be passivated, the weight of charge traps may be further away from the interface or the number of charges Dit at the interface may be fewer, thanks to thermal treatment.

D_{it} can experimentally be calculated by eq. ((7-6);

$$D_{it=}\frac{2G_m}{q\omega} \qquad (7\text{-}6)$$

Where G_m is the max conductance of the G-V at V_{FB} and ω is the frequency of the G-V test in Hz. *Table 7-2* shows the list of fixed oxide charges and density of interface states of n-Si.

The distribution of interface trap levels across the energy bandgap is crucial for high-efficiency devices. The density of interface traps is determined by this distribution as in eq. ((7-5) and calculated in eq. ((7-6). It is also noted that thermal treatment in particular conditions, such as oxygen-free or hydrogen environments can passivate the trap states at the interface [129, 131]. Even though the thermal treatment at 450°C in vacuum condition, the D_{it} does not change significantly as calculated in eq. ((7-6). As presented in *Table 7-2*, the number of states does not change considerably as a result of RTA since the D_{it} value is close to the theoretical value for <100> Si wafer. The interface charge density has significantly been lowered, as seen in Figure 7-1(a). CV measurement of the annealing increase the slope of the depletion region as seen in Figure 7-1(a), which is sign of lower interface trap charges after RTA annealing [131, 223].

As discussed above, the other finding in the Figure 7-1 is the fixed oxide charge in the sputtered oxide layer, and the fixed oxide charge can be calculated by eq. (7-7).

$$Q_f = dC \times dV_{FB} \qquad 7\text{-}7$$

where dC are the differences between the maximum (or oxide, C_{ox}) and minimum (or inverse, C_{inv}) capacitances at accumulation and inversion respectively, and dV_{FB} is the shift in the flat band voltage between the forward and reverse voltage sweep.

Table 7-2 Fixed oxide charge in D_R devices with and without RTA treatment.

Devices	Q_f (C.cm^{-2})
D_R (without RTA)	1.24×10^{12}
D_R (with RTA)	7.52×10^{11}

Oxide-trapped charges are linked to imperfections in the silicon dioxide. These charges can be generated by X-ray radiation or high-energy electron bombardment during the sputtering of SiO_2

on the silicon wafer [129]. The traps are distributed throughout the oxide layer. Partial reduction of these impurities can be achieved through a heat treatment. *Table 7-2* provides the Q_f values for both samples. Following the RTA, the fixed oxide charge is 3/2 times lower than as-deposited MOS.

The steep slope of the annealed MOS formation in the C-V plot signifies high charge carrier mobility, enabling rapid charge and discharge of the oxide layer. This rapid transition reflects the quick switching between low and high conductivity states in the devices. Conversely, the gentler slopes observed in non-annealed samples indicate the presence of interface states that significantly vary with the applied bias, referred to as voltage-dependent interface states [129, 130].

As shown in Figure 7-1(b), the double voltage sweeps for a 60 nm PMMA deposition on the 30 nm thick annealed SiO_2 oxide layer exhibited a narrow hysteresis window. The fact that the base MOS device has already shown a negative flat band voltage at only -2.7 V indicates some initial interface and oxide charge Si/SiO_2 interface with positive charge traps. Incorporating PMMA on the Si/SiO_2 structure (D_B MIS device) results in a more significant negative shift in V_{FB} (-6.1 V) compared to base MOS. This suggests a higher presence of positive defects in the PMMA batch used, despite reports indicating minimal charge incorporation within PMMA [71].

This section focused on processing the base MOS device to ensure the dielectric properties of the e-beam sputtered SiO_2 TO layer. As shown in Figure 7-1(a), the RTA process significantly improved the dielectric constant of the TO layer. The figure also illustrated a marked increase in the slope of the depletion layer, indicating enhanced charge mobility after RTA. Analysis of the PMMA BO layer in Figure 7-1(b) revealed that the dielectric constant of the combined dielectric layer was 3.04 at 100 kHz. Consequently, this section concludes that the RTA process under vacuum conditions is crucial and will be applied to all MIS samples intended for use in non-volatile device applications.

7.2.4 Non-volatile Memory Applications of ZnO

The previous section concluded that e-beam-sputtered TO exhibits intrinsic charge trapping, as evidenced by a small flat-band voltage (V_{FB}) shift in C-V analysis, even after RTA treatment. Although the V_{FB} shift window disappeared when a PMMA BO layer was spin-coated onto the TO, the fixed oxide charge remains present. This section explores the non-volatile memory behaviour of MIS devices incorporating ZnO nanowires sandwiched between the TO (SiO_2) and BO (PMMA) layers.

ZnO nanoparticles have demonstrated significant potential in non-volatile memory applications, with prior studies showcasing various approaches to enhancing memory performance. Ho et al. embedded ZnO nanoparticles within Si_3N_4 layers, achieving an enhanced V_{FB} shift of up to 2.4 V. Atab et al. advanced memory performance further by embedding indium nitrate nanoparticles between two ZnO layers, resulting in an enhanced V_{FB} shift of 5.5 V. Additionally, by integrating graphene sheets within ZnO layers, they achieved a notable VFB shift improvement of up to 6.5 V. Further research by Atab et al. demonstrated that ZnO nanowire islands, when employed as floating gates in MOS capacitors, produced a substantial threshold voltage shift of approximately 8.5 V. These findings underscore the versatility and efficacy of ZnO-based nanostructures in improving non-volatile memory characteristics, paving the way for their integration into advanced memory devices. This section will focus on the specific role of ZnO nanowires within the MIS architecture and their contribution to enhanced memory performance.

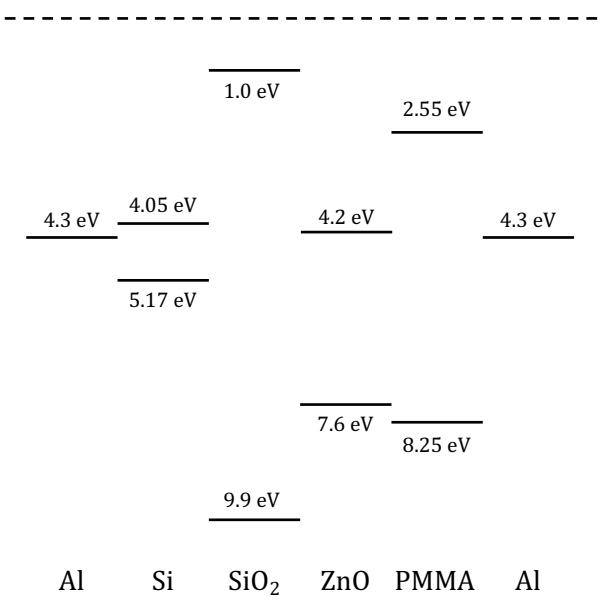

Figure 7-3: Energy band diagram of an MIS device structure for $Si/SiO_2/ZnO/PMMA/Al$.

The energy band diagram of the structure with MIS is illustrated in Figure 7-3, utilizing the reported work-function, electron affinities, and bandgap of the various materials. The conduction band offset between the Si substrate and tunnel oxide is smaller than the valence band offset, resulting in a significantly higher electron emission probability (1.47 eV compared to 4.08 eV). This is corroborated by the anti-clockwise C-V cycle in the programmed and erased states showing in the characteristics of the ZnO nanowire-embedded MISs, indicating electron storage in the

charge-trapping layer. Since ZnO nanowire networks provide relatively few trap states, most electrons are expected to tunnel through the tunnelling oxide into the ZnO layer. These electrons are then swept by the electric field and trapped within the surface defects and nanowire-nanowire junctions [71, 225-227].

Figure 7-3 depicts the energy band diagram of the memory device. The conduction band offset between the channel and the TO is larger than their valence band offset (2.3 eV vs. 3.2 eV). This discrepancy leads to a higher probability of electron emission compared to hole emission. Additionally, the substantial conduction band offset between ZnO and PMMA reduces the chances of back tunnelling and electron leakage, ultimately ensuring excellent data retention characteristics.

The ZnO network, known for its unique properties such as high thermal stability, excitation band energy (60 eV), and tuneable direct bandgap, is a key component that makes these devices suitable for memory applications [6, 7]. The memory mechanism in random ZnO nanowire network-based devices is a fascinating process. It involves trapping and releasing charges within the floating gate stack, with the ZnO nanowire's presence being crucial in inducing hysteresis and enhancing memory characteristics [21, 69, 226]. The charge transfer principle for reading and erasing memory in these devices is complex. It involves manipulating charges within the floating gate stack under positive and negative bias. The energy band diagram of the memory cells, as shown in the figure, is constructed based on XPS measurements and reported values of the band offsets and bandgaps of the varied materials.

The programming and erasing mechanisms involve injecting or emitting electrons in the nanowire network, which stores charge in the floating gate. A negative bias on the top electrode achieves this by causing electrons to tunnel from the channel trap into oxygen vacancies in the ZnO nanowire lattices, defects, and nanowire surfaces. This shifts the C-V memory characteristics, illuminating the mechanism. During reading, a negative voltage bias on the top electrode creates an electric field across the blocking PMMA dielectric layer, causing electrons to emit from oxygen vacancies and junctions, tunnelling through the SiO_2 layers, while holes tunnel into the ZnO quantum well. This shifts the C-V characteristics back [44, 69].

In summary, applying negative gate voltage during programming results in electrons emitted to the channel and holes tunnelling through the oxide to be trapped in the deep ZnO quantum well. This cycle causes a left shift in the C-V characteristic. During erasing, electrons tunnel back into trap states while holes return to the channel, shifting the C-V characteristic to the right. Due to quantum confinement in 1D, ZnO nanowires improve bandgap offset and reduce electron affinity [44, 45]. As charge-trapping layers, ZnO nanowires show promise for memory devices with a significant 4V window at low operating voltages. They enhance memory retention due to

increased defect states from tensile stress relaxation. These properties make ZnO nanowires ideal for future non-volatile charge-trapping memory devices.

7.2.5 Memory Performance

Integrating ZnO nanowires into the dielectric layer of MOS transistors significantly enhances the memory characteristics of the device. This study examines three distinct doping levels of ZnO NWs—0.25, 0.5, and 1.0 wt.%—to evaluate their impact on memory performance as $D_{NW,0.25}$, $D_{NW,0.5}$ and $D_{NW,1.0}$ devices. The selected doping ratios are based on the percolation behaviour of ZnO NWs, as detailed in Chapter 4. At 0.25 and 0.5 wt.%, the device operates in the lower percolation regime, where tunnelling conduction predominates, while 1.0 wt.% represents the percolation threshold, marking a critical transition in conduction behaviour. Additionally, the observed decrease in capacitance for the 30 nm SiO_2 layer on n-Si with increasing frequency is attributed to the dominance of localised state polarisation at the n-Si/SiO_2 interface at low frequencies and serial resistance at high frequencies. This frequency-dependent behaviour leads to higher charge accumulation at lower frequencies. This section will present the results, highlighting the distinct roles of ZnO NWs in enhancing the memory performance compared to the reference device [228, 229].

Figure 7-4 shows the initial cycles of the C-V scan, ranging between -10 V and 10 V, for the 0.25 wt.% ZnO nanowire deposited $D_{NW,0.25}$ on device. The outcomes indicate that the C-V characteristic does not remain stable in identical hysteresis within preliminary cycles before presenting repeatable, stable cycles. This observation suggests that further cycles may be necessary to achieve consistent capacitive behaviour, highlighting the C-V characteristics' dynamic nature during the deposition process's initial phase [129, 130].

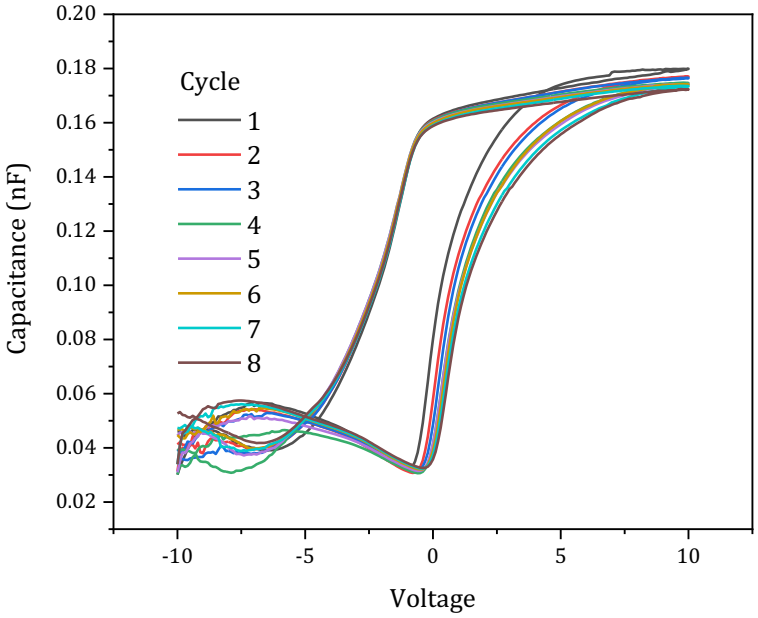

Figure 7-4 The C-V characteristics of $D_{NW,0.25}$ MIS devices over eight cycles. The V_{FB} shifts from initial values of -0.1 V and -2.3 V to 0.7 V and -2.5 V after 8 cycles, indicating changes in charge distribution and interface states within the device.

Figure 7-4 displays the C-V characteristics of $D_{NW,0.25}$ MIS devices initial multiple cycles, ranging from Cycle 1 to Cycle 8. Each curve represents a distinct cycle, revealing the evolution of capacitance as a function of applied voltage. The gradual shift in these C-V curves is indicative of changes in the V_{FB} of the devices. Initially, the V_{FB} erasing and programming values were recorded at approximately -0.1 V and -2.3 V. However, after undergoing eight cycles, these values shifted to 0.7 V and -2.5 V, respectively. This shift suggests modifications in the charge distribution within the MIS structure, potentially due to trapping and de-trapping phenomena in the dielectric layer or interface states [129-131].

The observed shift in V_{FB} across the cycles is critical as it reflects the stability and reliability of the ZnO nanowire-embedded MIS devices under cyclic operation. The initial negative V_{FB} values suggest the presence of positive charges or donor-like states within the insulator or at the interface. The shift towards more positive V_{FB} values after multiple cycles could be attributed to

the accumulation of additional charges [44], alterations in the interface states, or structural changes within the ZnO nanowires themselves.

Table 7-3: Memory window parameters of $D_{NW,0.25}$, and $D_{NW,0.5}$ MIS devices before and after stabilisation. The table lists the memory window (ΔV_{FB}), capacitance change (ΔC), and charge density (Q_f) for the first and last cycles of Figure 7-4 and Figure 7-5.

Cycles	Memory Window $\Delta V_{FB}(V)$	$\Delta C\ (nF)$	Charge Density Q_f (10^{11} cm^{-2})
1st (Figure 7-4)	2.40	0.129	1.17
8th (Figure 7-4)	3.20	0.124	1.45
1st (Figure 7-5)	5.75	0.125	2.58
10th (Figure 7-5)	6.15	0.128	2.57

Table 7-3 displays the memory window parameters of the $D_{NW,0.25}$ and $D_{NW,0.5}$ MIS devices, explicitly focusing on the stored charge by the oxide before and after stabilisation, as seen in Figure 7-5. For the first cycle (Figure 7-4), the memory window (ΔV_{FB}) is 2.40 V with a capacitance change (ΔC) of 0.129 nF and a charge density (Q_f) of 1.17×10^{11}cm^{-2}. By the eighth cycle, the memory window expands to 3.20 V with a ΔC of 0.124 nF and Q_f of 1.45×10^{11} cm^{-2}, indicating increased charge storage capacity and a more significant shift in flat-band voltage.

Compared to the base MOS devices shown in Figure 7-1, the shift in V_{FB} is significantly more pronounced. The data clearly show that the incorporation of 0.25 wt.% ZnO nanowires between the TO and BO layers greatly enhance charge-trapping, 3.2 V, as summarised in *Table 7-3*. This suggests that ZnO nanowires are crucial in charge-trapping, even under a physical percolation regime. Similar findings have been reported, indicating that 0D ZnO nanowire islands deposited via the ALD technique exhibit a 4 V_t shift [69], and 6 V and 8.2 V when 5 nm ZnO particles have

spin and deep-coated, respectively [45]. The charge-storing behaviour of 1D nanostructures, including oxygen vacancies in ZnO nanostructures, is also illustrated.

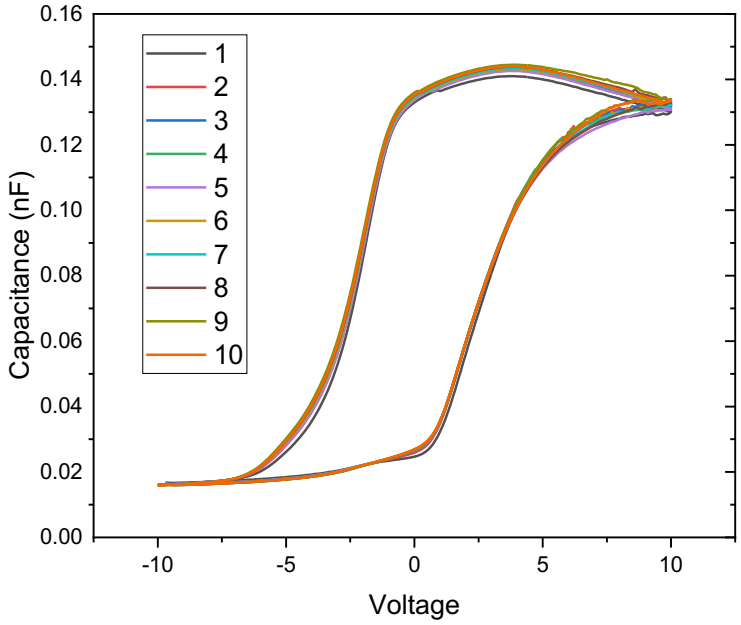

Figure 7-5: C-V characteristics of $D_{NW,0.5}$ MIS devices after several initial cycles, recorded over ten cycles. The V_{FB} shows a minor shift from 2.15 V and -3.6 V to 2.15 V and -4.0 V, suggesting that the device has achieved a more stable and consistent operational state.

Figure 7-5 presents the C-V characteristics of the same $D_{NW,0.5}$ MIS devices after several initial cycles, capturing a period during which the devices exhibit more stable and repeatable behaviour. In this case, V_{FB} demonstrates a significantly reduced shift compared to the initial cycling, as presented in Figure 7-4. The V_{FB} values start at approximately 2.15 V and -3.6 V and experience a minor shift to 2.15 V and -4.0 V after ten cycles. This minor shift indicates a stabilisation in the charge distribution and interface states within the MIS structure. The reduced variability in V_{FB} suggests that the trapping and de-trapping processes or other mechanisms [44, 130] affecting the device's electrical characteristics have reached a more equilibrium state.

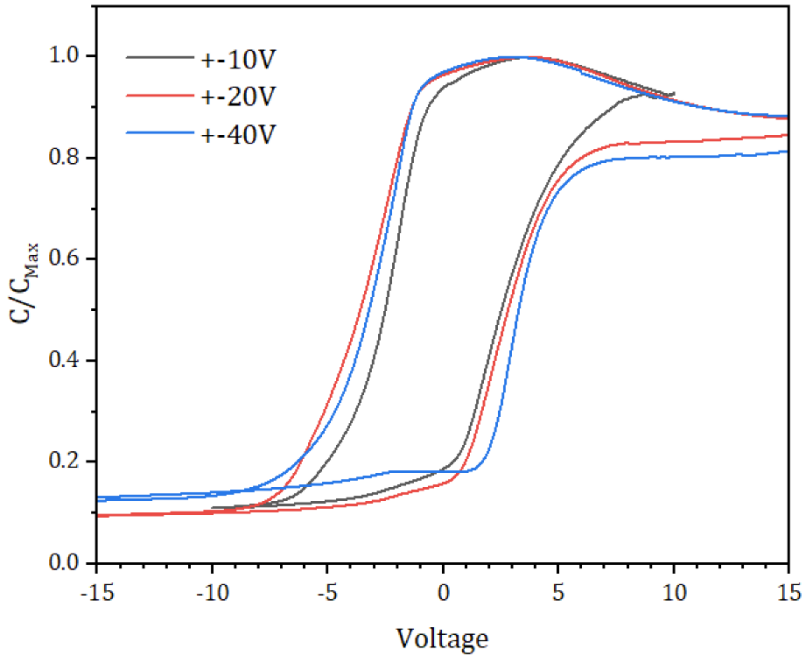

Figure 7-6: C-V characteristics of $D_{NW,0.5}$ MIS devices under various voltage sweep ranges of ±10 V, ±20 V, and ±40 V. The C-V curves, normalised to the maximum capacitance (C/C_{max}), demonstrate the effect of increasing voltage sweep range on the memory window and charge storage properties of the devices.

The observations combined with the initial data illustrate the dynamic changes in the performance of MIS devices. In the beginning, the devices show notable shifts in V_{FB}, indicating significant alterations in charge dynamics and interface states. Over continued cycling, however, the devices reach a more stable operating condition with minimal V_{FB} shifts. This stability is essential for the practical use of ZnO nanowire-embedded MIS devices, as it ensures consistent performance over extended use. The gradual stabilisation highlights the necessity of an initial conditioning phase to achieve optimal and reliable device characteristics.

Table 7-4: Memory window parameters for ZnO nanowire embedded MIS devices under different voltage sweep ranges. The table lists the ΔV_{FB}, ΔC, and stored charge density (Q_f) for ±10 V, ±20 V, and ±40 V sweeps. The charge density is calculated by eq. 7-7.

C-V Sweep Range	Memory Window $\Delta V_{FB}(V)$	$\Delta C\ (nF)$	Charge Density Q_f (10^{11} cm^{-2})
$\pm 10\ V$	6.20	0.128	2.58
$\pm 20\ V$	7.50	0.141	3.69
$\pm 40\ V$	6.15	0.123	2.64

Figure 7-6 and the accompanying *Table 7-4* provide an analysis of the C-V characteristics of the same MIS device, which is 0.5 wt.% ZnO nanowire embedded, under different voltage sweep ranges of ±10 V, ±20 V, and ±40 V. The primary objective of this study is to evaluate how varying voltage ranges influence the memory window and charge density of the devices. The C-V curves, normalised to the maximum capacitance (C/C_{max}), illustrate the device response under the different voltage sweep conditions. As the sweep range increases from ±10 V to ±40 V, distinct shifts in the C-V curves are observed, reflecting changes in the ΔV_{FB} and the associated charge storage properties.

Table 7-4 summarises the memory window parameters derived from these C-V sweeps in Figure 7-6. For the ±10 V sweep range, the memory window is 6.20 V, with a ΔC of 0.128 nF and a charge density (Q_f) of $2.58 \times 10^{11}\ cm^{-2}$, calculated using eq. (7-7). When the sweep range is increased to ±20 V, the memory window expands to 7.50 V, ΔC rises to 0.141 nF, and Qf increases to $3.69 \times 10^{11}\ cm^{-2}$, indicating a higher charge storage capacity. Interestingly, at the highest sweep range of ±40 V, the memory window reverts to 6.15 V, with ΔC slightly decreasing to 0.123 nF and Q_f stabilising at $2.64 \times 10^{11}\ cm^{-2}$. The results show that the memory window increases initially with the applied voltage sweep, reaching a peak at ±20 V, and then decreases back towards the initial value at the higher voltage sweep of ±40 V. This suggests that while a moderate increase in the voltage sweep enhances charge trapping and storage capacity. Further increase may lead to charge leakage over the thin PMMA layer or variation of the thickness of PMMA stack thickness over the device [227].

The positive shift in the V_{FB} for the voltage sweep from 40 V to -40 V is attributed to the breakdown in the PMMA dielectric strength, resulting in a leakage current and electrons transfer through the PMMA film to the floating gate. Typical values for PMMA dielectric strengths are 4.4 MV/cm and thickness dependent. Hence, for a 60 nm thick PMMA layer, the breakdown voltage is very close to 26 V [230]. However, it has also been noted that the dielectric strength of the PMMA

is examined as 3.2 MV/cm on MIS devices due to the influence of the impurities and surface charges or the interface states in the Si substrate [231].

The PMMA insulator layer plays a crucial role in maintaining the stability of memory devices. Revised C-V analysis, conducted on a device with an increased nanowire concentration of 1.00 wt.%, shows significant findings. Despite the higher concentration, the first ten cycles matched earlier tests at 0.50 wt.%, displaying a gradual increase in the memory window and a decrease in peak capacitance with each cycle. Interestingly, the last two cycles demonstrated notable stabilisation, maintaining consistent performance. This observed trend highlights the important relationship between nanowire concentration and capacitance behaviour, offering a pathway for optimising charge storage in these devices.

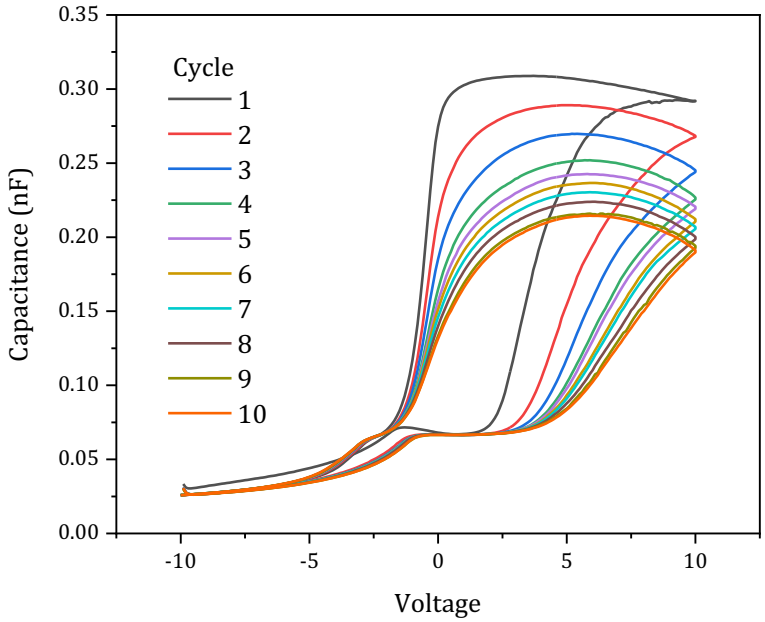

Figure 7-7: The initial 10 cycles of C-V characteristics of the $D_{NW,1.0}$ MIS device showing unstable memory window behaviour due to unreliable PMMA layer formation.

Figure 7-7 depicts the C-V characteristics of the $D_{NW,1.0}$ MIS device, which exhibits an unstable memory window due to unreliable PMMA layer formation, leading to leakage current and soft breakdown. *Table 7-5* summarises the changes in ΔV_{FB}, ΔC, and stored charge density (ρ) across the initial ten cycles. Initially, the memory window (ΔV_{FB}) increases from 4.35 V in the first cycle to 7.4 V by the tenth cycle, suggesting a growing instability in the device, as seen in *Table 7-5*. Simultaneously, the peak capacitance (ΔC) decreases from 0.242 nF to 0.149 nF, indicating a reduction in the effective capacitance of the device. This reduction can be attributed to the formation of leakage paths within the PMMA layer, which compromises the device's insulating

properties and results in unreliable memory behaviour [130, 222]. This leakage may result from a poor encapsulation of ZnO nanowires in the devices produced, as reported elsewhere[71]. The charge density (ρ) also shows variations, i.e., initially increasing from $3.68 \times 10^{11} cm^{-2}$ to $4.61 \times 10^{11} cm^{-2}$, before stabilising around $3.85 \times 10^{11} cm^{-2}$ in the later cycles.

This instability highlights the critical need to optimize the formation of the PMMA layer to prevent leakage currents and ensure consistent memory performance. The observed data underscore the delicate balance required in the device's design to maintain stable capacitive properties and reliable memory behaviour over multiple cycles. This issue may stem from fabrication errors or potential damage to the PMMA layer by the load cell during C-V testing. To address this, another device was produced to facilitate a better comparison and observe the effect of nanowire concentration on charge storage, which will be presented in the following section.

Table 7-5: Summary of changes in flat-band voltage (ΔV_{FB}), capacitance (ΔC), and charge density (ρ) across ten cycles for $D_{NW,1.0}$ *MIS device.*

Cycle	Memory Window $\Delta V_{FB}(V)$	ΔC (nF)	ρ ($\times 10^{11} cm^{-2}$)
1	4.35	0.242	3.68
2	5.8	0.222	4.50
3	6.5	0.203	4.61
4	6.7	0.185	4.33
5	6.8	0.176	4.18
6	7.1	0.17	4.22
7	7.25	0.163	4.13
8	7.4	0.157	4.06
9	7.4	0.149	3.85
10	7.4	0.149	3.85

This evaluation highlights the relationship between memory window expansion and the reduction of differential capacitance and how these factors together affect the charge storage efficiency of the device over multiple C-V cycles. The results show a complex balance between increasing the memory window size and managing capacitance changes to optimise charge storage capabilities. Figure 7-8 illustrates the relationship by comparing the memory window of the base MOS device with ZnO-embedded MIS devices at varying nanowire concentrations. This comparison highlights the significant influence of nanowire concentration on device performance, emphasizing its role in optimizing charge storage efficiency. The results demonstrate how adjusting nanowire concentration can improve the device's memory capabilities, leading to enhanced overall performance.

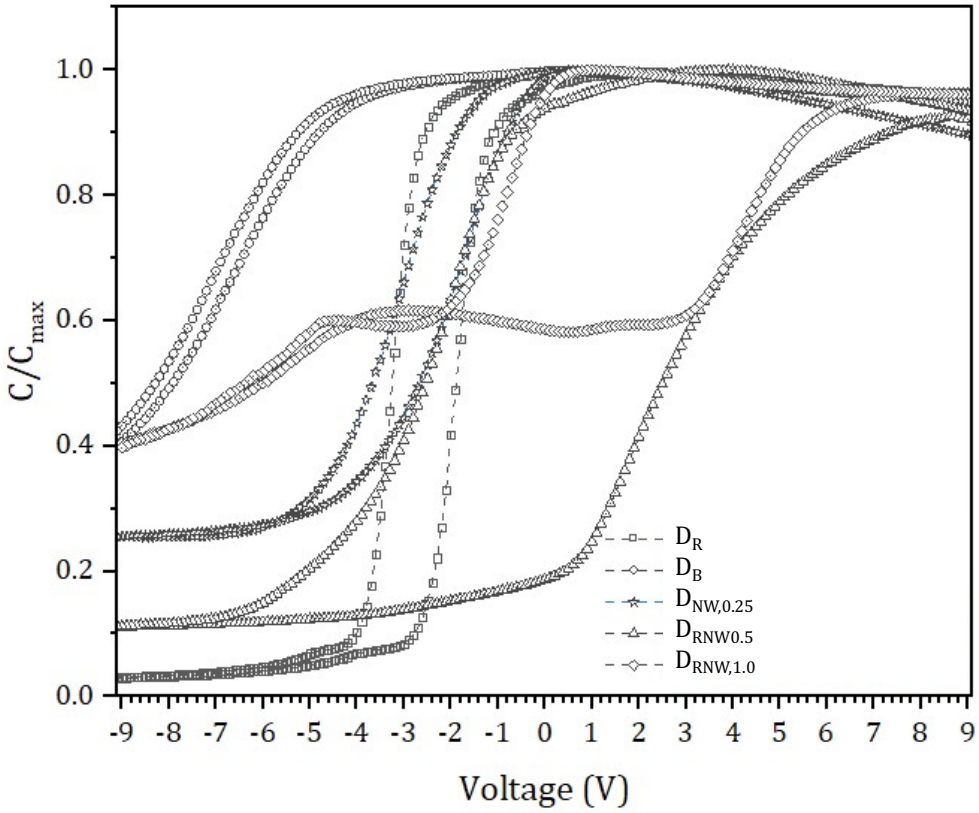

Figure 7-8: C-V characteristics normalized to maximum capacitance (C/C_{max}) for various devices: MOS, MIS with PMMA, and MIS with different concentrations of ZnO nanowires ($D_{NW,0.25}$, $D_{NW,0.5}$ and $D_{NW,1.0}$).

Figure 7-8 illustrates the C-V characteristics normalised to maximum capacitance (C/C_{max}) for all the devices presented in this section. The base MOS device shows a distinct C-V curve compared to the MIS devices, highlighting the impact of the PMMA insulator and ZnO nanowire embedding. As the concentration of ZnO nanowires increases, the C-V curves display increased hysteresis, indicating a broader memory window. Specifically, the MIS devices with higher ZnO concentrations exhibit more pronounced hysteresis loops, signifying enhanced charge trapping and storage capabilities. This increased hysteresis with higher nanowire intake underscores the influence of nanowire density on the capacitive performance and memory window stability of the MIS devices, demonstrating the complex interplay between nanowire concentration and device reliability.

Table 7-6: Performance overview of non-volatile memory devices used in this Chapter.

Samples	Memory Window $\Delta V_{FB}(V)$	ΔC (nF)	ρ ($\times 10^{11} cm^{-2}$)
D_R	0.90	2.393	4,23
D_B	0.45	0.222	0.52
$D_{NW,0.25}$	1.90	0.712	4.73
$D_{NW,0.5}$	6.15	0.128	2.57
$D_{NW,1.0}$	7.80	0.188	5.12

For the reference MOS device, the memory window is 0.90 V with a high capacitance change of 2.393 nF and a charge density of 4.23× $10^{11} cm^{-2}$. Introducing PMMA without ZnO results in a reduced memory window of 0.45 V, indicating a decrease in charge trapping capabilities, as evidenced by the lower capacitance change of 0.222 nF and charge density of 0.52× $10^{11} cm^{-2}$ [45, 71].

When ZnO nanowires are embedded between TO and BO layers, the memory window and charge density notably increase. This improvement is due to the unique electronic properties of ZnO nanowires, which contribute to enhanced charge storage and retention capabilities [43]. Specifically, for the MIS device incorporating 0.25 wt.% ZnO, the memory window expands significantly to 3.20 V, accompanied by a capacitance change of 0.712 nF. This suggests that even a minor addition of ZnO can substantially enhance the device's performance. Moreover, as the concentration of ZnO nanowires is doubled to 0.50 wt.%, the memory window further escalates to 6.15 V. However, this increase in the memory window is coupled with a notable reduction in capacitance change, dropping to 0.128 nF. This inverse relationship between the memory window and capacitance change highlights the complex interplay of factors in optimising the device's performance. The findings indicate that while higher ZnO content boosts the memory window, it simultaneously challenges maintaining capacitance stability, necessitating a balanced approach in design and material composition for optimal device functionality.

7.3 Summary

In summary, the ZnO nanowire networks drop-casted between TO and BO layers demonstrate a significantly larger memory window than the spin-coated and dip-coated ZnO nanoparticles between $Al2O_3$ high dielectric constant TO and BO layers. Additionally, the devices exhibit similar

performance to ZnO nano-islands deposited by the ALD layer, which is the most sophisticated and expensive technique. The calculation of their memory window is based on monitoring V_t values at the midpoint of the forward and reverse voltage sweeps. Utilising this method, our values exceed those previously reported. Our findings confidently indicate that the ZnO nanowire-based MIS devices have a substantially higher memory window than those documented in earlier studies. Furthermore, these ZnO-based MIS devices show a sharper accumulation regime, indicating faster charge mobility when they are heat treated. Consequently, it is concluded that ZnO nanowires-based MIS devices present superior non-volatile MIS performance.

Chapter 8

MULTI FUNCTIONALITY OF THE MIS DEVICES UNDER PRESSURE

8.1 General Overview

In this chapter, we explore the multifunctionality of the ZnO nanowire-embedded MIS device by first demonstrating its performance as a capacitive pressure sensor, and then evaluating its other functionalities—UV photodetection and non-volatile memory—under applied pressure. In Sections 6.5 and 7.2, we have already demonstrated that the ZnO-NW-based MIS device, where the ZnO nanowire network is embedded between SiO_2 and PMMA layers on a silicon substrate, can operate as both a UV photodetector and a non-volatile memory device. In this chapter, we expand on those results by applying semi-automated pressure loading to the same device configuration. The objective is to confirm that the device can also function effectively as a pressure sensor, proposing its potential as a truly multifunctional system. The ability to perform multiple tasks—pressure sensing, UV detection, and non-volatile memory storage—within a single device platform represents a significant advancement in the field of multifunctional electronics and paves the way for versatile, scalable, and low-cost device applications.

8.2 Capacitor Pressure Sensors

MIS pressure sensors have a wide range of applications across the human-computer interface (HCI) [52], electronic skins [81, 232-234], and aerospace industries, particularly for their ability to detect touch. These applications often require high sensitivity in low-pressure ranges, up to about 1 MPa [234]. Two-dimensional pressure profiling is useful in determining contact area and inferring stress concentrations at the contact interface. *Table 8-1* lists common applications for flexible pressure sensing arrays and their corresponding pressure ranges.

Table 8-1: Pressure range of capacitive pressure sensor usage (taken from [53]).

Application	Pressure
Vascular pulse (75-150 mmHg)	10-20 kPa
Human fingertip texture, shape sensing	10-40 kPa
Hand grip	0-100 kPa
Fingerprint sensor	1-2 kPa
In-shoe pressures	1-2 kPa
Tactile robotics	10-100 kPa +

Earlier reports have used various types of pressure sensors, such as piezoelectric, resistive, and capacitive. Among these, capacitive pressure sensors are favoured due to their straightforward fabrication, cost-effectiveness, high sensitivity, and exceptional environmental stability [81, 232]. With advantages like long-term drift stability and low power consumption, capacitive pressure sensors find numerous applications [235]. Typically, a capacitive pressure sensor consists of two parallel plate electrodes separated by a dielectric interlayer. The sensor's capacitance, C, depends on the dielectric permittivity, ε_r, of the interlayer material, the effective electrode area, A, and the distance between the two electrodes, d, with ε0 representing the vacuum permittivity.

8.2.1 Principle of Capacitor Pressure Sensor

If the area (A) of the Al gate electrode is much larger than the thickness of the insulator, the capacitance of a parallel plate capacitor can be calculated using eq. (7-3). When the material experiences strain perpendicular to the capacitive plates, the change in the distance between the plates leads to a change in capacitance. This strain can be estimated by differentiating the capacitance using eq.(8-1) and solving for the strain using eq. (8-2). A positive change in capacitance, indicating that the plates move closer together, corresponds to a negative (compressive) strain [53].

$$\frac{dC}{dd_{ox}} = \frac{\varepsilon_0 \varepsilon_r A}{d_{ox}^2} \tag{8-1}$$

$$strain \approx -\frac{\Delta C d_{ox}}{\varepsilon_0 \varepsilon_r A} \tag{8-2}$$

Because all the factors in eq. (8-2) is a constant and material and structure-dependent; the change in the capacitance is directly proportional to the applied strains to the MIS devices. Therefore, the

change in the capacitors is directly related to the pressure on the parallel plate capacitor. The sensitivity (S) of the devices is calculated using eq. (8-3) [236].

$$S \approx \frac{\Delta C}{C_i} \times 100 \qquad (8\text{-}3)$$

The sensor detects the strain perpendicular to its surface but is also affected by the Poisson ratios of materials. To minimise the impact of shear and in-plane stresses, one plate is made larger than the other. This design makes the sensor selectively sensitive to loading and allows it to be placed close to a contact surface. The sensor is "solid state" and has no moving parts. The choice of dielectric medium controls pressure ranges and output capacitance. Stiffer dielectrics allow for higher pressure operating ranges, while softer dielectrics offer a better resolution for lower pressure ranges. The dielectric constant of the material determines the nominal capacitance and influences the change in capacitance under a given load, making materials with higher dielectric constants more desirable [53].

8.2.2 Testing of Pressure Sensitivity

Figure 8-1(a-c) shows the change in capacitance $\left({}^{\Delta C}/_{C_0}\right) \times 100$ (S in % eq. (8-3) versus applied 15 sec periodic 8 kPa pressure on the various ZnO nanowire ratio MIS devices, where C_0 is the capacitance without applied pressure and ΔC is the change in the capacitance with applied gradual pressure. Each step of applied pressure is approximately 8 Pa for each 0.5 sec reading step as described in Section 2.2. The test-rig is highly precise and applicable to the minimum detectable pressures used in complicated designs: 5 Pa [237] and 9 Pa [237]. Thus, the tests were conducted using a capacitance reading under 5 V at a frequency of 500 kHz, with readings taken every 0.25 seconds. Each pressure cycle involved applying pressure for 15 seconds, releasing it, and then waiting 15 seconds before starting the next cycle. The detailed cycle of pressure application is presented in Section 2.2.

(a)

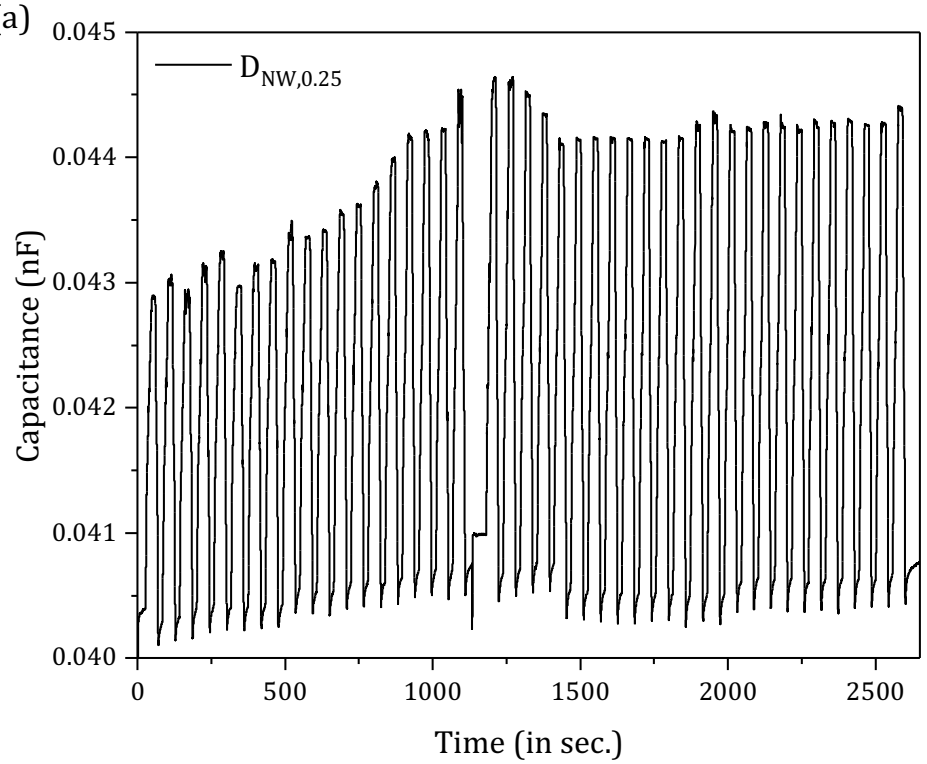
$D_{NW,0.25}$
Capacitance (nF)
0.045
0.044
0.043
0.042
0.041
0.040
0
500
1000
1500
2000
2500
Time (in sec.)

(b)

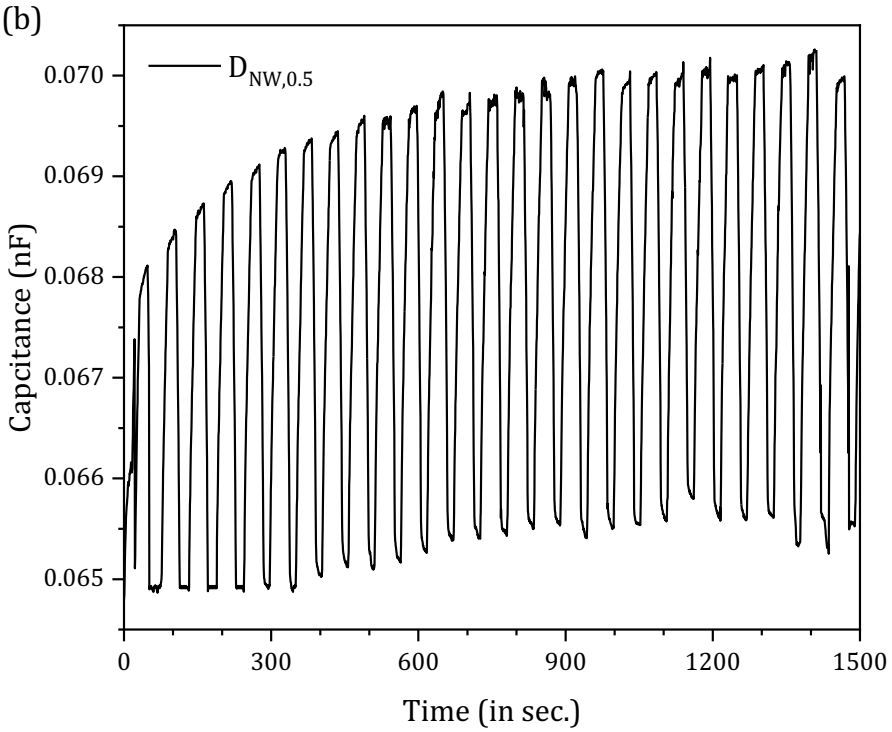
$D_{NW,0.5}$
Capcitance (nF)
0.070
0.069
0.068
0.067
0.066
0.065
0
300
600
900
1200
1500
Time (in sec.)

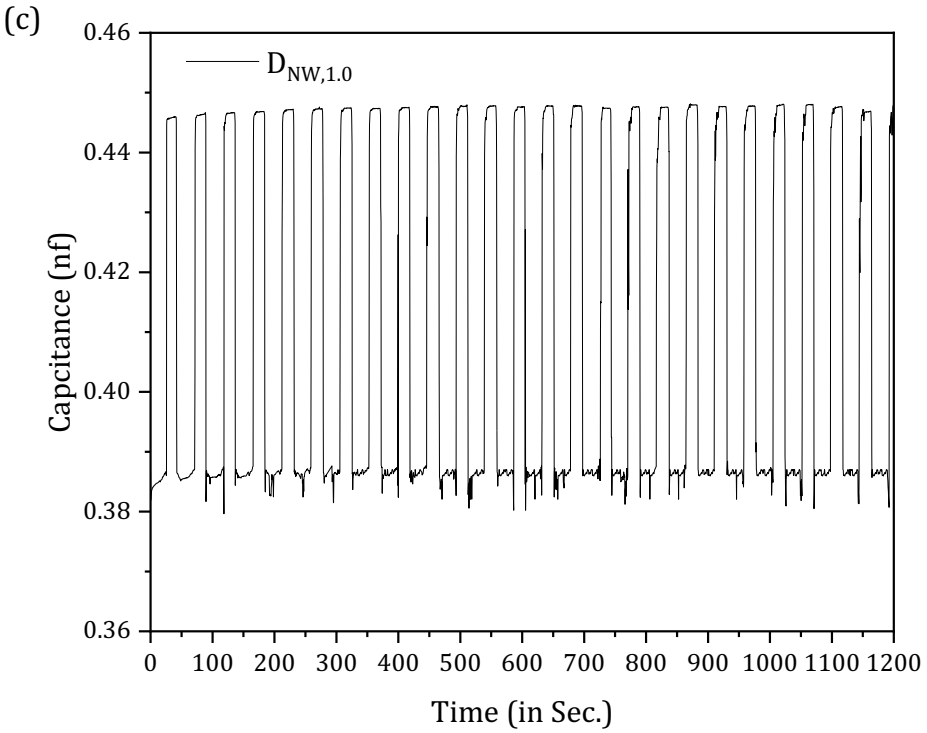

Figure 8-1: Capacitive 9.6 kPa pressure sensing results for MIS devices with varying ZnO nanowire concentrations in the insulator layer: (a) $D_{NW,0.25}$, (b) $D_{NW,0.5}$, and (c) $D_{NW,1.0}$. Tests were conducted using a C-V 500 kHz, with readings taken every 0.5 seconds. Each pressure cycle consisted of applying pressure for 15 seconds, releasing it, and waiting 15 seconds before the next cycle.

Figure 8-1 reveals diverse pressure sensitivities for different concentrations of ZnO nanowires. The capacitance changes for the 0.25 wt.% sample are modest but display a periodic response to the applied pressure cycles, with some drift over the initial cycles. The 0.50 wt.% sample has more noticeable capacitance changes, indicating greater sensitivity to pressure. This sample also shows a more consistent periodic pattern, suggesting better stability under cyclic loading. The 1.00 wt.% sample demonstrates the most significant capacitance changes, reflecting the highest sensitivity among the three concentrations.

*Table 8-2: Pressure Sensitivity (S) (by eq. (*8-3*) for MIS devices with different concentrations of ZnO nanowires during the initial, mid, and last cycles of 9.6 kPa pressure loading.*

Samples	Initial Cycles	Mid-Cycles	Last Cycles
$D_{NW.0.25}$	6.18	9.61	9.260.093
$D_{NW.0.5}$	4.93	8.06	9.24±0.096
$D_{NW.1.0}$	16.15	16.02	16.02±0.023

Table 8-2 presents the pressure sensitivity for various ZnO nanowire concentrations, as shown in Figure 8-1, during the initial, mid, and final cycles of pressure sensing. For the $D_{NW,0.25}$ sample, the sensitivity starts at 6.18 in the initial cycle, increases to 9.61 in the mid-cycle, and slightly decreases to 9.26 in the final cycle. This suggests an overall improvement in sensitivity over time, with some stabilisation during the later cycles. For the $D_{NW,0.5}$ sample, the sensitivity is 4.93 in the initial cycle and increases consistently to 8.06 in the mid-cycle and 9.24 in the final cycle. This indicates a consistent enhancement in sensitivity and stability as the device undergoes more pressure cycles.

The $D_{NW.1.0}$ sample starts at a sensitivity value of 16.15 in the initial cycle, which changes slightly to 16.02 in both the mid and final cycles. This indicates that the highest concentration of ZnO nanowires provides the most significant and stable strain response to pressure. These observations suggest that increasing the ZnO nanowire concentration enhances the pressure sensitivity of MIS devices. However, the device adjusts to the applied pressure cycles during an initial stabilisation. Higher concentrations of ZnO nanowires improve charge trapping and release mechanisms, leading to greater sensitivity and a more pronounced capacitive response to pressure changes. This enhanced sensitivity can be attributed to the increased number of charge-trapping sites provided by the greater density of ZnO nanowires within the insulator layer.

Research has demonstrated, through both numerical simulations [238] and experiments [233, 238-240], that the integration of randomly oriented ZnO nanowires significantly improves capacitive pressure sensing. This effect is particularly pronounced when the nanowires are positioned near the gate electrode, attributable to their piezoelectric characteristics. Upon exerting pressure, the ZnO nanowires undergo longitudinal stress, resulting in the polarisation of the internal ions and the creation of a piezoelectric potential. This potential is generated by the relative displacement of Zn^{2+} and O^{2-} ions within the crystal lattice of ZnO. The induced polar charges persist until the removal of the applied stress. Numerical analyses have indicated that the capacitive sensing efficiency of horizontally aligned ZnO nanowires is double that of their vertically aligned counterparts [238].

The previous report on a ZnO nanowire/PMMA composite between two parallel plate electrodes showed approximately 0.975 cm^2/Pa and 0.258 cm^2/Pa between the 0 to 300 Pa range [240]. The findings demonstrate that the device exhibits greater sensitivity within a low-pressure range (<300 Pa). The MIS capacitor containing 1.00 wt.% ZnO nanowires achieve a sensitivity of 0.198 cm^2/Pa across the 400 Pa to 8 kPa range. Although this value is slightly lower than previously reported[240], it remains comparable due to the broad pressure scale considered.

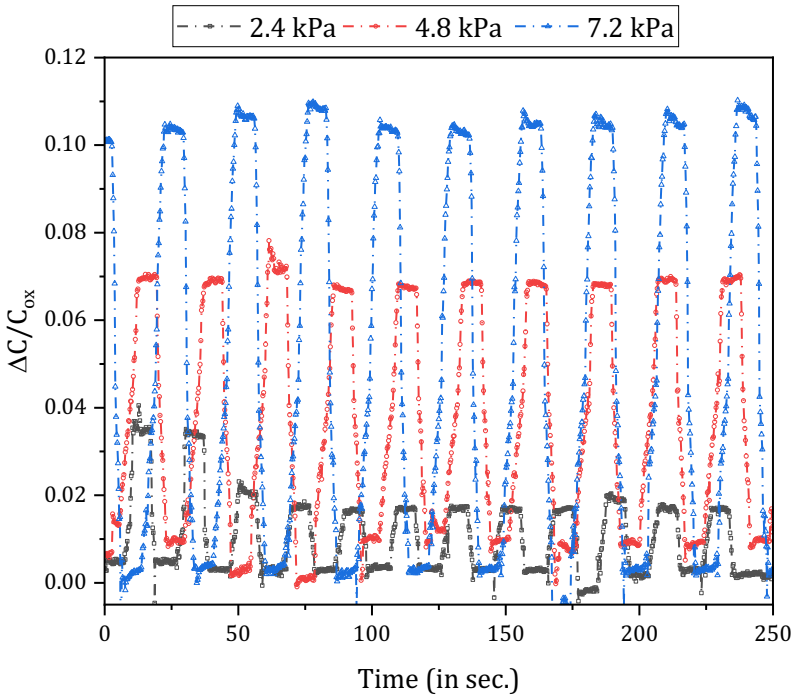

Figure 8-2: Capacitive response of $D_{NW.0.5}$ MIS devices under three different applied pressures: 2.4 kPa, 4.8 kPa, and 7.2 kPa. The tests were conducted with a Capacitive test frequency of 500 kHz, and readings were taken every 0.25 seconds.

Figure 8-2 illustrates the capacitive response of $D_{NW,0.5}$ ZnO embedded MIS devices under three different applied pressures: 2.4 kPa, 4.8 kPa, and 7.2 kPa. The tests were conducted under the same conditions as previous experiments, with a C-V test frequency of 500 kHz and readings taken every 0.5 seconds. Each pressure cycle involved applying pressure for 15 seconds, releasing it, and then waiting 15 seconds before the next cycle.

The results indicate that the device exhibits sensitivity across different pressure ranges, showing unique capacitive responses at each level. Specifically, at 2.4 kPa, the capacitance variation ($\Delta C/C_{ox}$) is minimal yet displays a noticeable periodic response to the pressure cycles. At 4.8 kPa, the device demonstrates a greater capacitance shift, suggesting enhanced sensitivity and a more significant reaction to the applied pressure. The highest capacitance changes occur at 7.2 kPa, presenting a consistent periodic pattern, thereby proving the device's effectiveness in responding to elevated pressure levels. This evidence suggests that the MIS device offers substantial sensitivity over a broad pressure spectrum (dynamic range), with an explicit and quantifiable response that amplifies with increasing pressure. Such characteristics render the device ideal for applications necessitating the detection of variable pressures, highlighting its potential for high-resolution pressure sensing [52, 238].

8.3 Multifunctional Device Testing

In an innovative approach to the multifunctional device concept, multiple functions are being executed simultaneously. While numerous studies have proven various applications of ZnO nanowires and their diverse applications, these functionalities have typically been examined in isolation rather than concurrently.

Previously, we highlighted the remarkable sensitivity of MIS devices to UV light, emphasising their potential in UV photodetection. Building on that, this chapter further establishes that these devices exhibit non-volatile memory capabilities and responsive pressure sensing across various loads. These functionalities highlight the versatility of MIS devices, positioning them as potential all-in-one solutions. In this section, we will explore the individual capability while concurrently exposing the devices to multiple stimuli to assess their true multifunctional potential.

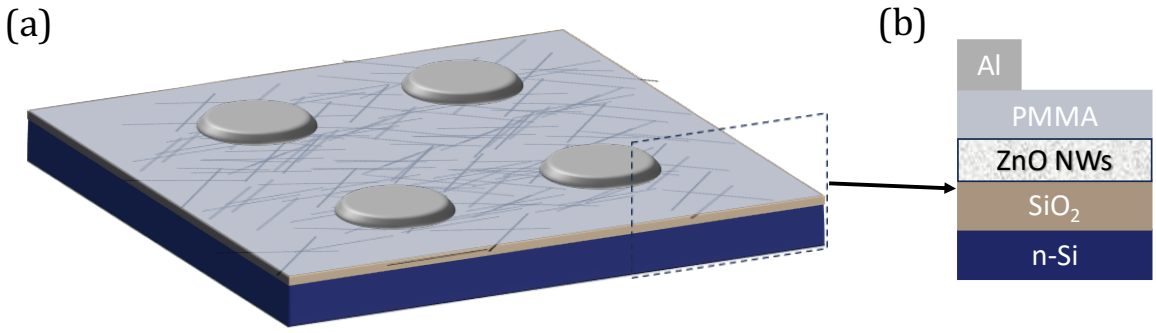

Figure 8-3: (a) The MIS capacitor formation of $D_{NW,025}$, $D_{NW,0.5}$, and $D_{NW,1.0}$, (b) cross-section of ZnO nanowire embedded the MIS capacitors.

The UV PD and memory functionalities of the MIS capacitors ($D_{NW,025}$, $D_{NW,0.5}$, and $D_{NW,1.0}$) will be tested under certain amount of force applied on the one of the tops Al electrodes illustrated in Figure 8-3(a). Varied ratios of ZnO nanowires ($D_{NW,0.25}$, $D_{NW,0.5}$ and $D_{NW,1.0}$) are embedded between two insulating layers, as illustrated in Figure 8-3(b). These varying nanowire concentrations aim to demonstrate how each functionality responds under applied pressure. In the following sections, the non-volatile memory performance of the MIS capacitors will be evaluated under three different pressure ranges. Afterward, we will test the pressure sensitivity of the capacitors under UV on/off conditions, followed by an examination of UV PD performance during pressure loading and unloading cycles. This will demonstrate how each capacitor is individually sensitive to memory and UV detection under different conditions.

8.3.1 Non-volatile Memory Under Loading

This section aims to demonstrate that the memory functionality of the MIS devices remains reliable even when subjected to various applied pressures in parallel. To illustrate the versatility of our device prototype, we have chosen a composition of $D_{NW,1.0}$ for this section, as it demonstrated superior performance. By evaluating the devices' memory window stability under mechanical stress, we can confirm their potential for multifunctional applications, where they can serve as both tactile pressure sensors and memory devices within electronic circuits.

The test conditions involved applying specific amounts of pressure to the gate electrode and conducting ten double-sweep C-V measurements at 100 kHz to ensure device stabilisation for each specific pressure loading by the test rig. The final figure presents data from the last cycle of these ten cycles. The V_{FB} was determined using the $1/C^2$ method. All testing setups and measurement techniques are detailed in Chapter 3, providing a comprehensive overview of the experimental procedures.

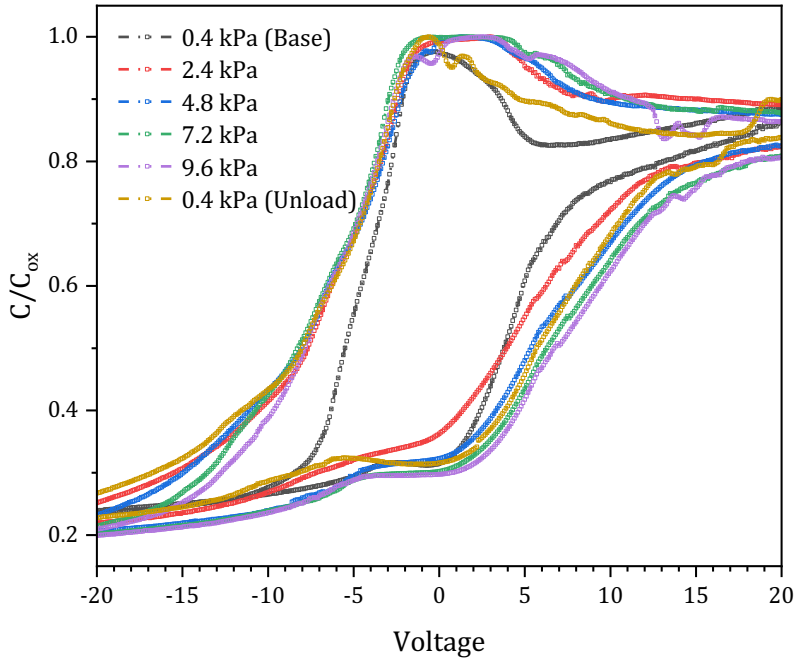

Figure 8-4: C-V characteristics normalised to maximum capacitance (C/C_{ox}) for $D_{NW.1.0}$ MIS devices under different applied pressures: 0.4 kPa (Base), 2.4 kPa, 4.8 kPa, 7.2 kPa, 9.6 kPa, and 0.4 kPa (Unload).

Figure 8-4 shows the normalised C-V curves for the MIS devices under different pressures: 400 Pa (Base), 2.4 kPa, 4.8 kPa, 7.2 kPa, 9.6 kPa, and 400 Pa (Unload). As the applied pressure increases, the C-V curves shift, reflecting changes in the memory window. Despite these shifts, the

device consistently exhibits a distinct and measurable memory window, underscoring its reliability in memory storage even under mechanical stress. The ΔV_{FB} is enlarging with the magnitude of the pressure applied. However, the increment in the ΔV_{FB} may not only be linked with the magnitude of the pressure.

Table 8-3 quantifies these observations, detailing the memory window (ΔV_{FB}), differential capacitance (ΔC), and charge density (ρ) for each pressure condition. At a base pressure of 100 Pa, the device has a memory window of 9.75 V, a capacitance changes of 31.57 pF, and a charge density of $1.09 \times 10^{11} cm^{-2}$. As pressure increases to 9.6 kPa, the memory window expands to 16.55 V, with corresponding increases in capacitance change and charge density. Notably, when the pressure is reduced to 400 Pa (Unload), the memory window remains substantial at 13.35 V, demonstrating the device's resilience and stable performance.

Figure 8-4 and accompanying *Table 8-3* present the memory window characteristics of 1.00 wt.% ZnO nanowire embedded MIS devices subjected to various pressures. The primary objective is to demonstrate that the device retains a stable and reliable memory window even when pressure is applied, thereby confirming its dual functionality as both a tactile pressure sensor and a memory device.

Table 8-3: Summary of the memory window (ΔV_{FB}), differential capacitance (ΔC), and charge density (ρ) for $D_{NW.1.0}$ MIS devices under different applied pressures.

Loading	Memory Window $\Delta V_{FB}(V)$	ΔC (pF)	ρ ($\times 10^{11} cm^{-2}$)
400 Pa (Base)	9.75	31.57	1.09
2.4 kPa	11.90	46.03	1.91
4.8 kPa	15.30	47.95	2.57
7.2 kPa	16.25	50.05	2.84
9.6 kPa	16.55	51.03	2.95
400 Pa (Unload)	13.35	43.71	2.05

Each cycle of the run can also attribute the larger window, as discussed in Chapter 7, because the repeated C-V test cycles have run under each step of gradually increased pressure loading listed in *Table 8-3*,. Therefore, the increment in the ΔV_{FB} from 9.75 V to 16.55 V because of the consequence of repeated C-V tests and pressure may be the result of both repeated C-V tests and applied pressure altogether. Because the sharp decrease in the ΔV_{FB} from 16.55 V to 13.35 V after

unloading from 9.6 kPa to 400 Pa of the MIS device is clear evidence that the unloading pressure direct link for a sharp decrease in ΔV_{FB} shifts.

These results highlight the robustness of the ZnO nanowire-embedded MIS devices, which maintain functional integrity as memory devices while also acting as sensitive pressure sensors. This dual functionality makes them highly suitable for applications in advanced electronic circuits where both memory storage and pressure sensing are required. The consistent performance under varying pressures confirms the potential of these devices for multifunctional use, offering a reliable solution for integrating tactile sensing and memory capabilities in a single electronic node.

8.3.2 Pressure/Tactile Testing Under UV On/Off

The objective of this section is to demonstrate the detection of pressure sensitivity in the MIS devices when exposed to periodic UV light. In order to enhance the multifunctional capability of the MIS devices to detect both pressure and UV exposure, the pressure sensitivity of the devices will be tested under periodic UV exposure. Thus, the goal is to differentiate pressure signals under UV exposure.

Figure 8-5 (a-c) demonstrates the behaviour of MIS capacitors, each embedded with different concentrations of ZnO nanowires ($D_{NW,0.25}$, $D_{NW,0.5}$ and $D_{NW,1.0}$) when subjected to 9.6 kPa pressure and alternating 600-second cycles of UV light and darkness. The experimental setup consistently applied 9.6 kPa pressure with a 15-second load-unload cycle frequency and alternating 600-second periods of UV exposure and darkness. Capacitance was continuously recorded to analyze the devices' dynamic response to the combined stimuli, thereby evaluating their multifunctional capabilities.

(a)

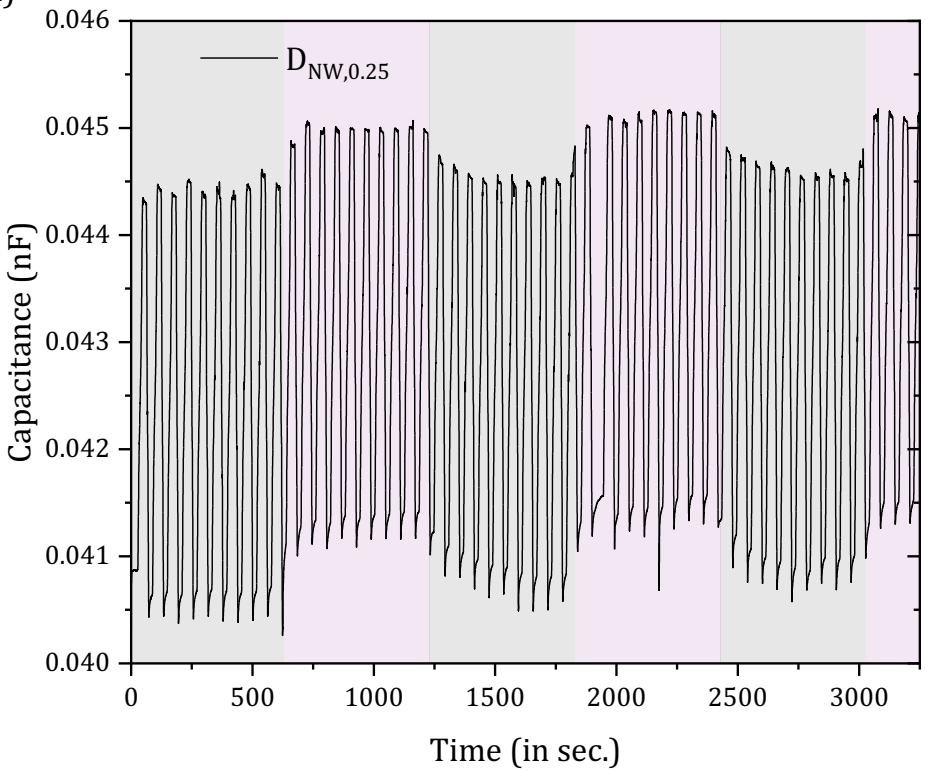
D NW,0.25
Capacitance (nF)
0.046
0.045
0.044
0.043
0.042
0.041
0.040
0
500
1000
1500
2000
2500
3000
Time (in sec.)

(b)

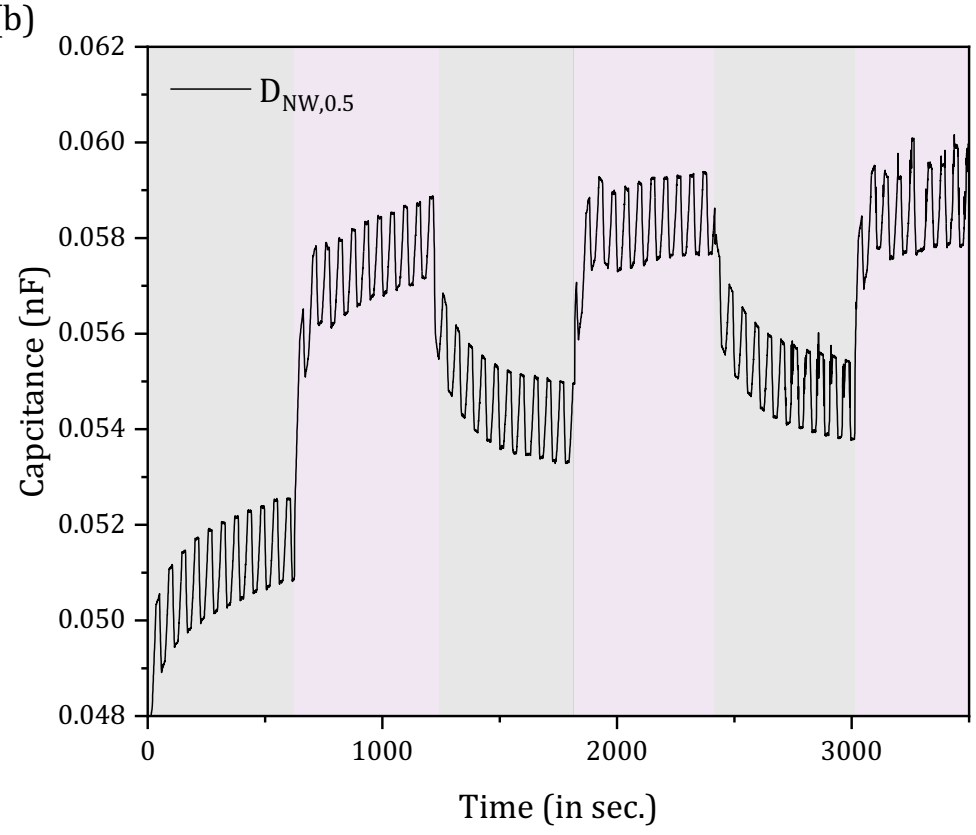
D NW,0.5
Capcitance (nF)
0.062
0.060
0.058
0.056
0.054
0.052
0.050
0.048
0
1000
2000
3000
Time (in sec.)

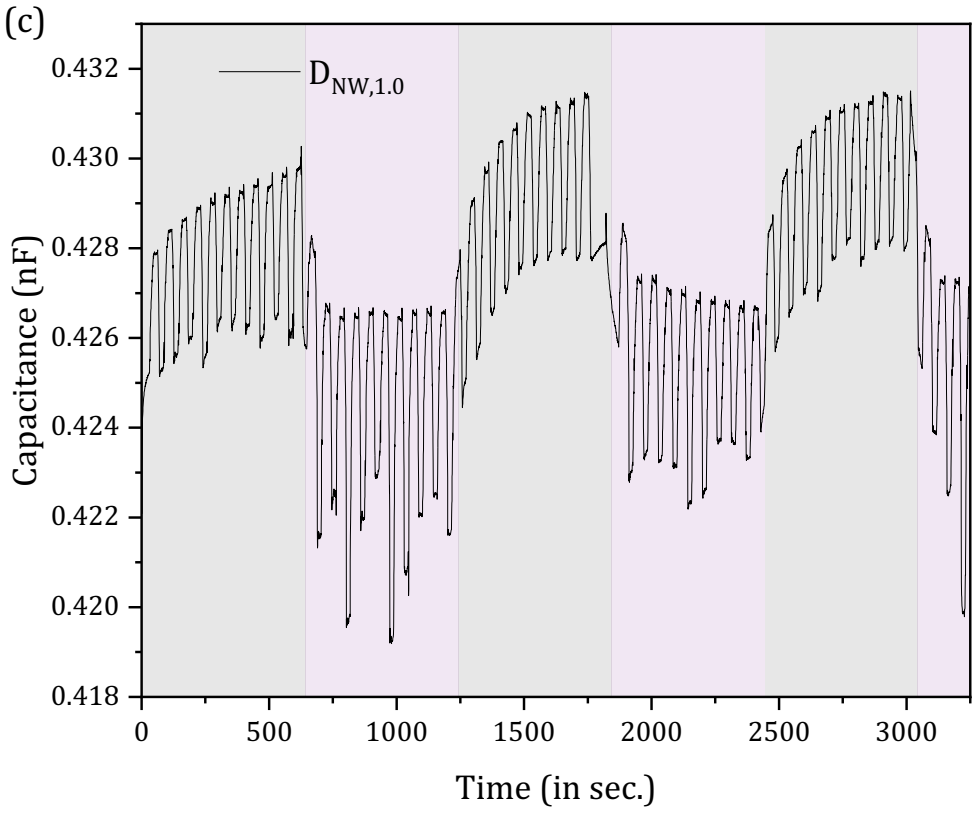

Figure 8-5: Capacitance response of MIS capacitors embedded with different concentrations of ZnO nanowires under combined 9.6 kPa pressure and alternating UV light exposure. (a) $D_{NW.0.25}$, (b) $D_{NW.0.5}$, and (c) $D_{NW.1.0}$. The devices were subjected to 600-second UV on/off cycles of, with 30-second ~8 kPa loading/ unloading intervals.

In Figure 8-5(a) for the $D_{NW,0.25}$ MIS capacitor, the capacitance fluctuates between approximately 0.041 nF and 0.045 nF as a result of applied combination of UV-exposure and pressure. A noticeable pattern of capacitance change corresponds to the UV light and dark cycles, indicating the device's sensitivity to light exposure. The pressure response is evident from the periodic variations within each light/dark cycle, although the changes are relatively moderate. This suggests that while the device is responsive to UV light and pressure, the sensitivity at this concentration is somewhat limited.

For the $D_{NW,0.5}$ MIS capacitor, the capacitance ranges from about 0.048 nF to 0.062 nF (Figure 8-5(b)). The device shows an apparent step-wise increase in capacitance during UV exposure and a corresponding decrease during darkness. Pressure sensitivity is obvious, with sharp fluctuations superimposed on the UV response pattern, demonstrating higher sensitivity compared to the $D_{NW,0.25}$ sample in the case of UV photosensitivity. This indicates that increasing

the nanowire concentration enhances the device's responsiveness to both stimuli, making it more suitable for applications requiring higher sensitivity.

Figure 8-5(c) for the $D_{NW,1.0}$ ZnO nanowire MIS capacitor shows capacitance variations between approximately 0.418 nF and 0.432 nF. This device exhibits a pronounced increase in capacitance during UV exposure and a decrease during dark periods. The response to pressure is significant, with large oscillations indicative of the highest sensitivity among the three samples. This level of sensitivity suggests that the device can effectively function as both a highly sensitive pressure sensor and a UV light detector, making it ideal for multifunctional applications.

The study shows that MIS capacitors respond to pressure under UV light stimuli, with sensitivity varying based on the concentration of ZnO nanowires. The $D_{NW,0.25}$ sample is moderately sensitive, while the $D_{NW,0.5}$ sample is more sensitive, exhibiting apparent changes in capacitance. The $D_{NW,1.0}$ sample is the most sensitive, showing substantial changes in response to both stimuli. These findings indicate that higher concentrations of ZnO nanowires enhance sensitivity, making these capacitors suitable for multifunctionally detecting environmental changes in optoelectronics and pressure sensing. The devices' consistent response under alternating conditions highlights their robustness and versatility. In summary, ZnO nanowire-embedded MIS capacitors are promising multifunctional devices due to their adjustable sensitivity and reliable performance under dual stimuli.

8.3.3 UV Photodetection Under Loading/Unloading Pressure

In the previous section, we tested how sensitive MIS devices are to pressure when exposed to UV light. Now, we aim to evaluate the UV detection capability of these MIS devices when subjected to a periodic pressure of 9.6 kPa. Specifically, we will investigate the devices' response to alternating short bursts of UV light and sustained periods of high pressure. This contrasts with the previous tests, where we used prolonged UV exposure.

In this experiment, the devices experienced a pressure of 9.6 kPa applied in cycles of 600 seconds, where the pressure was loaded and then unloaded. During this time, UV light was switched on and off every 30 seconds. Capacitance readings were taken continuously to monitor the devices' real-time reaction to these dual stimuli, as detailed in 3.4.3. This testing setup helped us evaluate how sensitive the devices are rapid changes in UV exposure while under constant pressure.

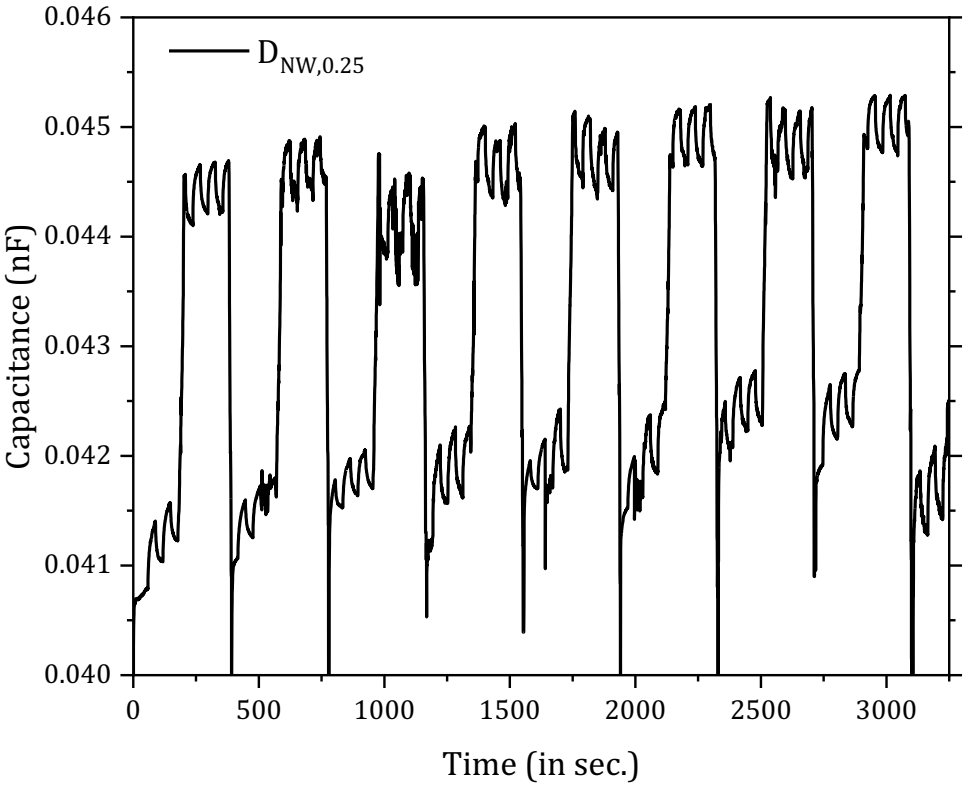
D NW,0.25
Capacitance (nF)
0.046
0.045
0.044
0.043
0.042
0.041
0.040
0
500
1000
1500
2000
2500
3000
Time (in sec.)

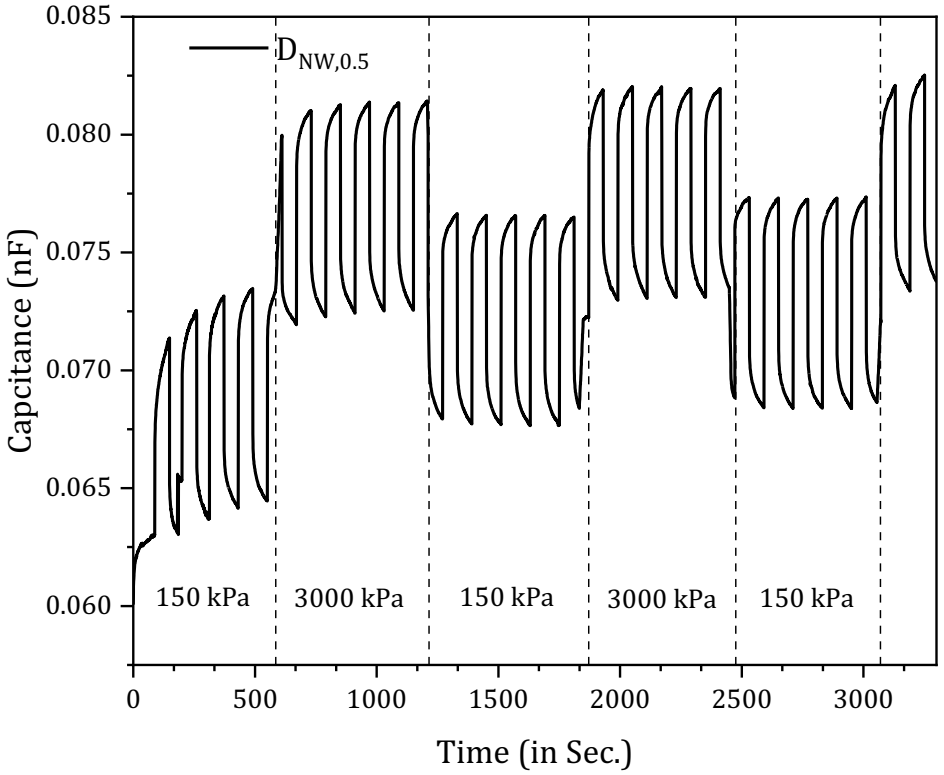
D NW,0.5
Capcitance (nF)
0.085
0.080
0.075
0.070
0.065
0.060
150 kPa
3000 kPa
150 kPa
3000 kPa
150 kPa
0
500
1000
1500
2000
2500
3000
Time (in Sec.)

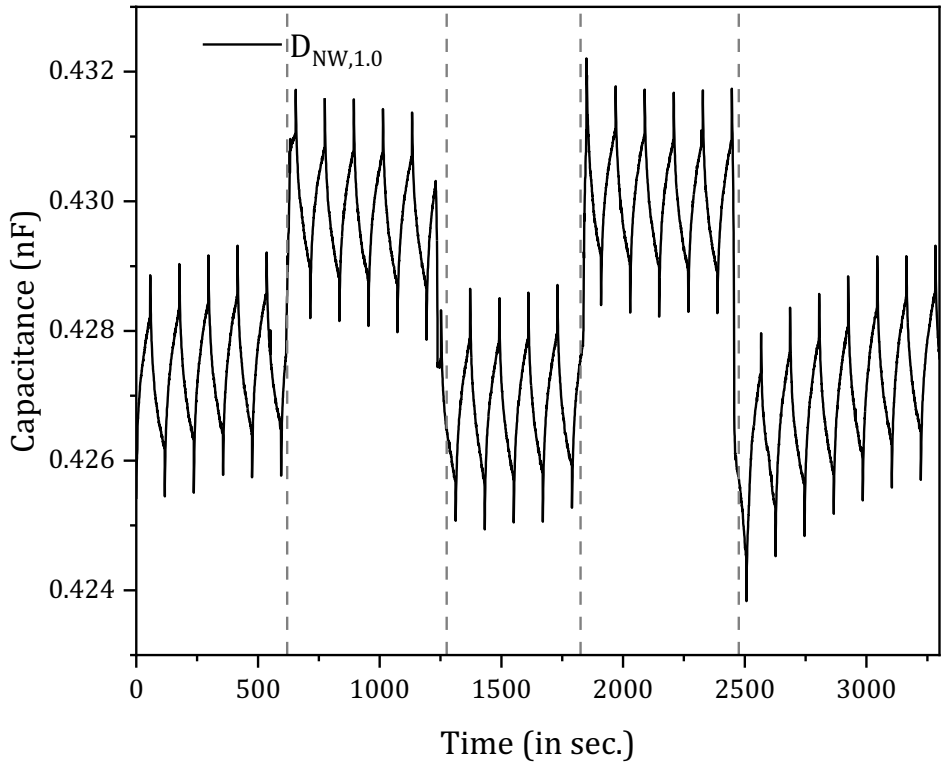

Figure 8-6: Capacitance response of MIS capacitors embedded with different concentrations of ZnO nanowires under combined ~8 kPa pressure and alternating UV light exposure. (a) $D_{NW,0.25}$, (b) $D_{NW,0.5}$, and (c) $D_{NW,1.0}$. The devices were subjected to 600-second loading and unloading cycles of pressure, with 30-second on/off UV light intervals.

In Figure 8-6(a), the capacitance of $D_{NW,0.25}$ MIS Capacitor fluctuates between approximately 0.041 nF and 0.045 nF, which was similar as presented in Figure 8-5. The response to UV light is relatively subdued, with minor variations in capacitance during the 30-second on/off cycles. The pressure sensitivity is evident, as shown by the periodic variations in capacitance corresponding to the 600-second loading and unloading cycles. Overall, the device demonstrates lower UV sensitivity while maintaining clear pressure responsiveness. This result is consistent with Figure 8-5(a).

Figure 8-6(b) shows the C-t result of the $D_{NW,0.5}$ MIS Capacitor. The capacitance ranges from about 0.048 nF to 0.062 nF. The device exhibits a noticeable stepwise increase in capacitance during UV exposure and a decrease when the UV light is turned off. Pressure sensitivity is marked by sharp fluctuations superimposed on the UV response pattern. This sample shows a higher UV sensitivity

than the $D_{NW,0.25}$ sample, indicating that increasing the nanowire concentration enhances responsiveness to UV light.

Figure 8-6(c) shows C-t result of the $D_{NW,1.0}$ MIS Capacitor. The capacitance varies between approximately 0.418 nF and 0.432 nF. The device demonstrates a pronounced increase in capacitance during UV exposure and a decrease during dark periods. The response to pressure is significant, with large oscillations indicating high sensitivity. This sample shows the highest sensitivity to both UV light and pressure among the three samples, consistent with previous findings.

The results confirm that all MIS capacitors are sensitive to UV light under pressure, indicating that the external load does not affect the UV detection ability of the MIS devices. Due to low percolation regime of ZnO nanowires, the sample with $D_{NW,0.25}$ device show lower UV light sensitivity but still respond clearly to pressure. As the concentration of ZnO nanowires increases to $D_{NW,0.5}$ and $D_{NW,1.0}$, the devices become more sensitive to UV light. The $D_{NW,1.0}$ sample exhibits the highest overall sensitivity. These findings are consistent with previous results, supporting the conclusion that higher concentrations of ZnO nanowires enhance the multifunctional capabilities of MIS capacitors. These results clearly show that the prototype can perform UV detection and pressure sensing in parallel, making it a promising multifunctional device prototype.

The multifunctional capabilities of ZnO nanowire-embedded MIS capacitors, demonstrated here for UV photodetection and pressure sensing, are highly promising for the simultaneous use of the device for both functionalities. While ZnO nanowires have been explored in the literature for individual applications, such as UV detection [10, 47, 176, 241] and pressure sensing [242], this work uniquely combines both functionalities within a single MIS device. Furthermore, the ability to tune the sensitivity through nanowire concentration provides a significant advantage over existing technologies. The $D_{NW,1.0}$ exhibited the highest sensitivity, aligning with previous studies suggesting that higher nanowire densities improve device performance [9, 243]. This work also expands on the scalability and low-cost fabrication techniques (drop-casting), which are rarely discussed in the context of multifunctional devices in the literature [179, 243].

8.4 The Multifunctional Device Prototype

The comprehensive evaluation of MIS devices embedded with varying concentrations of ZnO nanowires has demonstrated their remarkable and unique multifunctional capabilities. These devices have shown high responsiveness to UV light, highlighting their potential for optoelectronic applications, which aligns with previous studies that have explored ZnO nanowires for similar purposes [9, 10, 23, 24, 47, 211, 244]. In addition, MIS devices with 0.50 wt.% and 1.00

wt.% ZnO nanowire concentrations exhibit non-volatile memory behaviour, while all devices effectively perform capacitive pressure sensing. Notably, there is no existing example in the literature of MIS devices capable of simultaneously achieving UV detection, pressure sensing, and memory functionality in a single configuration, making this work a significant contribution to the field.

The interaction between these functionalities was also analysed, revealing that memory behaviour improves under applied pressure, without affecting the devices' performance as memory devices. This simultaneous functionality of memory and pressure sensing has rarely been reported in ZnO-based MIS devices, further emphasising the novelty of this study. The devices responded reliably to both UV light and pressure stimuli, with pressure-sensing capability remaining stable even during alternating UV exposure, and UV detection unaffected by applied pressure.

These findings emphasise the novelty, robustness, and multifunctionality of ZnO nanowire-embedded MIS devices, capable of operating as memory devices, pressure sensors, and UV detectors concurrently—a remarkable achievement. Their consistent performance under diverse conditions, a feature not extensively documented in prior studies, positions them as strong candidates for integrated circuit applications. These multifunctional devices can respond to multiple environmental stimuli without compromising any individual functionality, offering new possibilities for integrated sensing and memory applications.

Chapter 9

CONCLUSION AND FUTURE WORKS

9.1 Conclusion

The main goal of this thesis was to address a fundamental gap in the literature: understanding charge transport mechanisms in random semiconductor nanowire networks to develop large-area, commercially applicable, and multifunctional devices. ZnO nanowires, with their unique properties and potential for scalability, were identified as ideal candidates for this purpose. However, challenges related to the random nature of nanowire networks and the difficulty in achieving consistent performance across large areas have hindered their commercial viability. This research sought to overcome these challenges by investigating the behaviour of ZnO nanowire networks, focusing on their application in UV-PDs, pressure sensors, and non-volatile memory devices.

The thesis is structured around four core result chapters, each addressing different aspects of the problem. Through the integration of percolation theory, Monte Carlo simulations, experimental analysis, and device fabrication, this research provides a comprehensive approach to understanding and optimizing the performance of random ZnO nanowire networks for practical device applications.

9.1.1 Application of Percolation Theory to Random Nanowire Networks

In Chapter 4, percolation theory was applied to investigate the behaviour of random ZnO nanowire networks in finite system size analysis by Monte Carlo simulations. The shortest-path algorithm was chosen for its computational efficiency over traditional methods, such as the weighted Union-Find algorithm. The results demonstrated that this approach was not only faster but also more reliable in predicting the percolation threshold in parallel with the current literature, which is a critical factor in understanding the connectivity and charge transport mechanisms in random networks. The percolation threshold obtained was consistent with the values reported in existing literature, validating the model's applicability.

This chapter established the foundation for later analyses by confirming that the shortest-path algorithm is suitable for percolation studies of random nanowire networks. It also set the stage for the charge transport analysis in the subsequent chapter by demonstrating that the method

could be applied to model real-world devices. This work contributes to addressing a significant gap in the literature: the need for efficient and reliable models to study the large-scale behaviour of random nanowire networks, a necessary step toward making such devices commercially viable.

9.1.2 Conductivity Analysis and Correlation with Simulations

Building on the findings from Chapter 4, Chapter 5 focused on the conductivity behaviour of random ZnO nanowire networks in different intake and scale with respect to electrode size. Simulations using LTspice were conducted to model the charge transport mechanisms within these networks, and the results were compared with experimental data obtained from ZnO nanowires drop-cast on variable gap microelectrode arrays. The correlation between the simulations and the experimental results was strong, indicating that the shortest-path algorithm used for percolation studies in the previous chapter was also effective for modelling charge transport in these networks.

A key finding in this chapter was the discovery of a two-step, stair-like conductivity pattern at 10 V. While percolation theory provided a good baseline for understanding the overall connectivity in the network, it became clear that percolation alone could not fully explain the observed conductivity behaviour, particularly below the effective percolation threshold. Tunnelling conduction mechanism emerged as a dominant factor, where charge transport occurred through a single critical path in the network. This insight is critical for the design of efficient, large-area devices, as it highlights the importance of considering tunnelling effects when modelling and optimizing random nanowire networks.

Chapter 5 addressed the research question by providing a deeper understanding of charge transport mechanisms in random ZnO nanowire networks, which is essential for creating scalable, reliable devices. The findings demonstrated that the integration of percolation theory and tunnelling conduction models could lead to more accurate predictions of device performance, paving the way for practical applications.

9.1.3 UV Photodetection in MSM and MIS Devices

The first part of Chapter 6 focused on the performance of ZnO nanowire networks in UV-PDs on variable gap microelectrode arrays. The results showed that MSM devices exhibited the highest performance when the ZnO nanowire concentration was just below the percolation threshold. In this regime, tunnelling conductivity dominated before full percolation was reached, allowing for efficient charge transport and high UV sensitivity. The 4.00 wt.% ZnO nanowire sample, with a 50 μm electrode separation, demonstrated the best performance, achieving a sensitivity of 4.17×10^5

and a response time as fast as 0.25 seconds under UV exposure. This result highlights the critical role of nanowire concentration and electrode separation in optimizing device performance. The ability to achieve such fast response times and high sensitivity in a scalable, low-cost device configuration addresses the main research question by demonstrating the practical potential of ZnO nanowire networks for UV-PDs.

In contrast, the MIS devices exhibited a different behaviour, with the 1.00 wt.% ZnO nanowire sample showing the fastest response and decay times (1.25 sec and 0.5 sec, respectively). However, as the concentration of nanowires increased beyond 1.00 wt.%, signal instability occurred due to charge leakage. This finding suggests that while higher concentrations may enhance sensitivity, they also increase the risk of signal degradation, underscoring the need for careful optimization of nanowire density in MIS devices.

The results from this chapter provide a clear answer to the research question, demonstrating that both MSM and MIS devices can achieve high performance when nanowire concentration and electrode separation are optimized. The findings also offer new insights into the trade-offs between sensitivity and stability in these devices, which are critical for large-area, commercially viable applications.

9.1.4 Multifunctionality in ZnO Nanowire-Embedded MIS Devices

In Chapter 6, the UV photodetection capabilities of ZnO nanowire-embedded MIS devices were thoroughly explored. Building on these results, Chapter 7 focused on the multifunctionality of the same MIS device configuration, particularly investigating non-volatile memory behaviour and capacitive pressure sensing. Furthermore, this chapter examined the combined effects of UV exposure and applied pressure in sequence, to demonstrate the versatility of these multifunctional devices.

In Chapter 7, the study found that MIS devices with $D_{NW,0.5}$ and $D_{NW,01.0}$ ZnO nanowire concentrations exhibited reliable non-volatile memory performance. These results were consistent with other published work on ZnO nanostructured devices, indicating that the random ZnO nanowire networks investigated in this study provide comparable memory windows. Additionally, the memory performance remained stable even under applied pressure, highlighting the robustness of the devices in handling multiple environmental stimuli without compromising their memory functionality.

When sequences of UV exposure and pressure were applied to the devices, the results revealed different sensitivities based on nanowire concentration. Devices with lower nanowire intake demonstrated higher sensitivity to pressure but reduced sensitivity to UV exposure, whereas the

$D_{NW,1.0}$ was more responsive to UV light while being less sensitive to pressure. This finding underscores the flexibility of ZnO nanowire-embedded MIS devices, where adjustments in nanowire concentration can optimize performance depending on the specific application, whether for pressure sensing or UV detection.

Furthermore, the devices successfully performed memory storage and pressure sensing simultaneously without any degradation in performance. In fact, memory behaviour improved under applied pressure, revealing the synergistic relationship between these functionalities. This multifaceted performance demonstrates the robustness and adaptability of ZnO nanowire-embedded MIS devices for multifunctional applications.

Overall, the results of Chapter 8 demonstrate the versatility of these devices in performing UV detection, pressure sensing, and non-volatile memory storage in a single configuration. No previous example of devices capable of integrating these functions exists in the literature, marking this work as a significant contribution to the field. These findings present new opportunities for the development of integrated electronic systems, particularly in areas such as wearable electronics, environmental monitoring, and smart sensor networks, where multifunctionality and device stability are critical.

9.2 Contextualisation and Contribution to the Knowledge

This thesis significantly contributes to the understanding of charge transport in random ZnO nanowire networks, addressing the control of randomness in semiconductor nanowire networks and their potential application in nanoelectronics. Integrating percolation theory, tunnelling conduction models, and experimental validation has resulted in a comprehensive framework for designing and optimizing large-area, multifunctional devices. The findings have important implications for the development of low-cost, high-performance devices capable of UV detection, pressure sensing, and memory storage.

Demonstrating that ZnO nanowire-based devices can be scaled for large-area applications while maintaining high sensitivity and multifunctionality promises the way for the commercial deployment of these technologies. The novelty gained from this research offers new opportunities for the development of integrated electronic systems that can perform multiple tasks simultaneously, addressing the growing demand for versatile, high-performance devices as Moore's Law reaches its limits. The main contributions are listed below.

- The Shortest-Path algorithm has been demonstrated to provide the same universality function as the extensively studied Union-Find algorithm in the literature. This establishes

the algorithm as a faster and more computationally efficient method for analysing percolation in anisotropic systems of random sticks.

- A robust and comprehensive example of conductivity analysis in random semiconductor networks, derived from a universalized random stick model based on Percolation Theory, has been presented. This approach offers a clear and systematic framework for achieving more detailed and reliable comparative results.
- The UV-PD mechanism in random ZnO nanowire networks has been directly correlated with Percolation Theory. This work bridges the theoretical and experimental gaps, establishing a coherent link between the two and advancing the understanding of charge transport in random nanostructured networks.
- While various studies explore the multifunctionality of devices, no clear evidence exists in the literature of a single device simultaneously performing multiple functions. This thesis introduces a novel and challenging example of a multifunctional device prototype that successfully integrates non-volatile memory, UV photodetection, and pressure sensing within a single platform. This achievement highlights the potential for advancing integrated and multifunctional device technologies.

9.3 Future Works

While the aim of this thesis was to develop a device prototype using silicon-based electronic technology, the findings have revealed a significant potential for applying the percolation theory of semiconductor nanowires in flexible MOS transistor applications. This opens new avenues for further research, particularly in the field of flexible electronics, where the integration of random semiconductor nanowire networks could address some of the limitations of current technologies.

First, organic electronics, a popular option for flexible devices, often suffer from lower charge carrier mobility, leading to reduced efficiency compared to traditional inorganic MOS transistors. However, incorporating random semiconductor nanowire networks into MOS transistors offers the promise of higher charge transport and improved efficiency in flexible electronics. The multifunctional nature of semiconductor nanowires—stemming from their electronic, optical, and mechanical properties—makes them particularly suited for developing flexible, multifunctional MOS transistors.

Second, blending inorganic nanomaterials with polymers in these devices could enhance their performance by providing a high dielectric constant, a feature that is particularly beneficial for device miniaturization and stabilization. This approach could overcome many of the limitations in flexible electronics, enabling more efficient and compact devices.

Third, this prototype has demonstrated its potential for scalability and adaptability for large-area production using printing techniques. The findings provide a strong basis for developing large-area applications directly onto chips through printing technology. This methodology allows for seamless integration into the Internet of Things (IoT) platforms, particularly for health monitoring systems. Such integration could enable real-time data collection and analysis, offering a pathway for advanced wearable electronics and smart health monitoring devices.

Finally, the large-area producibility of these nanowire-based prototypes makes them highly commercially applicable to various fields, including wearable electronics, flexible sensors, and other next-generation technologies. The scalability and versatility of this approach provide a promising platform for future device development.

Given the potential of this research direction, it represents an exciting opportunity with a high likelihood of attracting funding. After graduation, I plan to focus on exploring these applications further, aiming to push the boundaries of flexible MOS transistor technology by leveraging the advantages of random semiconductor nanowire networks and their integration into IoT-enabled systems for health and environmental monitoring.

References

1. Das, U.K., et al., *Limitations on Lateral Nanowire Scaling Beyond 7-nm Node.* IEEE Electron Device Letters, 2017. **38**(1): p. 9-11.

2. IEEE, *INTERNATIONAL ROADMAP FOR DEVICES AND SYSTEMS: More Moore*. 2022, IEEE.

3. Sanjay, V. Kumar, and A. Vohra, *Triple-metal gate work function engineering to improve the performance of junctionless cylindrical gate-all-around Si nanowire MOSFETs for the upcoming sub-3-nm technology node.* Journal of Computational Electronics, 2024. **23**(2): p. 267-278.

4. Puers, R., et al., *Nanoelectronics: Materials, Devices, Applications, 2 Volumes*. 2017: John Wiley & Sons.

5. Lieber, C.M., Z.L. Wang, and G. Editors, *Functional Nanowires.* MRS Bulletin, 2011. **32**: p. 99-108.

6. Heo, Y.W., et al., *ZnO nanowire growth and devices.* Materials Science and Engineering: R: Reports, 2004. **47**(1-2): p. 1-47.

7. Özgür, U., et al., *A comprehensive review of ZnO materials and devices.* Journal of Applied Physics, 2005. **98**(041301).

8. Janotti, A. and C.G. Van de Walle, *Fundamentals of zinc oxide as a semiconductor.* Reports on Progress in Physics, 2009. **72**(12).

9. Gedamu, D., et al., *Rapid fabrication technique for interpenetrated ZnO nanotetrapod networks for fast UV sensors.* Adv Mater, 2014. **26**(10): p. 1541-50.

10. Ilickas, M., et al., *ZnO tetrapod morphology influence on UV sensing properties.* Nanotechnology, 2024. **35**(1): p. 015502.

11. Vanheusden, K., et al., *Correlation between photoluminescence and oxygen vacancies in ZnO phosphors.* Applied Physics Letters, 1996. **68**(3): p. 403-405.

12. Sekar, K., et al., *Control of ZnO nanowires growth in flexible perovskite solar cells: A mini-review.* Heliyon, 2024. **10**(3).

13. Lin, P., et al., *Self-Powered UV Photosensor Based on PEDOT:PSS/ZnO Micro/Nanowire with Strain-Modulated Photoresponse.* ACS Applied Materials & Interfaces, 2013. **5**(9): p. 3671-3676.

14. Zhang, Y., Y. Liu, and Z.L. Wang, *Fundamental theory of piezotronics.* Adv Mater, 2011. **23**(27): p. 3004-13.

15. Zhang, Y., Y. Yang, and Z.L. Wang, *Piezo-phototronics effect on nano/microwire solar cells.* Energy & Environmental Science, 2012. **5**(5).

16. Asture, A., et al., *Investigation of properties and applications of ZnO polymer nanocomposites.* Polymer Bulletin, 2023. **80**(4): p. 3507-3545.

17. Kolmakov, A. and M. Moskovits, *Chemical Sensing and Catalysis by One-Dimensional Metal-Oxide Nanostructures.* Annual Review of Materials Research, 2004. **34**(1): p. 151-180.

18. Pan, C., et al., *High-resolution electroluminescent imaging of pressure distribution using a piezoelectric nanowire LED array.* Nature Photonics, 2013. **7**(9): p. 752-758.

19. Dikici, T. and S. Demirci, *Influence of thermal oxidation temperature on the microstructure and photoelectrochemical properties of ZnO nanostructures fabricated on the zinc scraps.* Journal of Alloys and Compounds, 2019. **779**: p. 752-761.

20. Wang, Z.L., *Piezopotential gated nanowire devices: Piezotronics and piezo-phototronics.* Nano Today, 2010. **5**(6): p. 540-552.

21. Wu, W. and Z.L. Wang, *Piezotronic nanowire-based resistive switches as programmable electromechanical memories.* Nano Lett, 2011. **11**(7): p. 2779-85.

22. Wang, Z.L. and J. Song, *Piezoelectric nanogenerators based on zinc oxide nanowire arrays.* Science, 2006. **312**(5771): p. 242-246.

23. Law, J.B.K. and J.T.L. Thonga, *Simple fabrication of a ZnO nanowire photodetector with a fast photoresponse time.* APPLIED PHYSICS LETTERS, 2006. **88**(133114).

24. Jin, Z.W., et al., *Graphdiyne:ZnO Nanocomposites for High-Performance UV Photodetectors.* Advanced Materials, 2016. **28**(19): p. 3697-3702.

25. Menzel, A., et al., *Multifunctional ZnO ‐nanowire ‐based sensor.* Advanced Functional Materials, 2011. **21**(22): p. 4342-4348.

26. Pan, Z.W., Z.R. Dai, and Z.L. Wang, *Nanobelts of semiconducting oxides.* Science, 2001. **291**(5510): p. 1947-1949.

27. Wang, N., Y. Cai, and R.Q. Zhang, *Growth of nanowires.* Materials Science and Engineering: R: Reports, 2008. **60**(1): p. 1-51.

28. Alejandro, G.G., *On the growth of zinc oxide nanowires towards photoelectrochemical applications*, in *Department of Engineering Faculty of Science*. September 2020, Durham University: Durham E-thesis.

29. Chandramohan, A., *Fabrication of semiconductor nanowire multifunctional devices*, in *Department of Engineering and Computing Sciences*. September 2023, Durham University: Durham E-thesis.

30. Seager, C.H. and G.E. Pike, *Percolation and conductivity: A computer study. II.* Physical Review B, 1974. **10**(4): p. 1435-1446.

31. Legallais, M., et al., *Role played by the nanowire/nanowire junctions in the electrical properties of semiconductor percolating silicon nanowire networks.* Journal of Applied Physics, 2020. **128**(20).

32. Stauffer, D. and A. Aharony, *Introduction To Percolation Theory: Second Edition (2nd ed.). Taylor & Francis.*, ed. T. Francis. 1992.

33. Balberg, I. and N. Binenbaum, *Computer study of the percolation threshold in a two-dimensional anisotropic system of conducting sticks.* PHYSICAI. REVIEW B, 1983. **28**(7): p. 3799-3812.

34. Li, J. and S.L. Zhang, *Finite-size scaling in stick percolation.* Phys Rev E Stat Nonlin Soft Matter Phys, 2009. **80**(4 Pt 1): p. 040104.

35. Marianna Ambrico, P.F.A.a.R.d.M., *Electrical transport Features of SiNWs Random Network on Si Support After Covalent Attachment of New Organic Functionalities.* Nanomaterials and Nanotechnology, 2012. **2**(2).

36. Grimaldi, C., *Theory of percolation and tunneling regimes in nanogranular metal films.* Physical Review B, 2014. **89**(21).

37. Mukherjee, R., Z.-F. Huang, and B. Nadgorny, *Multiple percolation tunneling staircase in metal-semiconductor nanoparticle composites.* Applied Physics Letters, 2014. **105**(17).

38. She, M., et al., *JVD silicon nitride as tunnel dielectric in p-channel flash memory.* IEEE Electron Device Letters, 2002. **23**(2): p. 91-93.

39. Lee, C.-H., K.-C. Park, and K. Kim, *Charge-trapping memory cell of SiO2/ SiN/ high‐k dielectric Al2O3 with TaN metal gate for suppressing backward-tunneling effect.* Applied Physics Letters, 2005. **87**(7).

40. Ma, T. and J.-P. Han, *Why is nonvolatile ferroelectric memory field-effect transistor still elusive?* IEEE Electron Device Letters, 2002. **23**(7): p. 386-388.

41. Zhang, G., et al., *Spatial distribution of charge traps in a SONOS-type Flash memory using a high-$ k $ trapping layer.* IEEE transactions on electron devices, 2007. **54**(12): p. 3317-3324.

42. Zhao, C., et al., *Review on Non-Volatile Memory with High-k Dielectrics: Flash for Generation Beyond 32 nm.* Materials (Basel), 2014. **7**(7): p. 5117-5145.

43. Nayfeh, A. and N. El-Atab, *Nanomaterials-Based Charge Trapping Memory Devices*. 1 ed. 2020, San Diego: Elsevier.

44. Nayfeh, A. and N. El-Atab, *Overview of charge trapping memory devices—charge trapping layer engineering*, in *Nanomaterials-Based Charge Trapping Memory Devices*. 2020. p. 45-66.

45. El-Atab, N. and A. Nayfeh, *1D versus 3D quantum confinement in 1-5nm ZnO nanoparticle agglomerations for application in charge-trapping memory devices (vol 27, 275205, 2016).* Nanotechnology, 2016. **27**(41).

46. Xu, Q., et al., *Flexible Self-Powered ZnO Film UV Sensor with a High Response.* ACS Applied Materials & Interfaces, 2019. **11**(29): p. 26127-26133.

47. Yılmaz, M., et al., *Photodiode behavior and capacitive performance of ZnO nanoflakes synthesized by electrochemical deposition.* Journal of Physics D: Applied Physics, 2023. **56**(49).

48. Keem, K., et al., *Photocurrent in ZnO NWs grown on Au.* Applied Physics Letters, 2004. **54**(22).

49. Pallavolu, M.R., et al., *High-responsivity self-powered UV photodetector performance of pristine and V-doped ZnO nano-flowers.* Optics & Laser Technology, 2023. **157**.

50. Bayan, S. and D. Mohanta, *ZnO nanorod-based UV photodetection and the role of persistent photoconductivity.* Philosophical Magazine, 2012. **92**(32): p. 3909-3919.

51. Takei, K., et al., *Nanowire active-matrix circuitry for low-voltage macroscale artificial skin.* Nat Mater, 2010. **9**(10): p. 821-6.

52. Dempsey, S.J., M. Szablewski, and D. Atkinson, *Tactile sensing in human–computer interfaces: The inclusion of pressure sensitivity as a third dimension of user input.* Sensors and Actuators A: Physical, 2015. **232**: p. 229-250.

53. Pritchard, E., et al. *Flexible capacitive sensors for high resolution pressure measurement*. in *SENSORS, 2008 IEEE*. 2008.

54. Han, D., et al., *Fabrication and characteristics of ZnO MOS capacitors with high-K HfO 2 gate dielectrics.* Science China Technological Sciences, 2010. **53**: p. 2333-2336.

55. Keysigth, *B2902A Precision Source/Measure Unit*. BK Precise.

56. Precision, B. *BK Precision 894 LCR Meter*. Model 894; Available from: https://www.bkprecision.com/products/component-testers/894.

57. Whittaker, H., D. Zeze, and I. Amit, *A Nanomaterials-Based Electromechanical Characterisation Apparatus*. 2020, Department of Engineering: Durham University.

58. Canning, H., *Development of a highly responsive ultraviolet photodetector using random ZnO nanowire networks*. 2024, Department of Engineering: Durham University.

59. Keysigth. *16065A 200 Vdc External Voltage Bias Fixture*. Available from: https://www.keysight.com/gb/en/options/16065A/200-vdc-external-voltage-bias-fixture.html.

60. Systèmes, D., *Solidworks*, in *SP3*. 2022.

61. (n.d.), A. *Arduino Uno*. microcontroller 2022; Available from: https://www.arduino.cc.

62. Vyas, D.C., J.G. Patel, and M.H.A. Shah, *Microstepping of stepper motor and sources of errors in microstepping system.* International Journal of Engineering Research and General Science, 2015. **3**(2): p. 1375-1382.

63. Ward, A., *Development of Nanomaterials-Based Tactile Pressure Sensor*, D. University, Editor. 2021, Department of Engineering: Durham University.

64. Specialties, M., *FS20 Low Force Compression Load Cell*. RoHS.

65. Tullsen, D.M., S.J. Eggers, and H.M. Levy. *Simultaneous multithreading: Maximizing on-chip parallelism*. in *Proceedings of the 22nd annual international symposium on Computer architecture*. 1995.

66. Steiner, E.C. and J.M. Gilbert, *The acidities of weak acids in dimethyl sulfoxide. II. The Hammett acidity function.* Journal of the American Chemical Society, 1965. **87**(2): p. 382-384.

67. Parker, A., *The use of dipolar aprotic solvents in organic chemistry.* Advances in organic chemistry, 1965. **5**: p. 3.

68. Rodríguez-Gattorno, G., et al., *Novel synthesis pathway of ZnO nanoparticles from the spontaneous hydrolysis of zinc carboxylate salts.* The Journal of Physical Chemistry B, 2003. **107**(46): p. 12597-12604.

69. El-Atab, N., et al., *~3-nm ZnO Nanoislands Deposition and Application in Charge Trapping Memory Grown by Single ALD Step.* Scientific Reports, 2016. **6**.

70. Bhatt, V. and S. Chandra, *Silicon dioxide films by RF sputtering for microelectronic and MEMS applications.* Journal of micromechanics and microengineering, 2007. **17**(5): p. 1066.

71. Alba-Martin, M., et al., *Improved memory behaviour of single-walled carbon nanotubes charge storage nodes.* Journal of Physics D: Applied Physics, 2012. **45**(295401).

72. Kim, W.T., J.H. Jung, and T.W. Kim, *Carrier transport mechanisms in nonvolatile memory devices fabricated utilizing multiwalled carbon nanotubes embedded in a poly-4-vinyl-phenol layer.* Applied Physics Letters, 2009. **95**(2).

73. Wendt, H., et al., *Improvement of oxide quality by rapid thermal annealing.* Journal of Applied Physics, 1990. **67**(12): p. 7531-7535.

74. O'Sullivan, B.J., et al., *Si(100)–SiO2 interface properties following rapid thermal processing.* Journal of Applied Physics, 2001. **89**(7): p. 3811-3820.

75. Gao, P., et al., *Photoconducting response on bending of individual ZnO nanowires.* Journal of Materials Chemistry, 2009. **19**(7): p. 1002-1005.

76. Yuan, J., et al., *Concurrent Improvement of Photocarrier Separation and Extraction in ZnO Nanocrystal Ultraviolet Photodetectors.* Journal of Physical Chemistry C, 2019. **123**(23): p. 14766-14773.

77. Young, S.J., et al., *Erratum: ZnO-based MIS photodetectors.* Sens Actuators A Phys, 2008. **141**(1): p. 225-229.

78. Guo, L., et al., *Enhanced fluorescence detection of proteins using ZnO nanowires integrated inside microfluidic chips.* Biosensors and Bioelectronics, 2018. **99**: p. 368-374.

79. Chen, Z., et al., *Detection of exosomes by ZnO nanowires coated three-dimensional scaffold chip device.* Biosensors and Bioelectronics, 2018. **122**: p. 211-216.

80. Cheng, A.J., et al., *Recent Advances of Capacitive Sensors: Materials, Microstructure Designs, Applications, and Opportunities.* Advanced Materials Technologies, 2023. **8**(11).

81. Dahiya, R., et al., *Developing Electronic Skin with the Sense of Touch.* Information Display, 2015. **31**(4): p. 6-10.

82. Yang, Q., et al., *Enhancing light emission of ZnO microwire-based diodes by piezo-phototronic effect.* Nano Lett, 2011. **11**(9): p. 4012-7.

83. Guo, Z., et al., *Dynamic carrier transport modulation for constructing advanced devices with improved performance by piezotronic and piezo-phototronic effects: a brief review.* Semiconductor Science and Technology, 2017. **32**(8).

84. Lin, T., S. Ramadurgam, and C. Yang, *Design of Contact Electrodes for Semiconductor Nanowire Solar Energy Harvesting Devices.* Nano Lett, 2017. **17**(4): p. 2118-2125.

85. Chen, C.Q., et al., *Size dependence of Young's modulus in ZnO nanowires.* Phys Rev Lett, 2006. **96**(7): p. 075505.

86. Peić, A., et al., *Effect of AZO Substrates on Self-Seeded Electrochemical Growth of Vertically Aligned ZnO Nanorod Arrays and Their Optical Properties.* Journal of Nanomaterials, 2012. **2012**: p. 1-14.

87. Vissol-Gaudin, E.G.B., *Evolutionary computation based on nanocomposite training: application to data classification*, in *Advanced Materials, Electronics and Communications Research Challenge Department of Engineering*

Faculty of Science. March 2020, Durham University: Durham E-thesis.

88. Nizar, B.M., et al., *Highly C-oriented (002) plane ZnO nanowires synthesis.* RSC Adv, 2023. **13**(22): p. 15077-15085.

89. Herth, E., et al., *Modeling and characterization of piezoelectric beams based on an aluminum nitride thin ‐film layer.* physica status solidi (a), 2016. **213**(1): p. 114-121.

90. Herth, E., et al., *Thermal annealing of AlN films for piezoelectric applications.* Journal of Materials Science: Materials in Electronics, 2020. **31**(6): p. 4473-4478.

91. Ameh, E., *A review of basic crystallography and x-ray diffraction applications.* The international journal of advanced manufacturing technology, 2019. **105**(7): p. 3289-3302.

92. Diffract, P. and J.I. File, *Centre Diffract.* Data, PA, 2001: p. 19073-3273.

93. Hu, H., et al., *Hydrothermal synthesis of ZnO nanowires and nanobelts on a large scale.* Materials Chemistry and Physics, 2007. **106**(1): p. 58-62.

94. Alshehri, N.A., et al., *Investigation of the growth parameters of hydrothermal ZnO nanowires for scale up applications.* Journal of Saudi Chemical Society, 2018. **22**(5): p. 538-545.

95. Siegbahn, K., *Electron spectroscopy for atoms, molecules, and condensed matter.* Reviews of Modern Physics, 1982. **54**(3): p. 709.

96. Rumble Jr, J., D. Bickham, and C. Powell, *The NIST x ‐ray photoelectron spectroscopy database.* Surface and interface analysis, 1992. **19**(1 ‐ 12): p. 241-246.

97. Fadley, C., *Instrumentation for surface studies: XPS angular distributions.* Journal of Electron Spectroscopy and Related Phenomena, 1974. **5**.

98. Tanuma, S., C.J. Powell, and D.R. Penn, *Calculations of electron inelastic mean free paths. V. Data for 14 organic compounds over the 50–2000 eV range.* Surface and interface analysis, 1994. **21**(3): p. 165-176.

99. Chen, T., et al., *The effects of deposition temperature and ambient on the physical and electrical performance of DC-sputtered n-ZnO/p-Si heterojunction.* Applied Physics A, 2010. **98**: p. 357-365.

100. Tuomisto, F., et al., *Observation of Zn vacancies in ZnO grown by chemical vapor transport.* physica status solidi (b), 2006. **243**(4): p. 794-798.

101. Xu, S. and Z.L. Wang, *One-dimensional ZnO nanostructures: Solution growth and functional properties.* Nano Research, 2011. **4**(11): p. 1013-1098.

102. Hofmann, D.M., et al., *Properties of the oxygen vacancy in ZnO.* Applied Physics A, 2007. **88**(1): p. 147-151.

103. Park, C.H., S.B. Zhang, and S.-H. Wei, *Origin of p-type doping difficulty in ZnO: The impurity perspective.* Physical Review B, 2002. **66**(7): p. 073202.

104. Tsukazaki, A., et al., *Repeated temperature modulation epitaxy for p-type doping and light-emitting diode based on ZnO.* Nature Materials, 2005. **4**(1): p. 42-46.

105. Gao, P., et al., *Electrically Driven Redox Process in Cerium Oxides.* Journal of the American Chemical Society, 2010. **132**(12): p. 4197-4201.

106. Grinberg, I., et al., *Perovskite oxides for visible-light-absorbing ferroelectric and photovoltaic materials.* Nature, 2013. **503**(7477): p. 509-512.

107. Janotti, A. and C.G. Van de Walle, *Native point defects in ZnO.* Physical Review B, 2007. **76**(16): p. 165202.

108. Lany, S. and A. Zunger, *Assessment of correction methods for the band-gap problem and for finite-size effects in supercell defect calculations: Case studies for ZnO and GaAs.* Physical Review B, 2008. **78**(23): p. 235104.

109. Halliburton, L.E., et al., *Production of native donors in ZnO by annealing at high temperature in Zn vapor.* Applied Physics Letters, 2005. **87**(17).

110. Liu, L., et al., *Oxygen vacancies: The origin of n-type conductivity in ZnO.* Physical Review B, 2016. **93**(23): p. 235305.

111. Anantachaisilp, S., et al., *Nature of red luminescence in oxygen treated hydrothermally grown zinc oxide nanorods.* Journal of Luminescence, 2015. **168**: p. 20-25.

112. Parashar, S.K.S., et al., *Investigation of intrinsic defects in core-shell structured ZnO nanocrystals.* Journal of Applied Physics, 2012. **111**(11).

113. Lai, L.-W. and C.-T. Lee, *Investigation of optical and electrical properties of ZnO thin films.* Materials Chemistry and Physics, 2008. **110**(2-3): p. 393-396.

114. Chen, M., et al., *X-ray photoelectron spectroscopy and auger electron spectroscopy studies of Al-doped ZnO films.* Applied Surface Science, 2000. **158**(1-2): p. 134-140.

115. McCluskey, M.D. and S.J. Jokela, *Defects in ZnO.* Journal of Applied Physics, 2009. **106**(7).

116. Léonard, F. and J. Tersoff, *Role of Fermi-Level Pinning in Nanotube Schottky Diodes.* Physical Review Letters, 2000. **84**(20): p. 4693-4696.

117. Kim, C., et al., *Fermi Level Pinning at Electrical Metal Contacts of Monolayer Molybdenum Dichalcogenides.* ACS Nano, 2017. **11**(2): p. 1588-1596.

118. Sotthewes, K., et al., *Universal Fermi-Level Pinning in Transition-Metal Dichalcogenides.* The Journal of Physical Chemistry C, 2019. **123**(9): p. 5411-5420.

119. Bampoulis, P., et al., *Defect Dominated Charge Transport and Fermi Level Pinning in MoS2/Metal Contacts.* ACS Applied Materials & Interfaces, 2017. **9**(22): p. 19278-19286.

120. Léonard, F. and A.A. Talin, *Electrical contacts to one- and two-dimensional nanomaterials.* Nature Nanotechnology, 2011. **6**(12): p. 773-783.

121. Sapankaew, M., W. Dumnernpanich, and Y. Jompol, *Near-infrared photodetection using random networks of single-walled carbon nanotubes with asymmetrical work-function electrodes.* Materials Research Express, 2021. **8**(6).

122. Covington, L.R. and J.C. Moore, *Photoconductivity and transient response of Al:ZnO:Al planar structures fabricated via a thermal oxidation process.* Thin Solid Films, 2013. **540**: p. 106-111.

123. Sapankaew, M., W. Dumnernpanich, and Y. Jompol, *Near-infrared photodetection using random networks of singlewalled carbon nanotubes with asymmetrical work-function electrodes.* Mater. Res. Express, 2021. **8**(066303).

124. Manning, H.G., et al., *Emergence of winner-takes-all connectivity paths in random nanowire networks.* Nat Commun, 2018. **9**(1): p. 3219.

125. Kotsilkova, R., et al., *Effects of sonochemical modification of carbon nanotubes on electrical and electromagnetic shielding properties of epoxy composites.* Composites Science and Technology, 2015. **106**: p. 85-92.

126. Wang, J., et al., *Investigation of nonlinear I–V behavior of CNTs filled polymer composites.* Materials Science and Engineering: B, 2016. **206**: p. 55-60.

127. Ouyang, W., et al., *Enhancing the Photoelectric Performance of Photodetectors Based on Metal Oxide Semiconductors by Charge‐Carrier Engineering.* Advanced Functional Materials, 2019. **29**(9).

128. Alba-Martin, M., et al., *Improved memory behaviour of single-walled carbon nanotubes charge storage nodes.* Journal of Physics D: Applied Physics, 2012. **45**(29).

129. Engström, O., *The MOS System*. 2014: Cambridge University Press.

130. Sze, S.M., Y. Li, and K.K. Ng, *Physics of semiconductor devices*. 2021: John wiley & sons.

131. Zeze, D.A., *Metal Oxide Semiconductor Devices Basic MOS structure*. Vol. in: Handouts 01-ENGI

3331- Semicond. Phys. Devices. 25.

132. Fiissel, W., et al., *Defects at the Si:SiO 2 interface- their nature and behaviour in technological processes and stress.* Nuclear Instruments and Methods in Physics Research, 1996(377): p. 177-183.

133. Ziff, R.M., *Spanning probability in 2D percolation.* Phys Rev Lett, 1992. **69**(18): p. 2670-2673.

134. Reynolds, P.J., H.E. Stanley, and W. Klein, *LARGE-CELL MONTE-CARLO RENORMALIZATION-GROUP FOR PERCOLATION.* Physical Review B, 1980. **21**(3): p. 1223-1245.

135. Hovi, J. and A. Aharony, *Scaling and universality in the spanning probability for percolation.* Phys Rev E Stat Phys Plasmas Fluids Relat Interdiscip Topics, 1996. **53**(1): p. 235-253.

136. Newman, M.E.J. and R.M. Ziff, *Efficient Monte Carlo algorithm and high-precision results for percolation.* Physical Review Letters, 2000. **85**(19): p. 4104-4107.

137. Langlands, R.P., et al., *On the Universality of Crossing Probabilities in Two-Dimensional Percolation.* Journal of Statistical Physics, 1992. **67**.

138. Pike, G.E. and C.H. Seager, *Percolation and conductivity: A computer study. I.* Physical Review B, 1974. **10**(4): p. 1421-1434.

139. Balberg, I. and N. Binenbaum, *COMPUTER STUDY OF THE PERCOLATION-THRESHOLD IN A TWO-DIMENSIONAL ANISOTROPIC SYSTEM OF CONDUCTING STICKS.* Physical Review B, 1983. **28**(7): p. 3799-3812.

140. Ambrosetti, G., I. Balberg, and C. Grimaldi, *Percolation-to-hopping crossover in conductor-insulator composites.* Physical Review B, 2010. **82**(13).

141. Li, J. and S.L. Zhang, *Conductivity exponents in stick percolation.* Phys Rev E Stat Nonlin Soft Matter Phys, 2010. **81**(2 Pt 1): p. 021120.

142. Yook, S.-H., W. Choi, and Y. Kim, *Conductivity of stick percolation clusters with anisotropic alignments.* Journal of the Korean Physical Society, 2012. **61**(8): p. 1257-1262.

143. Žeželj, M. and I. Stanković, *From percolating to dense random stick networks: Conductivity model investigation.* Physical Review B, 2012. **86**(13).

144. Klatt, M.A., G.E. Schröder-Turk, and K. Mecke, *Anisotropy in finite continuum percolation: threshold estimation by Minkowski functionals.* Journal of Statistical Mechanics: Theory and Experiment, 2017. **2017**(2).

145. Ni, X., et al., *Monte Carlo simulations of electrical percolation in multicomponent thin films with nanofillers.* Nanotechnology, 2018. **29**(7): p. 075401.

146. Benda, R., E. Cancès, and B. Lebental, *Effective resistance of random percolating networks of stick nanowires: Functional dependence on elementary physical parameters.* Journal of Applied Physics, 2019. **126**(4).

147. Pike, G.E., & Seager, C. H., *Percolation and conductivity: A computer study I.* Phys Rev B, 1974. **10**(4).

148. Baara, Y., et al., *Modeling percolation in polydisperse systems.* EPL (Europhysics Letters), 2013. **102**(4).

149. Mahmassani, H.S., *50th Anniversary Invited Article—Autonomous Vehicles and Connected Vehicle Systems: Flow and Operations Considerations.* Transportation Science, 2016. **50**(4): p. 1140-1162.

150. Talebpour, A., H.S. Mahmassani, and S.H. Hamdar, *Effect of Information Availability on Stability of Traffic Flow: Percolation Theory Approach.* Transportation Research Procedia, 2017. **23**: p. 81-100.

151. Glauche, I., et al., *Continuum percolation of wireless ad hoc communication networks.* Physica A: Statistical Mechanics and its Applications, 2003. **325**(3): p. 577-600.

152. Liu, L., X. Zhang, and H. Ma, *Percolation Theory-Based Exposure-Path Prevention for Wireless Sensor Networks Coverage in Internet of Things.* IEEE Sensors Journal, 2013. **13**(10): p. 3625-3636.

153. Barabási, A.-L., *Network science.* Philosophical Transactions of the Royal Society A: Mathematical, Physical and Engineering Sciences, 2013. **371**(1987): p. 20120375.

154. Li, M., et al., *Percolation on complex networks: Theory and application.* Physics Reports, 2021. **907**: p. 1-68.

155. Zezelj, M., I. Stankovic, and A. Belic, *Finite-size scaling in asymmetric systems of percolating sticks.* Phys Rev E Stat Nonlin Soft Matter Phys, 2012. **85**(2 Pt 1): p. 021101.

156. Tarasevich, Y.Y. and A.V. Eserkepov, *Percolation of sticks: Effect of stick alignment and length dispersity.* Physical Review E, 2018. **98**(6).

157. Brereton, T., et al., *A critical exponent for shortest-path scaling in continuum percolation.* Journal of Physics A: Mathematical and Theoretical, 2014. **47**(50).

158. Newman, M.E. and R.M. Ziff, *Fast Monte Carlo algorithm for site or bond percolation.* Phys Rev E Stat Nonlin Soft Matter Phys, 2001. **64**(1 Pt 2): p. 016706.

159. Ziff, R.M. and M.E. Newman, *Convergence of threshold estimates for two-dimensional percolation.* Phys Rev E Stat Nonlin Soft Matter Phys, 2002. **66**(1 Pt 2): p. 016129.

160. Yao, H., et al., *Modelling electrical conduction in nanostructure assemblies through complex networks.* Nat Mater, 2020. **19**(7): p. 745-751.

161. Alhalabi, M., et al. *Modelling of SiC Power MOSFET in Matlab, Simulink, and LTSpice*. in *2018 IEEE International Conference on Environment and Electrical Engineering and 2018 IEEE Industrial and Commercial Power Systems Europe (EEEIC / I&CPS Europe)*. 2018.

162. Devices, A. *LTspice XVII*. LTspice XVII 2024; Available from: https://www.analog.com/en/resources/design-tools-and-calculators/ltspice-simulator.html.

163. Cazimajou, T., et al., *Analysis of the role of inter-nanowire junctions on current percolation effects in silicon nanonet field-effect transistors.* Solid-State Electronics, 2020. **168**.

164. Fata, N., et al., *Effect of junction-to-nanowire resistance ratio on the percolation conductivity and critical exponents of nanowire networks.* Journal of Applied Physics, 2020. **128**(12).

165. Hicks, J., A. Behnam, and A. Ural, *Resistivity in percolation networks of one-dimensional elements with a length distribution.* Phys Rev E Stat Nonlin Soft Matter Phys, 2009. **79**(1 Pt 1): p. 012102.

166. BALBERG, I., et al., *PERCOLATION AND TUNNELING IN COMPOSITE MATERIALS.* International Journal of Modern Physics B, 2004. **18**(15): p. 2091-2121.

167. Balberg, I., et al., *Excluded volume and its relation to the onset of percolation.* Physical Review B, 1984. **30**(7): p. 3933-3943.

168. Bauhofer, W. and J.Z. Kovacs, *A review and analysis of electrical percolation in carbon nanotube polymer composites.* Composites Science and Technology, 2009. **69**(10): p. 1486-1498.

169. Behnam, A. and A. Ural, *Computational study of geometry-dependent resistivity scaling in single-walled carbon nanotube films.* Physical Review B, 2007. **75**(12).

170. White, S.I., et al., *Electrical Percolation Behavior in Silver Nanowire–Polystyrene Composites: Simulation and Experiment.* Advanced Functional Materials, 2010. **20**(16): p. 2709-2716.

171. Hu, T. and B.I. Shklovskii, *Theory of hopping conductivity of a suspension of nanowires in an insulator.* Physical Review B, 2006. **74**(5).

172. Vodolazskaya, I.V., et al., *Effect of tunneling on the electrical conductivity of nanowire-based films: Computer simulation within a core–shell model.* Journal of Applied Physics, 2019. **126**(24).

173. He, L., E. Kogan, and D. Luo, *Shortest path across a mesoscopic system.* Physical Review B, 2003. **67**(11).

174. Miranda, E., G. Milano, and C. Ricciardi, *Compact Modeling of the I-V Characteristics of ZnO Nanowires Including Nonlinear Series Resistance Effects.* IEEE Transactions on Nanotechnology, 2020. **19**: p. 297-300.

175. *<1983 - Computer study of the percolation threshold in a two-dimensional anisotropic system of conducting sticks .pdf>.*

176. Yingying, L., et al., *Facile fabrication of UV photodetectors based on ZnO nanorod networks across trenched electrodes.* Journal of Semiconductors, 2009. **30**(6).

177. Kumar, M., H. Jeong, and D. Lee, *UV photodetector with ZnO nanoflowers as an active layer and a network of Ag nanowires as transparent electrodes.* Superlattices and Microstructures, 2019. **126**: p. 132-138.

178. Abdalla, J.T., et al., *Enhanced Ag@SnO₂Plasmonic Nanoparticles for Boosting Photoluminescence and Photocurrent Response of ZnO Nanorod UV Photodetectors.* Journal of Electronic Materials, 2020. **49**(9): p. 5657-5665.

179. Ilickas, M., et al., *ZnO UV sensor photoresponse enhancement by coating method optimization.* Journal of Photochemistry and Photobiology, 2023. **14**: p. 100171.

180. Jun, J.H., et al., *Ultraviolet photodetectors based on ZnO nanoparticles.* Ceramics International, 2009. **35**(7): p. 2797-2801.

181. Young, S.J. and Y.H. Liu, *Pd Nanoparticle Adsorption ZnO Nanorods for Enhancing Photodetector UV-Sensing performance.* Ieee Journal of the Electron Devices Society, 2021. **9**: p. 265-270.

182. Pei, J.N., et al., *Effect of Pt NPs in the film on the performances of ZnO-based metal-semiconductor-metal structured ultraviolet photodetector.* Acta Physica Sinica, 2015. **64**(6).

183. Pallavolu, M.R., et al., *High-responsivity self-powered UV photodetector performance of pristine and V-doped ZnO nano-flowers.* Optics and Laser Technology, 2023. **157**.

184. Lin, S.S., et al., *Hybrid UV Photodetector Design Incorporating AuPt Alloy Hybrid Nanoparticles, ZnO Quantum Dots, and Graphene Quantum Dots.* Acs Applied Materials & Interfaces, 2023. **15**(1): p. 2204-2215.

185. Li, M., et al., *Optimizing the performance of ZnO/Au/MgZnO/SiO₂ sandwich structured UV photodetectors by surface plasmons in Ag nanoparticles.* Applied Physics a-Materials Science & Processing, 2020. **126**(4).

186. Kumar, Y., et al., *Spectrum Selectivity and Responsivity of ZnO Nanoparticles Coated Ag/ZnO QDs/Ag UV Photodetectors.* Ieee Photonics Technology Letters, 2018. **30**(12): p. 1147-1150.

187. Khan, R., et al., *Enhanced photocurrent performance of partially decorated Au nanoparticles on ZnO nanorods based UV photodetector.* Materials Research Bulletin, 2019. **115**: p. 176-181.

188. Hwang, J.D., et al., *Annealing effects of Au nanoparticles on the surface-plasmon enhanced p-Si/n-ZnO nanorods heterojunction photodetectors.* Journal of Applied Physics, 2014. **115**(17).

189. Hsu, C.L., K.C. Chen, and T.J. Hsueh, *UV Photodetector of a Homojunction Based On p-Type Sb-Doped ZnO Nanoparticles and n-Type ZnO Nanowires.* Ieee Transactions on Electron Devices, 2014. **61**(5): p. 1347-1353.

190. Hosseini, Z.S., et al., *High-performance UV-Vis-NIR photodetectors based on plasmonic effect in Au nanoparticles/ZnO nanofibers.* Applied Surface Science, 2019. **483**: p. 1110-1117.

191. Dolatyari, M., et al., *UV/IR Dual-Wavelength Photodetector Design Based on ZnO/PMMA/PbSe Nanocomposites.* Ieee Transactions on Nanotechnology, 2018. **17**(3): p. 574-581.

192. Dang, V.Q., et al., *Ultrahigh Responsivity in Graphene-ZnO Nanorod Hybrid UV Photodetector.* Small, 2015. **11**(25): p. 3054-3065.

193. Hong, S.H. and J.W. Kang, *Plasmonic Enhancement of UV Photoresponse in Graphene/ZnO Schottky Diode with Pt Nanoparticles.* Applied Science and Convergence Technology, 2022. **31**(6): p. 133-136.

194. Zeng, H., et al., *Blue Luminescence of ZnO Nanoparticles Based on Non‐Equilibrium Processes: Defect Origins and Emission Controls.* Advanced Functional Materials, 2010. **20**(4): p. 561-572.

195. Soci, C., et al., *ZnO Nanowire UV Photodetectors with High Internal Gain.* Nano Letters, 2007. **7**(4): p. 1003-1009.

196. Zhao, X., et al., *Recent Progress in Ohmic/Schottky-Contacted ZnO Nanowire Sensors.* Journal of Nanomaterials, 2015. **2015**: p. 1-20.

197. Cheng-Ying, C., et al., *Enhanced Recovery Speed of Nanostructured ZnO Photodetectors Using Nanobelt Networks.* IEEE Journal of Selected Topics in Quantum Electronics, 2012. **18**(6): p. 1807-1811.

198. Ayaz, S., et al., *Tunable ultraviolet sensing performance of Al-modified ZnO nanoparticles.* Journal of Alloys and Compounds, 2021. **884**.

199. Lupan, O., et al., *UV nanophotodetectors: A case study of individual Au-modified ZnO nanowires.* Sensors and Actuators A: Physical, 2019. **296**: p. 400-408.

200. Noh, Y., et al., *Decoration of Ag Nanoparticle on ZnO Nanowire by Intense Pulsed Light and Enhanced UV Photodetector.* Chemosensors, 2021. **9**(11).

201. Nasiri, N., et al., *Ultraporous Electron-Depleted ZnO Nanoparticle Networks for Highly Sensitive Portable Visible-Blind UV Photodetectors.* Advanced Materials, 2015. **27**(29): p. 4336-4343.

202. Gu, X., et al., *Influences of different interdigital spacing on the performance of UV photodetectors based on ZnO nanofibers.* Applied Surface Science, 2014. **307**: p. 20-23.

203. Noh, Y., H. Jeong, and D. Lee, *Enhanced ultraviolet photodetector using zinc oxide nanowires with intense pulsed light post-treatment.* Journal of Alloys and Compounds, 2021. **871**: p. 159537.

204. Lien, D.H., et al., *Surface effects in metal oxide-based nanodevices.* Nanoscale, 2015. **7**(47): p. 19874-84.

205. Singh, S., *Al doped ZnO based MISIM ultraviolet photodetectors.* Microsystem Technologies, 2016. **23**(4): p. 999-1003.

206. Young, S.J., et al., *Fabrication of Silicon Dioxide by Photo-Chemical Vapor Deposition to Decrease Detector Current of ZnO Ultraviolet Photodetectors.* ACS Omega, 2020. **5**(42): p. 27566-27571.

207. Ouyang, W.X., et al., *Improved Photoelectric Performance of UV Photodetector Based on ZnO Nanoparticle-Decorated BiOCl Nanosheet Arrays onto PDMS Substrate: The Heterojunction and Ti₃C₂T_x MXene Conduction Layer.* Advanced Electronic Materials, 2020. **6**(6).

208. Mishra, Y.K., et al., *Direct Growth of Freestanding ZnO Tetrapod Networks for Multifunctional Applications in Photocatalysis, UV Photodetection, and Gas Sensing.* ACS Applied Materials & Interfaces, 2015. **7**(26): p. 14303-14316.

209. Lupan, O., et al., *Wavelength-Emission Tuning of ZnO Nanowire-Based Light-Emitting Diodes by Cu Doping: Experimental and Computational Insights.* Advanced Functional Materials, 2011. **21**(18): p. 3564-3572.

210. Agrawal, J., et al., *Development of Reliable and High Responsivity ZnO-Based UV-C Photodetector.* Ieee Journal of Quantum Electronics, 2020. **56**(1).

211. Lin, J.-C., et al., *Improvement of a capacitive UV-sensor by porous silicon powders embedded in epoxy on porous silicon film.* Optical Materials Express, 2022. **12**(8): p. 3143-3151.

212. Saha, T., T.Q. Lin, and A.A. Mohanan, *Flexible Capacitive UV Sensor for Future Wearables*, in *IEEE International Conference on Flexible and Printable Sensors and Systems (FLEPS)*. 2019, IEEE.

213. Sakthivelpathi, V., et al., *Advancements and applications of micro and nanostructured capacitive sensors: A review.* Sensors and Actuators A: Physical, 2024. **377**: p. 115701.

214. Guterman, D.C., et al., *An electrically alterable nonvolatile memory cell using a floating-gate structure.* IEEE Transactions on Electron Devices, 1979. **26**(4): p. 576-586.

215. El-Atab, N., et al., *Nanoislands-Based Charge Trapping Memory: A Scalability Study.* Ieee Transactions on Nanotechnology, 2017. **16**(6): p. 1143-1146.

216. Kim, K. and J. Choi. *Future outlook of NAND flash technology for 40nm node and beyond*. in *2006 21st IEEE Non-Volatile Semiconductor Memory Workshop*. 2006. IEEE.

217. Pavan, P., et al., *Flash memory cells-an overview.* Proceedings of the IEEE, 1997. **85**(8): p. 1248-1271.

218. Jung, J.-W. and W.-J. Cho, *Tunnel barrier engineering for non-volatile memory.* JSTS: Journal of Semiconductor Technology and Science, 2008. **8**(1): p. 32-39.

219. El-Atab, N., et al., *Enhanced memory effect via quantum confinement in 16 nm InN nanoparticles embedded in ZnO charge trapping layer.* Applied Physics Letters, 2014. **104**(25).

220. Zhao, C., et al., *Grain size dependence of dielectric relaxation in cerium oxide as high-k layer.* Nanoscale Research Letters, 2013. **8**(1): p. 172.

221. Kim, H.J., S.Y. Cha, and D.J. Choi, *Memory characteristics of Al2O3/La2O3/Al2O3 multi-layer films with various blocking and tunnel oxide thicknesses.* Materials Science in Semiconductor Processing, 2010. **13**(1): p. 9-12.

222. Neamen, D.A., *An introduction to semiconductor devices.* Boston: McGraw Hill, 2006.

223. TREDWELL, T.J. and C.R. VISWANATHA, *DETERMINATION OF INTERFACE-STATE PARAMETERS IN A MOS CAPACITOR BY DLTS.* Solid-State Electronics, 1980. **23**: p. 1171-1178.

224. Kimbugwe, N.T. and E. Yilmaz, *Impact of SiO2 interfacial layer on the electrical characteristics of Al/ Al2O3/SiO2/n ‑ Si metal ‑oxide ‑semiconductor capacitors.* Journal of Materials Science: Materials in Electronics, 2020. **31**: p. 12372–12381.

225. Lee, S.H., Y. Jung, and R. Agarwal, *Highly scalable non-volatile and ultra-low-power phase-change nanowire memory.* Nat Nanotechnol, 2007. **2**(10): p. 626-30.

226. Oh, D.-H., et al., *Enhancement of the Memory Effects for Nonvolatile Memory Devices Fabricated Utilizing ZnO Nanoparticles Embedded in a Si3N4 Layer.* Journal of Nanoscience and Nanotechnology, 2010. **10**: p. 3508–3511.

227. Sleiman, A., et al., *Pentacene-based metal-insulator- semiconductor memory structures utilizing single walled carbon nanotubes as a nanofloating gate.* APPLIED PHYSICS LETTERS, 2012. **100**(023302): p. 1-4.

228. Gullu, H.H. and D.E. Yildiz, *Temperature and frequency effects on electrical and dielectric properties of n-4H SiC based metal–insulator-semiconductor (MIS) diode interlayered with Si3N4 thin film.* Journal of Materials Science: Materials in Electronics, 2020. **31**(11): p. 8705-8717.

229. Tanrıkulu, E.E., et al., *On the anomalous peak and negative capacitance in the capacitance–voltage (C–V) plots of Al/(%7 Zn-PVA)/p-Si (MPS) structure.* Journal of Materials Science: Materials in Electronics, 2017. **29**(4): p. 2890-2898.

230. I. Zailer, et al., *Crosslinked PMMA as a high-resolution negative resist for electron beam lithography and applications for physics of low-dimensional structures.* Semiconductor science and technology, 2021. **11**: p. 1235.

231. Zhang, H.Q., Y. Jin, and Y. Qiu, *The optical and electrical characteristics of PMMA film prepared by spin coating method.* IOP Conf. Series: Materials Science and Engineering, 2015. **87**(012032).

232. Núñez, C.G., et al., *Energy-Autonomous, Flexible, and Transparent Tactile Skin.* Advanced Functional Materials, 2017. **27**(18): p. 1606287.

233. Ma, S., et al., *Highly Sensitive Flexible Capacitive Pressure Sensor with ZnO NW interlayers*, in *2021 IEEE International Conference on Flexible and Printable Sensors and Systems (FLEPS)*. 2021. p. 1-4.

234. Cho, S., et al., *Large-Area Cross-Aligned Silver Nanowire Electrodes for Flexible, Transparent, and Force-Sensitive Mechanochromic Touch Screens.* ACS Nano, 2017. **11**(4): p. 4346-4357.

235. Liu, C., et al., *Highly stable pressure sensor based on carbonized melamine sponge using fully wrapped conductive path for flexible electronic skin.* Organic Electronics, 2020. **76**: p. 105447.

236. Li, T., et al., *Flexible Capacitive Tactile Sensor Based on Micropatterned Dielectric Layer.* Small, 2016. **12**(36): p. 5042-5048.

237. Ayling, J.K., R.D. Moore, and G.K. Tu. *A high-performance monolithic store*. in *IEEE Int Solid-State Circuits*. 1969. Philadelphia.

238. Mishra, S., et al., *Sensitivity Analysis of ZnO NWs Based Soft Capacitive Pressure Sensors using Finite Element Modeling*, in *IEEE International Conference on Flexible and Printable Sensors and Systems (FLEPS)*. 2022, IEEE.

239. Kumaresan, Y., et al., *Soft Capacitive Pressure Sensor With Enhanced Sensitivity Assisted by ZnO NW Interlayers and Airgap.* IEEE Sensors Journal, 2022. **22**(5): p. 3974-3982.

240. Chen, Y.S., et al., *Zinc oxide nanowire-poly(methyl methacrylate) dielectric layers for polymer capacitive pressure sensors.* ACS Appl Mater Interfaces, 2015. **7**(1): p. 45-50.

241. Shang, S.G., et al., *Fabrication and Performance of UV Photodetector of ZnO Nanorods Decorated with Al Nanoparticles.* Nanomaterials, 2022. **12**(21).

242. Dang, Z.-M., et al., *Dielectric behavior and dependence of percolation threshold on the conductivity of fillers in polymer-semiconductor composites.* Applied Physics Letters, 2004. **85**(1): p. 97-99.

243. Inamdar, S.I. and K.Y. Rajpure, *High-performance metal-semiconductor-metal UV photodetector based on spray deposited ZnO thin films.* Journal of Alloys and Compounds, 2014. **595**: p. 55-59.

244. Yun, J., et al., *A Patterned Graphene/ZnO UV Sensor Driven by Integrated Asymmetric Micro-Supercapacitors on a Liquid Metal Patterned Foldable Paper.* Advanced Functional Materials, 2017. **27**(30): p. 1700135.